VALIDATION AND APPLICATION OF THE SMALL SAMPLE PUNCH TEST FOR TOUGHNESS MEASUREMENT OF STEELS

Prepared by:

ANDREW HLUPO

HLPAND001

Department of Mechanical Engineering

University of Cape Town

Supervisor:

Professor Robert Knutsen

PLAGIARISM DECLARATION

I, Andrew Hlupo, hereby declare that this dissertation is based on my original work except which is properly acknowledged. I declare that I understand the meaning of plagiarism and its consequences. I understand that neither the whole work nor part of has been, is being or will be submitted for another degree. I confirm I have the consent of my supervisor to submit this dissertation as any concerns that might arise has been resolved.

I have applied the IEEE referencing style in this dissertation. I give the university the right to reproduce the whole or part of this dissertation for research.

Signature: Signed by candidate

Date: 17/02/2025

ABSTRACT

Power generation plants and utilities are ideally supposed to last for decades, thus there is need for suitable and innovative analytic methods that enhance the life of these vital components. The integrity, efficiency, and capacity of these components is impaired by damage mechanisms like creep and embrittlement which in turn affect the safety and operation of the power generating plants. The quasi-non-destructive small punch test (SPT) method was developed to determine the integrity and mechanical properties of materials with use of minimal material removal from components being examined, improving on the conventional mechanical test methods which require a substantial amount of material for analysis.

Numerous attempts have been made to examine, validate, and interpret the data and information that is obtained from SPTs, resulting in various methods and approaches adopted. Previous work has failed to provide a less complex and more straightforward interpretation of the inhomogeneous and multiaxial stress and deformation distribution in an SPT sample during and after testing. A key concern in proving the reliability of the SPT is the determination of the onset of cracking during the test, hence the introduction of Digital Image Correlation (DIC) to advance the crack detection.

The SPT method, carried out with a rig designed and built in the CME at UCT, was then validated using an “off the shelf” material whose properties could be reliably determined using conventional mechanical test techniques. The material underwent carefully controlled and repeatable heat treatments to obtain the required range in toughness properties from the same material. The tensile test, fracture toughness test and the Charpy V-Notch (CVN) test were conducted on MACSTEEL VRN 500, a high hardness low alloy martensitic steel grade which was heat treated in order to demonstrate high, medium, and low fracture toughness properties. The results from these conventional mechanical tests were characterised reliably, then correlated with the findings from the SPT technique using arithmetic and empirical correlations which exhibited high goodness of fit values.

The use of DIC and the Dantec Istra 4D software on the SPTs was adopted and utilised to characterise the data that was obtained from the test further, allowing the observation of both the top surface (deflection with DIC) and bottom surface in contact with the SPT punch (displacement). A combination of DIC and strain energy density (SED) analysis was employed to detect the crack initiation on the specimen surface. The results from this study demonstrated the effectiveness of using the SPT method as a suitable quasi-non-destructive method to evaluate mechanical properties, including yield strength, ultimate tensile strength and toughness of steel structures, using small specimen samples.

ACKNOWLEDGEMENTS

First and foremost, I would like to take this opportunity to thank God for taking me this far, only He knows where I would have been today if it was not for him and the gift of life that he grants us each day.

I would also like to express my sincere gratitude to my supervisor, Professor Robert Knutsen, for his invaluable guidance, support, and encouragement throughout the course of this research. I would like to show my appreciation for his patience, insights and expertise which have been instrumental in shaping this dissertation.

I would also like to extend my heartfelt thanks to the staff and colleagues at the University of Cape Town particularly the team in CME and in the workshop, whose assistance and support made my experimental work possible. Special thanks to Dr Richard Curry for his help in framing the approach for this dissertation, to Penny Louw, Chenesai Nyakunu and Soraya von Willingh for their help with the laboratory equipment, testing procedures, and technical support during my research. I would also like to thank the University of Cape Town for being the institution that has guided my Engineering career, from my first day studying the BSc in Mechanical Engineering to who I am today.

A special mention goes to the Eskom Power Plant Engineering Institute (EPPEI) for providing the financial support that allowed me to undertake this project. I would also like to thank the Board of Directors at Sinani Energy for their support in my pursuit of this MSc qualification. I am also grateful to my fellow research colleagues and friends, Tinashe Jambo, the Derodor boys and the Orpington Oga family for the countless discussions, encouragement, and moments of camaraderie that made this journey possible.

Finally, I would like to thank my family, mom, dad, Junior, Mufaro, Lisa, Cordula and Kunashe, who have all contributed by being a constant source of strength, inspiration and motivation for me throughout this journey.

TABLE OF CONTENTS

TABLE OF FIGURES

LIST OF TABLES

NOMENCLATURE

SPT	Small Punch Test
LDC	Load Displacement Curve
DIC	Digital Image Correlation
LVDT	Linear Variable Differential Transformer
AR	As Received
HT1	Heat Treatment 1
HT2	Heat Treatment 2
E_{SP}	Small Punch Energy (J)
E_{crack}	Small Punch Energy up to crack initiation (J)
DBTT	Ductile to Brittle Transition Temperature (^{o}C)
FATT	Fracture Appearance Transition Temperature (^{o}C)
UTS	Ultimate Tensile Stress (MPa)
U_T	Modulus of Toughness (MJ/m^3)
YS	Yield Stress (MPa)
S-o-D	Standoff Distance (mm)
FCC	Face-Centred Cubic
BCC	Body-Centred Cubic

BCT	Body-Centred Tetragonal
USE	Upper Shelf Energy (J)
LSE	Lower Shelf Energy (J)
CWA	CEN Workshop Agreement
EPRI	Electrical Power Research Institute
CVN	Charpy V-Notch
SED	Strain Energy Density (J/m^3)

CHAPTER 1: INTRODUCTION

1.1 BACKGROUND

Analysis of engineering components in a safe, economic and convenient way has been of critical importance in recent years. The performance analysis of traditional testing techniques is hindered by severe conditions encountered during operation such as high temperatures, high pressure, irradiation and high prices. There is also a case of high volumes of material being required for conventional measurement which in turn restricts the investigation of in-service components. Thus, various miniature specimen tests to evaluate the mechanical properties of materials in engineering practice, such as small punch tests, shear punch tests, nano- indentation etc. have been proposed [1].

Toughness can be defined as the energy absorbing ability of a material before fracture, making it a critical mechanical property required in engineering applications. A combination of yield strength, elongation and tensile strength collectively determines the ability of the material to withstand deformation and resist failure [2], [3], [4]. The ability of a material to absorb energy before fracture is affected by phenomena like embrittlement, which result in premature fracture occurring with less energy absorbed.

Experience suggests that the number of instances where the necessary combination of circumstances required for rapid brittle fracture to occur is small. However, when fractures of this type do occur, the consequences can be catastrophic [5]. Power generation plants are usually expected to last for decades, thus there is need for innovation in material testing and research so that remaining life analysis can be enhanced. Damage mechanisms like creep, hydrogen embrittlement, hydrogen attack and temper embrittlement can impair the integrity of the plant. The efficiency, capacity and safety of plants critically depends on the integrity of the components and their materials [6].

Many components in power plants, e.g. pressure vessels and steam pipes, operate at demanding conditions causing gradual degradation of the material properties and mechanical performance required for structural integrity. Miniaturized test techniques like the Small Punch Test (SPT) enable assessing this degradation and, hence, the residual lifetime during which safe operation of a component can be ensured. In applications where small-scale material sampling does not affect the structural integrity, SPT can be practically considered a non-destructive test that allows the mechanical performance assessment of structural materials to be evaluated with minimal material removal [7].

1.2 Research Justification and Objectives

The aim of this research is to establish and validate the reliability of the SPT for toughness measurement in steels. The SPT is a quasi-non-destructive test method that aims to provide the mechanical properties of a material using minimal test material. This enables the testing of vital mechanical components, assessing their material integrity while allowing operation and avoiding down time. Non-destructive testing can prove to be very beneficial particularly in the energy industry, as power plants can continue with operation but have components under material integrity assessment. Previous work has assessed material integrity through the SPT but the determination of the onset of crack detection has not been properly utilised in characterising the properties obtained from the test. This point of crack initiation in a load displacement curve (LDC) when identified could enable more elaborate information to be obtained from the SPT sample. The introduction of Digital Image Correlation (DIC) aims to assist in the establishment of an accurate method to detect crack onset and subsequently correlate the findings from the SPT curve with conventional mechanical tests.

This project therefore has the following objectives:

- Identify an "off the shelf" steel and carry out controlled and repeatable heat treatments to obtain required range in toughness properties
- Conduct conventional mechanical tests on the as-received and heat-treated materials (tensile, fracture toughness and Charpy V-Notch (CVN) tests) and obtain mechanical properties
- Carry out the SPTs on the as-received and heat-treated materials and obtain mechanical properties
- Utilise DIC to identify crack initiation on SPT specimens
- Validate and correlate the SPT findings with the results from the conventional mechanical tests (yield stress, tensile stress, toughness)

1.3 Research Scope and Limitations

This project investigates the mechanical properties and toughness of VRN500 steel, a NiCrMoV steel, through tensile, impact, fracture toughness and small punch testing. Attention was paid to the orientation of the material and subsequently the specimens to be tested, to ensure the consistency in the loading plane during tests. The tensile test specimens were machined and tested according to the ASTM E8 (**Chapter 3.5**). The fracture toughness specimens were machined in accordance with the ASTM E1820 and tested in accordance with the size insensitive approach proposed in the ASTM E399 (**Chapter 3.7**). The CVN and the SPT specimens were machined and tested according to the ASTM E23 (**Chapter 3.6**) and the CEN SIST EN 10371 (**Chapter 3.8**) respectively. All tests except for the CVN tests were conducted at room temperature. The SPT was carried out with DIC, allowing the test specimen deformation to be assessed through both the DIC cameras and the punch.

The SPT rig used in this project was designed by Ibrahim Stracey [8], a master's scholar in the Mechanical Engineering Department in 2019. The machine was limited in terms of elevated and low temperature tests, and the design could only cater to room temperature tests at the time of testing. This resulted in the small punch transition temperature not being established for the tested material, limiting the analysis and correlation of the fracture toughness and the CVN with the SPT.

Cryogenic testing was limited to use of liquid nitrogen, and these low temperature tests could only be done for CVN tests as these were manageable experiments with the available resources. High temperature tests for the CVN tests were limited to the boiling point of water, as a Bunsen burner, glass beaker and distilled water were the available resources. The fracture toughness test method that was adopted was to ensure results were obtained with minimal material usage as test material was limited and the required specimen sizes for valid fracture toughness, K_{IC} were unattainable. Attempts at using the fracture toughness machine at Stellenbosch University to instead obtain the plane strain fracture toughness, J_{IC}, were not successful as the machine was limited to a peak load of 20 kN, which would not suffice for the load unload procedure required for the J-R curve determination.

1.4 Theoretical Framework

In literature, the SPT is carried out at both cryogenic and elevated temperatures, and the material behaviour can be assessed under various conditions. The LDC provides data and load points that can be utilised in the correlation with conventional mechanical tests. The different load points on an LDC can be used to describe the condition of the material during the test and a direct relationship between these points and the mechanical properties observed in the conventional tests can be established. The area under the LDC represents the energy absorbed during the test and can be utilised as a valuable indicator of the toughness of the material. The use of test apparatus, methods in measuring test parameters and analysis can be inherited from literature. This research builds on existing literature by integration of DIC analysis techniques which allow the assessment of the specimen deformation to be improved, as both surfaces of the SPT specimen can be observed. This project adopts these various improved analytical methods and makes use of DIC to observe the test specimen surface opposite the punch contact, identify crack initiation and subsequently add depth to the characterisation of the material through this test. Formulations proposed in literature are used in this project to validate and correlate the SPT results with those obtained from the conventional mechanical tests.

1.5 Organisation of Dissertation

The next chapter in this dissertation, **Chapter 2**, contains the relevant literature that was reviewed. The chapter reviews briefly the power generation steel components, how integral they are in power plant production as well as the degradation factors that affect their toughness and integrity. It further outlines the evolution of the SPT and its test methods and examines the

limitations in existing studies that this study seeks to address**. Chapter 3** details the experimental methodology used in this project to obtain the mechanical properties of the material being tested, from the heat treatments to the post test results and analytical approaches employed. The results are presented and discussed in **Chapter 4**, and the relevant conclusions and recommendations are contained in **Chapter 5** and **Chapter 6** respectively.

CHAPTER 2: LITERATURE REVIEW

2.1 COAL-FIRED POWER PLANT

A power plant is a major source of contemporary electrical power which is a vital commodity in the modern world. Power plants comprise vital components in the entire system, and the performance of the materials used to manufacture these components has a direct influence on the functionality of the plant.

The designing of power plants now aims at lower fuel cost and carbon emissions through improving efficiency by increasing the steam pressure and temperatures to higher ranges. This led to the need to conduct research with emphasis on improvement of mechanical properties, corrosion resistance and fabricability of heat-resistant steels [9]. **Figure 1** below shows Kriel Power station in Mpumalanga province in South Africa.

Figure 1:Exterior view of Kriel Power Station [10]

Kriel Power Station generates 3000 MW, with an average production of 17 880 GWh over a three-year span, particularly between 2018 and 2021 [10]. In this section focus will be on the basic operations of a coal-fired power station. It will also look at the relevant steel components and structures, particularly those components exposed to extreme steam conditions, how they have evolved over time and how they function. An important aspect to assess as well is how these components relate to this project. The operating conditions of these components will assist in the comprehension of the effect of ageing and degradation on steel mechanical properties and subsequently the importance of a non-destructive test method to evaluate these properties.

2.1.1 Boiler

A boiler is a closed vessel that serves the purpose of producing heat by the combustion of fuel. This heat is then transferred to water in order to convert it into steam at desired temperature and pressure [11]. In coal power stations, there are high pressure and temperature ratings, and thus water-tube boilers are employed [12].

These boilers have three general types that can be supplied to meet all the requirements of operation. There is the natural circulation boiler type where circulation is due to the difference in density between the pipes feeding heated circuits and the steam and water mixture in the steaming tubes [12]. There is also the forced circulation type of unit which has pumps to ensure and assist circulation. Lastly, there is the once-through boiler which has a feed pump of appreciable pressure pumping the feedwater through the economizer through to the radiant and convective superheaters. The choice of the system to employ depends on the condition of operation, as some supercritical operations engage with pressures exceeding 41 MPa [12].

Figure 2: Boiler [13]

A control system is put in place as well, to maintain the steam outlet temperature to within $\pm 5^{o}$ of 593 ^{o}C [12]. Boilers are subjected to these high temperatures and pressures and as a result are constructed using heat resistant steel, a material suitable for the conditions of operation [14]. It is these materials that need to be tested non-destructively, in order to provide information on the state of the material.

2.1.2 HP and LP Turbines

The turbines derive their power from high pressure steam that exits the boiler. Burning fuel in the combustion chamber contributes heat energy to the superheater and the high-pressure steam is supplied at the inlet of the steam turbines. The steam turbines of large coal power stations are broken down into High-Pressure, Intermediate-Pressure and Low-Pressure turbines, each set with different blade size and function [15].

Modern coal-fired power plants with ultra-supercritical boilers can come close to 47% efficiency operating at standard temperatures. It is possible to reach 50% efficiency if the steam temperature is raised to 700 ^{o}C and 55% efficiency if steam temperature is pushed to 750 ^{o}C [15]. The temperature of this steam is limited by the creep life properties of the turbine material and these elevated steam temperatures push existing materials to the extremes of their capabilities [15]. For temperatures of steam exceeding 593 ^{o}C, it becomes necessary to use stronger steel materials because of the extra centrifugal stress in the rotor, blades, and other rotating parts. This results in resistivity to thermal fatigue and creep fatigue associated with repeated large thermal stresses being a critical material property [9]. **Figure 3** shows a high-pressure turbine at Majuba Power Station in Mpumalanga Highveld.

Figure 3: HP turbine at Majuba Power Station [16]

To reduce thermal stresses, it is desirable to use materials with a low coefficient of thermal expansion and high conductivity, as a low coefficient of thermal expansion reduces the difference in expansion between rotating and stationary parts. Ferrite steels are better than austenitic steels in this regard [9]. **Figure 4** shows a low-pressure turbine at Majuba Power Station, equipped with two double flow low-pressure cylinders and constructed with an internal and external steel casing to allow fast starting and rapid variations in load [16].

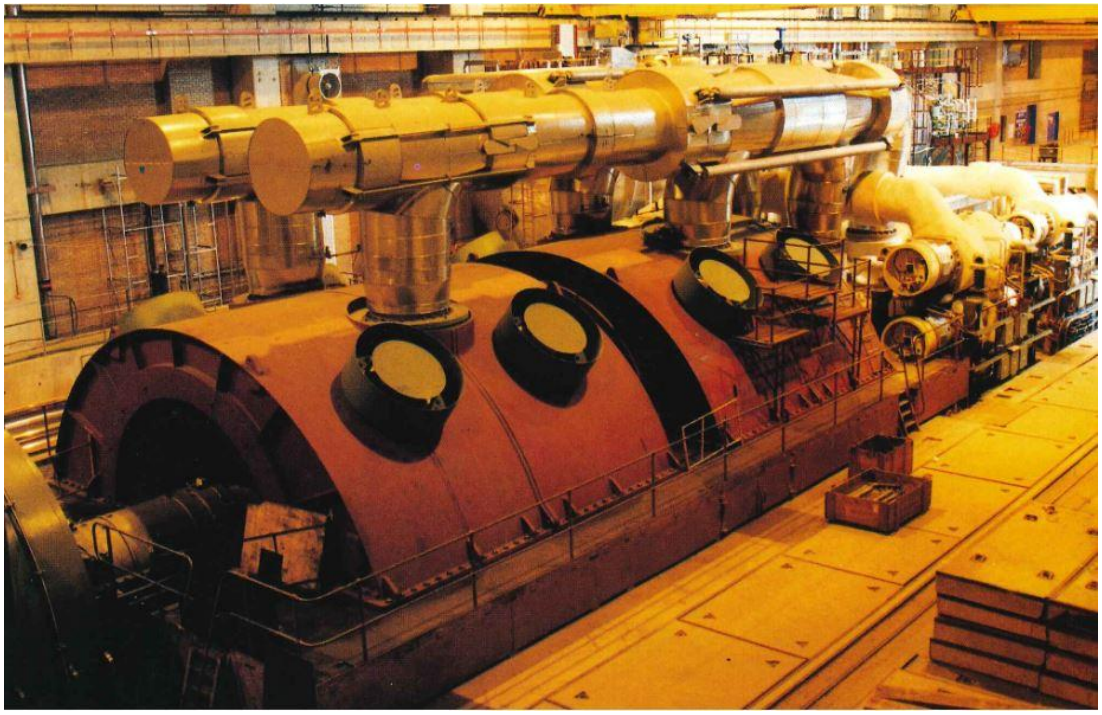

Figure 4: LP turbine at Majuba Power Station [16]

Non-destructive testing of these components will allow the material conditions to be evaluated while operation is not disrupted.

2.2 Effects of Embrittlement on Toughness of Power Plant Steels

Embrittlement can be described as a phenomenon whereby materials suffer a loss of ductility and toughness, with minimal change in other mechanical properties, such as strength and hardness [5]. Considering the extreme conditions in power plants, a reheating temperature of over 593 °C for a component like the rotor may cause some tempering brittleness in the steel, meaning there is need for high temperature strength and toughness in the material selection to overcome the loss in mechanical properties [9].

Failure of critical components like turbine materials, high energy piping and pressure vessels can result in high costs, extended downtime, loss of life and the revoking of operating licences by power plant regulators [17]. **Figure 5** shows the brittle fracture of a steel pressure vessel which was normally operated at elevated temperatures but failed as a result of hydrostatic testing with cold water [5].

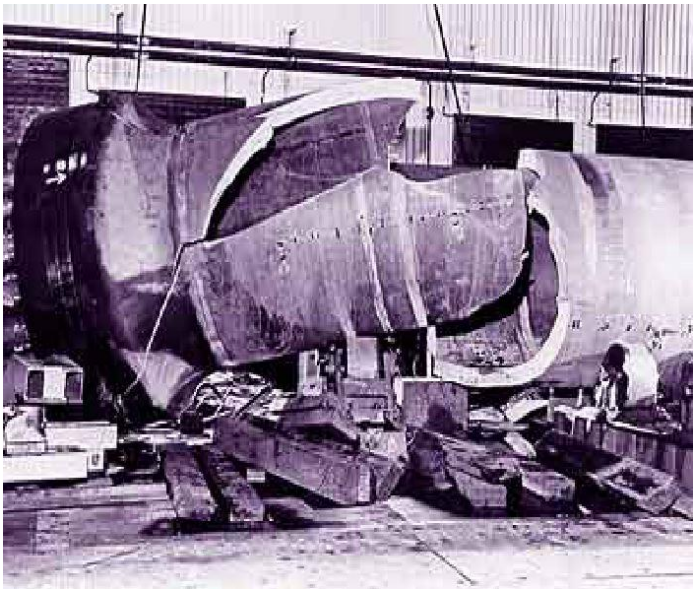

Figure 5: Brittle fracture in steel pressure vessel caused by hydrostatic testing with cold water [5]

This section will be looking at embrittlement in power plant steel material and the effects it has on material mechanical properties. This includes how fracture initiates, propagates, and occurs, as well as the factors affecting the embrittlement, types of embrittlement and the traditional methods that were adopted to analyse this phenomenon in the past.

2.2.1 Fracture Behaviour

Fracture behaviours of steels in power plants vary with dependence on certain circumstances. To establish this behaviour the factors associated include [5]:

- Operating temperature – steels usually exhibit brittle, low energy fracture at low temperatures and ductile, high-energy fracture at higher temperatures.
- Local stress – the material will be affected by the local geometry and loading, as well as crack or notch presence which assume the role of stress concentrators.

- Material microstructure – in particular, grain size and the presence and distribution of second phase particles and alloy elements. This is mainly because in power generating plants, components operate at temperatures that render them susceptible to metallurgical changes with time in service.

2.2.2 Factors Affecting Embrittlement in Power Plant Steels

Embrittlement occurs in steels because of several internal and external factors in a power plant operation that include [4], [5], [17]:

Metallurgical changes

During operation, power plant steels are exposed to high temperatures and pressures, which in turn results in formation of carbide precipitates. Carbides grow to reduce surface energy during high temperature operation, in order for the system (steel material and its environment) to reach a more stable thermodynamic state. Through diffusion the larger carbide precipitates replace the smaller precipitates especially at grain boundaries where diffusion is faster than inside the grains. This results in aging occurring at these grain boundaries.

Manufacturing processes during steel production

During manufacturing, the heat treatments, quenching methods or chemical compositions of the materials are factors that affect embrittlement. Martensitic steel can be tempered around 500 °C and that results in the formation of large precipitates that affect the toughness of the material.

Microstructural phase changes

Usually during operation, the exposure of components to high temperature and pressures results in ageing of the material, changes in grain sizes and graphitization of C-Mn and C-Mo steels particularly.

Operating procedures, operational stresses and temperatures

High stress zones in the component materials, especially with the presence of cracks and surface notches, serve as fracture criterion leading to the failure of the material during operation.

Maintenance procedures

These are practices that are implemented in condition monitoring programs which can lead to fluctuation of conditions in the event of maintenance occurring. Some instances may involve the shutting down of a component for assessment.

Increase in rate of load application

In situations where the power plant is required to meet consumer power demands, maximum load can be applied on components thus exacerbating the effect of embrittlement.

Environmental influence

Corrosive environments can cause degradation in components because of external reactions of the materials with the atmospheric gases.

2.2.3 Types of Embrittlement in Power Plant Steels

There are several types of embrittlement in steels that are a result of various manufacturing and in-service causes. These causes may be attributed to the environment, operating temperatures and pressures, material element compositions and reactions, or even treatment of the material prior to operation and service. The types of embrittlement in steel include [4], [5], [17]:

Temper embrittlement

High temperatures have an influence on aging of the material, resulting in microstructural changes. It has been observed that aging is responsible for strengthening of the ferrite phase. This strengthening can be because of several metallurgical processes which may include:

- heterogeneous precipitation of G-phase in steels with Ni and Nb (Ni-Nb silicides formed at interdendritic boundaries [18]),
- spinodal decomposition
- α (ferrite) and γ (austenite) precipitation.

These processes all contribute to the embrittlement of steel [19]. There is also the occurrence of impurity segregation to prior austenite grain boundaries, which results in the deterioration of the fracture toughness [6].

Oxygen embrittlement

The environment introduces or accelerates cracking due to intergranular corrosion, stress corrosion, or liquid metal embrittlement. The presence of dissolved oxygen has been found to contribute to the wetting of steel material, which is coincident with the onset of embrittlement [20].

Liquid metal embrittlement

This phenomenon occurs when steel is exposed to liquid metals, resulting in corrosion in the material. This in turn leads to fracture of the steel changing from ductile to brittle. This process is exacerbated by the presence of dissolved oxygen as it influences wetting, a necessity for liquid metal embrittlement to occur [20].

Hydrogen embrittlement

This is a type of failure that is also environmentally assisted and caused by the action of hydrogen in combination with applied or residual stress, resulting in the decline in a component's load bearing capacity. A small quantity of hydrogen is sufficient to cause failure as it has the ability to enhance its effect by migrating to regions of high triaxial stress [21].

Thermal embrittlement

In high temperature environments, carbides tend to grow to reduce surface energy. Smaller precipitates are then replaced by fewer larger precipitates through diffusion, which is faster at grain boundaries. Diffusion is slower within grains than at the boundaries, thus aging at grain boundaries occurs.

2.2.4 Embrittlement in Turbine Steels

The material chosen for steam turbines is selected based on allowable stresses and operating temperatures. A typical high pressure (HP) turbine operating over 500 °C will be made of 1CrMoV steel (1% chromium, 1% molybdenum and 0.25% vanadium), with high temperature creep resistance [17]. Owing to the cyclical nature of turbine rotor operation, temper embrittlement is a damage mechanism of significance as impurity segregation to austenite grain boundaries occurs, reducing critical flaw size changing fracture from ductile to brittle cleavage [6].

On the other hand, a typical low pressure (LP) turbine that operates below 399 °C will be made of NiCrMoV steel and will be more susceptible to stress corrosion failure [17]. The following section discusses some of the traditional mechanical methods used to evaluate embrittlement in steel.

2.2.5 Traditional Analysis of Embrittlement in Power Plant Steels

Traditionally, the assessment of allowable or applied stresses for structural designs can be determined based on the safety factors, applied stress and the yield or ultimate tensile stress. This approach is called the strength of materials approach which can be adopted to prevent material failure against brittle fracture [22]. Another approach is the fracture mechanics approach, which unlike the strength of materials approach which consists of two variables, consists of three: applied stress, fracture toughness and flaw size. These variables serve as the minimum operational requirement to avoid fracture during operation [17], [22], as shown in **Figure 6**.

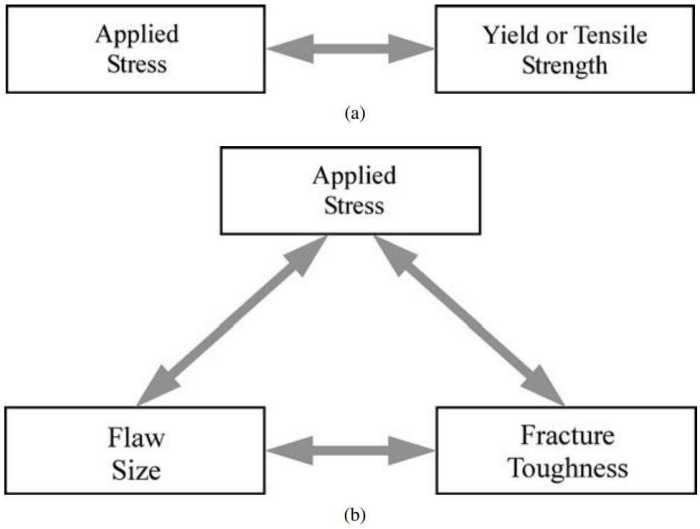

Figure 6: Comparison of approaches to structural design and material selection: (a) the strength of materials approach and (b) the fracture mechanics approach [22].

The American Society for Testing Materials (ASTM), the International Organizations for Standardization (ISO) or the European Standards (EN) are common standard mechanical tests which assess the structural integrity of a material. These standard methods can be adopted to evaluate the embrittlement and subsequently toughness in steels.

Metallurgical techniques that assess microstructural changes and mechanical tests (CVN, tensile, fracture toughness, etc.), can be used to evaluate the degree of embrittlement and the toughness in power plant components. The CVN test evaluates the resistance of a material to failure by use of flexural shock. This impact is absorbed by the material and the amount of energy absorbed indicates the impact toughness, whether the material is ductile or brittle. The tensile test is used to measure the response of a material to application of tensile (pulling) forces. The tensile toughness and failure of different materials is not the same and so the fracture modes after a tensile test can be used to indicate the ductility or brittleness of the material, as seen in **Figure 7**. The fracture toughness test measures the resistance of a material to increasing load conditions that cause either ductile or brittle crack propagation.

Figure 7: Ductile and brittle failure of steel specimens [23]

Brittle fracture is a rapid failure when the material is exposed to a critical stress. This type of fracture can be identified in the data obtained during mechanical tests. It could be the minimal amount of energy absorbed in a CVN test, the reasonably smooth fracture surface after a tensile test or the low fracture toughness values in the event of a fracture toughness test.

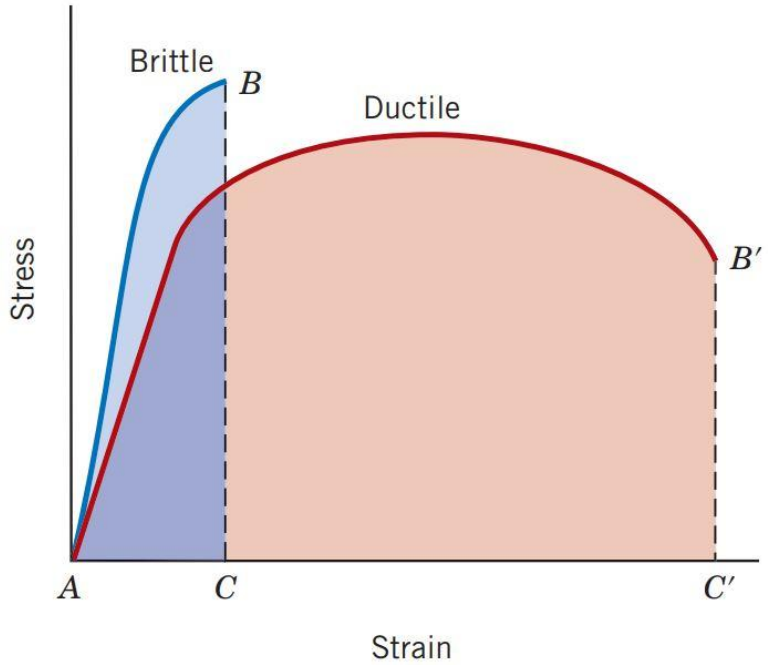

Figure 8: Ductile vs Brittle material stress-strain curve [4]

Ductile fracture exhibits plastic deformation when the material is subject to a critical stress. As seen in **Figure 8**, the ductility is displayed in the increase in the length of the plastic strain region. Unlike a brittle specimen in a tensile test, the ductile specimen shows a greater percentage of elongation and reduction of area as necking occurs. Crack propagation also takes longer in a fracture toughness test and more energy is absorbed during a CVN test.

Although the motivation behind this study was to validate the SPT for reliable and specimen efficient toughness assessment of power plant steels, an “off the shelf” material was selected as the material of choice. This study focused on exploring the mechanical behaviour of this commercially available specialised steel with the goal of establishing robust methodologies to characterise toughness and other relevant material properties. The use of such a material in this context provided a controllable and reproducible baseline to evaluate the SPT analytical methods, serving as a foundation for future application to in-service power plant components.

The uniaxial tensile test, the CVN test and the fracture toughness test are the standard tests that are going to be used in this project to assess the material and will be discussed in this dissertation.

2.3 SPT Background

This section will focus on the background of the SPT method of mechanical testing. The historic aspect of how this method was developed will be looked at, as well as the developments that have taken place up until modern times. This section will also elaborate on the code of practice adopted, the working principle of this test as well as the risks involved in the use of this mechanical method for material condition assessment.

2.3.1 Introduction

The SPT was developed as early as the 1980's to determine mechanical properties of component materials without the need for post-removal repair [24], [25]. It is based on the penetration of miniature test specimens which are usually disc shaped, with a diameter that ranges from 3 mm to 10 mm and a thickness of 0.1 mm to 0.75 mm [17], [26]. Other instances use square shaped specimens of 10 mm by 10 mm. As shown in **Figure 9**, the SPT is carried out on a specimen that is clamped by a lower and upper die.

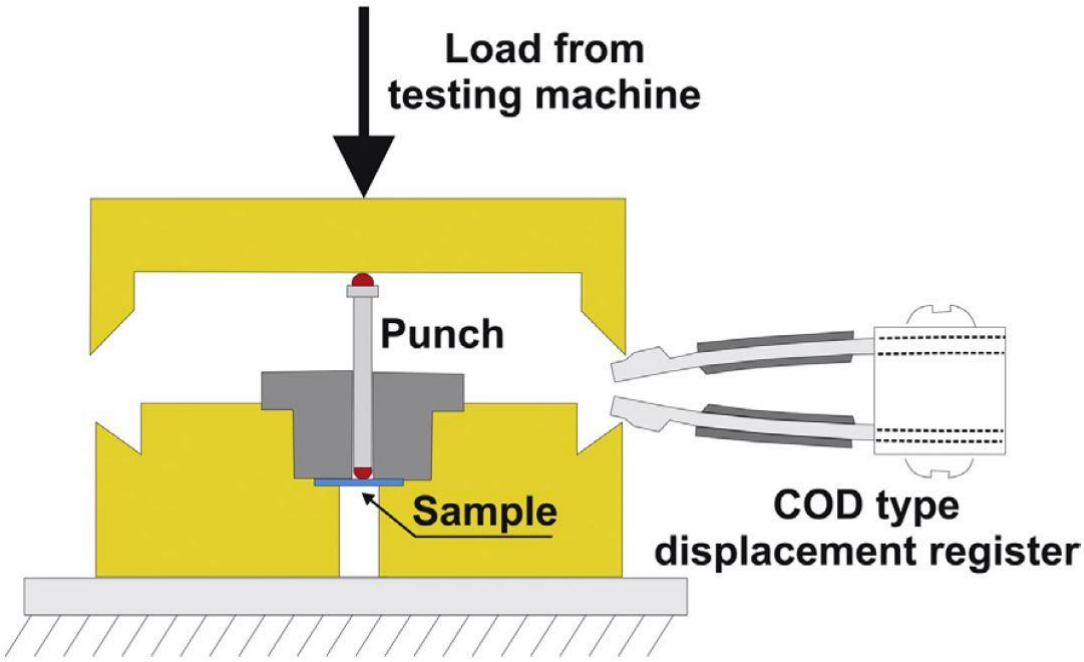

Figure 9: Schematic representation of the SPT testing device [27]

It can also be carried out on an unclamped specimen, where the perimeter of the specimen may displace during the test [24]. However, this dissertation utilises the specimen clamping method.

2.3.2 History of SPT

The idea of non-destructive testing being adopted in the actual determination of structural integrity of materials and components is always favourable. Considering that the current standardized mechanical tests require large volumes of test material, and that extraction of this amount of material from in service components results in post-material removal repair, there was a need for a test method that could provide the mechanical properties (yield stress, tensile strength, toughness, ductile to brittle transition temperature, DBTT etc.) without leaving a damage imprint that would necessitate repair [24], or a halt in operation. This is what led to the development of the SPT, a quasi-non-destructive test technique.

The first reports of the SPT were in 1981, at Massachusetts Institute of Technology (MIT), developed for radiation embrittlement studies [24]. Since then, new good ideas continued to be developed and implemented. Results and findings from the test have had improvements due to technological advancements in the methodology. The addition of new approaches that include Finite Element Modelling (FEM), special equipment like high-definition cameras and local approach theory have enabled the acquisition of more precise and encouraging results and information [24].

2.3.2.1 Developments on SPT

The Westinghouse Hanford researchers introduced the SPT technique during a transmission electron microscopy (TEM) test for a reactor vessel in the 1980s [17], [26]. The Westinghouse Hanford researchers continued to develop a method to interpret stress-strain behaviour and evaluate the irradiated fracture toughness and tensile properties based on the miniature specimen test and FEM [17]. This resulted in the initial reports of the SPT in 1981 at MIT as mentioned in the section prior.

The SPT was then extensively developed in Japan, particularly at Tohoku University [24]. More progressive work was carried out by Japanese researchers Mao, Saito and Takahashi [17], [26], leading to the initial SPT standardizing attempts. With regards to the standardization of the SPT, the first collaborative efforts were reported by Japanese Atomic Energy Research Institute (JAERI) in 1988 [24]. The drafted report recommended a transmission electron microscopy (TEM) specimen disc and provided guidance to obtain DBTT, fracture toughness and equivalent fracture strain but not the stress-strain behaviour determination [17].

As the years progressed, the technique was introduced to more territories. Swansea University and the Electrical Research Association (ERA) in the UK adopted the technique from 1992 [24]. In the US work was being done by the Electronic Power Research Institute (EPRI) and Failure Analysis Associates (FAA), resulting in further developments with more extensive application through a continuous program between 1990 and 1999 [24], [28]. EPRI researched fracture appearance transition temperature (FATT), fracture toughness

and tensile stress-strain behaviour of power plant rotor steels and also improved the irradiation embrittlement method by using FEM [17].

The use of the high precision of computer aided mechanical testing facilities has enabled the development of the SPT technique, even though the test is still limited by the lack of an agreed standardized procedure. The CEN Workshop Agreement (CWA) of 2007, the CWA 15627, published in 2006 and revised in December 2007, was followed by the CEN Slovenski standard, the CEN SIST EN 10371 published in 2021. This dissertation will adopt the harmonization of current SP testing practices in these Codes of Practice, as well as analysis from existing literature. This dissertation will aim at resolving the uncertainty associated with using correlation to establish the properties obtained from the miniature disc tests.

2.3.3 Application of CWA 15627:2007 Code of Practice

The CEN Workshop Agreement (CWA 15627) was developed in 2006 to guide the SPT test rig design and to also provide a procedure to carry out the test and data reporting. The agreement was revised in December 2007, and this section references this agreement [24]. The CWA 15627 document summarizes the minimum requirements for the test to be done.

2.3.3.1 Testing Rig

Emphasis of the CWA 15627 is on the working part of the test rig, that is the punch and the two dies. **Figure 10** is an extract from the code of practice illustrating the cross-sectional schematic of the test apparatus.

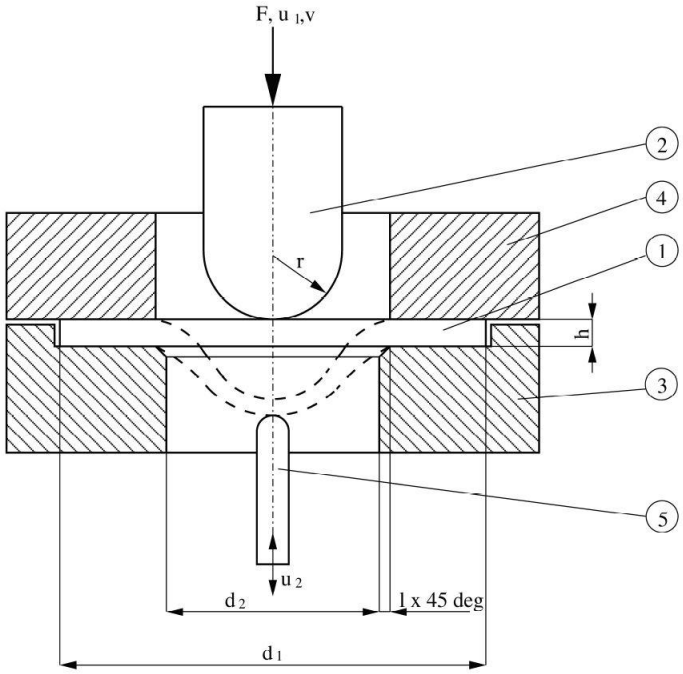

Figure 10: Cross section schematic of SPT apparatus: 1 - specimen, 2 - punch, 3 - receiving die, 4 - clamping die, 5 - deflection measurement rod [24]

From **Figure 10**, the highlighted variables can be identified as follows [17], [24]:

- U_1 and U_2 are displacement for punch and specimen respectively,
- F is load applied (constant for time dependent behaviour),
- V is velocity (constant for time independent behaviour, 0.2 to 2mm/min),
- h is specimen thickness (recommendation is 0.5 mm but it can range from 0.1 to 0.75 mm),
- l is the chamfer edge length (0.2 mm at 45° is recommended),
- d_1 is the diameter of the specimen (8 mm is recommended but it can also range from 3 to 10 mm and can be a square shaped specimen of 10 x 10 mm),
- r is the punch tip radius (range from 1 to 1.25 mm),
- d_2 is the receiving die hole (4 mm in diameter is recommended)

2.3.3.1.1 Loading System

The SPT test makes use of a screw-driven test machine equipped with a test rig which will hold and load the test specimen. The test rig shall have a spherical punch that will be able to force the central part of the test specimen through the receiving die hole until the end point of the test is observed. The spherical portion of the punch and the two dies shall be of a hardness of 55 HRC or greater, in order to avoid deformation of the apparatus during testing. The rig shall have a force measurement system, and it will have percentage error not exceeding ±1% of the actual measured force [24].

2.3.3.1.2 Displacement and Deflection Measuring System

The rig will also have a displacement and deflection measuring system. An accuracy of at least ±1% of the specimen thickness will be required for the displacement monitoring indicator [24].

2.3.3.1.3 Heating and Cooling System

The heating or cooling system shall provide a uniform temperature distribution throughout the entire test specimen and will also have a temperature measuring system equipped with appropriately located standard suitable thermocouples. The temperature measuring system shall be capable of maintaining a temperature not exceeding the range of ±3 ^{o}C of the designated temperature. The tests are to be carried out in a controlled environment (heating furnaces for elevated temperatures, liquid nitrogen coolant/cold water for low temperature tests) [24].

2.3.3.1.4 Data Recording

The equipment to be used in the data recording shall automatically record test parameters with a resolution that is accurate to within ± 1% of the measured signal [24]. Correlation methods are then to be adopted in order to evaluate the data from the test.

2.3.3.2 Sample Preparation

The test specimen is to be acquired from standard test material in such a way that the acquisition of the material is minimally invasive. **Figure 11** shows a scoop cutter sampler, which removes surface material in a manner likened to an ice-cream scoop.

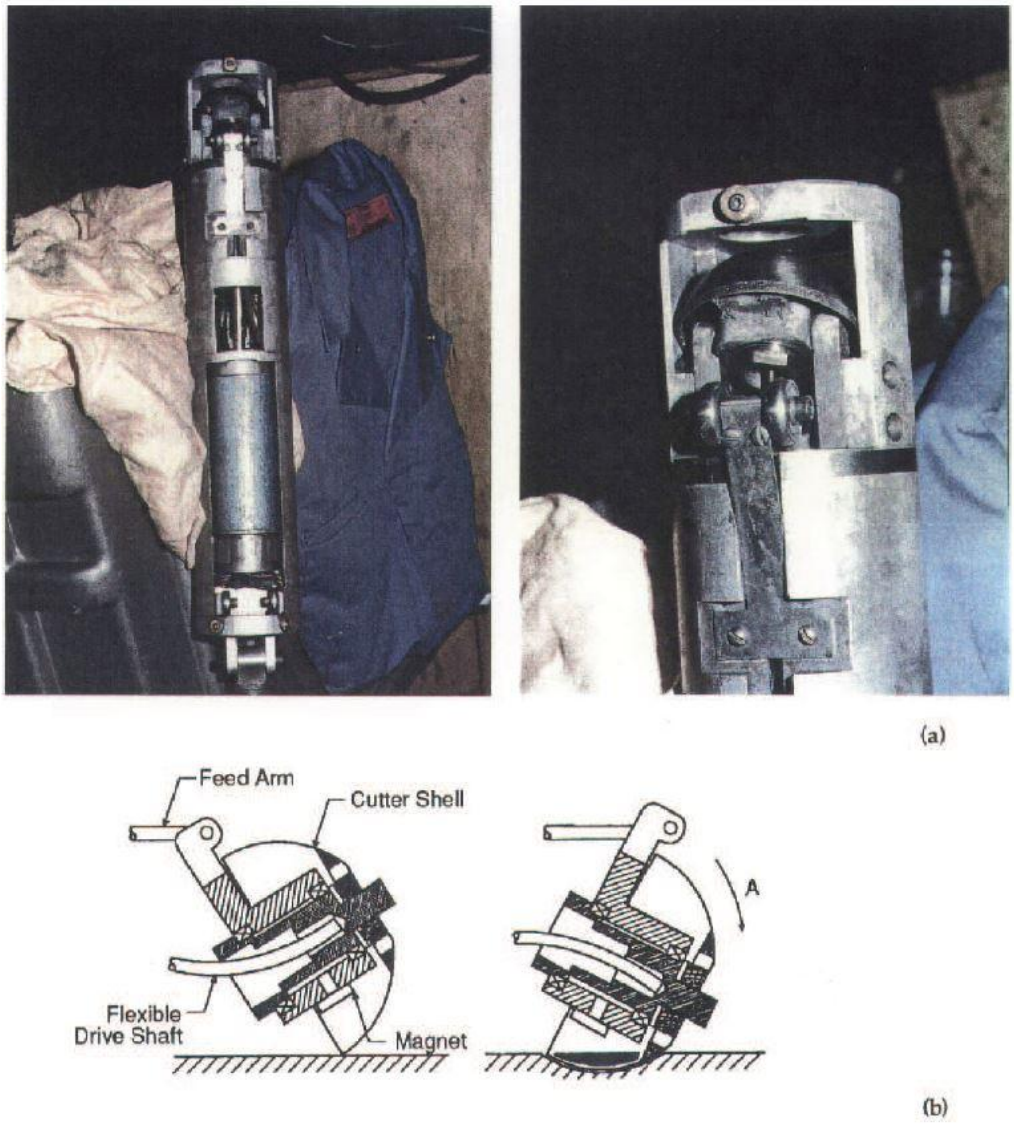

Figure 11: Scoop cutter: a) photograph b) schematic [24]

The scoop cutter is a hemispherical cutter plated with cubic boron nitride (CBN) grit abrasive, which spins about its axis of symmetry while slowly advancing about a perpendicular axis feeding the cutter into the base material, as seen in **Figure 11b** [17], [24]. Coolant is introduced to cool and assist in clearing the swarf. Depending on the scoop cutter size, sample depths ranging from 3-4mm of material are normally cut with 25mm diameter as shown in **Figure 12**.

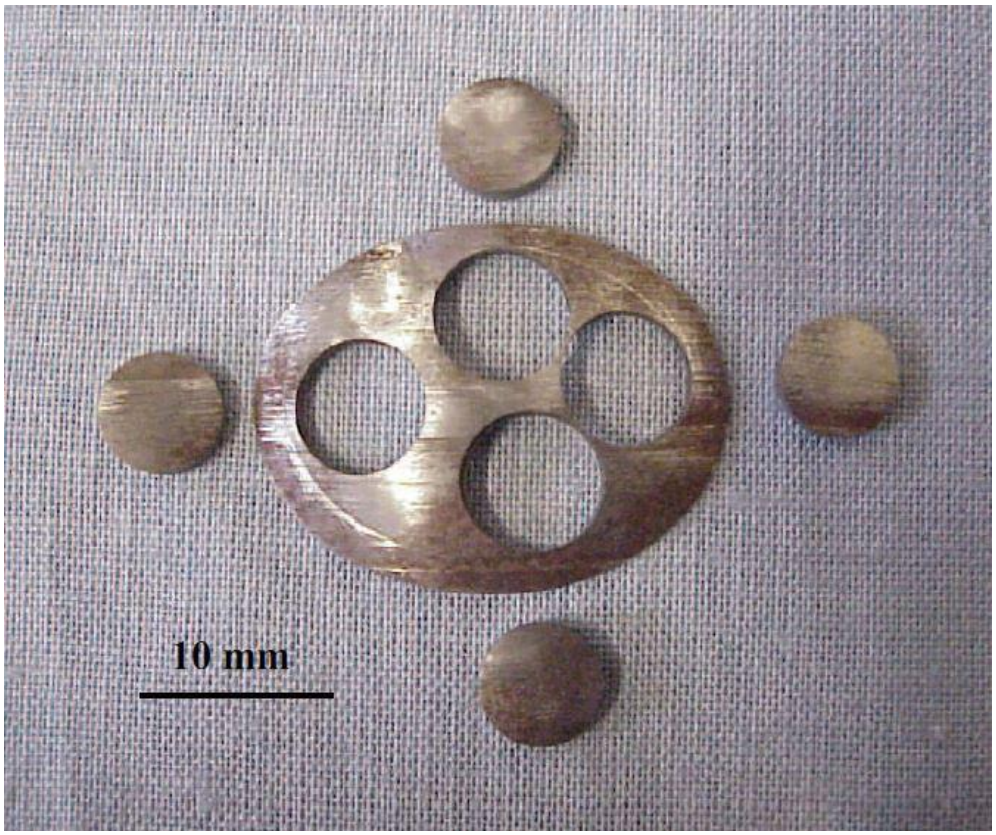

Figure 12:Sample removed by scoop cutter with SPT specimens cut using EDM [24]

With use of electrical discharge machining (EDM), SPT specimen blanks are cut from the miniature sample obtained by the scoop mechanism, at thicknesses ranging from 0.55 mm to 0.8 mm [24]. To minimize work hardening in the surface of the test specimen, the disc should be machined to approximately 1.1 times the desired thickness of 0.5 mm. It should then be ground with recommended grit size designation P320 followed by fine grinding with grit designation P1200 to the final thickness ±1% *h* (where h is the thickness 0.5 mm) [24]. The test specimen thickness should be measured at four positions around the perimeter at 90° intervals and at the centre of the specimen, and the diameter at two points positioned at 90° [17], [24].

2.3.3.3 Damage/Failure Modes and Properties of Interest

The CWA 15627 document [24] provides a framework on failure modes and properties of interest that can be obtained from an SPT LDC. Strength measurements address the load bearing capacity of the material as well as margins against overload failure, plastic collapse or yielding [24]. **Table 1** summarizes the various failure modes and properties of interest that may be derived from the SPT, as well as the minimum number of specimens required for property determination during tests.

Damage/ Failure Mode	SP-Derived Properties	Minimum Number of SP Test Specimens	Comments
Overload, Yielding, Plastic Collapse	Yield Strength, Tensile Strength	2	Properties typically measured as part of some other measurement, such as toughness.
Creep/Creep Rupture	Rupture Strength	5	Methods for acceleration may be as used for standard test specimens
Time-Independent Fracture	FATT (or DBTT)	7	Applicable to carbon and low alloy (body-centered cubic) steels
Time-Independent Fracture	Fracture Initiation Toughness, K_{Ic}, J_{Ic}	2	Tests at desired temperature; empirical and semi-empirical approaches available

Table 1: Summary of damage modes and SPT properties of interest [24]

2.3.3.4 Test Output – LDC

The test will result in the outcome of an LDC, as shown in **Figure 13**. The load from the punch is plotted against the displacement of the miniature specimen, showing the progression of the test from initial contact to failure. After the adoption of DIC, a load-deflection curve can be obtained, with the load from the punch being plotted against the deflection on the top surface of the miniature specimen (opposite side to contact surface).

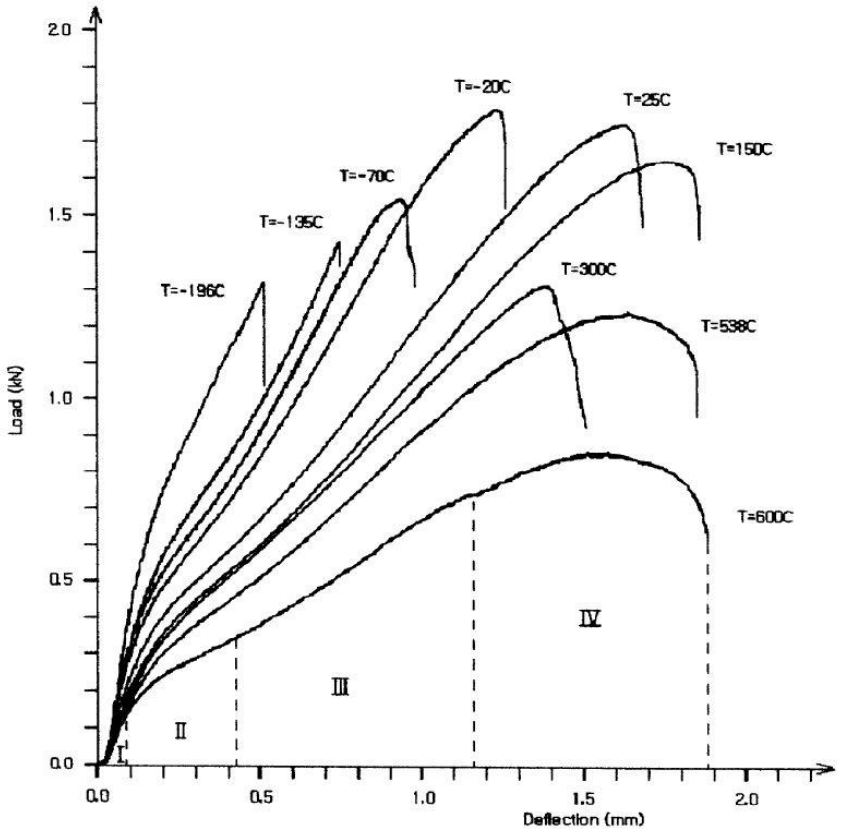

Figure 13: LDC at various temperatures for 12Cr-1Mo steel [29]

The nature of failure is highly dependent on the temperature and as seen in **Figure 13**, the LDCs at the different temperatures are not similar. High temperatures result in the specimen exhibiting ductile behaviour and at lower temperatures the specimen exhibits brittle behaviour [29]. Temperature variations affect the mechanical properties of metallic materials, and where the different temperatures resulted in different LDCs, different mechanical properties in materials also resulted in different responses [25], [30], [31]. Ductility and brittleness can be assessed from an LDC as the load against displacement/defection function can be correlated closely to the stress against strain in a tensile test [29], [32], [33], [34].

2.3.3.4.1 Deformation Stages

The LDC can be typically divided into as much as four deformation zones, highlighting the different phases the specimen would have undergone in the test, as shown in **Figure 14**. The stages are as follows [27], [29]:

1. **Stage 1 – Elastic bending deformation region.** This region is associated with local surface micro-yielding in the sample, along with the indentation on the sample surface which is a result of the punch coming into contact with the specimen. The bending deformations occur by reversible elastic strains on the specimen [27], [29].

2. **Stage 2 – Plastic bending deformation region.** This section of the LDC describes the onset of the elasto-plastic transition and the yield load P_Y [35]. The yield point P_Y is used to estimate the yield stress in the empirical correlation with tensile tests [33], [34]. This plastic bending deformation zone carries on describing the progressive extension of plastic deformation in the specimen [27].

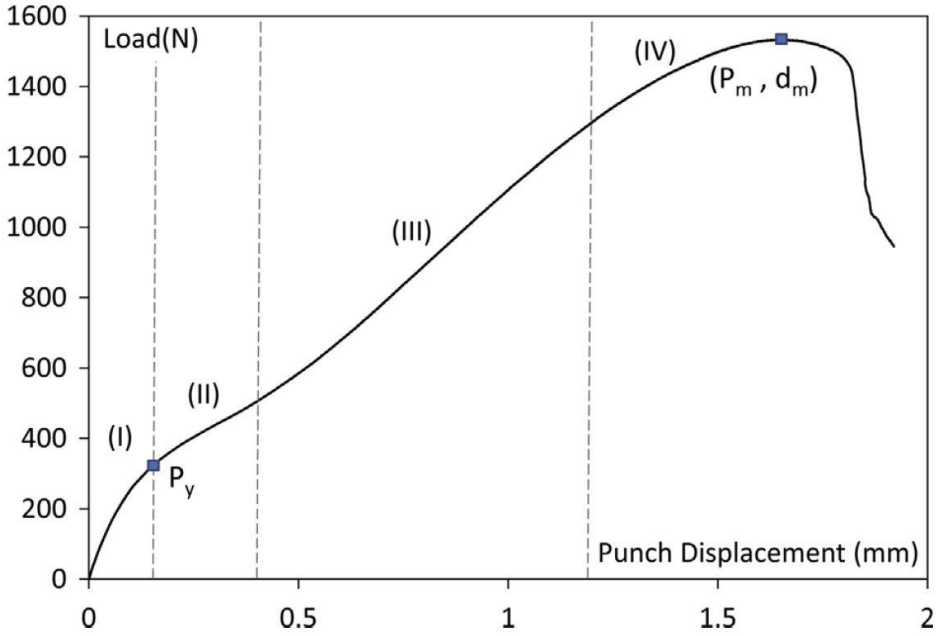

Figure 14: LDC displaying the deformation stages [27]

3. **Stage 3 – Membrane stretching region.** This region is a result of plastic deformation progression in the sample to a particular extent, where membrane stretching behaviour predominates most of the curve. In brittle materials or embrittlement situations, the membrane stretching region is non-existent, as the graph moves from a plastic bending deformation region directly to the plastic instability region [36].

4. **Stage 4 – Plastic instability region.** In this region the onset of failure micro mechanisms is observed. These mechanisms include necking and internal cracking. As the maximum load on the curve P_m is approached, the slope starts to decrease [27]. The ultimate tensile strength can be estimated using the maximum load P_m in an empirical correlation with tensile tests [33], [34]. It is in this zone where necking commences and a visible crack is produced, resulting in a decrease in load leading to the failure of the specimen.

In high temperatures the failure of the specimen is associated with the formation of local deformation or necking much like the ductile material behaviour in conventional tensile tests [29], resulting in the specimen going through all four zones of deformation. However, in lower temperatures early crack initiation and rapid crack propagation within the plasticity regime is observed and this leads to brittle failure before the membrane stretching or plastic instability phases are reached [29]. Therefore, the LDC, depending on the material being tested or the temperature at which the test is carried out, might not display all the expected features.

2.3.3.4.2 Small Punch Energy

The area under the LDC up to the maximum load (P_m in **Figure 14**) observed signifies the energy absorbed during the test [37]. This absorbed energy is referred to as the total small punch energy, E_{SP} [33], [37], [38].

The energy in the elastic bending deformation region of the LDC is referred to as elastic energy, while the energy in the second and third region of the SPT LDC is called plastic energy. The plastic energy is obtained from the difference between the E_{SP} and the elastic small punch energy [33].

Since toughness is the ability of a material to absorb energy before failure, the E_{SP} can serve as a vital parameter for the assessment of the toughness properties of the material.

2.4 DIC

The DIC is a non-contact measuring technique that determines the displacement field of a specimen based on the undeformed or deformed states of specimen surface images [39]. For this optical technique, the surface of interest must have random speckle patterns that will enable the comparison of the captured images before and after deformation. The setup involves a light source, a charged-coupled device (CCD) camera and a computational device with a correlation software [39], [40].

The speckle pattern could be utilised to improve the accuracy in determining the damage on the specimen surface during an SPT. It can allow the close assessment of the points of failure on the tested sample during the test, as the cameras show the gradual progression of the test on the specimen surface. For the accuracy and precision of the of the measured values, the speckle pattern should meet the following requirements [39], [41]:

- Random distribution of pattern for specified area identification (non-periodic and non-repetitive)
- High contrast of speckle pattern
- 50:50 black/white ratio
- Isotropy (no pattern directionality)
- Stability of speckle pattern (pattern to adhere to specimen surface tightly even through deformation)
- Ground and polished specimen to avoid alteration of specimen surface

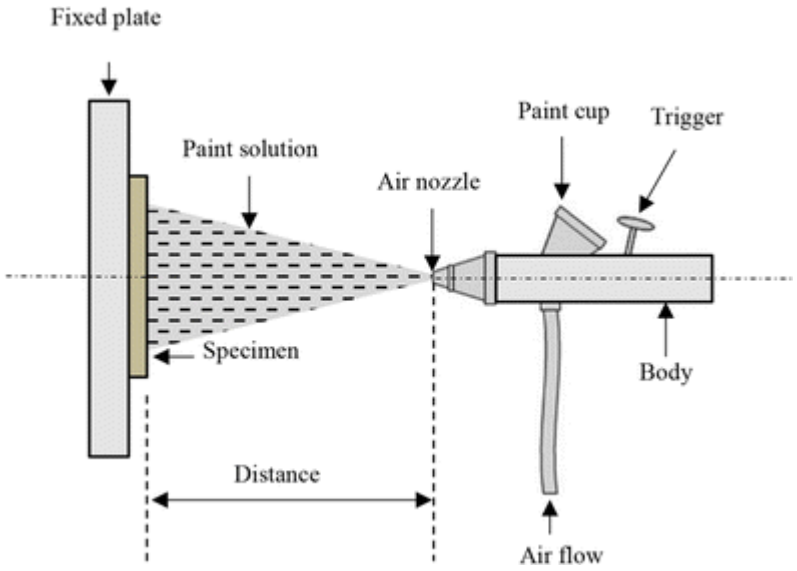

Figure 15: Schematic of airbrushing method in fabrication of speckle pattern on test specimen [41]

Figure 15 shows a common method of fabricating macro-scale speckle patterns on a test specimen where a spray bottle or airbrush is used. It is worth noting that at room

temperature white and black paints are applied as they are suitable to provide the contrast and the required speckle pattern [39].

DIC technique can be separated into 2D and 3D DIC techniques. 2D DIC can measure in plane deformation and utilise the use of one CCD camera positioned perpendicular to the specimen. In the event that out of plane deformation is to be assessed, 3D DIC is employed. The 3D DIC apparatus consists of two CCD cameras in a stereoscopic configuration, allowing for spatial analysis [42]. To establish the positioning of the CCD cameras, the baseline distance, B_d, stereo angle, α, and stand-off distance (S-o-D), D_s, needs to be determined.

$$D_s = \frac{FoV_H \cdot f}{s_w}$$

Where FoV is Field of View
f is focal length in mm
s_w is sensor width
Equation 1

$$B_d = 2 \cdot D_s \cdot \tan\left(\frac{\alpha}{2}\right)$$

Where B_d is Baseline distance
D_s is Stand-off Distance (S-o-D)
α is stereo angle
Equation 2

The stereo angle is recommended to range between 30 º - 50 º. The experimenter is to also ensure that the region of interest for both cameras is approximately in the centre of the image.

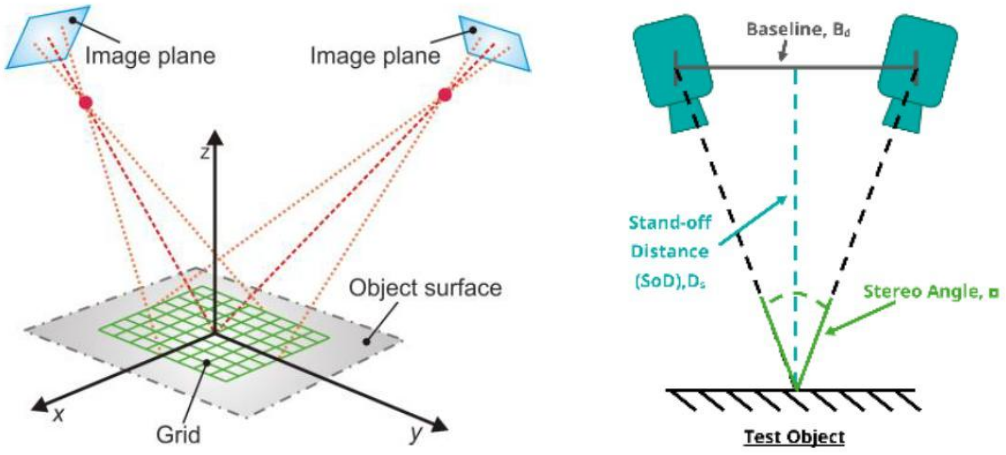

Figure 16: Principle of 3D DIC with two CCD cameras and Stand-off Distance (S-o-D) determination[42], [43]

Figure 16 shows the configuration that was to be followed in the mounting of the CCD cameras for 3D DIC. The advanced image processing techniques of the DIC are applied in the region of interest of the specimen being tested, and this region is comprised of multiple

subsets (facets) that are tracked by the software to determine the deformed specimen surface displacement. **Figure 17** shows the facet size and grid spacing, which are determined by the size of the created speckle pattern, as every facet has to contain white and black colours [44]. The facet size and grid spacing are therefore vital elements for the accuracy of the DIC correlation.

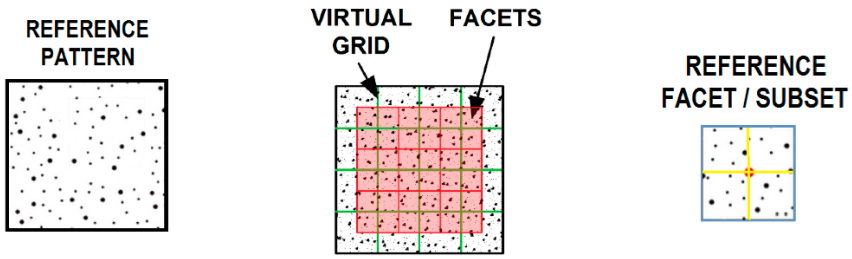

Figure 17: Image showing reference pattern, grids and facets on speckled surface for DIC

The DIC algorithm (Dantec Istra 4D), calculates displacement by matching the reference image facets to the deformed image facets, and subsequently calculating the facet centre's relative displacement between the reference and deformed images.

2.5 Analysis for Mechanical Properties

In this section focus will be placed on the sequence to be adopted in this project for the measurement of toughness. It details the heat treatment process and the necessary steps from literature required to manipulate and modify the mechanical properties of the selected materials. The various analytical methods used in literature for the assessment of the mechanical properties of the "off the shelf" steels that will be acquired alongside the SPT will also be assessed. Further analysis of the material will be done with metallographic examination and empirical formulations, in order to validate and reinforce the observed data obtained from the SPT.

2.5.1 Heat Treatment

In steels, the carbon content helps determine if the material is a hypoeutectoid, hypereutectoid or rather a eutectoid alloy. The inclusion of various metal elements affects the phase diagram, as some of these elements enhance or degrade mechanical properties. Some elements like manganese, nickel and titanium improve the toughness and ductility properties of the materials whereas other elements like phosphorus, sulphur and hydrogen act as impurities leading to phenomena such as brittleness [4]. The phase diagram in **Figure 18** can be manipulated by utilising the transformations in the steel system, focusing on the eutectoid reactions to obtain required mechanical properties.

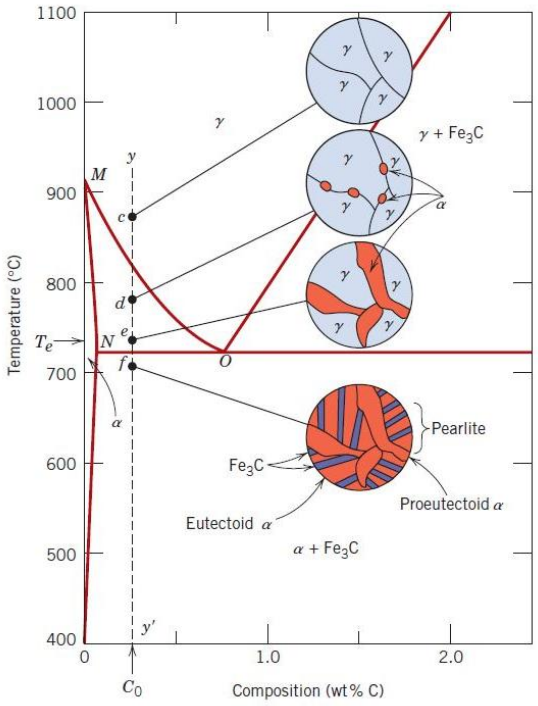

Figure 18: Schematic representation of microstructures for an iron-carbon alloy phase diagram [4]

At 850 °C in similar steels, there is a mixture of mostly face-centred cubic (FCC) austenite (γ) and body-centred cubic (BCC) ferrite (α) [4]. Cementite (Fe_3C) forms below 727 °C

(eutectoid temperature), and as we go lower $Fe_3C + \alpha$ (pearlite and proeutectoid ferrite) is formed. In addition to pearlite there is formation of bainite (ferrite and cementite phases), which forms as fine needles and plates (can only be seen using electron microscope).

Martensite is formed when eutectoid iron-carbon alloys are rapidly cooled or quenched at a rate greater than the critical cooling rate of 140 ^{o}C/s as shown in the continuous cooling transformation (CCT) phase diagram in **Figure 19**. Large numbers of martensite atoms experience cooperative movements and slight displacements of each atom relative to its neighbours. This occurs in such a way that the FCC austenite experiences a polymorphic transformation to a body-centred tetragonal (BCT) martensite [4]. This newly formed martensitic structure is distinctly different from BCC ferrite (α), as all the carbon atoms remain in the martensite as interstitial impurities. These impurities constitute supersaturated solid solution that if heated to temperatures at which diffusion rates become appreciable, is capable of rapid transformation to other structures. The majority of steels retain the martensitic structure at room temperature indefinitely [4].

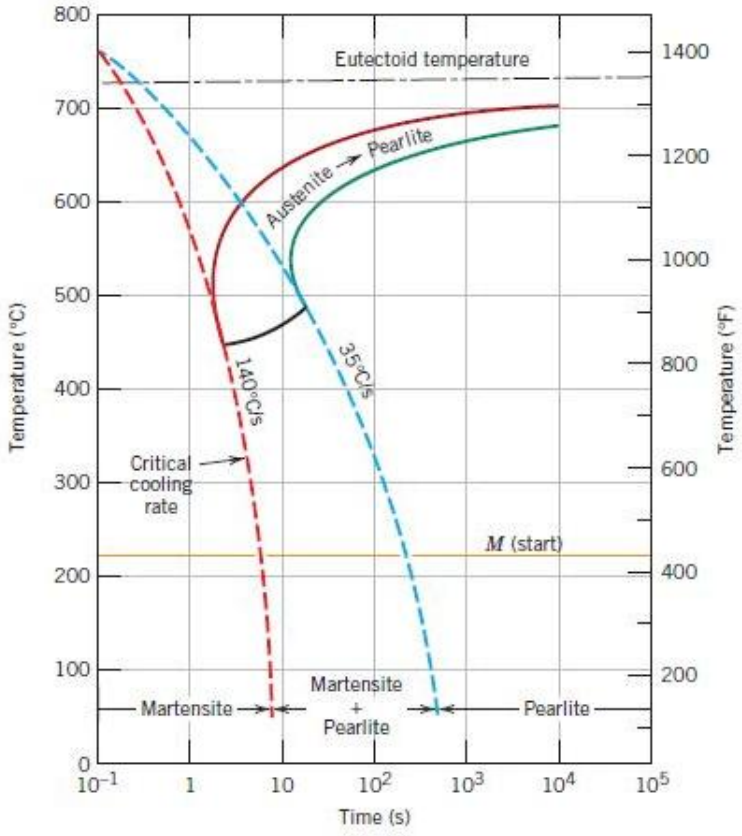

Figure 19: Continuous cooling transformation (CCT) phase diagram for a eutectoid iron-carbon alloy and the cooling curves [4]

In this as quenched state, martensite will be very hard and also brittle to the extent that it cannot be used for most applications. There is a weakening effect that is caused by any

internal stresses that may have been introduced during the quenching process and so to enhance ductility, toughness and relieve the internal stresses, a heat treatment known as tempering is employed [4]. Tempering is the process of reheating hardened (martensitic) or normalized steels to some temperature below the lower critical temperature [45].

The martensitic steel is heated to a temperature below the eutectoid temperature for a specified period, normally between 250 °C and 650 °C. It is worth noting that the internal stresses can be relieved at temperatures as low as 200 °C. The tempering heat treatment, through diffusional processes, results in the single-phase BCT martensite supersaturated with carbon, transforming into tempered martensite, composed of the stable ferrite and cementite phases [4].

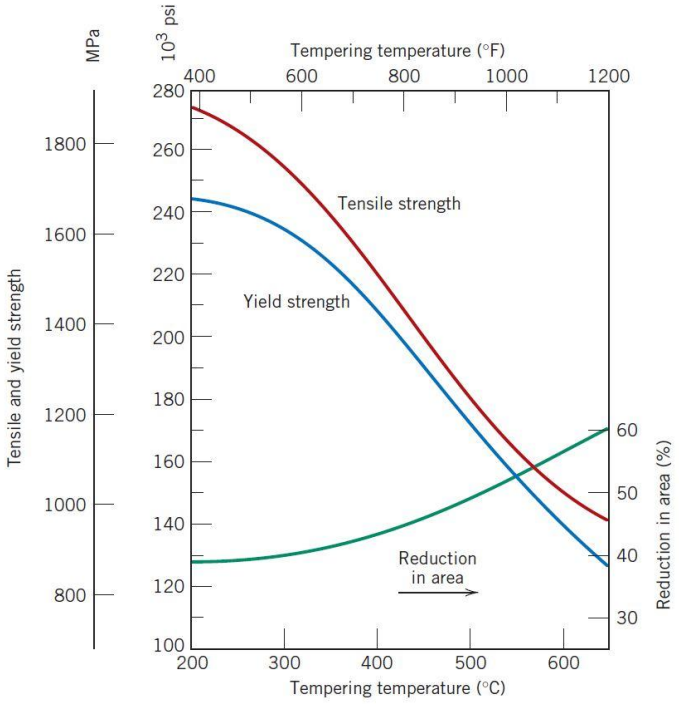

Figure 20: Tensile strength, yield strength and ductility at room temperature against tempering temperature for an oil quenched alloy steel [4]

Figure 20 shows the different effects that the tempering process can have on the mechanical properties of a quenched steel. The tempering process can be adopted and utilised to alter the mechanical properties of the test material.

2.5.2 Evaluation of Mechanical Properties using the SPT Technique

2.5.2.1 Arithmetic Approach/ Empirical Formulations to estimate uniaxial stress strain parameters using SPT

Various studies have been conducted, and numerous proposed analytical methods have been documented over the years. Proposals from the CEN documents [24], [38], Janca et al. [31], and Hahner et al. [7], were elaborate techniques of analysis, assessing the SPT curves to estimate mechanical properties. These methods were further investigated, to try and establish correlations from the data obtained through the SPT and the conventional mechanical tests.

2.5.2.1.1 Method CEN Workshop Agreement

According to the CWA document [24], and the updated CEN SIST 10371 from 2021 [38], the LDC contains information about the elastic-plastic deformation and the strength properties of the material. The maximum load obtained during the test, F_m, the load characterizing the transition from linearity to the stage associated with the spread of the yield zone through the specimen thickness (plastic bending stage), F_e and the displacements corresponding to the maximum load, u_m or v_m, are all vital parameters for the determination of tensile behaviour of the material.

Displacement, v, is defined as distance by which the punch tip has moved after initial contact with the specimen surface. Deflection, u, is defined as the measured distance of a point at the centre of the specimen, located on the opposite specimen surface to the specimen surface in contact with the punch [24], [38].

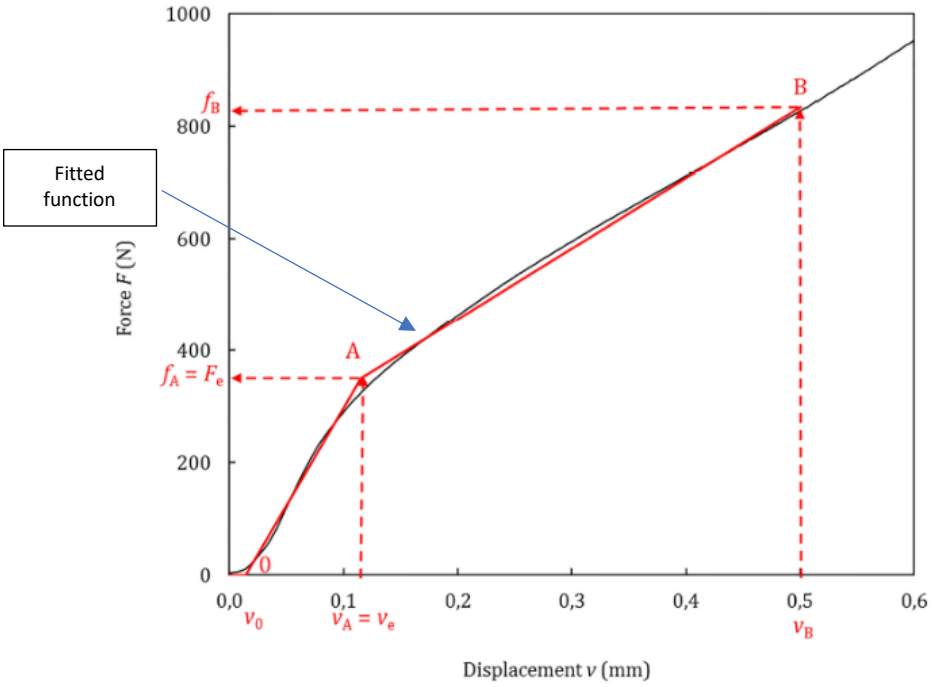

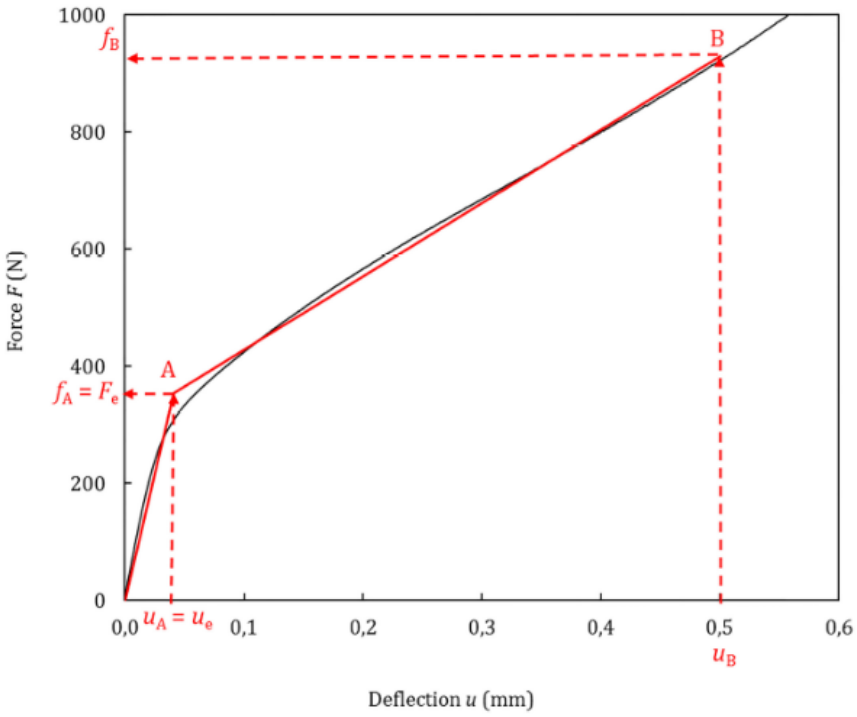

Figure 21: Determination of F_e by means of displacement and deflection curves [38]

As seen in **Figure 21**, the elastic to plastic transition force, F_e, can be determined by fitting a bilinear function, **Equation 3**, in the case of deflection curves and a trilinear function, **Equation 4**, in the case of displacement curves. For the free optimisation parameter on the curve, point B, a value of u_B or v_B = h (0.5 mm) is recommended at the end of the characteristic plateau [24]. **Equation 5** shows the correlation to estimate the yield stress using the established load point F_e.

$$f(u) = \begin{cases} \frac{f_A}{u_A} \cdot u & for\ 0 \le u < u_A \\ \frac{f_B - f_A}{u_B - u_A}(u - u_A) + f_A & for\ u_A \le u \le u_B \end{cases}$$

Where f_A and f_B are loads at point A and B respectively
u_A and u_B are deflections at point A and B respectively
u is deflection

Equation 3

$$f(v) = \begin{cases} 0 & for\ 0 \le v < v_0 \\ \dfrac{f_A}{v_A - v_0}(v - v_0) & for\ v_0 \le v < v_A \\ \dfrac{f_B - f_A}{v_B - v_A}(v - v_A) + f_A & for\ v_A \le v \le v_B \end{cases}$$

Where f_A and f_B are loads at point A and B respectively
v_0, v_a and v_b are displacements at point 0, A and B respectively
v is displacement
Equation 4

$$\sigma_{YS} = \beta_{YS} \cdot \left(\frac{F_e}{h_0^2}\right)$$

Where σ_{YS} is the calculated yield stress
β_{YS} is the yield stress correlation factor
h_0 is initial thickness of test specimen
F_e is elastic-plastic transition force
Equation 5

$$\sigma_{UTS} = \beta_{UTS} \cdot \left(\frac{F_m}{h_0 \cdot u_m}\right)$$

Where σ_{UTS} is the calculated ultimate tensile stress
β_{UTS} is the ultimate tensile stress correlation factor
h_0 is initial thickness of test specimen
F_m is maximum load during test
Equation 6

The E_{SP} can also be determined. The area under the SPT curves, as shown in **Figure 22**, as well as the maximum load and subsequent displacement could be obtained from the SPT curve. **Equation 6** shows the correlation to estimate the UTS utilizing the load point F_m and the deflection or displacement at that point. The same methodology of analysis could be applied in the case of deflection curves, but the E_{SP} is not to be interchanged between displacement and deflection curves [38].

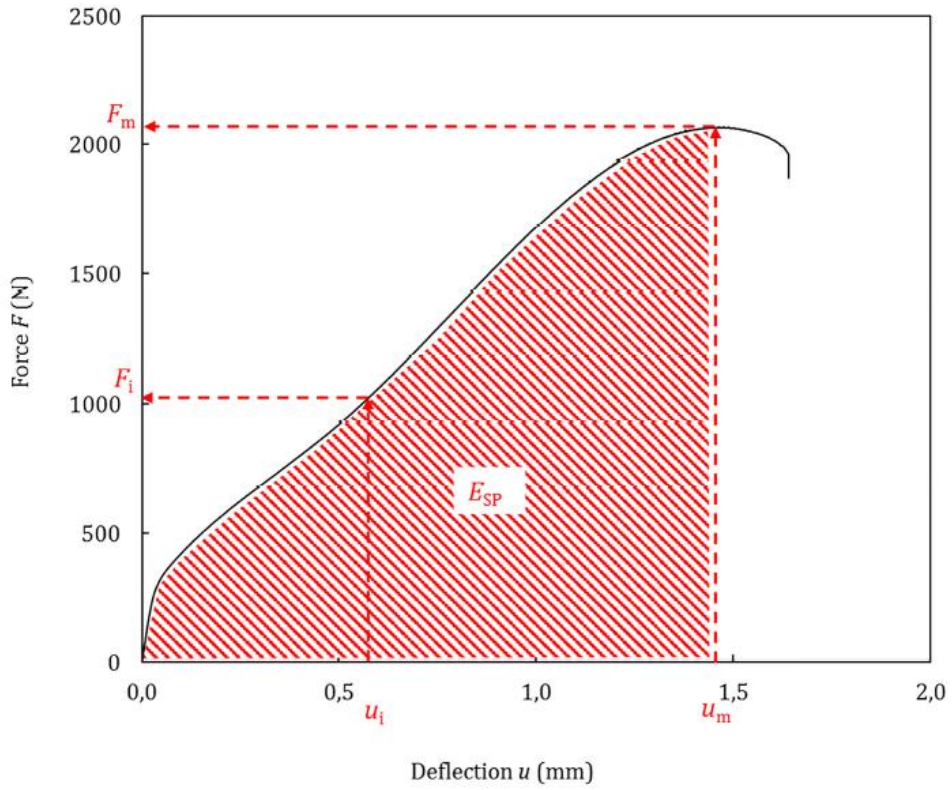

Figure 22: Determination of F_m, F_i, u_m, u_i and E_{SP} from LDC [24]

Another load point that could be determined is F_i, the onset of plastic instability at displacement, v_i or deflection, u_i during the test as seen in **Figure 22**. Identifying the crack initiation point during a test can be used to determine the onset of plastic instability as this phenomenon occurs when the material cannot accommodate any further plastic deformation leading to localised failure.

2.5.2.1.2 Method Janca

From Janca et al. [31], one of the solutions from the numerous methods in the paper is the energy criterion methodology to attain the yield point. The deviation from linearity can be solved by comparing the area under the curve A with its complement A_C above the curve. During the linear phase (before yield), the following **Equation 7** holds:

$$A = i \cdot A_C$$
$$with\ i = 1$$

Where A is the area under the LDC (energy $E_{e1.5}$)
A_c is the complement of A above the LDC (energy $E_{e1.5c}$)
i is a linearity coefficient
Equation 7

Figure 23 shows the relationship between the area under the curve and its complement in a typical LDC while zoomed in. The area under the curve, A, is shown as the energy $E_{e1.5}$ and complement A_C is displayed as the energy $E_{e1.5c}$ in the diagram.

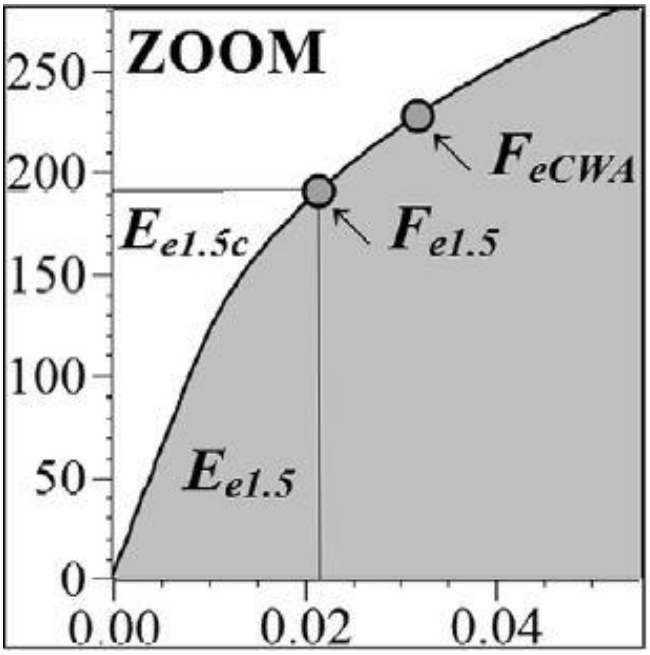

Figure 23: Characteristics derived from LDC, with load $F_{e1.5}$ located where equation $E_{e1.5} = 1.5E_{e1.5c}$ holds true [31]

As seen in **Figure 23** above, after the curve stops being linear, the linearity coefficient *i* deviates from 1 and the yield characteristic can be determined by defining the particular coefficient *i*. The best results were attained with the linearity coefficient *i* being equal to 1.5 [31], resulting in **Equation 8** below.

$$A = 1.5 \cdot A_C$$

Where A is the area under the LDC
A_c is the complement of A above the LDC
Equation 8

The characteristic load determined with this method is called $F_{e1.5}$, as shown in **Figure 23**, which characterises the transition from elastic response better than elastic to plastic transition load in accordance with the CWA document [24]. According to Janca et al. [31], the bilinear method for determination of F_e using the CWA method is not suitable for the proper treatment of the measured LDC. As illustrated in **Figure 24**, the residual imprints that resulted from the punching of A533B JRQ steel during SPTs, were all interrupted before the load reached the CWA document F_e load [31].

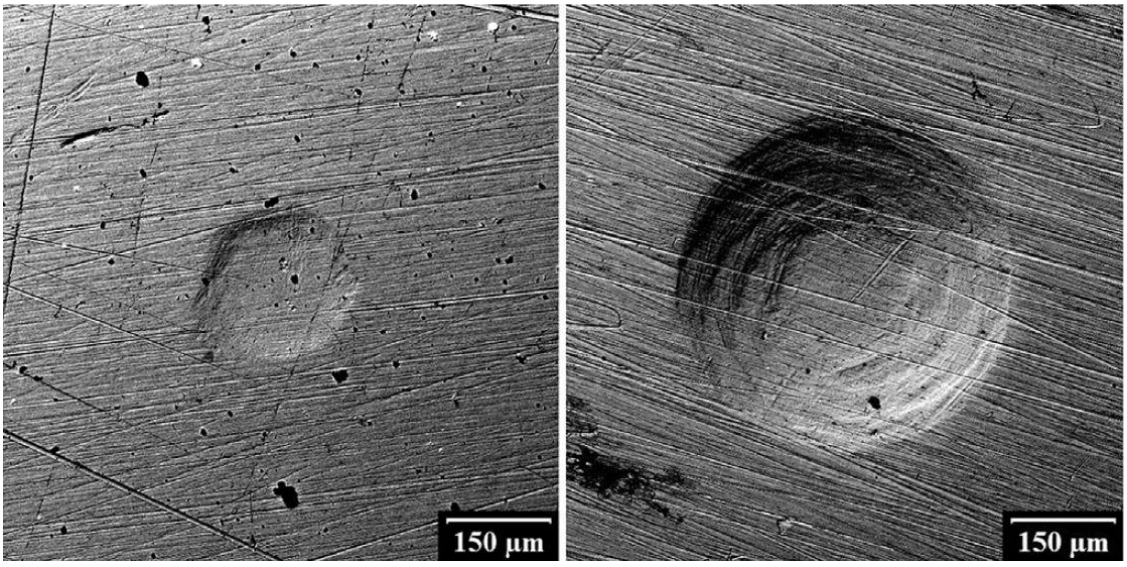

Figure 24: Residual imprints after punch tests of A533B JRQ steel were interrupted after reaching F = 50 N (left) and F = 225 N (right), considering F_e (according to the CWA document) = 237 N [31]

As a result, the value of F_e according to the CWA document is therefore too high to estimate the elastic to plastic transition accurately [31]. The energy criterion requires a sufficient number of experimental points and a 10 Hz sampling frequency at 0.4 mm/min crosshead velocity as a minimum is adequate. This resulting number of data points suffices to use a trapezoidal integration method for the precise calculation of energy.

$$\sigma_y = a\left(\frac{F_{e1.5}}{h_0^2}\right) + b$$

Where $F_{e1.5}$ is load derived from area under the LDC (energy), i.e., the point at which area under the curve is equal to 1.5 of its complement above the curve
h_0 is initial thickness of test specimen
σ_Y is the calculated yield stress
a and b are fitting parameters
Equation 9

Equation 9 and its fitting parameters can be transformed to **Equation 10**, with a correlation coefficient, α, that is for the specific material [7], to estimate the yield stress of the material.

$$\sigma_y = \alpha \left(\frac{F_{e1.5}}{h_0^2} \right)$$

Where α is the energy criterion yield stress correlation factor

Equation 10

With the definition of the elastic-plastic transition load being $F_{e1.5}$ from an LDC, and the yield stress, σ_y from a stress-strain curve (tensile test), of a material, the correlation coefficient can be identified as **Equation 11**.

$$\alpha = \left(\frac{h_0^2 \cdot \sigma_y}{F_{e1.5}} \right)$$

Equation 11

After attainment of the correlation coefficient value the yield stress can be estimated with low scatter and a very high coefficient of correlation when estimating the yield stress [31].

Janca et al. [31], [38], also offers a more accurate method of identifying the tensile properties from an LDC. In this method, the connection between the loading and the reaction of the material is prioritized through studying the evolution of the specimen deflection. Displacement is then specified to be the distance protruded by the punch (crosshead displacement, u_{dis}), whereas the deflection (measured on the opposite contact surface of the specimen, u_{def}) exhibits the degree of displacement of the specimen due to its deformation. Under special evaluation [31], the relationship of the non-contact surface and the contact surface through displacement, u_{dis} vs deflection, u_{def}, exhibits a maximum curvature point as shown in **Figure 25**. For this method the DIC camera can be utilised to measure the deflection on the non-contact surface and the Linear Variable Differential Transformer (LVDT) can be used to establish the displacement of the punch during the SP test.

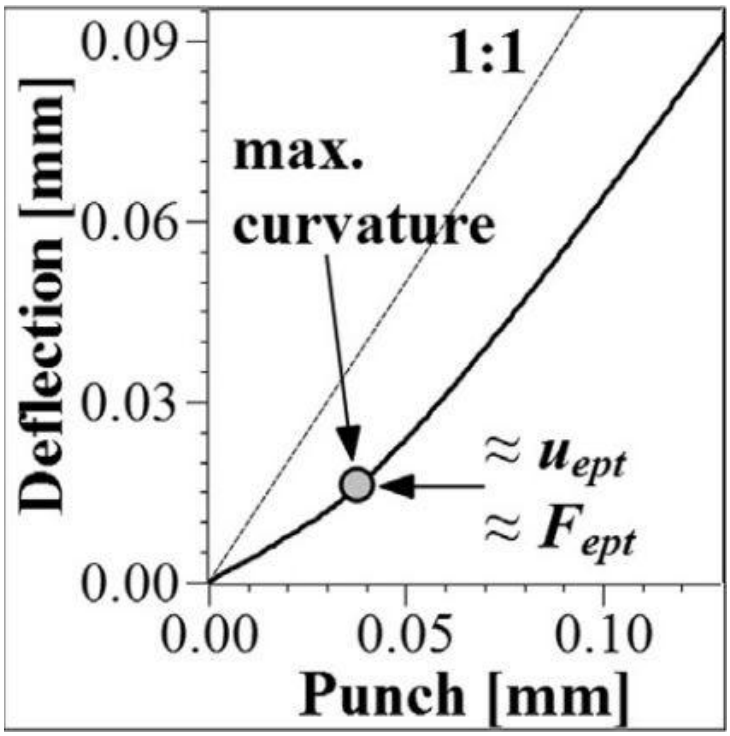

Figure 25: Specimen Deflection vs Punch Displacement [31]

This point of maximum curvature relates the behaviour of the deflection against punch displacement curve to the elastic plastic transition (ept), a point which closely exhibits the yield strength of material, u_{ept}. According to the relationship characterisation [u_{def}; F_{ept}] ≡ [u_{ept}; F_{ept}], the load at this point of maximum curvature can then be related to the yield load using **Equation 12**.

$$\sigma_y = a\left(\frac{F_{ept}}{h_0^2}\right) + b$$

Where σ_Y is the calculated yield stress
h_0 is initial thickness of test specimen
F_{ept} is the load at point u_{ept}
a and b are fitting parameters
Equation 12

$$\sigma_y = \alpha\left(\frac{F_{ept}}{h_0^2}\right)$$

Where σ_Y is the calculated yield stress
h_0 is initial thickness of test specimen
α is the yield stress correlation factor
F_{ept} is the load at u_{ept} deflection/displacement
Equation 13

Equation 13 displays the correlation of this load with the yield strength. **Figure 26** shows the correlation between the yield stress of the materials tested [31] and the elastic to plastic transition load, F_{ept}, derived from the SPT LDCs. As shown in the figure, there is a high degree of correlation reached since there is a linear trend in this relationship

between the yield stress and F_{ept}/h_0^2. This enhances the suitability of this approach to evaluate the yield stress from SPT and the determination of α, the yield stress correlation factor.

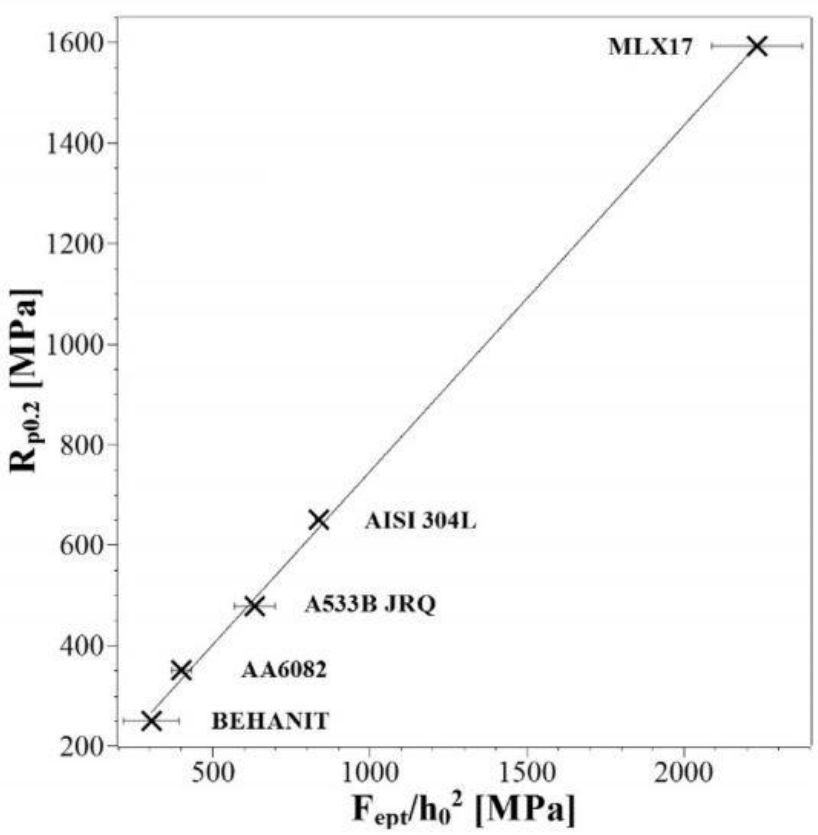

Figure 26: Yield Stress vs F_{ept}/h_0^2 correlation for AISI 304L, A553B JRQ, Behanit, MLX 17 and AA6082 steels [31]

For the UTS, Janca et al. propose characterising material strength with some measure of deformation additionally employed for proper normalisation. To cater for the measurement of the deformation aspect, the method involves the thinning phenomenon in attempt to formulate the UTS. Thinning can be defined by the difference between displacement, u_{dis} and deflection, u_{def}, as shown in **Equation 14**.

$$\Delta h = u_{dis} - u_{def}$$

Where u_{dis} is the displacement
u_{def} is the deflection
Equation 14

The material sensitive thinning method allows distinguishing materials with different mechanical behaviours. The thinning against u_{dis} relationship shown in **Figure 27** displays the material reaction phases as the SPT is carried out.

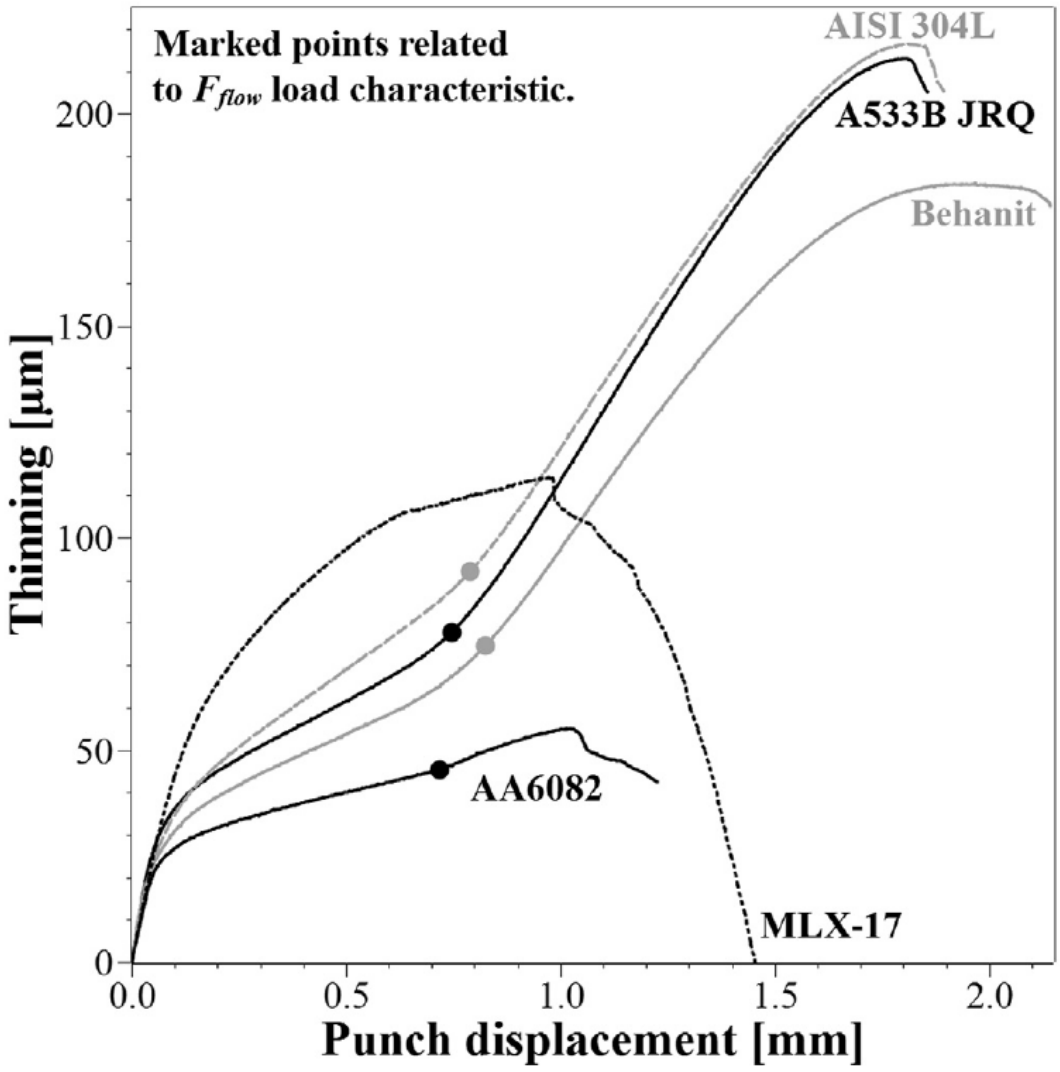

Figure 27: Thinning vs Punch displacement for AISI 304L, A553B JRQ, Behanit, MLX 17 and AA6082 steels [31]

These phases include the elastic-plastic transition as well as continuous material hardening up until the point of maximum curvature in the convex knee of the graph, where displacement point u_{flow} is determined. This point of maximal curvature was evaluated by solving **Equation 15** numerically [31]. After this point, the convex curvature turns concave, meaning the reaction force stops increasing and starts to decrease as in a tensile test scenario. This is as a result of the material beginning to soften and plastically flow meaning the material loses load bearing capacity [31].

$$\frac{d^3 u_{def}}{du_{disp}^3} = 0$$

Where u_{def} is the deflection on the specimen surface
U_{disp} is the displacement of the punch

Equation 15

This displacement point obtained from **Figure 27**, can be used to determine the corresponding load F_{flow} on the LDC. Load point F_{flow} can thus be related to the UTS using **Equation 16**.

$$\sigma_{UTS} = a\left(\frac{F_{flow}}{h_0 \cdot u_{flow}}\right) + b$$

Where σ_{UTS} is the calculated ultimate tensile stress
u_{flow} is deflection at the maximal curvature point
h_0 is initial thickness of test specimen
F_{flow} is the load at u_{flow} deflection
a and b are fitting parameters
Equation 16

$$\sigma_{UTS} = \beta\left(\frac{F_{flow}}{h_0 \cdot u_{flow}}\right)$$

Where σ_{UTS} is the calculated ultimate tensile stress
β is the ultimate tensile stress correlation factor
u_{flow} is deflection at the maximal curvature point
h_0 is initial thickness of test specimen
F_{flow} is the load at u_{flow} deflection
Equation 17

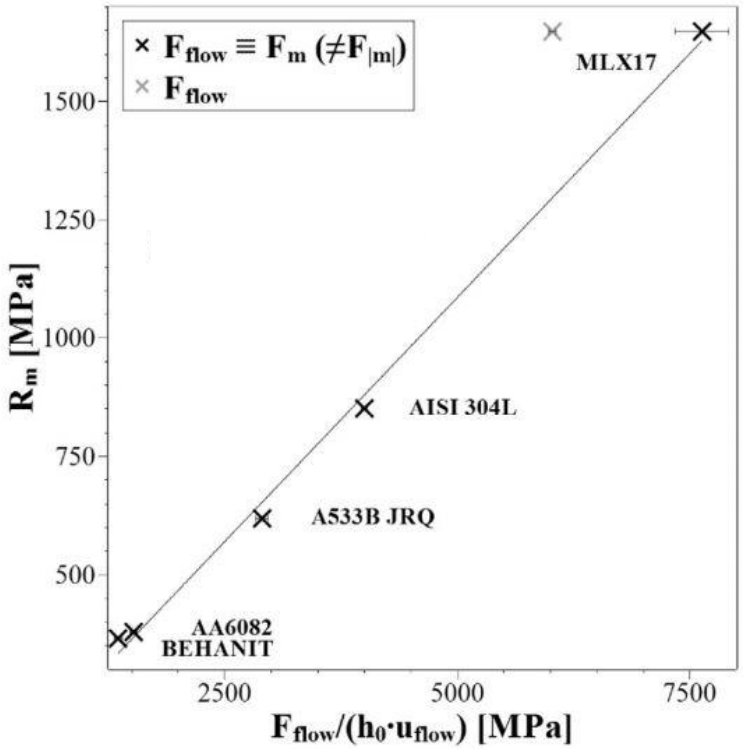

Figure 28: UTS vs $F_{flow}/(h_0 \cdot u_{flow})$ correlation for AISI 304L, A553B JRQ, Behanit, MLX 17 and AA6082 steels [31]

Figure 28 shows the correlation between the UTS and F_{flow} via **Equation 17**, and a linear relationship can be established. In the case of poorly ductile materials, F_{flow} can be defined as equal to the maximum load reached during the SPT, F_{max}. This trend highlights suitability of the method in predicting the UTS.

Characterisation of F_{ept} and F_{flow} in the SP test graphs will result in close correlation with yield stress and UTS respectively. The combination of a load variable and thinning delivers a curve that will be a good illustration tool to show how the material tested responds to loading during the test [46].

As in the CWA literature [24], Janca also proposes the establishment of an inflection point on the LDC. In his paper, Janca discussed that the maximum load on a LDC and the UTS describe different material states, and that the inflection point can be described as a characteristic point that precedes the peak point [31]. In this method the second inflection point on the LDC is evaluated to obtain the two load and displacement variables u_{infl} and F_{infl}. **Figure 29** shows the different obtainable characteristics on the SPT LDC as discussed in this section.

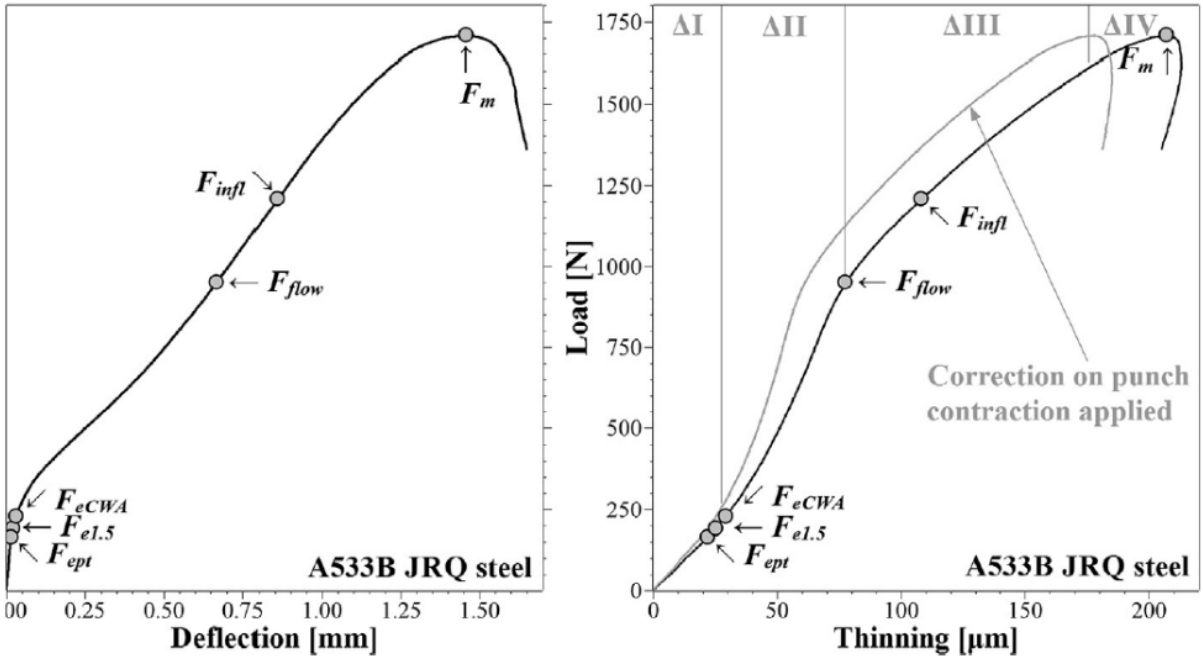

Figure 29: Load-deflection and Load-thinning curves with characteristic points shown for A533B JRQ steel [46]

$$\frac{d^2F}{du_{def}^2} = 0$$

Where F is the load in the LDC
u is the deflection
Equation 18

As shown in **Figure 29**, the second inflection point can be analytically determined through differential analysis of the LDC and subsequently the u_{infl} and F_{infl} values can be attained. The punch contraction was corrected to obtain absolute thinning for the A533B JRQ steel tested, resulting in a more accurate load-thinning curve observed. The second derivative of the LDC was used to identify the second inflection point using **Equation 18**. The F_{infl} points can be correlated with the UTS with the following expression **Equation 19**:

$$\sigma_{UTS} = a\left(\frac{F_{infl}}{h_0 \cdot u_{infl}}\right) + b$$

Where σ_{UTS} is the calculated ultimate tensile stress
u_{infl} is deflection at the second inflection point
h_0 is initial thickness of test specimen
F_{infl} is the load at u_{infl} deflection
a and b are fitting parameters
Equation 19

$$\sigma_{UTS} = \beta\left(\frac{F_{infl}}{h_0 \cdot u_{infl}}\right)$$

β is the ultimate tensile stress correlation factor
Equation 20

Figure 30 shows that there is good fitting accuracy and reproducibility and that the results can be compared to the traditional method results based on the maximum load on the LDC, F_m. **Equation 20** shows the correlation between the UTS and F_{infl} as seen in **Figure 30**.

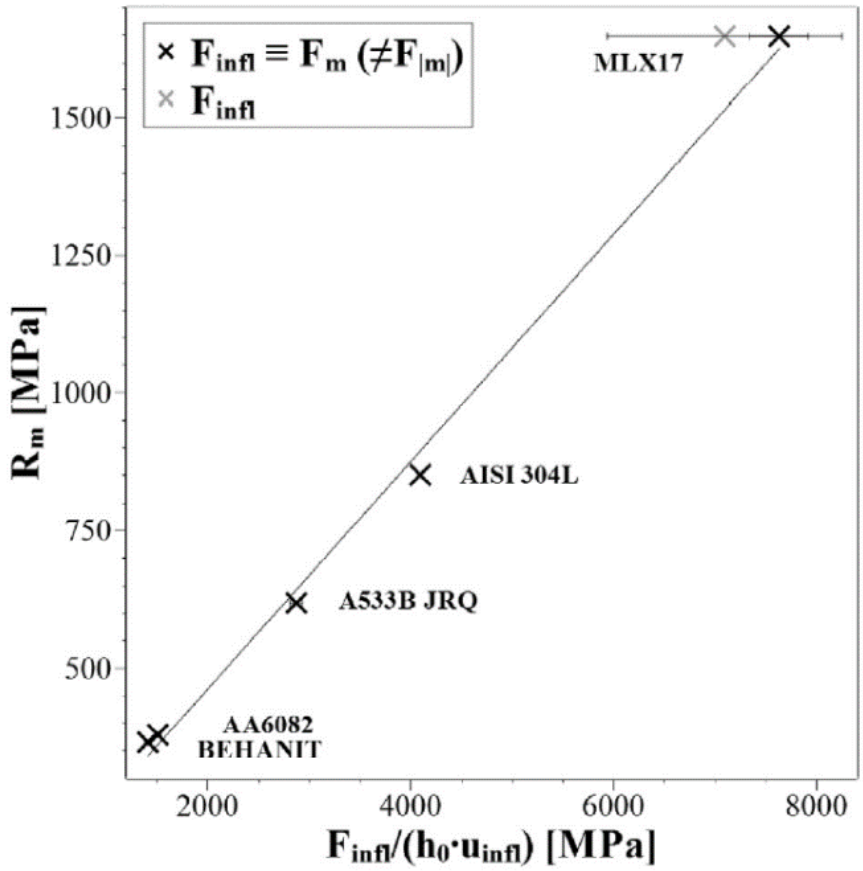

Figure 30: UTS vs $F_{infl}/(h_0 \cdot u_{infl})$ correlation for AISI 304L, A553B JRQ, Behanit, MLX 17 and AA6082 steels [46]

Most of these SPT evaluation methods proposed by Janca et al. [31] were newly proposed methodologies of analysis, which were a different but more advanced approach to the CWA standard. This project adopts some of these evaluation methods to further understand the data and information obtained from a LDC as well as utilise the CWA standard's approach. The correlation factors established in these relationships, are typically determined through a linear regression fit of the conventionally established mechanical properties of various materials plotted against the values of the equivalent SPT formulation [47], [48].

2.5.2.1.3 Method Hahner

According to Hahner et al. [7], a self-consistent data reduction scheme to determine tensile yield stress from the SPTs is introduced. The scheme is as a result of finite element simulations of a wide range of hardening exponents of power-law hardening and strength coefficients. The determination of the yield strength will be based on the curvature of the LDC and not restricted to a single elastic to plastic transition force, F_e. **Figure 31** shows the ternary (three colour coded) stress maps for different loading stages during an SPT, showing the von Mises stress in the specimen as the test progressed.

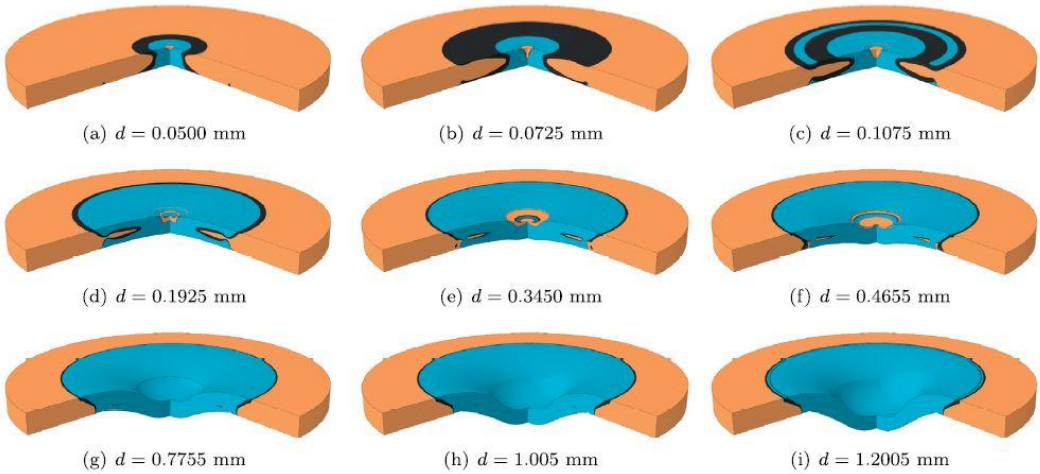

Figure 31: Ternary stress maps for different SPT loading stages (orange: largely elastic region; black: active yielding region; blue: highly stressed region – approaching plastic deformation) [7]

As seen in **Figure 31**, with *d* being the displacement due to the punch, the elastic to plastic transition force F_e is related to a complex yield pattern which involves stretching and bending of the material. This makes identifying a unique F_e value not possible for any material using the SPT, as there will be neglection of the strain hardening behaviour of the material [7].

In order to take note of the hardening phenomenon, Hahner et al. proposed the use of a triplet of forces at different offsets to fully capture the curvature of the LDC in this critical elastic to plastic stage. As shown in **Figure 32**, the scheme quantifies the curvature of the LDC by using three distinct displacement offsets.

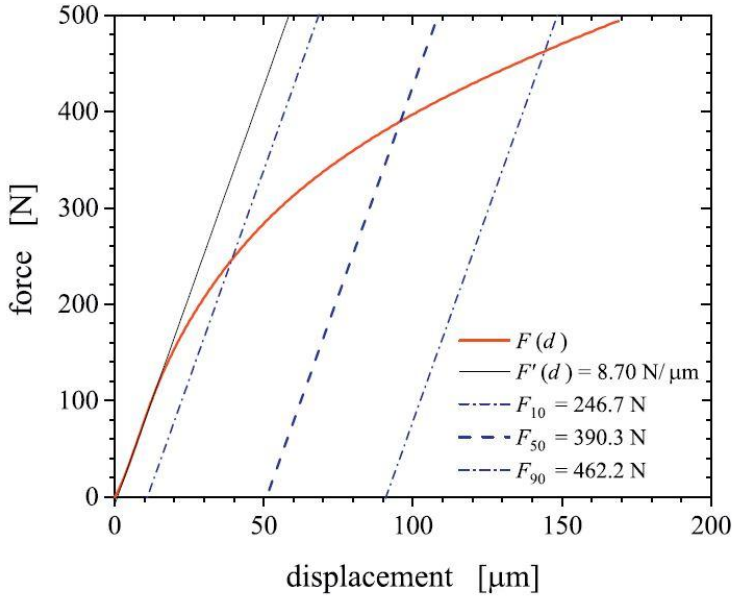

Figure 32: Illustration of scheme to quantify LDC curvature at distinct displacement offsets 10 µm, 50 µm and 90 µm for FE simulated P91 steel [7]

As shown in **Figure 32**, displacement offsets 10 µm, 50 µm and 90 µm are chosen to define the force triplets [F_{10}, F_{50}, F_{90}]. The Hollomon rule, shown in **Equation 21**, describes the prevalent strain hardening during metal forming processes [7].

$$\sigma = C\varepsilon^n$$

Where n is the strain hardening exponent
C is the strength coefficient (MPa)
σ is the true stress (MPa)
ε is the true plastic strain
Equation 21

According to Hahner et al. [7], strength coefficients ranging from *300MPa < C < 1500MPa*, with hardening exponents ranging from *0.02 < n < 0.6*, three different values of elastic modulus; *E = 70 GPa, E = 210 GPa and E = 400 GPa* as well as a Poisson ratio of *v = 0.3*, were used to numerically determine the curvature of the force-displacement curve [7]. The numerical simulations carried out were aimed at improving the accuracy of the yield stress estimation by examining how the load evolution in an LDC is influenced by the material strain-hardening behaviour. Instead of a single load point, the study explores the use of multiple load points at different displacements to improve the capturing of the elastic to plastic transition LDC curvature. The LDC curvature is then quantified by a dimensionless factor K which is defined in **Equation 22**.

$$K = 2\frac{F_{50} - F_{10}}{F_{90} - F_{10}} - 1 = \frac{[F_{50} - F_{10}] - [F_{90} - F_{50}]}{F_{90} - F_{10}}$$

Where F_{10} is the force at a displacement of 10 µm
F_{50} is the force at a displacement of 50 µm
F_{90} is the force at a displacement of 90 µm
Equation 22

From Hahner et al.'s adopted simulations, the relationship between the curvature K and the hardening exponent *n*, can be approximated from a linear fit for $0.1 \leq n \leq 0.6$, and for E = 210 GPa (Young's Modulus of steels). The following expression was obtained:

$$n = 1 - 3.034K \quad \text{for } K < 0.330$$

Equation 23

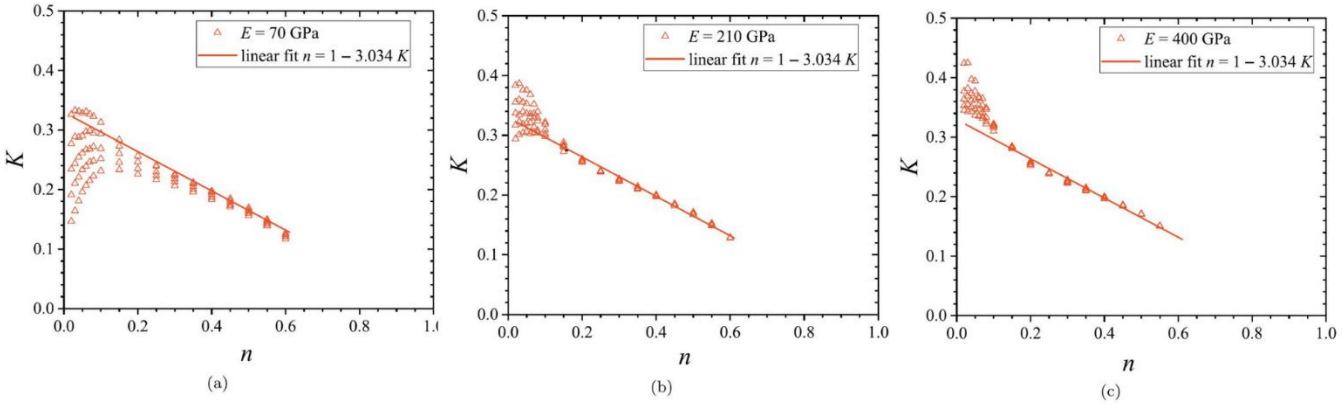

Figure 33: Dependence of the curvature factor, K, on the hardening exponent, n, as numerically determined for a variety of Hollomon-type power law hardening rules with strength coefficients 300 MPa < C < 1500 MPa and 0.02 < n < 0.6 for (a) E = 70 GPa, (b) E = 210 GPa, (c) E = 400 GPa [7].

As seen in **Figure 33**, the fit works well for E = 210 GPa, but at small *n* values the fit overestimates K for E = 70 GPa and underestimates K for E = 400 GPa. This is as a result of a dependence of K on the strength coefficient C, which becomes insignificant with larger values of *n*. The hardening exponent *n* can be inferred from the curvature K to derive a K-dependent yield coefficient α_{50} and a corresponding yield stress, σ_Y [7]. A linear fit on the data for E = 210 GPa provides the following expression:

$$\alpha_{50} = 0.360 - 0.422n \quad \text{for } n > 0$$

Where α_{50} is the yield corelation coefficient
Equation 24

As seen in **Figure 34**, this fit has satisfactory quality even for data from both Young's moduli E = 70 GPa and E = 400 GPa.

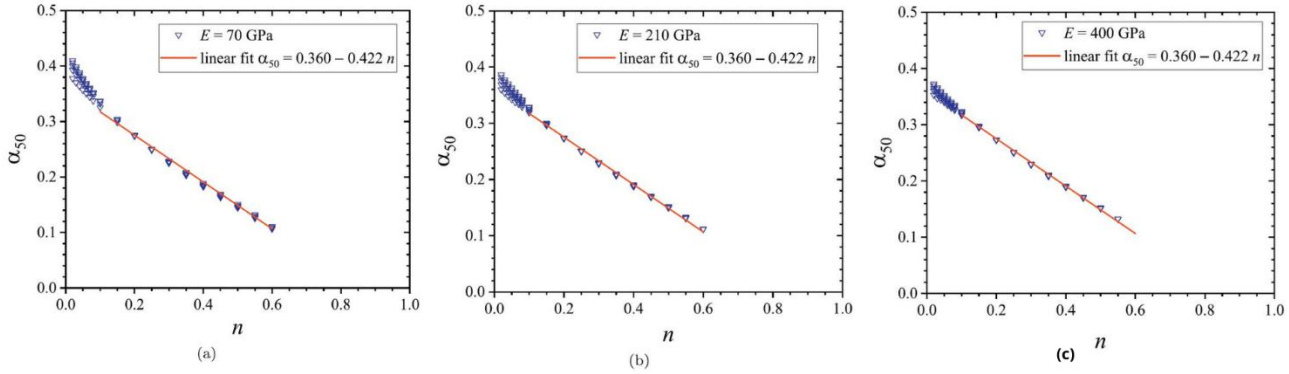

Figure 34: Correlation factor α_{50}, as a function of hardening exponent, n, numerically determined for power law hardening rules with strength coefficients 300 MPa< C <1500 MPa and 0.02 < n < 0.6 for (a) E = 70 GPa, (b) E = 210 GPa, (c) E = 400 GPa[7].

Hahner et al. then proposed combining **Equation 23** and **Equation 24** to obtain a stepwise linear K-dependence in **Equation 25**.

$$\alpha_{50} = \begin{cases} 1.28K - 0.062 & \text{for K} < 0.330 \\ 0.360 & \text{otherwise} \end{cases}$$

Equation 25

K = 0.330 is required for the consideration of only positive values of the hardening exponent *n*. The accuracy of the stepwise linear approximation increases with the increase in the Young's modulus, as shown in **Figure 35**.

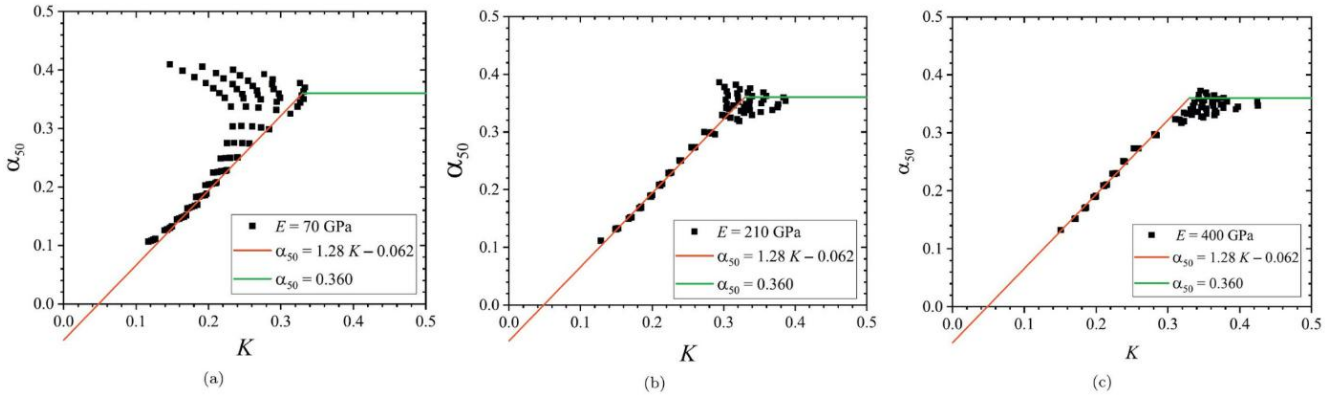

Figure 35: The curvature dependence of the correlation factor α_{50}, for power law hardening rules with strength coefficients 300 MPa < C < 1500 MPa and 0.02 < n < 0.6 for (a) E = 70 GPa, (b) E = 210 GPa, (c) E = 400 GPa [7].

As a result of the K-dependence of α_{50}, the K-dependent yield stress as derived from the load at 50 µm offset can be found using **Equation 26** [7].

$$\sigma_y = \begin{cases} [1.28K - 0.062]\dfrac{F_{50}}{h^2} & \text{for K} < 0.330 \\ 0.360\dfrac{F_{50}}{h^2} & \text{otherwise} \end{cases}$$

Where σ_y is the calculated yield stress, $\sigma_{Kfactor}$

Equation 26

The yield stress can then be derived with the knowledge of the three forces at the different offsets of 10 µm, 50 µm and 90 µm [7].

2.5.2.2 Arithmetic Approach/ Empirical Formulations to estimate toughness parameters using SPT

As defined earlier, toughness is the ability of a material to absorb energy until fracture [2], [3], [4]. Various mechanical tests provide a framework that can be used to assess the different concepts or aspects of toughness. Depending on the loading conditions, material application and environmental conditions, an appropriate selection of the toughness test is essential.

2.5.2.2.1 Fracture Toughness

Fracture toughness evaluates the resistance of a material to fracture in the presence of a sharp crack under linear-elastic stress and severe tensile constraint in a neutral environment. The fracture toughness, (K_{Ic}), values obtained can be used to estimate the relation between failure stress and crack size for a material in service. The specimen size is also a critical consideration as the fracture toughness analysis applied is highly dependent on specimen dimensions [49], [50].

The fracture toughness K_{Ic} can be correlated with the CVN impact test. The CVN test assesses the behaviour of materials subjected to an application of a force resulting in multi-axial stresses associated with a notch, coupled with high rates of loading. The test is carried out at various temperatures in order to determine the fracture accurately in different conditions, specifying toughness values that would ensure assessment of elastic-plastic behaviour for the fracture of fatigue cracked specimens [51]. The correlation between the fracture toughness and the CVN tests is obtained through the CVN transition temperature, as the Charpy impact transition curve is the most common basis for specifying toughness [52].

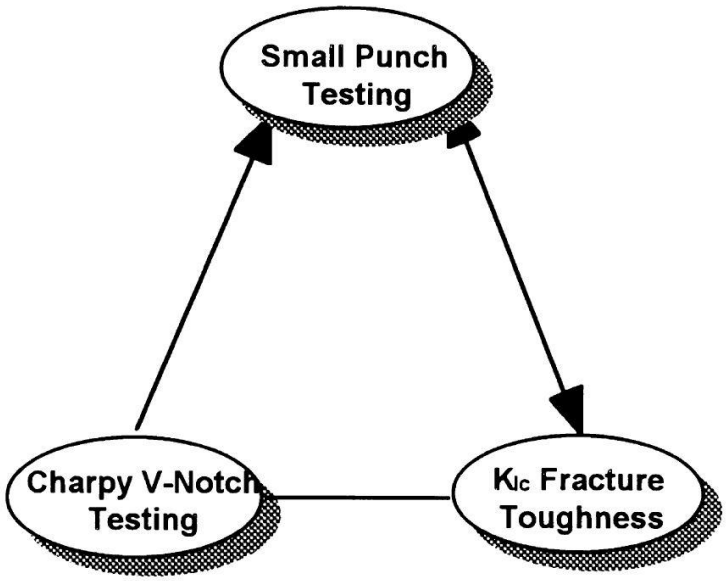

Figure 36: Mechanical testing correlations [52]

The SPT transition temperature, T_{SP}, from a series of SPTs through a range of various temperatures is defined as the temperature at which the fracture energy is equal to the mean of the upper and lower shelf energy [52]. The temperature dependence of the E_{SP} can be used in the correlation with CVN transition temperature through the T_{SP} and the Charpy DBTT as well as the Charpy FATT [37], [52]. As seen in the test triangle in **Figure 36**, the fracture toughness, CVN and SPT can be correlated empirically.

However, the T_{SP} from SP tests is lower than the $(FATT)_{CVN}$ as the SP specimen is deformed under static loading and in a biaxial stress state, which is less favourable for brittle failure as compared with dynamic loading and triaxial stress state in CVN tests [53]. **Equation 27** to **Equation 29** show the relationship between the fracture toughness, K_{IC} and the CVN, and subsequently the SPT and the CVN [38], [52], [54]:

$$K_{Ic} = {}^{6600}/_{60} - (T - FATT_{CVN})$$

Where $FATT_{CVN}$ is the FATT of the CVN test
K_{IC} is the fracture toughness
T is the test temperature
Equation 27

$$FATT_{CVN} = a + b(T_{SP})$$

Where $FATT_{CVN}$ is the FATT of the CVN test
T_{SP} is the SPT transition temperature
a and b are fitting parameters
Equation 28

$$T_{SP} = \alpha T_{CVN}$$

Where T_{CVN} is the CVN transition temperature (FATT/DBTT)
T_{SP} is the SPT transition temperature
α is a correlation factor
Equation 29

2.5.2.2.2 Modulus of Toughness

Another aspect of toughness in steels, besides fracture toughness and impact toughness discussed earlier, is the modulus of toughness, U_T [55]. According to Bandanadjaja et al., Manjunath et al. and Callister [2], [3], [4], the area under the stress strain curve up until the point of rupture in a tensile test represents the energy absorbed by the material until fracture and can be used as an indicator of the tensile toughness of the material. The U_T reflects a combination of the tensile strength, yield strength and elongation of a tensile test sample and is defined by **Equation 30** [3], [55]:

$$U_T = \int_0^{\varepsilon_f} \sigma \, d\varepsilon$$

Where U_T is the modulus of toughness
$\boldsymbol{\varepsilon}_f$ is the strain at fracture
σ is the applied stress
Equation 30

The U_T is a vital mechanical property in structural and component applications as it is significant in the assessment of the ability of a material to withstand deformation under tensile loading without fracturing. Given the U_T is an energy-based material property, a correlation between the tensile test and other energy-based mechanical tests can be drawn. The E_{SP} obtained from the area under the SPT LDC presents an opportunity to establish a relationship with U_T obtained from the tensile test. In cases with limited sample sizes where non-destructive testing methods are required, such a correlation could enhance the applicability of the SPT as a reliable method for the estimation of material toughness.

2.5.2.2.3 Power Law for Empirical Correlations

A power law is a mathematical model that can be used to describe correlation between two variables, where relative change in one variable results in a relative change in the other variable, independent of the size [56]. This model can be generally expressed as in **Equation 31**:

$$y = Ax^B$$

Where y and x are independent variables
A is a constant scaling factor
B is the exponent (power-law index)
Equation 31

This correlation is validated through use of experimental data. The natural logarithm, ln, of the above-mentioned variables is plotted in order to linearize the **Equation 31** to result in **Equation 32**:

$$lny = lnA + Blnx$$

Where A is the y-intercept
B is the slope of the line
Equation 32

The constants A and B can therefore be determined through regression analysis and can be reinforced by the statistical goodness of fit indicator (R^2) which evaluates the fit of the regression line to the plotted data [3], [57]. The power law can be a correlation formulation to establish a relationship between material properties.

2.5.3 Limitations in Literature

As a quasi-non-destructive testing technique, the SPT can be deemed a favourable method to assess material properties especially in situations where it is impractical to adopt standard mechanical tests. However, the literature explored presented a few shortcomings and challenges.

These challenges included the lack of standardization of the SPT procedures, limited high or low temperature tests and data, limited reproducibility of tests and specimen preparation variability. Finite element modelling (FEM) and simulation-based models have assisted in solving some of these challenges, addressing SPT temperature variations and reproducibility. With more SPTs being performed and more data collected, a standardized approach to the test to support the constantly updated European standard CWA 15627:2007 [24], will also improve the reproducibility of SPT experiments. At the time this project was initiated in February 2020, the ASTM E3205-20 was not yet available, and it was felt that the CEN documents significantly captured the scope of the work required.

The detection of the crack onset was one of the primary limitations identified in the literature. Unlike in fracture toughness tests where crack-tip opening displacement (CTOD) and crack growth are used, the SPT relies on the LDC which does not directly identify the crack initiation point of the test. As a result, various methods and approaches were proposed by researchers to define the crack initiation point, leading to inconsistency and variability of the crack initiation criteria. A potential solution to this limitation involved improving crack detection accuracy by the use of high-resolution cameras to introduce DIC-based specimen monitoring.

According to Stracey [8], DIC could be used to identify the point of crack initiation by observing discontinuity in the deflection data recorded during the test. This point in the LDC could then be used as the crack initiation point, as the speckle pattern on the specimen being tracked by the DIC would have ruptured at that point. However, a more sensitive approach could be adopted by using DIC to track strain mapping over the specimen surface and incorporate strain energy density (SED) analysis to identify crack initiation [4], [22], [58].

Even though literature includes the determination of the U_T as an energy-based material property, to the author's knowledge no reports were stated on the correlations of the U_T with the SPT E_{SP}.

2.5.3.1 DIC-SED Crack Initiation

Integrating the DIC strain measurements with SED analysis provides a physics-based quantitative approach to detect the onset of the crack during an SPT [58]. This approach relies less on the visual discontinuities observed using the DIC cameras, making the approach more robust as precision is enhanced.

SED can be calculated as in **Equation 33** [59]:

$$SED = \frac{1}{2}\sigma\varepsilon$$

Where σ is the applied stress
$\boldsymbol{\varepsilon}$ is the true strain
Equation 33

Stress can be estimated from specimen and punch geometry, as the contact area of the punch, assumed to be the top half of the spherical punch in contact with the flat surface of the specimen, can be determined in conjunction with each SPT load data point. The strain can be derived from the maximum surface principal engineering strain using DIC analysis on the specimen surface. The rate of change of SED (first derivative of SED curve), can be used to detect the initial sharp increase in the strain energy density, which suggests a crack initiation point in the material [27], [60].

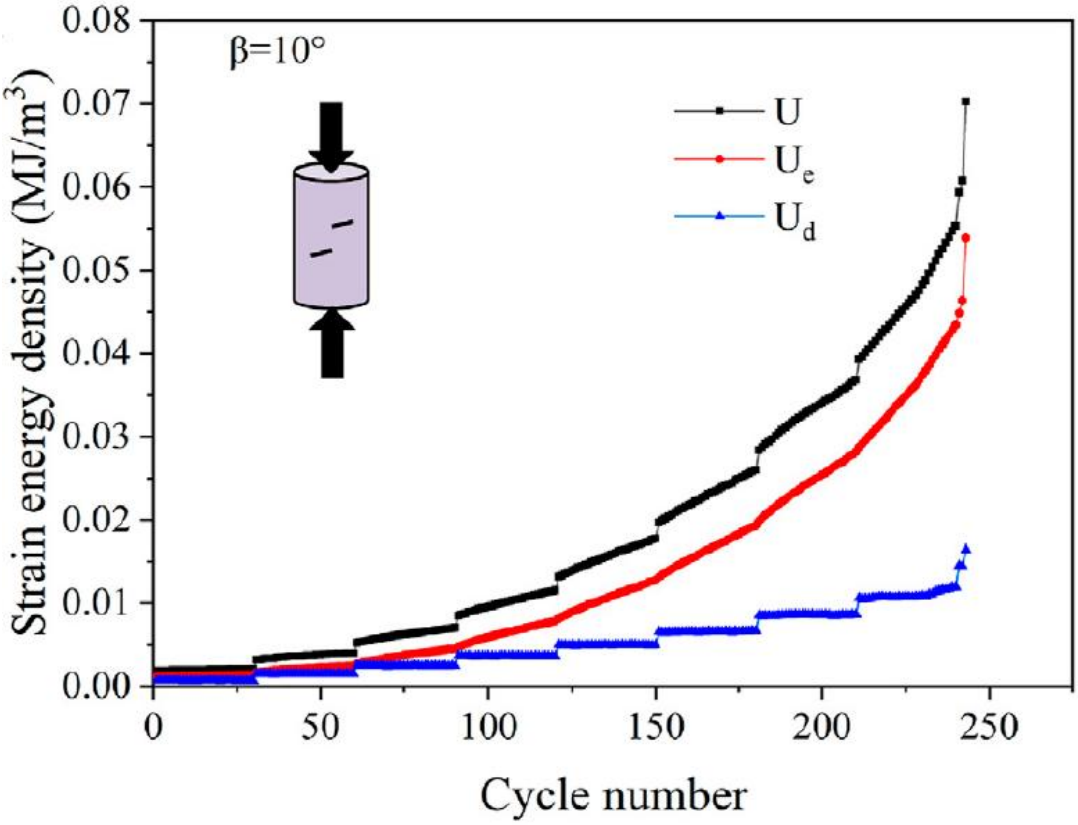

Figure 37: Strain Energy Density evolution of U (total strain energy density), U_e (elastic energy density) and U_d (dissipated energy density), as loading cycles increase on marble specimen with fissure angle, β,at 10^o [60]

As seen in **Figure 37**, the rate of the SED increases more rapidly as the loading cycles increase, signifying the crack propagation up until rupture of the material. This demonstrates the effectiveness of the SED approach in capturing crack initiation and propagation until the subsequent failure of the material. In the case of an SPT, the identification of the crack initiation point using DIC and SED allows the exploration of the material properties related to this point on an LDC.

2.5.3.2 Proposed Solution

Considering the complexity and difficulty of varying the SPT temperatures (high and cryogenic temperatures) to characterise the energy-based correlation with CVN impact energy and fracture toughness, a room temperature energy analysis of the SPT can be explored further. Similar to the SPT, the uniaxial tensile test conducted at room temperature can be utilised to evaluate the energy absorbed by the material during the test until fracture, an indication of its tensile toughness properties.

This study proposes to establish an energy-based correlation between the SPT and the tensile test by analysing the toughness properties derived from the two tests. The SPT LDC point of maximum load, the crack initiation point on the LDC identified using DIC and SED analysis and the tensile test stress strain data obtained from the same as-received and heat-treated steel samples in this study, shall be analysed to determine whether a robust correlation between the two test methods can be established.

2.6 SUMMARY

The literature review has explored several aspects that affect material integrity, including phenomena such as embrittlement, highlighting the importance of material assessment methods in evaluating the properties of materials, particularly in-service materials. The SPT has been presented as an effective quasi-non-destructive method for evaluating material properties, with emphasis on the importance of its reliability and accuracy. The integration of DIC as a measuring tool capable of tracking strain, deformation and specimen surface images during testing has enhanced the depth of the information that can be extracted from the SPT, making it a vital non-contact addition to the SPT setup.

In addition, the metallurgical behaviour of steel materials under different temperature conditions was examined, providing valuable insight to how temperature variations influence steel material properties in heat treatments. Analytical and empirical approaches in existing literature were explored to provide a baseline in understanding the SPT and the implications of the test results regarding material properties. The review identified limitations in the literature, particularly accurately establishing crack initiation during SPT and the correlation between U_T and the E_{SP}. The present study proposed an approach to assist in addressing these shortcomings.

In conclusion, this chapter has provided a comprehensive overview of the application of the SPT in the analysis of material properties. It emphasized on the importance of material toughness properties in real-world engineering applications, and the need for non-destructive techniques to evaluate service material properties reliably with minimal operational interruptions.

Chapter 3 outlines the experimental methodology adopted in this study. It elaborates on the selection of the VRN500 steel, the controlled heat treatment procedures employed to induce the varying toughness properties of the material investigated and the utilization of DIC for crack detection during the SPTs.

CHAPTER 3: EXPERIMENTAL METHOD

3.1 RESEARCH APPROACH

In order to validate and apply the SPT for measurement of the toughness of steels, Vickers Hardness (ASTM E92), Tensile (ASTM E8), Fracture Toughness (ASTM E399) and CVN (ASTM E23) tests needed to be carried out together with the SPT. From literature, the methods used to correlate and validate the SPT all followed standardized experimental procedures, with the mechanical tests results as well as the results obtained from SPTs being used to draw correlations and conclusions.

In this experimental process, the material that was under investigation was partitioned into the three distinct regimes (two heat treatments and one as-received). Before the three distinct regimes could be established, a series of heat treatments on the material were carried out and then evaluated using the Vickers Hardness test (ASTM E92). This was done to have the best results in varying the mechanical properties of the heat-treated specimens in terms of hardness. The specimens to be used in the experiments were then obtained from these material condition regimes, taking note of the heat treatment conditioning in the entire process.

The experimental method was then designed in accordance with the relevant standards, to ensure that the mechanical characteristic that would be measured by the tests gave an accurate depiction of the condition of the material investigated. The experimental procedure encompassed the conditioning of pre-machined blocks of material and the specimen preparation – selection, designing and machining of the conditioned material into samples ready for testing. The ASTM standards provided adequate guidelines for the full experimental process, and these steps will be elaborated on further on in this section. The adherence to these guidelines was required to meet the standard as well as provide a baseline for a standardized experimental procedure. The results obtained from these experiments were then used to formulate, compare and correlate the toughness properties from the different mechanical tests, enabling us to validate the use of the SPT.

3.2 MATERIAL INVESTIGATED

This section highlights the material characteristics of the material to be investigated as well as methods that were used to establish the rolling direction of the material plate from which the samples were to be obtained. This was to determine the orientation of the samples, ensuring consistency and specimen integrity.

3.2.1 Material Under Assessment

VRN 500: Hard-Wearing and Abrasion Resistant Steel acquired from Macsteel Service Centre was the material to be assessed in this project. Macsteel VRN, a division of Macsteel Service Centres SA (Pty) Ltd is the retailer that provided the material to be used in this project.

In order to validate the SPT method, an existing steel was to be assessed. The material to be assessed in this project was a high hardness, conventionally low alloy martensitic steel grade which could withstand high wear and abrasion, as well as exhibit high resistance to impact [61]. Some uses for this material include earthmoving machinery, wear plates, storage bin liners (heavy-duty machinery) etc. **Table 2** shows the chemical composition of the material.

Element	C	Si	Mn	P	S	Cr	Mo	Ni	V	B
wt.%	0.35	0.7	1.8	0.035	0.03	1.0	0.8	0.8	0.08	0.005

Table 2: Chemical composition of Macsteel VRN500 steel [61]

The VRN 500 material can be classified as a high hardness low alloy martensitic NiCrMoV steel. In the context of the steel phase diagram, the carbon content being at 0.35 wt.%, makes the material hypoeutectoid as it is below the eutectoid point of 0.76 wt.% C [4]. As for the other elements effects, silicon at 0.7 wt.% remains in solution within the ferrite thus slightly raising the eutectoid temperature and manganese at 1.8 wt.% acts as a deoxidiser and can increase the hardenability of the material by promoting the formation of martensite upon quenching. Phosphorus and sulphur are typically considered as impurities which in turn form inclusions (for instance MnS) which degrade mechanical properties [4].

Chromium stabilizes and expands the ferritic region, also raising the eutectoid temperature. Titanium forms carbides and nitrides, reducing the amount of free carbon for cementite formation, improving the strength properties within the material. Lastly molybdenum strengthens the ferrite phase and increases hardenability. Various properties are increased and improved by these elements. In the cases where brittleness can be induced by the impurities phosphorus and sulphur, these effects are mitigated by manganese and titanium [4]. Boron, even in very small amounts, strengthens the grain boundary and delays ferrite and pearlite transformation, promoting martensite formation and effectively enhance the hardenability of the material [4], [62].

Table 3 shows the mechanical properties of the material as specified in the datasheet.

GRADE	HARDNESS (HV)	Yield Strength (MPa)	Tensile Strength (MPa)	Minimum Elongation (%)
VRN500	470 - 530	1100	1600	14

Table 3: Mechanical properties of VRN500 steel

As shown in **Table 3**, the UTS in the as-received condition of the material is at 1600 MPa, and the yield stress at 1100 MPa, meaning that this material exhibits high strength. The yield stress shows that the material can withstand heavy loads before plastic deformation. The minimum elongation at 14% highlights the moderately ductile behaviour of the material for a martensitic steel. However, the material is relatively brittle in comparison to more ductile microstructures such as ferrite-pearlite steels. This reflects the limited plastic deformation capacity of the martensitic material under tensile loading. The material will not be expected to exhibit significant necking or elongation before fracture.

3.2.2 Orientation of Plate

Attention needed to be paid to the orientation of all the specimens to be machined. There was need for consistency in terms of orientation as materials are sensitive to the microstructure planes (some microstructure planes are weaker thus the ensuing easier crack propagation in comparison with other microstructure planes) [63]. There are different orientations which govern the plane directions of the steel material after manufacturing. The datasheet provided by the retailer did not specify the orientation of the steel plate provided for this project.

As shown in literature, a method to specify the rolling direction of the plate was the assessment of the microstructure on each face of a miniature excerpt from the entire plate. In order to establish the rolling direction, etching had to be carried out on the material obtained from the experiment material block. **Figure 38** shows the material blocks cut from the experiment material slab and marked to show the unspecified orientations A, B and C.

Figure 38: Image of unspecified orientation A, B and C on experimental blocks

3.2.2.1 Etching

As seen in literature, etching can be described as the process used to reveal particular structural characteristics of a metal that are not evident in the polished condition [64]. Etching allows us to highlight the ferrite grain boundaries and phases within the sample structure, as well as the orientation of the sample surface. The material to be tested was hot mounted in epoxy to produce an epoxy embedded sample which improved the logistical aspect of the etching process as the samples could now be handled and tested with ease.

The hot mount process was performed using a Struers Labopress-3 at 180 °C, a temperature not high enough to cause microstructural changes to the material. The specimen was subjected to a 20 minute hot mounting process at a force of 30 N, undergoing the warm condition of the mounting process for 12 minutes and cooled for 8 minutes. The mounted specimen was now prepared for the next stage of the experiment.

The mounted samples were marked A, B and C as shown in **Figure 38** (in different orientations and directions), then subjected to metallographic grinding and subsequently polishing to ensure that the surface of the specimen was smooth and had no scratches or deformations. The mounted specimens were wet-ground with SiC paper (at 200, 500, 800 and finally 1200 grit size), using a Struers LaboPol 2 Manual Polishing machine and water as a lubricant.

A Metaserve Universal Polisher was then used to polish the samples with a 3 μm polishing disc, and then a finer 1 μm disc. Since the material being assessed was a NiCrMoV low alloy martensitic steel, a 2% Nital etchant was used to etch the samples. A few drops of the Nital were dripped onto the sample surface using an eyedropper and a cotton swab was used to rub the etchant on the sample. After five seconds and after the surface of the

sample changed from the mirror finish of polishing to a cloudy finish, the sample was then washed under running water, rinsed with ethanol and then dried using an air blast. Instead of using the eyedropper, the mounted sample could also be immersed in the Nital in a 50 ml beaker for five seconds, and similarly washed under running water, rinsed in alcohol and then dried. The etched samples (A, B and C) were then transferred to a Nikon Eclipse MA200 metallurgical microscope for microstructural analysis.

Using the metallurgical microscope, the images obtained were used to distinguish the orientation of the plate. The rolling, long transverse and normal direction could now be identified, and the material could now be oriented in a consistent manner maintaining the loading axis in the same direction. **Figure 59** to **61** in the **Chapter 4** show the images obtained from the microscope, as well as the microstructural directions that were identified. After etching and microstructural analysis, A, B and C in **Figure 38** could be distinguished in their respective orientations. The directions highlighted in **Figure 39** and **Figure 40** were used to ensure the orientation of the machined samples would be easily identified thus helping in creating a consistent assessment of the material through the different mechanical tests and the SPT respectively. **Table 4** shows the specimen orientations chosen with attention paid to the consistent specimen machining in the same loading direction (T – transverse).

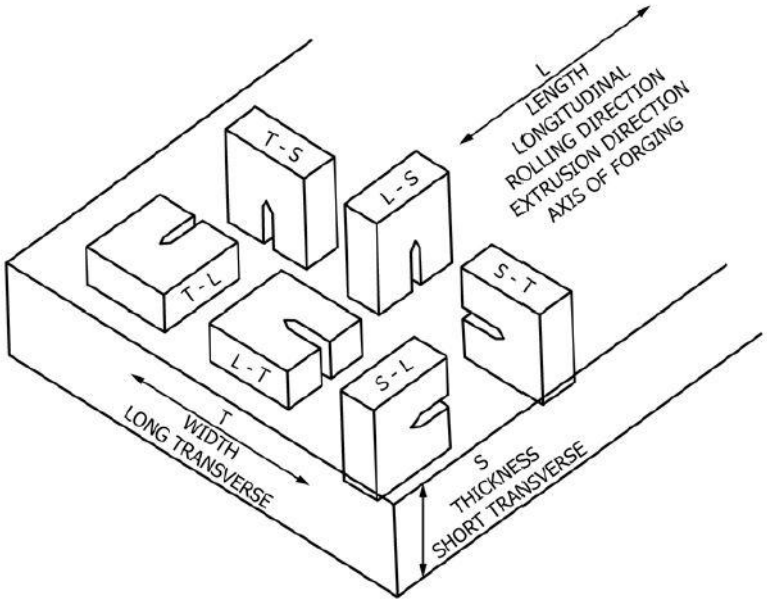

Figure 39: Schematic of fracture toughness specimen orientation for rolled plates (similar for notched rectangular specimens) [49]

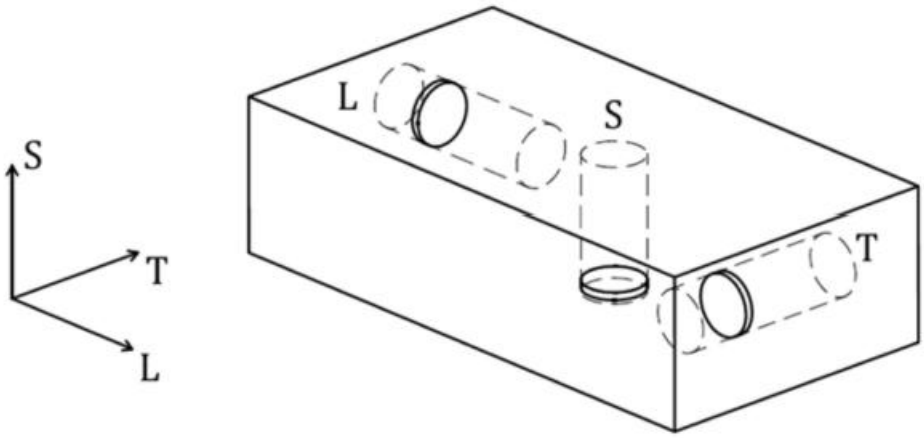

Figure 40: Orientation of SPT specimen (similar for round specimens)[1] [38]

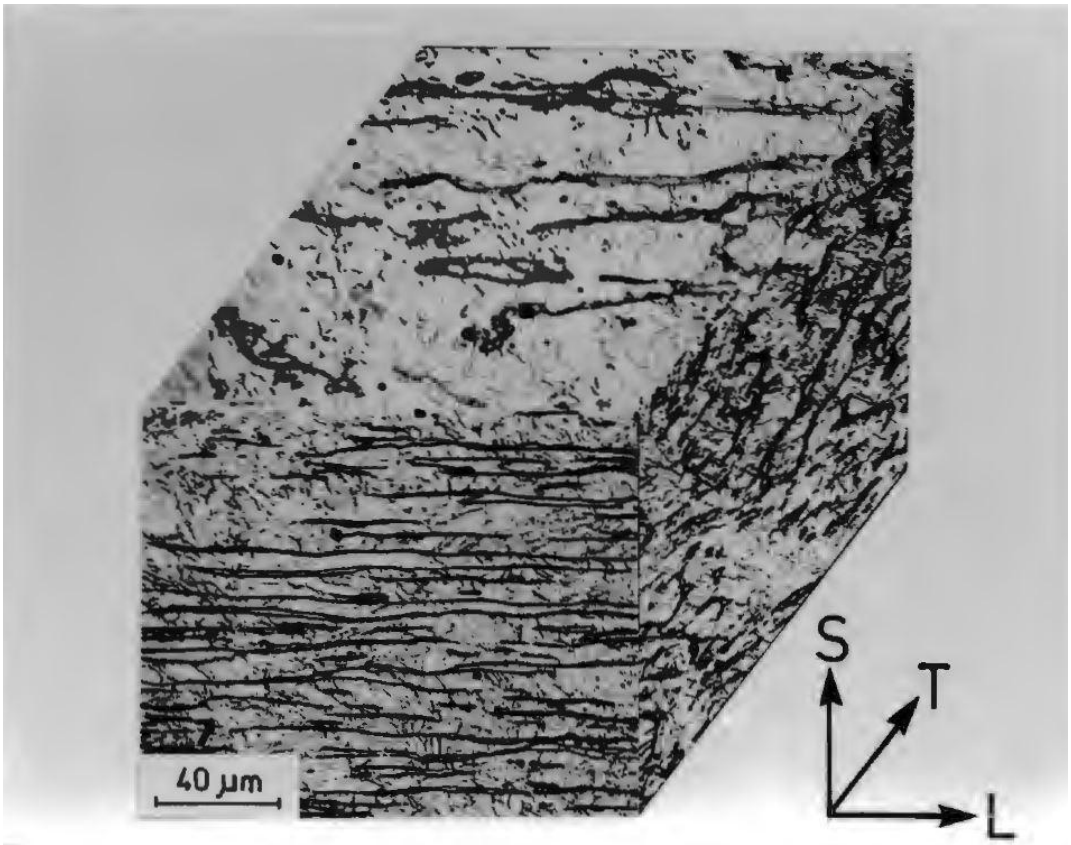

Figure 41: Micrograph showing orientation directions in a rolled plate [65]

[1] Orientation labels (e.g. S–L, S–T, T–L) in the context of round specimens refers to the plane of extraction, not the loading direction. For example, a disc or rod extracted with its cross section in the S–L plane will have its surface normal in the T direction, and will therefore be loaded along T during punch or tensile testing.

EXPERIMENT	AXIS OF LOADING (DIRECTION)	ORIENTATION OF SAMPLE
SPT	**T**	**S-L**
Fracture Toughness Test	**T**	**T-L**
Uniaxial Tensile Test	**T**	**S-L**
CVN Test	**T**	**L-T**

Table 4: Chosen specimen orientation directions for the experimental tests adopted ensuring the same loading axis plane

Due to the limited size of the available "off-the-shelf" block of material to be experimented on, the long transverse axis of loading was chosen to effectively evaluate the material properties of the various specimen geometries across the different mechanical test methods, ensuring consistency and comparability between tests. As seen in **Table 4**, the specimen orientation for the SPT and the tensile test are similar, as both test methods have axial load applied on the round specimens. In both test methods, for long transverse axis of loading (T), the applied load will be perpendicular to the S-L (short transverse-longitudinal) plane. However, as seen in **Figure 39** for the orientation of rectangular specimens, the long transverse axis of loading (T), corresponds to the T-L (long transverse-longitudinal) for the fracture toughness specimen and perpendicular to the L-T (longitudinal-long transverse) for the CVN test specimen.

3.2.3 Heat Treatment

The orientation specified allowed for consistent and quality assured specimens before heat treatment. In accordance with the ASTM standards, the machined specimen dimensions of all four mechanical tests in this project could now be used to determine the required size of the specimens before heat treatment. The ASTM standards used for this project stated the machining was to be done after the heat treatment process [49], [51], [63], [66].

Figure 42: Image of marked pre-heat treated CVN specimens in hot furnace tray

As seen in **Figure 42**, the specimens were then cut into blocks slightly larger than the ASTM standard's dimensions. A wire-cutter was used to accurately cut out samples required for the heat treatment processes. The first batch of as received material specimens that were machined were for the optimization of the heat treatment process, as the most effective heat treatment methods needed to be established before all the specimens to be tested underwent the conditioning. The uniaxial tensile test and the SPT required to be machined as cylindrical rods before heat treatment, and the fracture toughness and CVN tests as rectangular blocks. Attention was paid to the orientation of these blocks, especially the CVN blocks which had to be marked as the samples had similar faces but in different orientation directions.

The production of high, medium and low toughness material was the aim of the heat treatment processes. The samples, in their as received state before heat treatment, were placed strategically on the furnace trays inside the furnace and exposed to different conditions. The furnace had an interface that allowed the testing conditions for the specimens being heat treated to be entered and set up prior to the experiment. Prior to the heat treatment and conditioning of the final test specimens, the Vickers Hardness was used as the test to guide the material selection. This ensured clear differentiation between the three targeted heat treatment conditions: brittle, ductile and intermediate. As a result of the optimized final heat treatments, the SPT and the mechanical tests could then be carried out to assess the material's different responses to the heat treatment processes.

As part of the process, several heat treatment methods were carried out, recorded and observed in order to design the final treatment processes for the specimens to be tested.

In these treatments, the material was exposed to an elevated temperature of 850 °C. The furnace temperature rose at a rate of 5 °C/min and it took approximately 2 hours 45 minutes to reach the desired heat treatment temperature from room temperature. At 850 °C, the material was at a temperature higher than the critical temperature for steel, ensuring the austenisation of the material [4]. The material was held at this temperature for 30 minutes. From the 850 °C temperature, the cooling methods were varied with each heat treatment process, and some specimens were tempered after cooling. These different heat treatment processes can be seen in **Table 5**.

Experiment No.	Heat Treatment Conditions
1	As Received
2	850°C for 30 minutes, then water quenched
3	850°C for 30 minutes, then oil quench
4	850°C for 30 minutes, then air cool
5	850°C for 30 minutes, then furnace cool
6	850°C for 30 minutes, water quench, then 2-hour temper at 600°C, then air cool
7	850°C for 30 minutes, water quench, then 4-hour temper at 600°C

Table 5: Heat treatment variations adopted

Vickers Hardness tests needed to be carried out on the different materials which experienced different heat treatment conditions. The data collected would be expected to exhibit hardness values of adequate range. The Vickers test was now required to quantify and distinguish the three most distinct categories from the seven variations in terms of hardness. With the three distinct heat treatment regimes established, the specimens to be tested could now be heat treated en masse.

3.3 VICKERS HARDNESS TEST

Hardness is measured quantitatively, by noting the extent or depth of an indentation of a standard size and shape on a test specimen. It can also be correlated with the material's tensile strength [67]. To determine the hardness of the material, an experiment adhering to the ASTM E92 Standard test methods for Vickers Hardness for metallic materials was carried out in the UCT CME laboratory. For the hardness test, the specimens were indented in the S-L plane.

3.3.1 Hardness Test Specimen Preparation

Since the ASTM E92 standard specified that there is no standard size or shape for the test piece[2], a specimen was designed to better suit the functionality of the available laboratory equipment. However, a requirement in the ASTM standard was to have a flat specimen with a polished surface. Similar to the etched mounted samples, the specimens to be tested for hardness were 10 x 10 x 10 mm blocks that were also hot mounted at 180 °C using the Struers Labopress-3. The hot mounting process was carried out for 20 minutes at a force of 30 N, was placed under the warm condition of the mounting process for 12 minutes and cooled for 8 minutes as in the previous section. **Figure 43** shows the epoxy embedded specimen that was to be prepared for the evaluation of the hardness of the material.

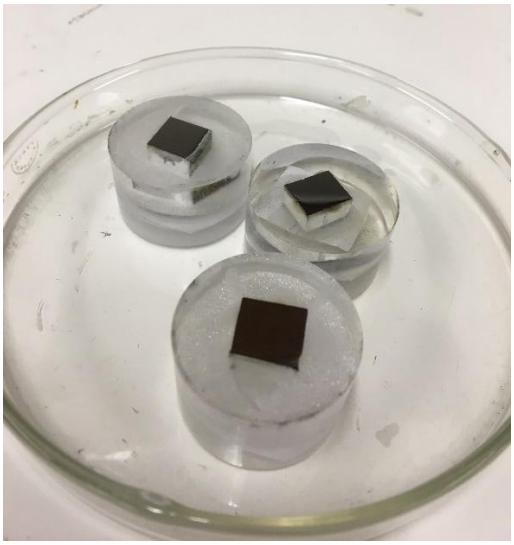

Figure 43: Figure of epoxy embedded samples with heat treatment labels

To eliminate potential surface effects such as thermal damage, decarburization and oxidation resulting from the prior abrasive cutting process, the 220-grit size sandpaper was used to grind down the embedded specimen surface at least 1 mm, before proceeding to grinding with finer grit sizes. The machined samples were ground using 220,

[2] The ASTM E92 standard however recommends the thickness of the material under test should be at least ten times the depth of the indentation. This was observed in the tests.

500 and finally 800 grit size sandpaper and then polished with a 3μm polishing cloth. In this condition the specimen was now prepared for the hardness test.

3.3.2 Vickers Hardness Test

The hardness test was done using a Zwick Roell ZHV Indentec Hardness Tester. The resultant HV values were ranged from 140 – 485 HV and from these results the final heat treatment processes were designed for experimentation. **Table 6** shows the different conditioning paths that each material regime had to undergo as these were the final designed processes to obtain the required high, medium and low toughness materials.

Final Heat Treatment Conditions	NOTATION
As Received	**AR**
850°C for 30 minutes, water quench, 2-hour temper at 600°C, then air cool	**HT1**
850°C for 30 minutes, then furnace cool	**HT2**

Table 6: Final heat treatment conditions and annotation for AR, HT1 and HT2 conditions

The different conditioning processes were used to manipulate the material characteristics in order to separate the material into three distinct categories ready for assessment. As seen in **Table 6** and **Figure 44**, HT1 was heated up to 850 °C for 30 minutes, and then was fast quenched with water for the formation of a hard martensitic structure.

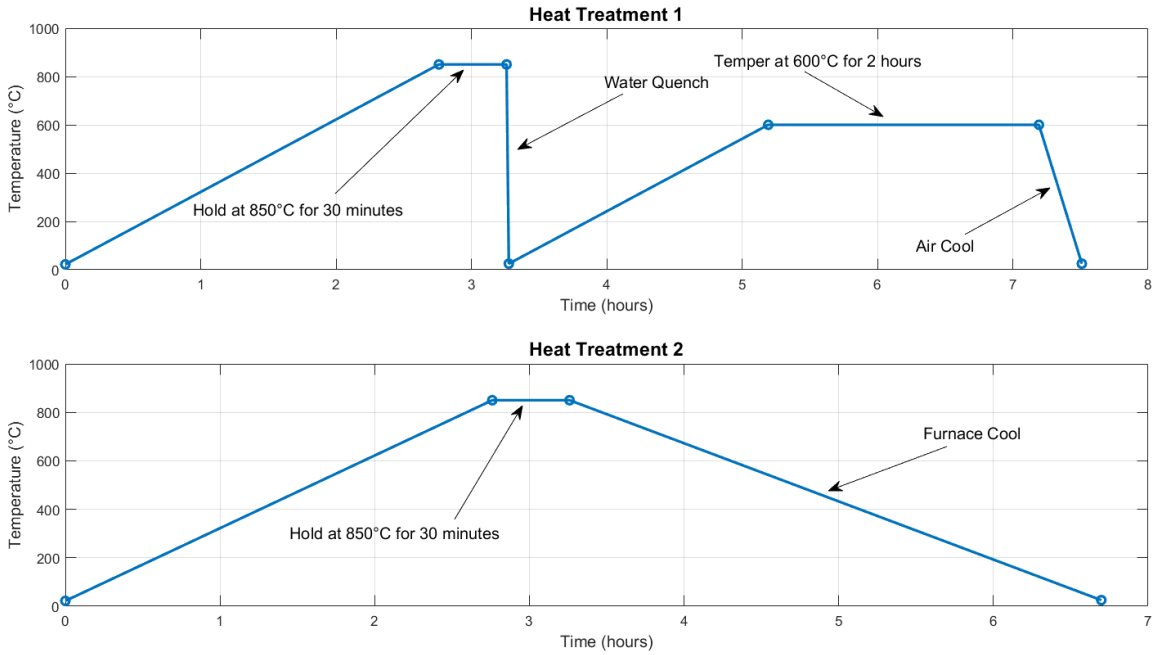

Figure 44: Graph of HT1 and HT2 heat treatment procedures

Considering the hardness expected due to this fast quenching, the material was then tempered at 600 °C for 120 minutes and was left to air cool down to room temperature. The tempering process was to affect the toughness by reducing the brittleness as well as the internal stresses. As seen in **Figure 44**, HT2 was also exposed to temperature elevated to 850 °C for 30 minutes but was then left to undergo slow furnace cooling. The slow cooling in the furnace resulted in the formation of a softer and more ductile microstructure, as the slow rate of cooling allowed the formation of bainite and pearlite. **Chapter 4** provides a detailed explanation of the rationale behind the selection of these heat treatment methods.

3.4 EXPERIMENTAL MATRIX

The experimental matrix served as a guideline for the full experimental process to be carried out. Considering the machinery at our disposal at the UCT Materials laboratory as well as machinery at nearby institutions (Stellenbosch University), the ideal temperatures proposed in literature to test the samples provided a benchmark even though not all these temperatures could be reached. The temperatures in the experimental matrix were the test temperatures adopted for this study.

3.4.1 Matrix for AR, HT1 and HT2

The temperature range for the uniaxial tensile tests, fracture toughness tests or the SPTs could have been broader, potentially resulting in more extensive and informative data, if the tests could have been carried out at both cryogenic and elevated temperatures. Due to this circumstance, temperature ranges were limited. **Table 7** shows the matrix that was adopted for each of the three distinct material regimes in this project.

Test Name		Test Temperature (°C)											
AR		-196	-140	-120	-100	-60	-40	-20	0	23	60	80	120
Tensile	Specimen Required/ Specimen Tested	x	x	x	x	x	x	x	x	3/3	x	x	x
Fracture Toughness		x	x	x	x	x	x	x	x	3/3	x	x	x
CVN		x	x	x	3/3	3/3	3/3	3/3	3/3	3/3	3/3	3/3	x
SPT		x	x	x	x	x	x	x	x	7/7	x	x	x

Table 7: Experimental Matrix for AR, HT1 and HT2 material regimes [3]

As seen in **Table 7**, the CVN test was the only mechanical test that could be tested with a temperature range. Various test temperatures were chosen in order to ensure a temperature range adequate to observe transition temperatures for the different regimes. The other mechanical tests and the SPT were carried out at room temperature

[3] For CVN tests:
- No tests for HT1 @ 23 °C and 60 °C
- Tests for HT1 @ -120 °C and -140 °C
- No tests for HT2 @ 0 °C

conditions. The results obtained through this experimental procedure could therefore be improved in future with the application of significant temperature ranges.

3.4.2 Test Name Notation and Convention

A naming notation was then chosen to identify the various experiments and the specimens tested. The notation needed to encompass the details required to specify each sample with regards to the heat treatment, temperature of test and the particular experiment number. As seen in **Table 8,** the test specimens could now be categorized and identified using the notation.

MATERIAL	HEAT TREATMENT CONDITION	TEST TEMPERATURE	TEST NUMBER
VRN500	AR0	RTP	T1
VRN500	HT1	RTP	T1
VRN500	HT2	RTP	T1

Table 8: Table showing name notation for AR0RTPT1, HT1RTPT1 and HT2RTPT1

For instance, the second tensile test for the AR material regime at room temperature will be recorded as *AR0RTPT2*. This naming notation was adopted for all the test samples that were used in the experiments in this dissertation.

3.5 UNIAXIAL TENSILE TEST

For the uniaxial tensile test, the ASTM E8 standard was adopted [66]. This test enabled the determination of the mechanical properties of metallic materials at room temperature. The particular properties of interest were the yield strength, the ultimate tensile strength (UTS), elongation and modulus of toughness. The test was carried out in the UCT CME laboratory on the three distinct material categories that were prepared.

3.5.1 Uniaxial Tensile Test Specimen Preparation

The specimens to be tested in this experiment were designed and machined in accordance with the ASTM standard. Following the heat treatment processes, the specimens were machined to the required dimensions. Owing to the limited material to be assessed, the specimen size choice had to be as minimal as possible. The specimen also had to be a size that was compatible with the grips available in the UCT laboratory facility. A specimen with a nominal diameter of 6 mm, a gauge length of 24mm, a minimum length of the reduced parallel section of 30 mm and an M10 thread was selected and drawn using SolidWorks 2022 software. **Figure 45** shows the drawing that was sent to the workshop for machining of the required specimen.

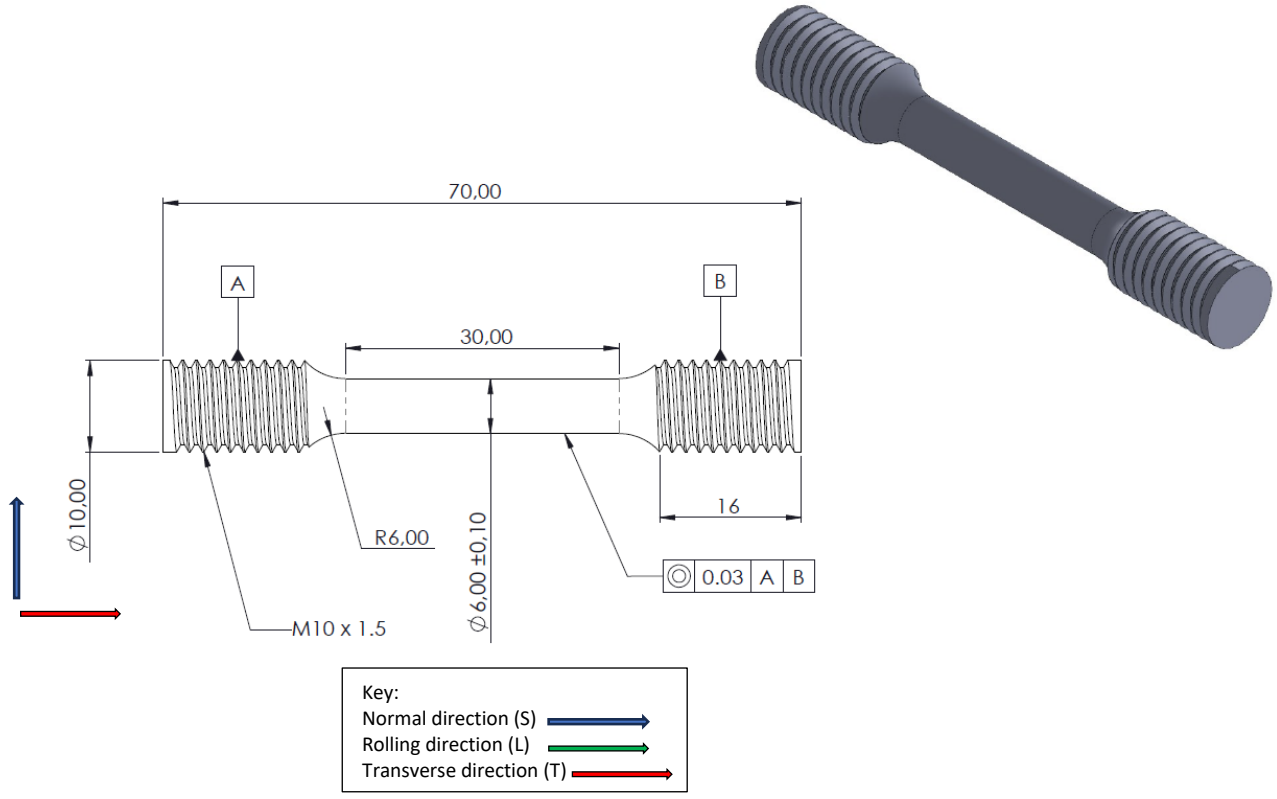

Figure 45: Drawing for ASTM E8 Tensile specimen showing S-T plane orientation for side profile

To ensure the axial loading of the tensile specimen was in the transverse direction, the specimen cross section was machined in the S-L plane. **Figure 45** shows the side profile of

the tensile specimen highlighting the transverse direction where tensile load will be applied. The specimen was threaded to assist the grips by providing a high friction contact region between the specimen and the specimen holders.

3.5.2 Uniaxial Tensile Test

3.5.2.1 Setup and Apparatus

To carry out the tensile testing of the prepared specimens, the Zwick Roell Tensile Testing machine was used. This machine was coupled with a video extensometer to provide an accurate strain measurement and a load cell of 200 kN, capable of handling a high strength steel like the material that was being tested. Before testing commenced, the specimen diameter dimensions were measured and confirmed using a micrometre and recorded. The diameter dimension data was required to provide the actual diameter of each specimen tested for more accurate stress strain calculations. **Figure 46** shows the tensile test machine grips with the specimen during the tensile test.

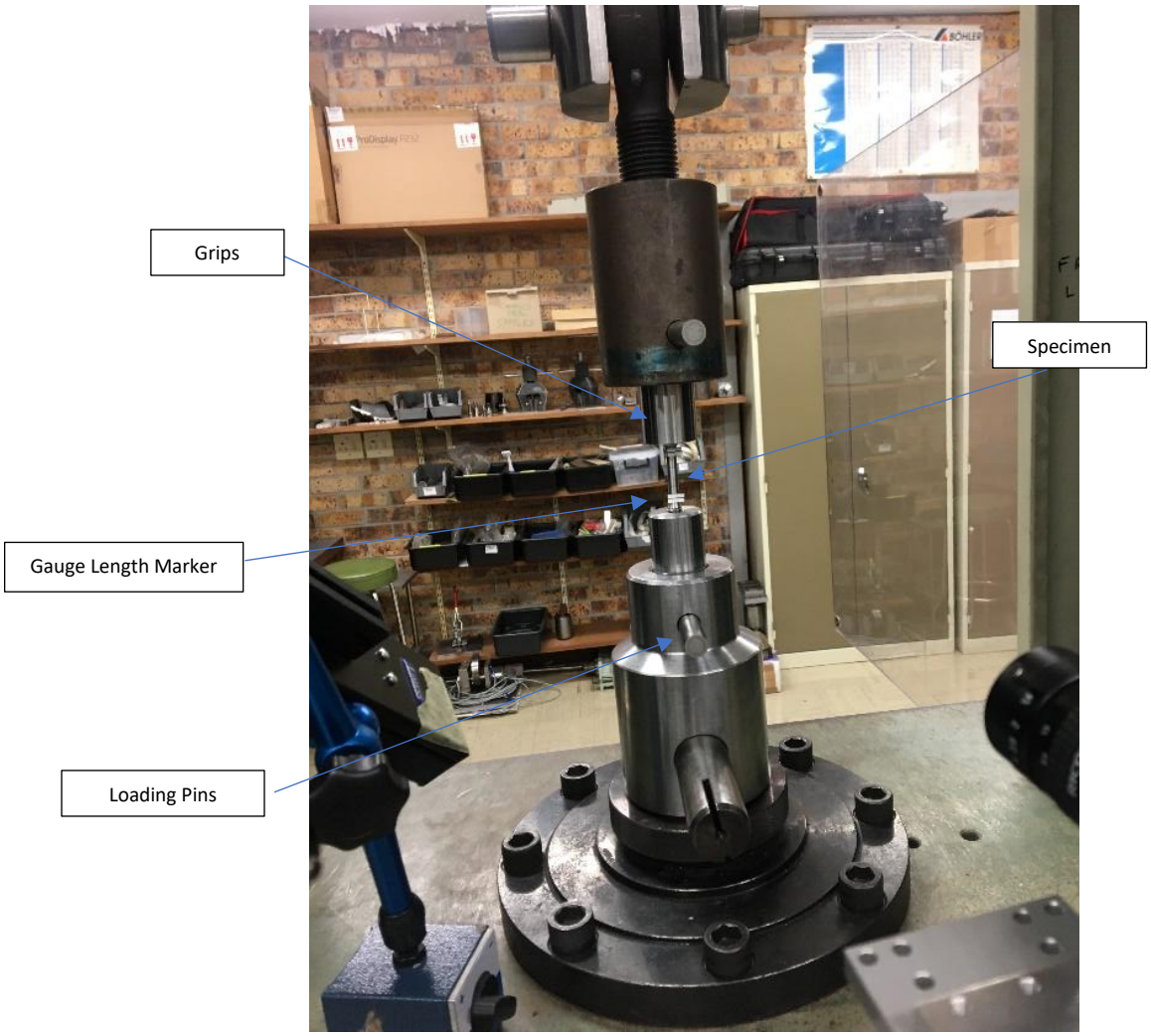

Figure 46: Image of secured tensile test specimen with marking stickers

The Zwick machine was equipped with gripping devices for threaded end specimens. Marking stickers were used to mark the specimens to assist the extensometer to identify the gauge length starting points in order to keep track of the elongation of the specimen during the test. The relevant grips and specimen holders were selected and integrated into the Zwick machine in preparation of the test as seen in **Figure 46**. The computer system controlling the machine required the input of several parameters, including measured specimen diameter, the gauge length as measured by the extensometer as well as the rate of testing (2mm/min) to be applied to the specimen in the experiment.

3.5.2.2 Testing

The tensile tests were carried out at room temperature until specimen fracture. The stress strain data was recorded by the computer, from which the yield and ultimate tensile stress values were obtained. This data was then transferred to an MS Excel file for further analysis.

3.6 CHARPY V-NOTCH TEST

This test elaborates the behaviour of metal when subjected to a single application of a force resulting in multi-axial stresses associated with a notch, coupled with high rates of loading and in some cases with high or low temperatures in accordance with ASTM E23-18 [51]. The CVN test at different temperatures allowed the 50% Shear FATT and 50% Energy absorbed DBTT (% Shear vs Test Temperature – FATT; Absorbed Energy vs Test Temperature – DBTT) to be obtained. The test was carried out in the UCT CME laboratory on the prepared specimens.

3.6.1 CVN Specimen Preparation

Upon completion of heat treatment, the specimens were machined down to the actual dimensions in accordance with the ASTM standard. The CVN specimen chosen was the standard 10 x 10 x 55 mm with the specified notch. In order to ensure consistency in the machining of the notch, the pre-heat treatment CVN blocks were marked in a way to make note of the long transverse, short transverse and longitudinal directions. **Figure 47** shows the CVN specimen drawing that was sent for machining.

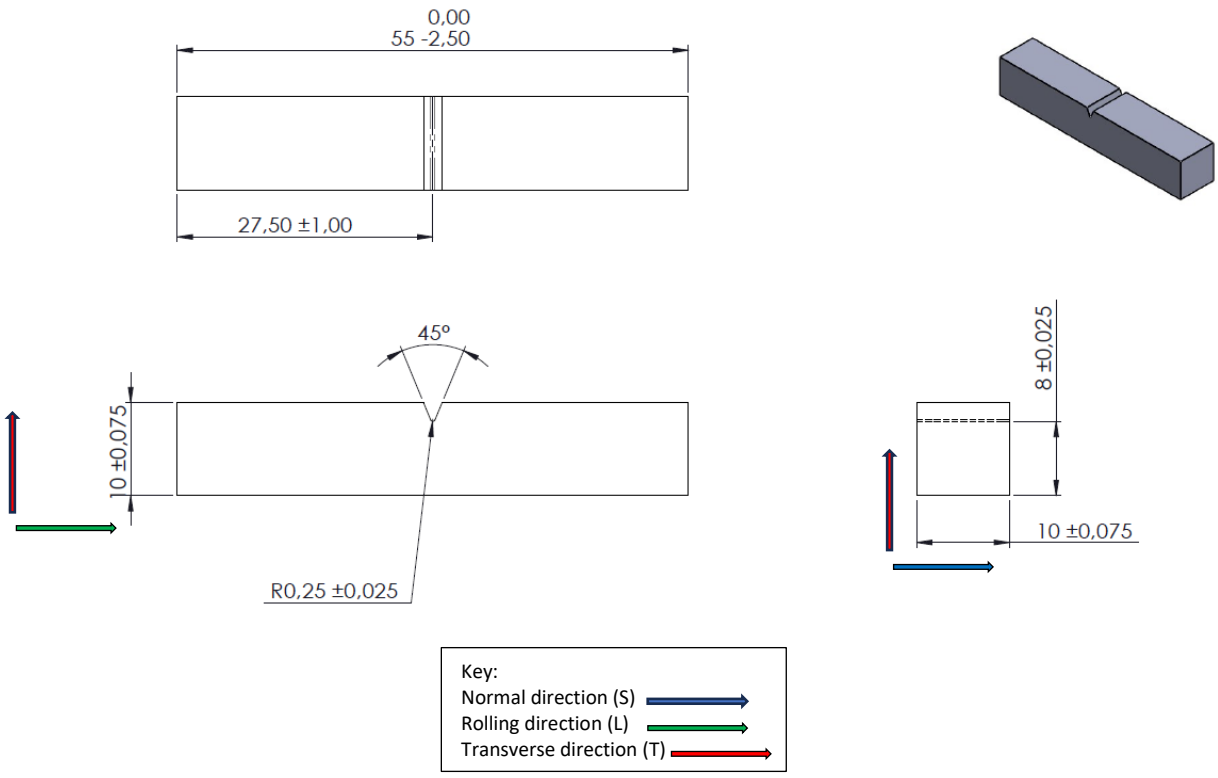

Figure 47: Drawing of ASTM E23 CVN specimen

The specimen was then ground using sandpaper to remove the oxidation and decarburization layer that resulted from the cooling process for the specimens after heat treatment [68]. To monitor the test temperature and provide an accurate measurement of the temperature of the specimen during the impact test, the specimen had to have a

K-type thermocouple welded near the notch. The K-type thermocouple is a temperature sensor containing Chromel and Alumel conductors (nickel-chromium/ nickel-alumel) and was chosen for use mainly because of its affordability, its temperature range of -270 ^{o}C to 1260 ^{o}C and its accuracy of ±2.2 ^{o}C [69]. Before the thermocouple was welded the specimen had to be ground using 200, 500 and finally 800 grit size sandpaper to ensure a smooth contact surface for the weld to be in good condition.

3.6.2 CVN Test

3.6.2.1 Setup and Apparatus

The weld machine was used to attach the thermocouples to the specimens and the Instron Dynatup 9210 Impact Tester was used to carry out the CVN impact test. After the specimens were ground for a smoother surface finish, the thermocouples were welded near the notch strategically. A strong weld was required to ensure that the thermocouple would remain in contact in the high and low temperatures the specimens were going to be subjected to. **Figure 48** shows the impact tester that was used to carry out the CVN tests.

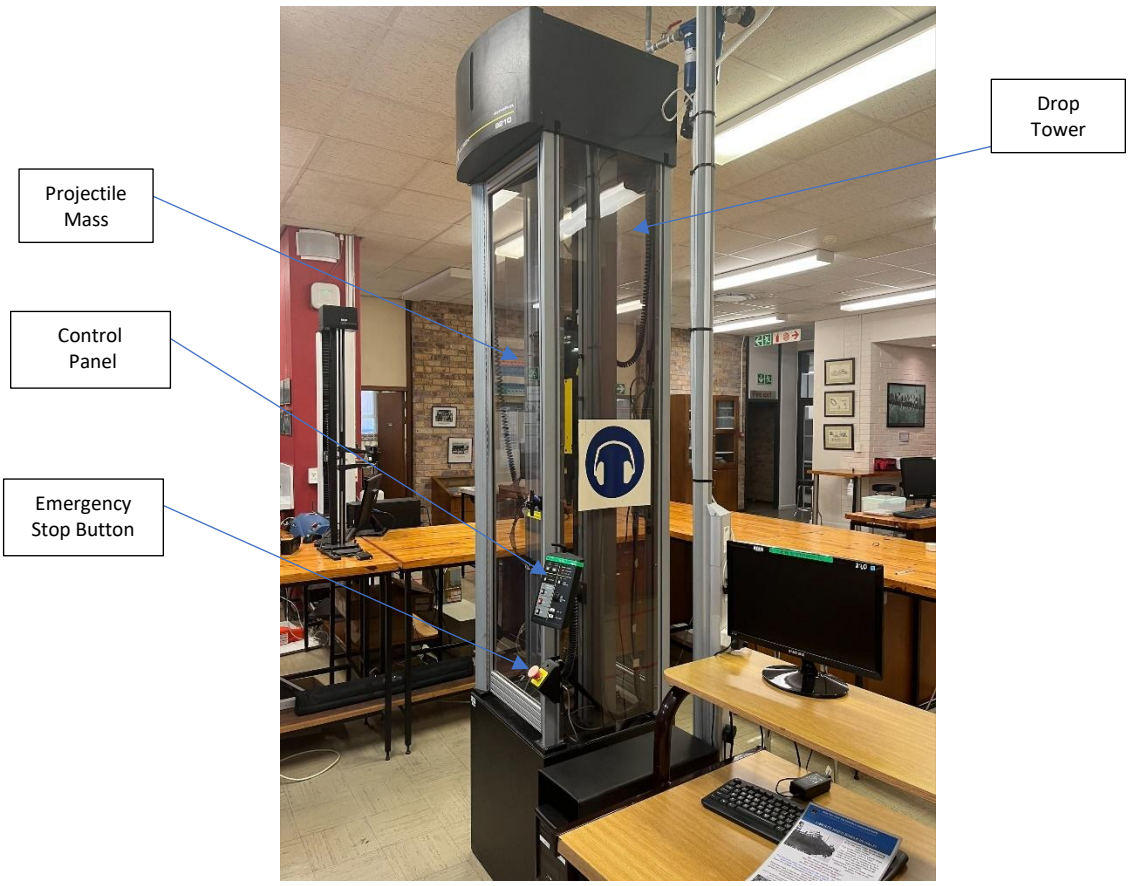

Figure 48: Image of Instron Dynatup 9210 Impact Tester

As established in literature, the CVN specimens could be immersed in a temperature medium in order to raise or drop the specimen temperature as required for the test. For high temperature tests, the specimens were immersed in boiling distilled water, utilising a beaker on a Bunsen flame. The thermocouple reader was constantly observed to monitor the temperature of the specimen.

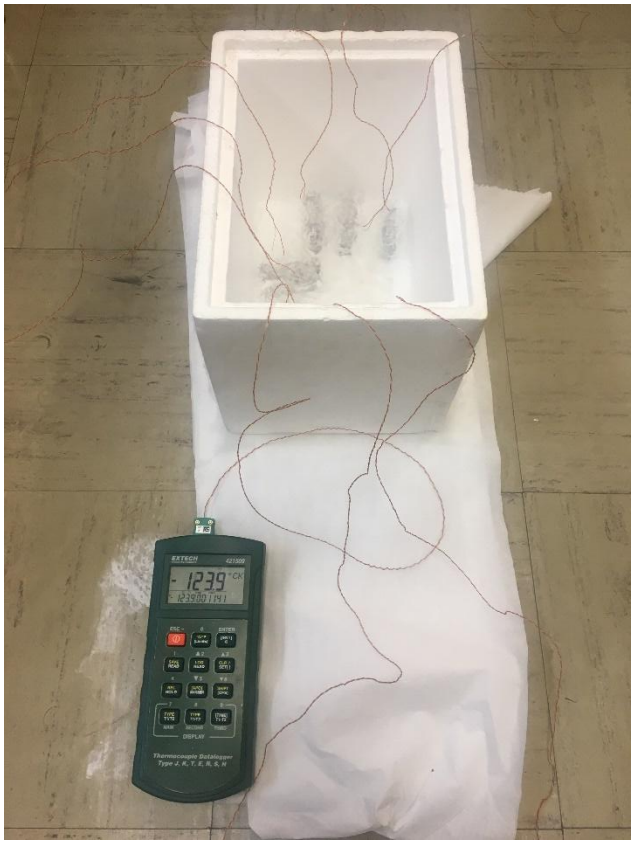

Figure 49: Image of CVN specimens with K-Type thermocouples immersed in liquid Nitrogen and attached to an Extech Instruments Thermocouple Thermometer probe

For cryogenic temperature tests, the specimens were immersed in liquid Nitrogen (LIN) in a Styrofoam container as shown in **Figure 49**. For extremely low temperatures, pure LIN was used as the medium but for low temperatures higher than -50 °C, the LIN was mixed with an alcohol to increase the temperatures by manipulating the boiling point. Likewise, the temperature values were under constant surveillance on the thermocouple reader.

3.6.2.2 Testing

For the three distinct material regimes, the following steps were carried out for the impact tests:

- Switch computer and Instron impact tester machine on, run the software
- Calibrate the CVN machine using the height settings:
    - Zero the indicator arrow for dynamometer and projectile at 0.83 m

- Jog up dynamometer to 1.35 m and set as target height
- Immerse CVN sample in the relevant temperature medium for 20 minutes, ensure uniform temperature for test specimen
- Constant eye on thermocouple reader for temperature of sample
- Enter required values (rate of test, specimen dimensions) in computer software interface
- When desired temperature is about to be reached, quickly transfer the sample to the impact tester (manoeuvre through heat loss or heat gain)
- Follow safety protocols and start the test
- Drop the impact projectile
- Observe the test process until specimen fracture
- Machine will record the impact energy absorbed upon impact
- Stop test
- Export the data into MS Excel files

3.6.2.3 Determination of FATT and DBTT

As established in literature, according to the standard, the evaluation of the shear FATT could be carried out after the impact on the specimen had damaged the specimen. The standard provided a guideline to estimate the shear fracture appearance. The chart shown in **Figure 50** showed the fracture appearance that was visually compared with the fractured specimen.

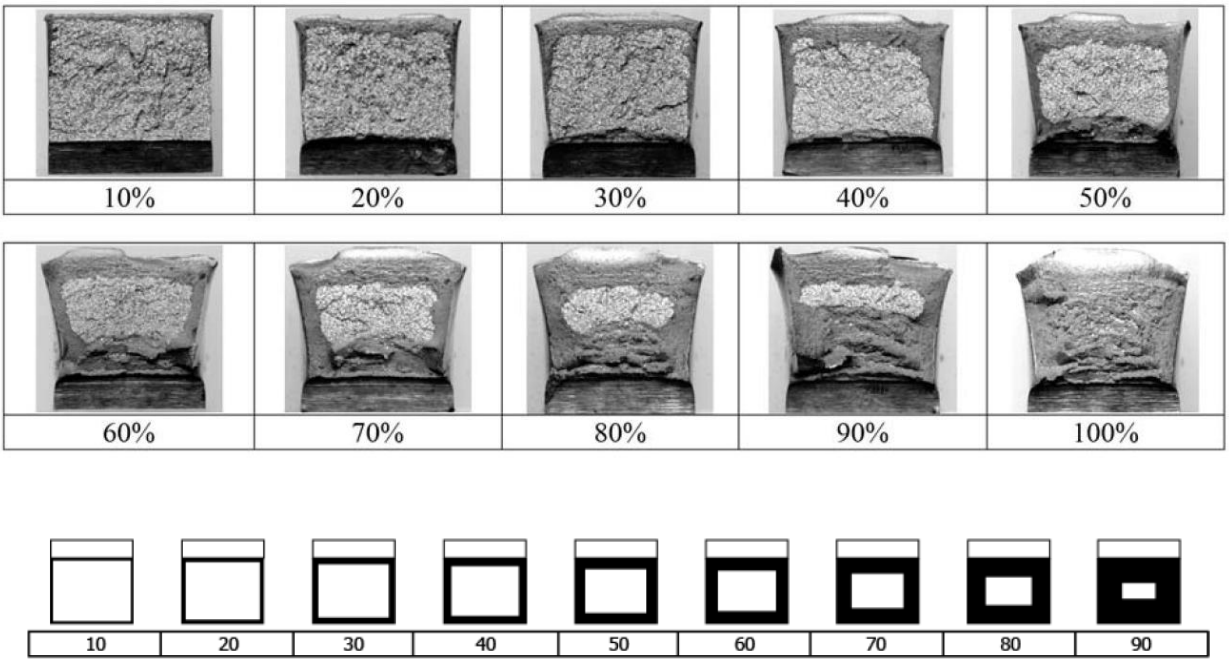

Figure 50: Images from ASTM Fracture Appearance chart and Shear Fracture Appearance Estimation guide [51]

The shear lips formed on the sides of the specimen were used to indicate the extent of the ductility of the material after the impact damage. This allowed the shear fracture appearance to be estimated and recorded. After the impact tests were completed, the specimens were assessed for the shear fracture appearance for each test.

From the data obtained after the CVN test, the 50% energy DBTT was determined by calculating the average of the upper and the lower shelf energy values from the energy absorbed vs test temperature plot across all test material regimes.

3.7 FRACTURE TOUGHNESS TEST

The ASTM E399 was adopted for the fracture toughness test [49]. This test method covers procedures and guidelines for the determination of plane strain fracture toughness of metallic materials using the parameter K_{Isi}, a size insensitive fracture toughness. The test was carried out in the UCT CME laboratory.

3.7.1 Fracture Toughness Specimen Preparation

After the heat treatment process, the specimens were machined to the dimensions congruent with the CT specimen in the ASTM E1820 standard [50]. The chosen specimen configuration was the CT specimen with a length of 37.5 mm, a width of 36 mm and a thickness of 15 mm with consideration of the limited material. The chosen configuration also had integral knife edges to simplify the engagement with the displacement gage. With the convention used in the ASTM standards, the specimen dimensions were W = 30 mm, B = 15 mm and the pin diameter of 8 mm. **Figure 51** shows the CT specimen that was designed for the fracture toughness test in the T-L orientation for loading in the transverse direction. The specimens were also scribed to ensure a specified heat-treated specimen (as-received, HT1 or HT2) was being tested.

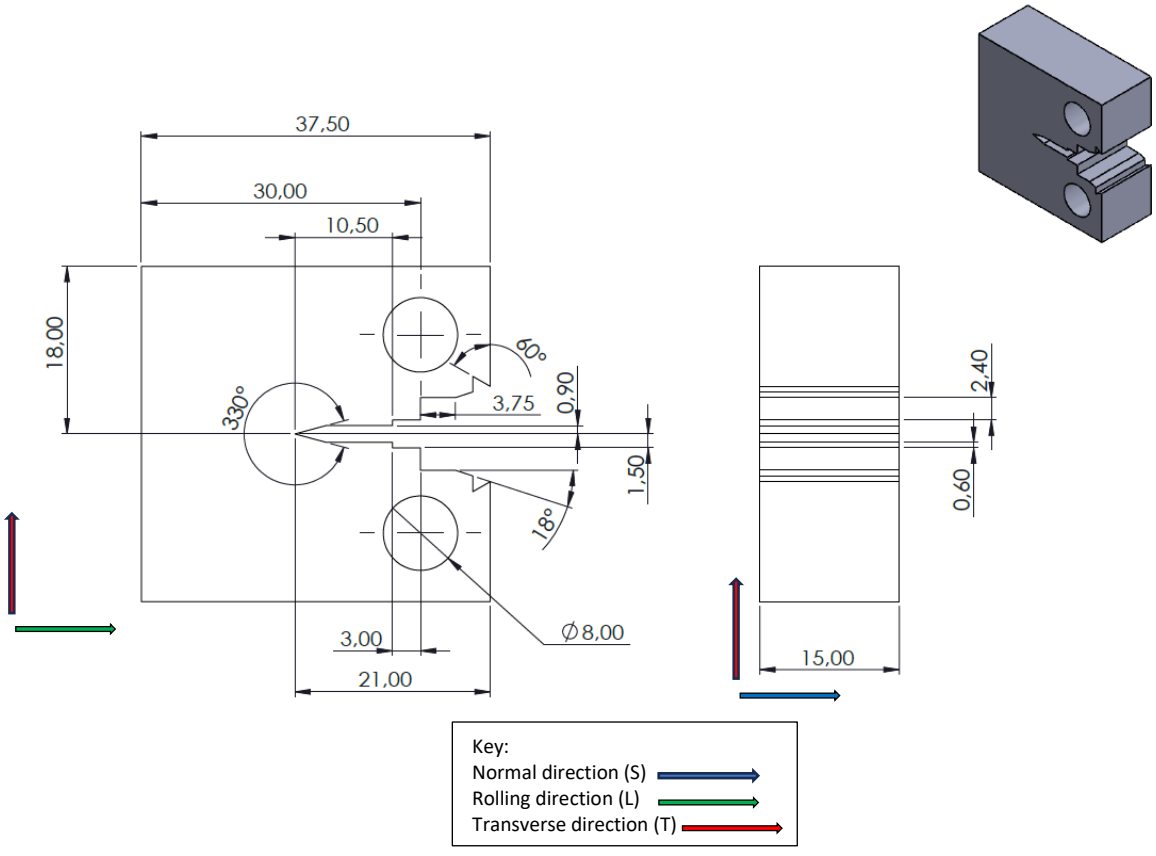

Figure 51: Drawing of ASTM E1820 fracture toughness specimen transferred to ASTM E399 test method

Following the final machining, the specimen was ground using the Struers Tegranin-25 automatic grinding machine. In their order, 200, 500, 800 and 1200 grit size sandpaper were used in the grinding, at 35 N force and speed of 300 rpm, using water as the lubricant. The specimen was then polished using 3µm polishing disc. This was to ensure that the surface could be assessed under a microscope during the fracture toughness pre-cracking procedure. 1 mm parallel markings were scribed on the specimen surface to allow the pre-crack to be monitored using the microscope. As the cyclic loading due to pre-cracking continued, the crack would propagate, and the 1 mm markings would assist in determining the pre-crack extension and subsequently the required original crack size.

3.7.2 Fracture Toughness Test

3.7.2.1 Setup and Apparatus

The ESH Fracture Toughness servo-hydraulic machine with a 45 kN load cell was used to carry out both the pre-cracking and the fracture toughness tests. The control software's used by the machine were the Instron WaveMatrix 1 software for the pre-cracking and the Instron Bluehill 2 fracture mechanics software for the fracture toughness test. The fracture toughness machine and set up used to carry out the test is shown in **Figure 52**.

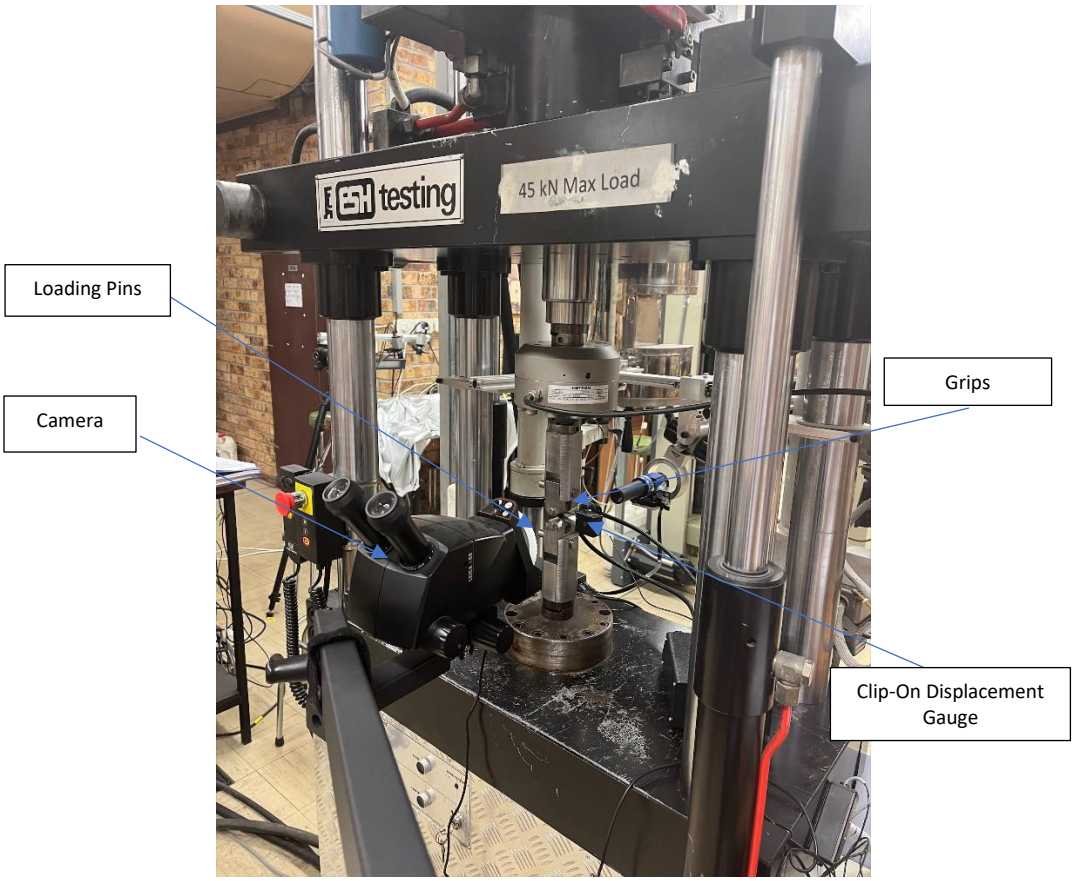

Figure 52: Instron Fracture Toughness Test Machine with specimen, clip-on displacement gauge and camera

After the samples were pre-cracked, the crack was then measured accurately using a Leica MZ8 metallurgical stereomicroscope. The microscope after being calibrated would give a value of the crack that would have developed from the notch during the pre-cracking process. The accurate crack length value was then recorded and used in the calculations for the fracture toughness values for this project. The fracture toughness test was then carried out on the specimen after the crack propagation values were recorded. After the test, the separated surfaces of the specimen were assessed, and using the Leica MZ8 metallurgical stereomicroscope, three measurements were made across the surface to determine the total crack size.

3.7.2.2 Testing

A summary of the steps taken for the fracture toughness test was divided into two sections, the pre-cracking and the actual fracture toughness test.

3.7.2.2.1 Pre-cracking

The pre-cracking process was crucial in the fracture toughness test as it ensured the crack initiation in a controlled manner using the Instron WaveMatrix 1 software. The hardest material according to the Vickers Hardness tests (as-received condition) determined the maximum force, minimum force, mean force and amplitude for the pre-cracking process. The frequency was determined from literature and past experiments on the machinery. Using **Equation 34** the maximum force, P_m [49], [50], that could be applied on the specimen for pre-cracking was calculated to be 23.2 kN.

$$P_m = \frac{0.4 \cdot B \cdot b_0^2 \cdot \sigma_Y}{2W + a_0}$$

Where P_m is the maximum allowable applied force
a_0 is initial specimen crack size
b_0 is uncracked ligament (W-a_0)
B is specimen thickness
W is specimen width
σ_Y is the yield stress
Equation 34

Even though the allowable load that could be applied to the material was as high as 20 kN, a lower maximum force was chosen in order to align with literature and previous fracture toughness tests on metals. The maximum load, F_{max} was chosen to be 12 kN, F_{min} was 1.2 kN, F_{mean} was 6.6 kN, a frequency for conventional tension-compression fatigue tests of 7 Hz and the amplitude used was 5.4 kN for the pre-cracking process. The fatigue stress ratio was 0.1. After the crack propagated to the desired length using the scribe markings (1 mm $\leq$ Crack Length $\leq$ 3 mm), the number of cycles was observed and recorded.

3.7.2.2.2 Fracture Toughness test

For the fracture toughness test procedure, the Instron Bluehill 2 software was used. After setting up the specimen for the test, the crucial calibration of the system displacement

gauge was done. A displacement rate of 0.2 mm/min was applied for the room temperature fracture toughness test and the test was carried out until the load dropped significantly with specimen fracture. The load vs crack tip opening displacement (CTOD) data was recorded for each test and exported to MS Excel.

3.7.2.3 Metallographic Analysis

Following the completion of the fracture toughness test, the broken specimen (ripped apart), could be assessed even further. Using the microscope, the surfaces of the separated specimen provided more information with regards to the failure of the material. Unlike the singular scribed surface of the specimen side profile, the separated specimen surfaces could be used to measure the crack length on both sides of the specimen. This provided a more accurate value for the crack length thus the values obtained from the post-test analysis of the specimens were used to determine the crack lengths.

3.8 SPT

This is a mechanical test carried out on a small disc shaped test piece by means of the application of a mechanical load applied to one surface of the test piece using a spherical shaped punch. This experiment allowed an investigation of the material's response to the load in accordance with the CWA 15627:2007 [24]. The SPT provides the LDC which would give the maximum load, the plastic to elastic load as well as energy absorbed by the specimen until fracture. The methodology to be adopted was done using the apparatus available in the UCT CME laboratory.

3.8.1 SPT Specimen Preparation

Following the heat treatment process, the specimen rods that were designated for the SPT were machined into small discs. Using the wire cutter, the SPT discs were sliced from the rods that were machined in the S-L plane orientation for loading in the transverse direction. The drawing that was sent for machining is shown in **Figure 53**.

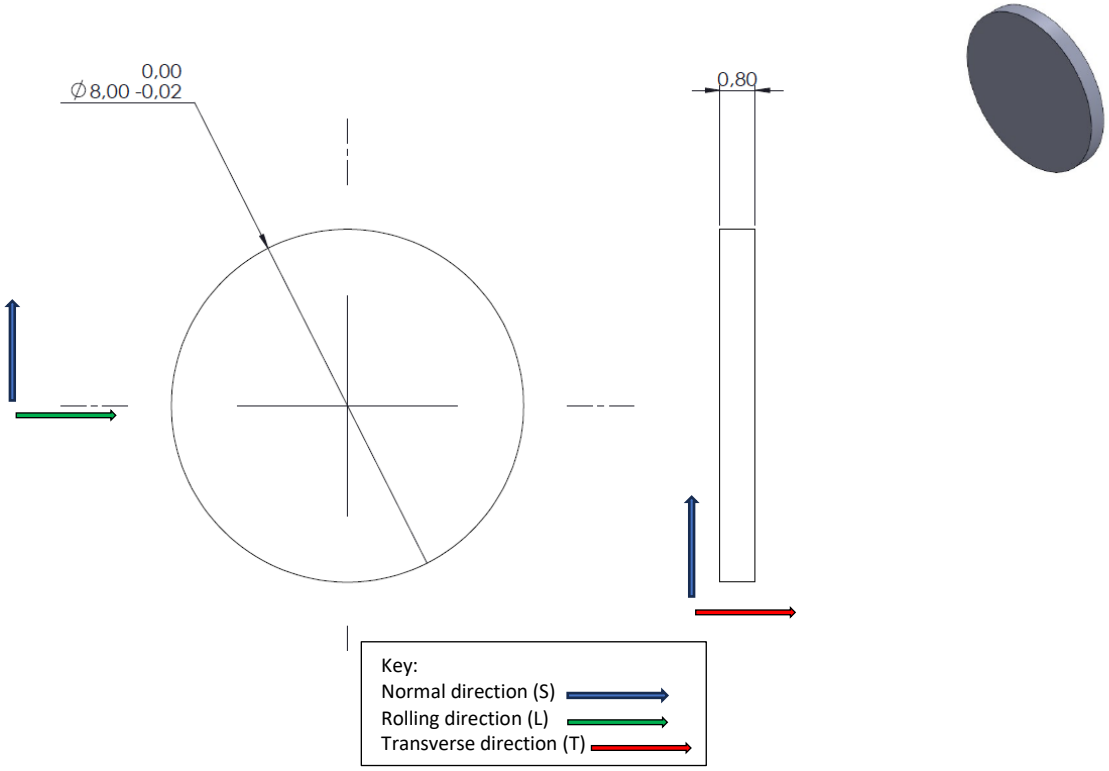

Figure 53: Drawing of CWA 15627:2007 SPT specimen in the S-L plane orientation

These discs were cut to 0.8 mm to 1 mm thicknesses and required to be ground down to the required 0.5 mm thickness. The specimens were held using the 8 mm grinding jig and were ground using 200, 500, 800 and 1200 grit size sandpaper down to the required thickness using water as the lubricant. The micrometer, accurate to 0.01 mm, was used to measure the specimen thickness at intervals, to ensure the specimens were the right

thickness [4]. Upon establishing the proper 0.5 mm thickness, the specimens were then rinsed in ethanol, air dried and stored in a re-sealable storage container marked in accordance with the heat treatment regimes (AR0RTP, HT1RTP and HT2RTP). To prepare for the DIC, the specimens were to be speckled with evenly distributed black on white dots using a spray can coating method. The specimens were placed on the adhesive side of the masking tape strategically, and were spray coated with white paint first and then finally speckled with black paint droplets. The specimens were allowed to dry in the open for 30 minutes to ensure the thin layer would not flake off during testing. The 8mm grinding jig, the unspeckled and speckled specimen can be seen in **Figure 54**.

Figure 54: Image of grinding jig, SPT specimen ground to thickness ≈ 0.5mm and speckled SPT specimen ready for testing

3.8.2 SPT Experiment

3.8.2.1 Setup and Apparatus

3.8.2.1.1 SPT Hardware

The SPT machine in the CME laboratory at UCT was used to carry out the SPT. The machine comprised components necessary for the testing and data capturing and was designed by Ibrahim Stracey [8], a UCT Masters student in 2019. In that project the student had to consider and ensure the compliance of the rig in accordance with the CWA 15627:2007 standard. **Figure 55** shows the SPT rig that was utilised in this study.

[4] Three specimens measured slightly outside the CWA stipulated requirement of ± 1% thickness tolerance for 0.5 mm discs (i.e., 0.495 mm and 0.505 mm) with observed values of 0.49 mm or 0.51 mm. While this is a minor deviation that could slightly affect LDC interpretation, it is however unlikely to have significantly influenced the overall conclusions of the study.

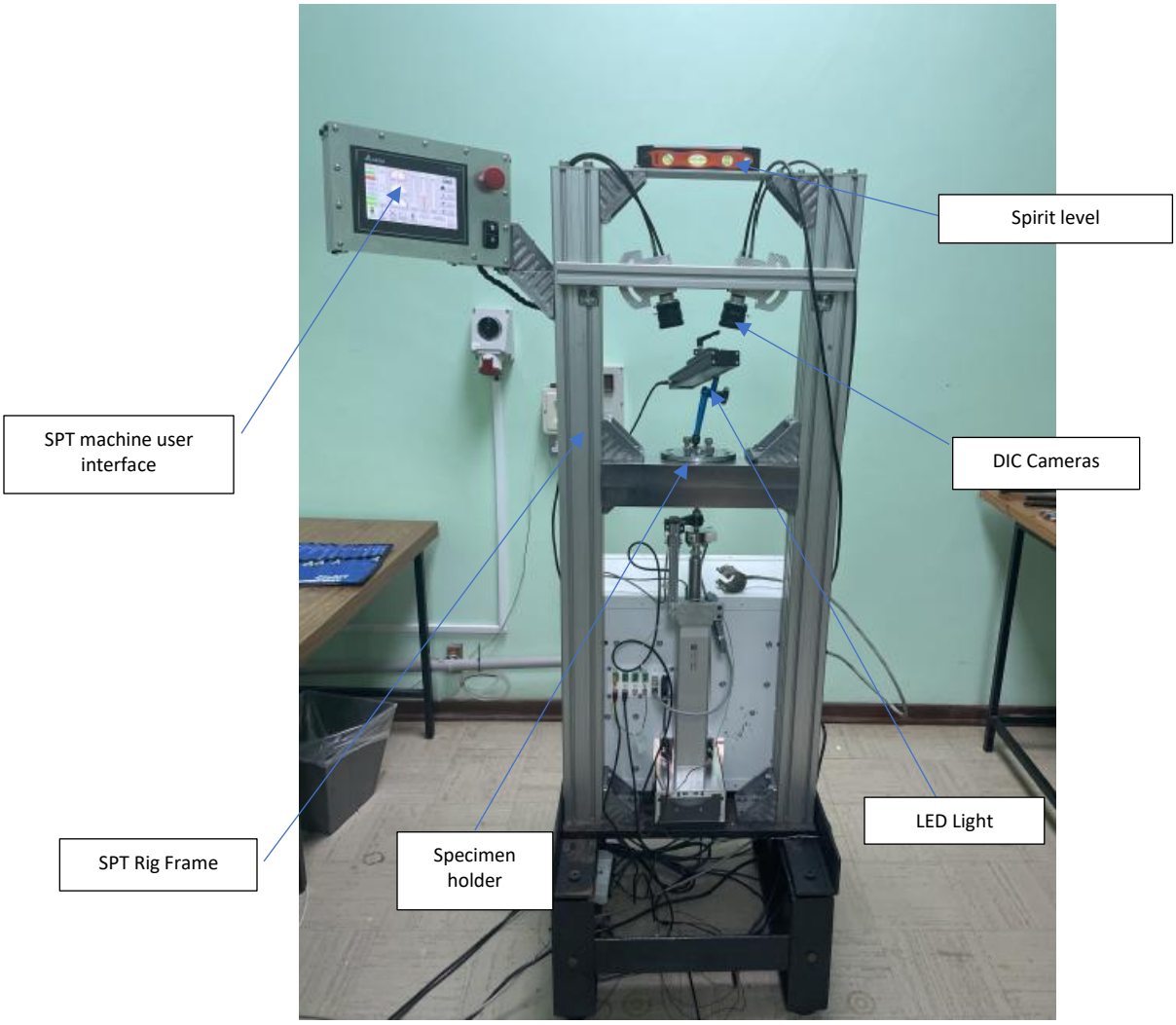

Figure 55: SPT rig in UCT CME laboratory [8]

The most vital hardware components included the punch, an M350 alloy steel cylindrical structure shown in **Figure 56**, with a carbide spherical ball of 2.5 mm diameter to protrude through sample material [8]. The specimen holder was made of highly thermally resistant M303 alloy steel. Controlling the punch was the HBM U2B load cell which had a load specification of 10 kN. The punch displacement was measured using the LVDT with an accuracy of 1 µm.

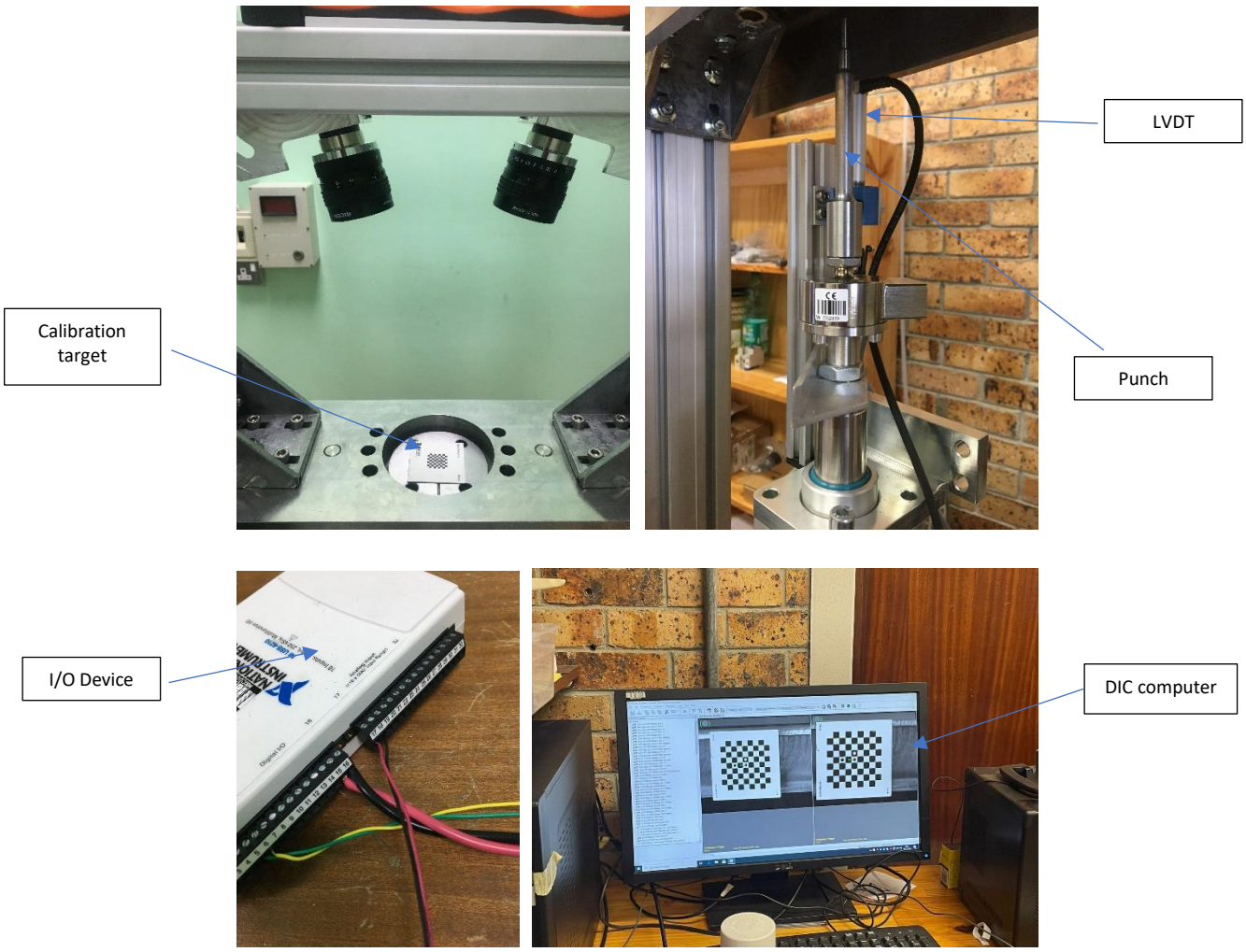

Figure 56: Images of SPT machine, National Instrument Multifunction I/O device and DIC computer

The DIC cameras were Baumer cameras with Ricoh lenses, and they were positioned at 19° as shown in **Figure 56**. **Table 9** shows the technical specifications of the SPT equipment. All SPT components could communicate with the DIC software on the computer through the National Instrument USB Multifunction I/O device. The displacement rate for the test was set to 0.03 mm/s (2 mm/min).

ITEM	TECHNICAL SPECIFICATION
CAMERA	Sony IMX250 Baumer USB 3.0 Camera VCXU-50M 2448 x 2048 pixel resolution 77 FPS 5 Megapixel
LENS	RICOH FL-BC1218A-VG VGA Lens 40.0 mm Lens length 12.5 mm Focal length
I/O Device	National Instrument USB-6210 16 inputs, 16 bit, 250 kS/s Multifunction I/O
LED	100 W Blue LED
LVDT	Heidenhain ST1278 1.0 µm accuracy 100 kHz max scanning frequency
LOAD CELL	HBM U2B Force Transducer type 2 mV/V sensitivity 0.1 kN accuracy 150% max operating force

Table 9: SPT Equipment Specifications [8]

3.8.2.1.2 DIC Calibration

In order to make use of DIC, the calibration was an integral step of the process. This was done for every new test session that was carried out to ensure accurate calibration and avoid inaccuracy that could be a result. A specified 9 x 9 calibration target was used to calibrate the DIC software. In the calibration process, the target was moved in different orientations, positions and angles while simultaneously being captured by the cameras allowing the detection of out of plane displacement. **Figure 57** shows the green circles on all the calibration target grid square intersections, which entailed successful calibration target recognition from the two cameras in use.

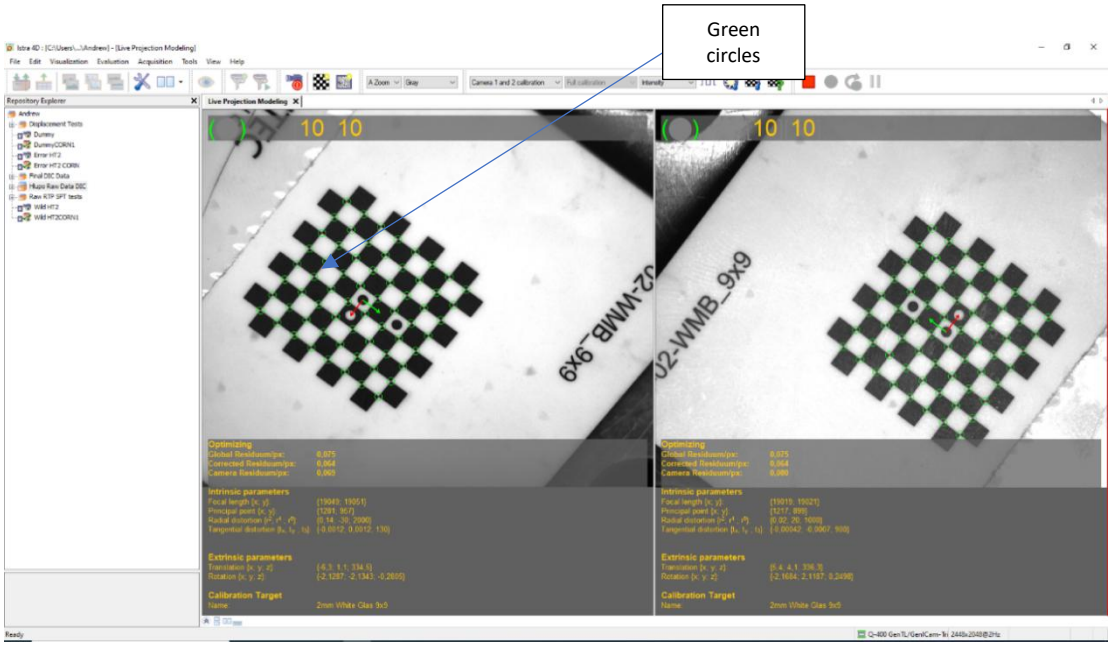

Figure 57: Calibration target successfully identified by DIC software during calibration of both cameras

3.8.2.1.3 SPT Rig Software

The SPT rig was designed with a test interface through which the experimenter could feed in the initial test conditions prior to the test. The rate of test, target load or target test speed could all be entered through the interface shown in **Figure 58** in preparation of the test. The DIC cameras would capture and keep track of the top surface of the sample during the test, recording and storing the data on the DIC computer in real time.

Figure 58: Image of SPT interface

Through the NI Multifunction I/O device, the data collected by the SPT rig could be synchronized and recorded through the DIC software as well. The DIC software could now have the readings from the LVDT displacement of the punch, the load cell of the SPT rig and the captured images from the cameras. Upon selection of the required data from the test, the DIC software would allow for data export to an MS Excel spreadsheet for the test.

3.8.2.2 SPT Technique

The SPT procedure had a sequence that needed to be observed like the other mechanical tests in this project. The rig operation procedure adopted from Stracey [8] was adopted to carry out the SPT. To familiarise with the test process before the use of the actual specimens was adopted, dummy brass specimens were used in the initial tests. The brass samples were secured in the rig, and the SPT was performed at a displacement rate of 2 mm/min until specimen fracture. These LDCs from the brass specimens provided a framework for the SPT, as they provided the needed experience from speckling the sample and adjusting the lighting for the DIC cameras to capturing the SPT data.

Prior to testing, the DIC software was used to verify that the fine speckle pattern applied to the specimen, secured in the sample holder, was detectable. The DIC parameters used during the evaluation of each test were a facet size and grid spacing of 35 pixels (≈ 0.72 mm) and 17 pixels (≈ 0.32 mm) respectively. The deflection reported for each corresponding load was the peak deflection on the specimen surface during the test [5]. The final SPTs were performed at a similar displacement rate of 2 mm/min. The load and displacement from the LVDT, the deflection through DIC and the maximum surface principal engineering strain from the DIC data was recorded.

[5] This approach was selected for simplicity and comparability, based on the assumption that peak deflection occurs at the point of contact with the punch. Alternative methods like utilising an average deflection value over the defined region of interest (specimen surface) could provide more insight on the deformation.

3.9 CORRELATION

For the process of correlating the data obtained from the SPT and the mechanical tests, the following **Table 10** containing the various correlations from literature was populated [7], [24], [46], [48], [52].

CORRELATION	FORMULATION
SPT – Tensile Yield	$\sigma_{YS} = \beta_{YS} \cdot \left(\frac{F_e}{h_0^2}\right)$ $\sigma_y = a\left(\frac{F_{ept}}{h_0^2}\right) + b$ $\sigma_y = a\left(\frac{F_{e1.5}}{h_0^2}\right) + b$ $\sigma_y = \begin{cases} [1.28K - 0.062]\frac{F_{50}}{h^2} & \text{for K} < 0.330 \\ 0.360\frac{F_{50}}{h^2} & \text{otherwise} \end{cases}$
SPT – Tensile UTS	$\sigma_{UTS} = \beta_{UTS} \cdot \left(\frac{F_m}{h_0 \cdot u_m}\right)$ $\sigma_{UTS} = a\left(\frac{F_{infl}}{h_0 \cdot u_{infl}}\right) + b$ $\sigma_{UTS} = a\left(\frac{F_{flow}}{h_0 \cdot u_{flow}}\right) + b$ $\sigma_{UTS} = \beta_{UTS} \cdot \left(\frac{F_{crack}}{h_0 \cdot u_{crack}}\right)$
SPT - CVN	$T_{SP} = \alpha T_{CVN}$
SPT - K_{IC}	$K_{Ic} = {}^{6600}/_{60} - (T - FATT)$

Table 10: Correlation formulations obtained from literature [7], [24], [46], [48], [52].

As established in the literature, the identification of a crack initiation point on the LDC was vital in providing an alternate analysis of the SPT outcome. Upon establishing the DIC step at which the rate of change of the SED evolution indicates the initial rapid increase of strain energy density for an SPT, the corresponding displacement/deflection point, u_{crack}/v_{crack}, can be subsequently identified on the SPT LDC. With the identification of u_{crack}/v_{crack} on the LDC, the load F_{crack} can also be determined. As with the correlation formulation in the CEN documents [24], [38], the correlation for the crack initiation point load and the UTS is linear as shown in **Table 11**.

CORRELATION	FORMULATION
SPT – Tensile UTS	$\sigma_{UTS} = \beta_{UTS} \cdot \left(\frac{F_{crack}}{h_0 \cdot u_{crack}}\right)$
SPT – Tensile U_T	$U_T = A(E_{crack})^B$

Table 11: Correlation formulations proposed in this dissertation

Since the proposed relationship between tensile toughness, U_T and E_{SP} is energy-based, the correlation between the two properties is most likely non-linear hence the hypothesized power-law formulation in **Table 11**. However, to determine that indeed the relationship between U_T and E_{SP} is governed by a power law correlation, the U_T and E_{SP} parameters obtained from the SPTs and the tensile tests in this study will be plotted on a logarithmic scale and a regression model will be developed using the experimental data. If a linear relationship is established in these ln-ln plots, the power law relationship proposed is confirmed [57], [70].

3.9.1 Test Required Data for Correlation

Considering the above correlation formulations **Table 12** contains the data that would need to be obtained from the SPT LDCs in order to carry out the correlations.

ANALYTIC METHOD	YIELD STRESS σ_y (MPa)	UTS σ_{UTS} (MPa)	Energy Absorbed (J)
JANCA	$F_{e1.5}$, F_{ept}	F_{infl}, F_{flow}	-
HAHNER	F_{10}, F_{50}, F_{90}	-	-
CWA	F_e, F_i	F_m	E_{SP}
DIC Crack Detection	-	F_{crack}	E_{crack}

Table 12: Data points required from SPT LDCs for correlation

3.10 SUMMARY

This chapter has elaborated on the heat treatment processes, specimen types, dimensions and orientations of the VRN500 steel samples used in this study. It outlined the experimental parameters and the methodologies that were employed to investigate the material mechanical properties essential to achieve the objectives of the research.

The next chapter, **Chapter 4**, presents the results that were obtained from these experimental investigations and discusses the analysis of the observed data.

CHAPTER 4: RESULTS AND DISCUSSION

4.1 SAMPLE PREPARATION

To prepare the specimen for the experimental process, the first step was to establish the orientation of the specimen material. Once the orientation was identified, the specimen material was then machined into relevant blocks, which were taken through heat treatments. These heat-treated specimens were then tested for hardness to determine the high, medium and low toughness regimes that would be required for testing.

4.1.1 Orientation of Test Material

4.1.1.1 Analysis Procedure/Method

As mentioned in **Chapter 3**, the specimens wire cut from the original block of material were ground and polished. These samples were taken through the etching process and then analysed using microscopy. The images were captured, and the orientation identified was labelled for post-test analysis. The following sections show the results that were obtained during the process.

4.1.1.2 Results Obtained

As seen in the **Figure 59** material, the elongation of the grain boundaries in parallel layers shows the rolling direction of the material in the normal-longitudinal (S-L) plane. This was the face marked C on the sampling material extracts in **Figure 38**. The etching highlighted the grain boundaries of the microstructure, as indicated by the lighter streaks or bands aligning with the rolling direction established in the micrograph [65]. The longitudinal direction shows longer grain boundaries as can be seen in **Figure 59**, as a result of the rolling force impact of stretching the grain of the material. The banded microstructure which features the elongated grains has characteristics that contribute to the directional fracture behaviour of the material and these properties will persist even after the heat treatment process [65].

Figure 59: Microscopic image as viewed in the transverse direction of the material displaying the S-L plane (orientation C)

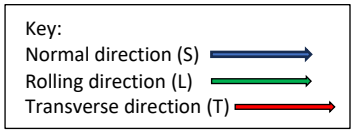

In **Figure 60** the elongation of the grain boundaries is visible, but the extent of elongation is not as pronounced as in the rolling direction. This led to the conclusion that this was the transverse direction of the material in the normal-transverse (S-T) plane as in this case the rolling force impact led to the rather shorter and spaced elongated grain structures. This was orientation B in **Figure 38**. The grains in this direction appear flattened leading to a compressed, pancake like structure as seen in **Figure 60**, where the lighter streaks are shorter in contrast to their elongated appearance in the rolling (longitudinal) direction [65].

Figure 60: Microscopic image as viewed in the rolling (longitudinal) direction displaying the S-T plane (orientation B)

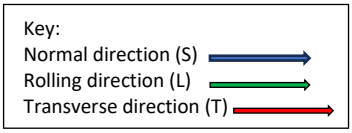

The remaining microstructure represented orientation A in **Figure 38**, the normal direction in the transverse-longitudinal (T-L) plane. However, from the image obtained, the normal direction can be identified as there is no clear elongated grain boundaries in the microstructure. This normal direction is perpendicular to the rolling plane and a mix of elongated grains and equiaxed grains can be observed through the lighter streaks as seen in the micrograph in **Figure 61**.

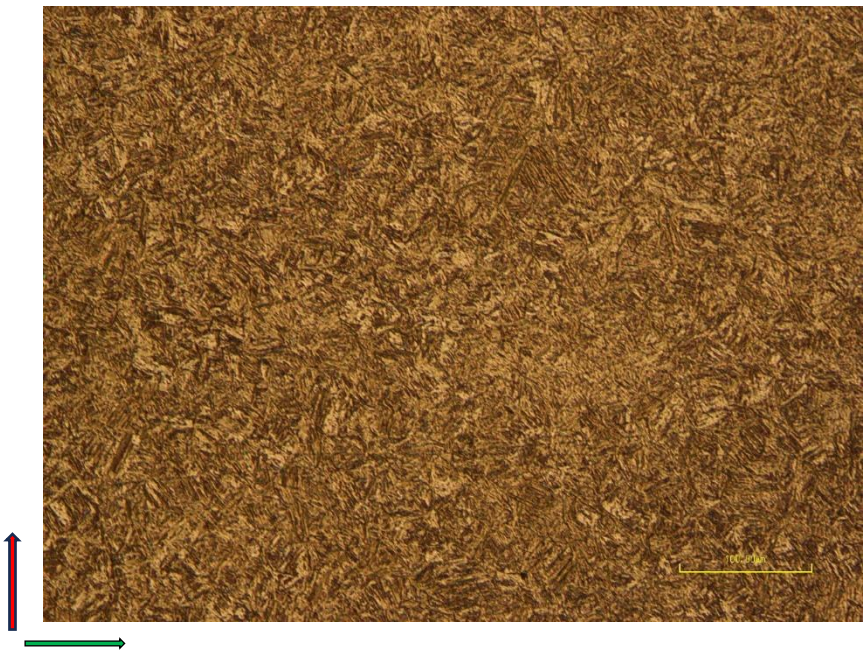

Figure 61: Microscopic image as viewed in the normal direction displaying the T-L plane (orientation A)

Key:
Normal direction (S)
Rolling direction (L)
Transverse direction (T)

When the orientation of the plate was established, the specimen orientation for the test samples was carefully specified to maintain consistency and test specimen integrity throughout the experimental process. The specimens were machined to ensure that the loading direction remained consistent across all the tests, specifically in the transverse direction as highlighted in **Table 4**. This approach was necessary because different grain morphologies of the material are responsible for different directional phenomena and anisotropic mechanical behaviours like splitting, delamination and fracture [65]. As discussed in **Chapter 3**, maintaining a uniform loading direction was vital to ensure reliable assessment during the mechanical tests.

4.1.2 Vickers Hardness Tests

Following the heat treatments carried out on the material, hardness tests were required to establish the hardness properties of each heat treatment regime. The test results helped in formulating the heat treatment procedures that would best demarcate the material into high, low and medium fracture toughness characteristics.

4.1.2.1 Results Obtained

The results obtained determined the heat treatment procedures that were going to be adopted in this project. There was need for three distinct regimes, and from the seven heat treatments, the hardness results would assist in the experimental design. **Table 13** shows the results obtained by the Vickers Hardness tests, averaged at five different indentations on the specimen surface.

Heat Treatment Conditions	Heat Treatment Test	VICKERS HARDNESS (HV)
As Received	AR	532
850°C for 30 minutes, then air cool	Method 1	253
850°C for 30 minutes, then furnace cool	Method 2	147
850°C for 30 minutes, then oil quench	Method 3	432
850°C for 30 minutes, then water quenched	Method 4	473
850°C for 30 minutes, water quench, 2-hour temper at 600°C, then air cool	Method 5	280
850°C for 30 minutes, water quench, then 4-hour temper at 600°C, then air cool	Method 6	274

Table 13: Vickers Hardness test results for various heat treatments adopted

Figure 62 shows the average hardness values corresponding to each heat treatment adopted.

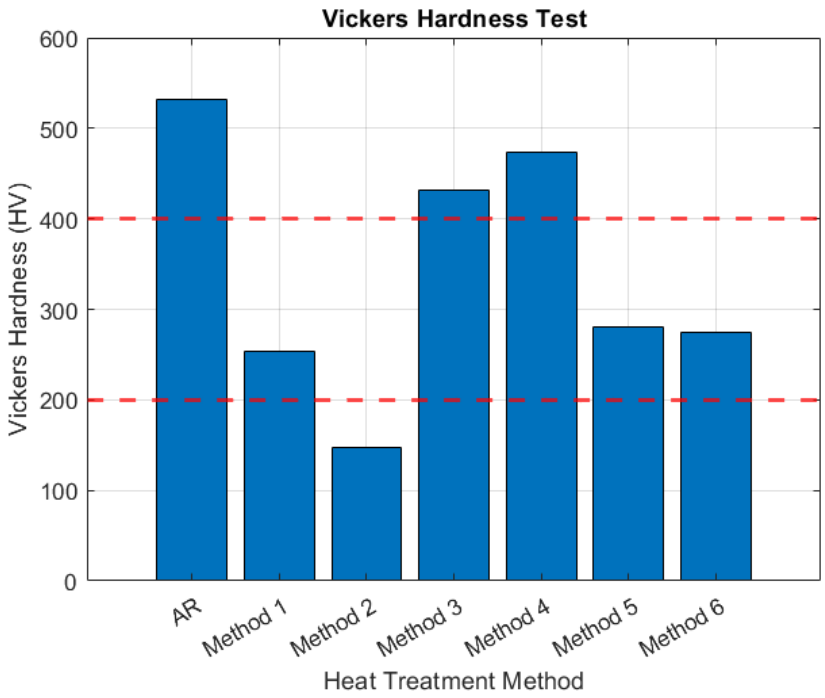

Figure 62:Graph of Vickers Hardness values for various heat treatment methods

As can be seen in **Figure 62**, the as received condition of the VRN500 material had the highest hardness of 532 HV in the top region with hardness values above 400 HV. Method 5, the treatment that required 850 °C for 30 minutes, water quench, 2-hour temper at 600 °C and a subsequent air cool had a hardness of 280 HV, the highest in the middle region of the graph (between 200 and 400 HV). Lastly, method 2, the treatment that was 850 °C for 30 minutes, then furnace cool, had the lowest hardness of 147 HV for all tests carried out. The three chosen heat treatment methods to be adopted for this project can be seen in **Figure 63**.

Figure 63:Graph of Vickers Hardness results for distinct heat treatment methods to be adopted

The notations for the selected heat treatment methods were determined as AR for as received, HT1 for method 5 heat treatment and HT2 for method 2. **Table 14** shows the distinct heat treatment conditions that were selected for the experiments in this project.

Chosen Heat Treatment Conditions	VICKERS HARDNESS (HV)	NOTATION
As Received	532	**AR**
850°C for 30 minutes, water quench, 2-hour temper at 600°C, then air cool	280	**HT1**
850°C for 30 minutes, then furnace cool	147	**HT2**

Table 14: Table showing distinct heat treatment methods to be adopted

Table 14 confirms that the AR condition material has high hardness. As indicated in the VRN specification datasheet [61], and the microstructures observed in **Figure 59** to **Figure 61**, the material was rolled and tempered below 600 ^{o}C. The prior austenite boundaries were represented as long thin grains during rolling and led to the formation of a fine martensitic microstructure during the cooling process after the rolling. This combination of the fine martensitic structure and low temperature tempering contributed to the high hardness, strength and toughness properties of the material.

During the hot rolling process in the manufacturing of the VRN steel, austenite grains were present in the microstructure. The HT1 process re-austenised the material at 850

^{o}C, resulting in the austenite grain size being potentially greater than the original austenite grains in the material microstructure. The rapid quenching that was adopted in the process resulted in the formation of a martensitic structure coarser than the structure in the AR condition. However, the tempering process that was administered reduced the brittleness and the hardness of the material as the process was at 600 °C and for a significant timeframe of 2 hours [4], [71].

The HT2 process resulted in the softening of the material, as the hardness was lowered during the furnace cooling. The slow cooling rate resulted in a controlled transformation of the microstructure as carbon could diffuse more easily in these conditions, leading to a more uniform microstructural distribution of alternating layers of ferrite (soft phase) and cementite (hard phase) in pearlite and bainite [4]. Formation of a bainitic-pearlitic structure resulted in the lower hardness and improved ductility [62].

4.2 TENSILE TESTS

As mentioned prior in this dissertation, the three chosen regimes were the heat treatment conditions and processes adopted. In preparation and according to the standard ASTM E8, the specimens were machined into blocks with marked orientations before heat treatment. Upon heat treatment completion the specimens were finally machined into the desired test sample dimensions required for testing. For the tensile test the specimen cross section orientation was in the S-L plane.

4.2.1 Analysis Procedure/Method

The tensile test was conducted to evaluate the material's response to uniaxial tensile loading applied during testing. The specimen dimensions, including gauge length and cross-sectional diameter, were measured and recorded for subsequent stress-strain calculations. The test was performed using the Zwick tensile test machine operated by the testXpert I software and the test was run until specimen fracture. The following section presents the results that were obtained during the tests.

4.2.2 Results Obtained

4.2.2.1 As Received Results

Figure 64 shows the stress strain behaviour of the As-Received material regime, showing the mechanical properties associated with the off-shelf material. The results obtained could be compared to the manufacturer's material data sheet, giving a valuable indication of the accuracy of the tensile tests carried out in the lab.

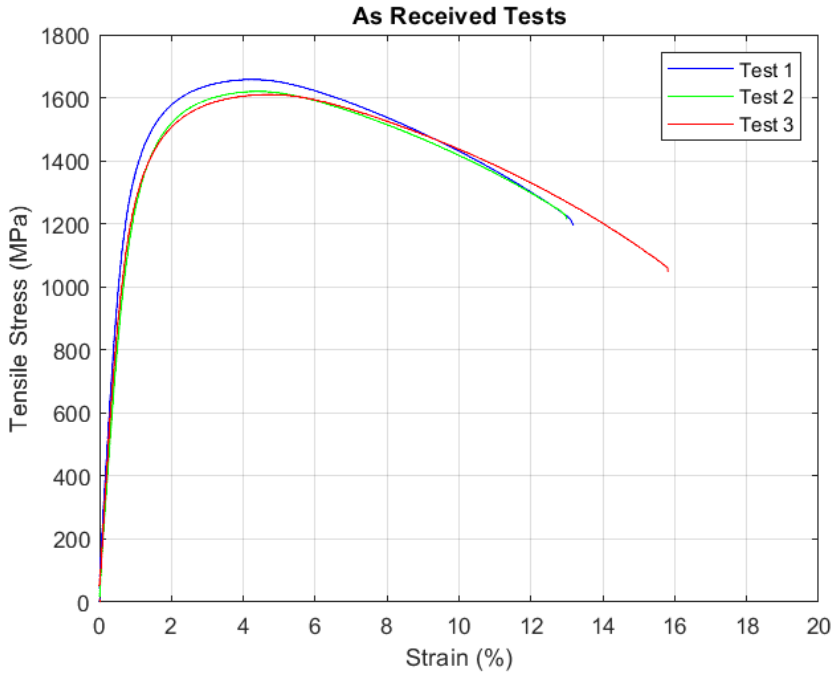

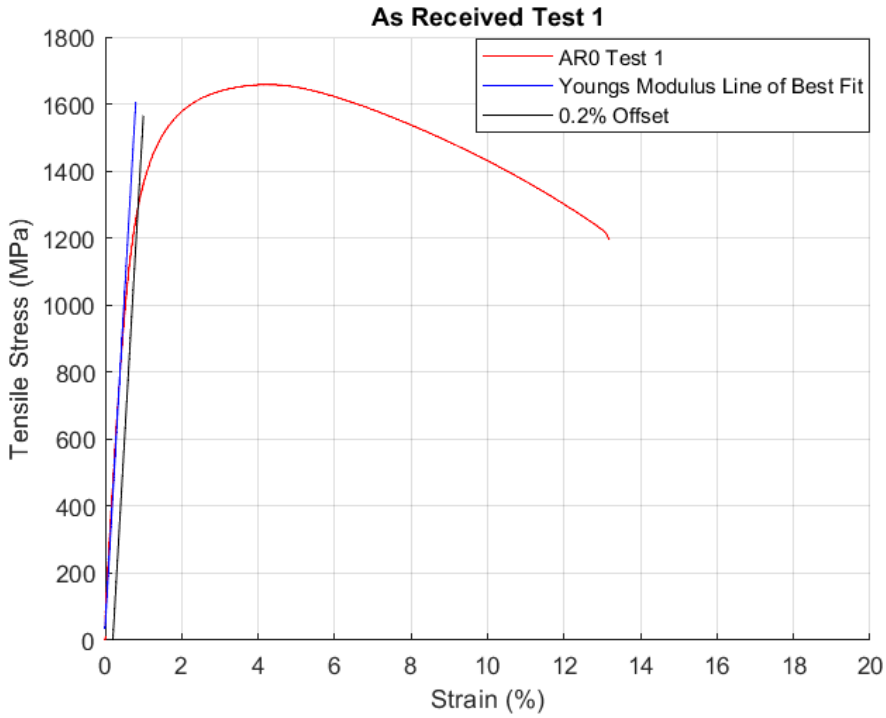
As Received Test 1
AR0 Test 1
Youngs Modulus Line of Best Fit
0.2% Offset
Tensile Stress (MPa)
Strain (%)
0
200
400
600
800
1000
1200
1400
1600
1800
0
2
4
6
8
10
12
14
16
18
20

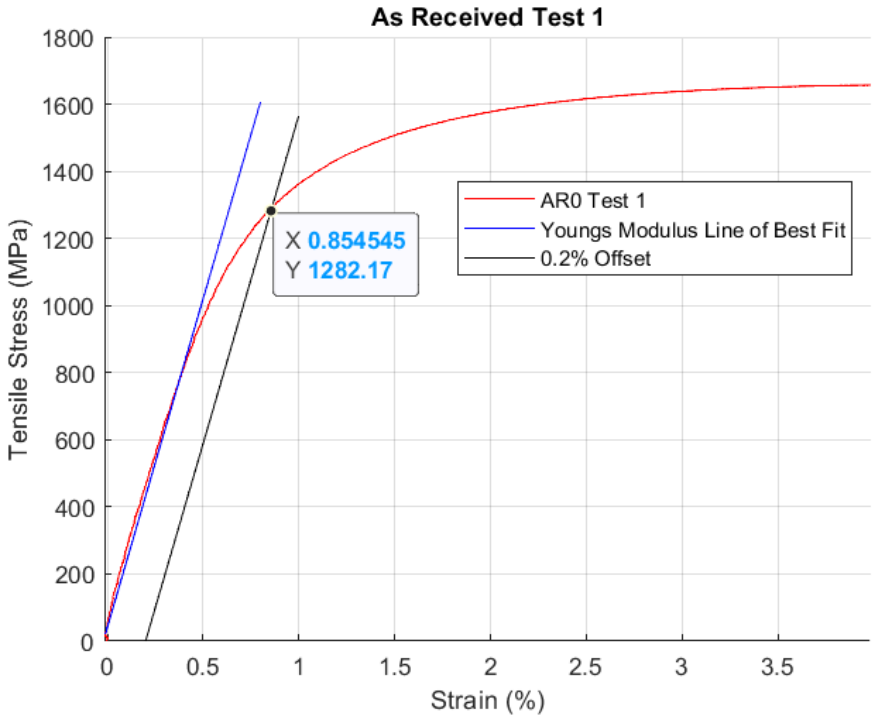
As Received Test 1
AR0 Test 1
Youngs Modulus Line of Best Fit
0.2% Offset
X 0.854545
Y 1282.17
Tensile Stress (MPa)
Strain (%)
0
200
400
600
800
1000
1200
1400
1600
1800
0
0.5
1
1.5
2
2.5
3
3.5

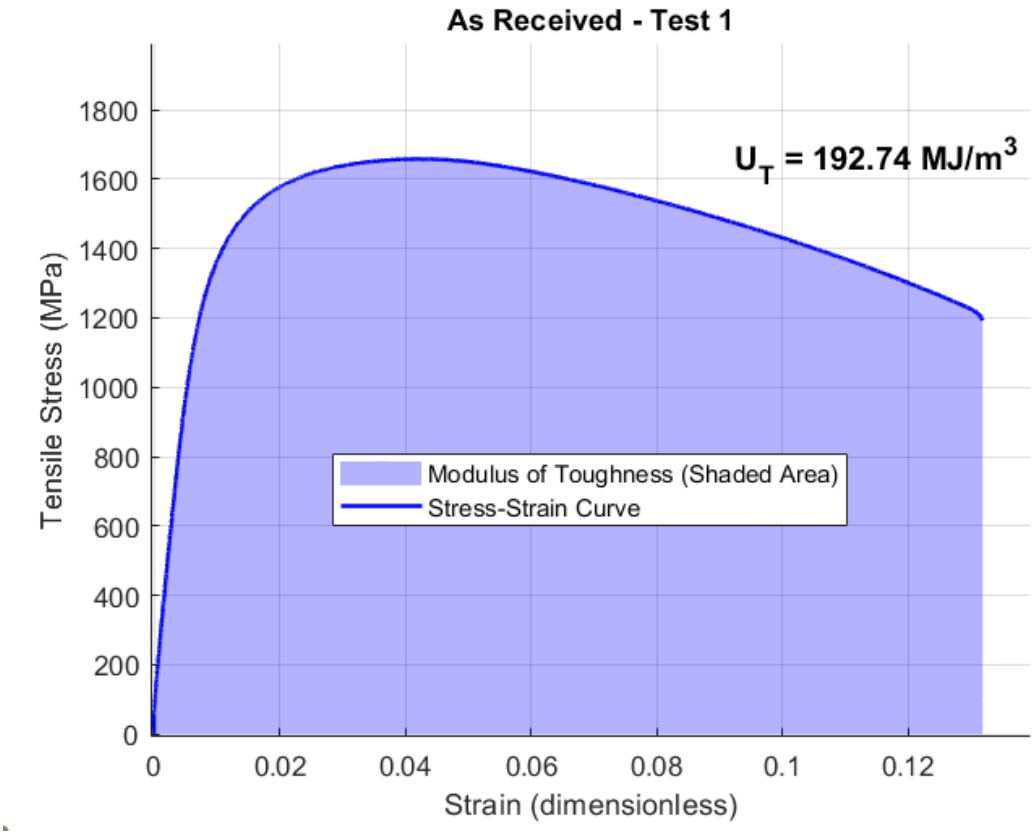

Figure 64: Graphs of the As Received tensile test results

As seen in **Figure 64**, the U_T was found to be 192 MJ/m^3 for AR0T1, a value indicating the energy absorbed during the tensile test. The tensile tests for the AR condition resulted in an elongation averaging at 13.7%. The 0.2% offset yield stress, σ_Y, for the as received condition was an average of 1229 MPa, a value that was similar to the yield stress provided by the manufacturer. There is absence of Lüders bands in the stress strain curve of the AR specimens, meaning this material does not exhibit localized plastic deformation during the elastic to plastic transition [72]. The dislocations glide through the crystal lattice as the microstructure undergoes changes, allowing the material to deform plastically and uniformly without breaking atomic bonds [62].

Table 15 contains the tabulated experimental results obtained for the material in the As-Received regime.

EXPERIMENT	Elongation (%)	YIELD STRESS (MPa)	UTS (MPa)	MODULUS OF TOUGHNESS (MJ/m^3)
AR0RTPT1	13.2	1282	1658	193
AR0RTPT2	12.2	1226	1620	174
AR0RTPT3	15.8	1179	1610	220
AVERAGE	13.7	1229	1629	196

Table 15: As Received tensile test results

It can be observed that the As-Received condition of the material has significant maximum tensile strength endured before failure, with the UTS at an average of 1629 MPa. This value also corresponds with the high UTS value in the material's data sheet. It can be seen that the material does not extensively deform before reaching the failure state in the test. This plastic deformation observed indicates that the material has low ductility behaviour, corresponding to the high yield and ultimate tensile stresses observed [4], [62].

A more in-depth analysis of the material behaviour is discussed in the next sections where the three material regimes are compared to each other.

4.2.2.2 Heat Treatment 1 Results

The tensile behaviour of the HT1 material condition can be seen in **Figure 65**. The graph also shows a steep elastic region as in the AR condition. The 0.2% offset yield stress, σ_Y, for the HT1 condition was found to be 755 MPa and the presence of Lüders bands can be observed [6]. This observation means that during the elastic to plastic transition, the HT1 regime exhibits localized plastic deformation [72].

There is dislocation motion occurring in the crystal lattice of the material, resulting in the development of these bands, a characteristic jerky appearance observed in the stress strain graph in **Figure 65**. The phenomenon of yield point elongation can also be observed as a result. The microstructure undergoes additional elongation before the onset of more uniform plastic deformation. This is because of the discontinuous yielding which occurred in the ferrite phase, as the dislocations became progressively unpinned from the carbon atoms in the microstructure. This resulted in the dislocation motion when the stress increased and consequently the formation of Lüders bands and yield point elongation [4], [72].

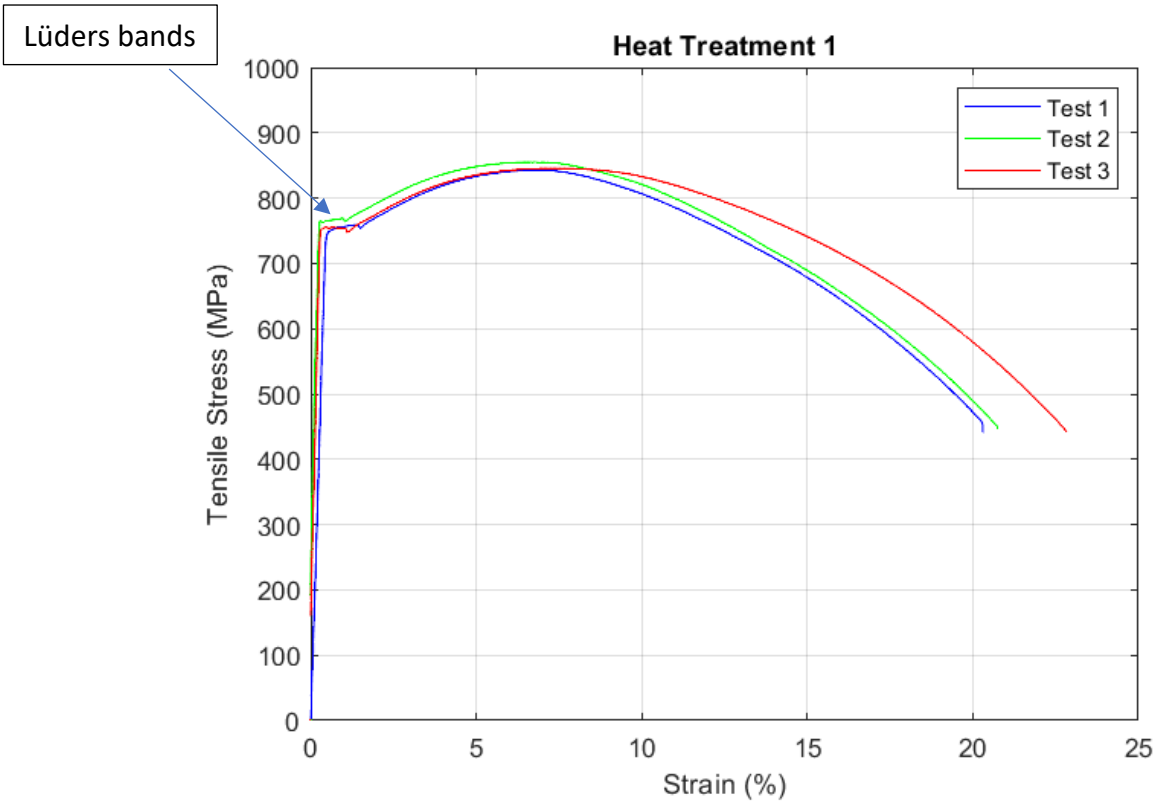

[6] A limitation to the analysis of HT1 tensile stress strain curves was the use of the 0.2% offset to establish the yield point. While this method was applied uniformly across all tensile tests in this dissertation for consistency, it is not fully compliant with the ASTM E8 standard in the case of materials exhibiting discontinuous yielding such as the HT1 regime where the appearance of Lüders bands is observed. Recommeded methods like identifying upper and lower yield points would accurately reflect the material yield behaviour.

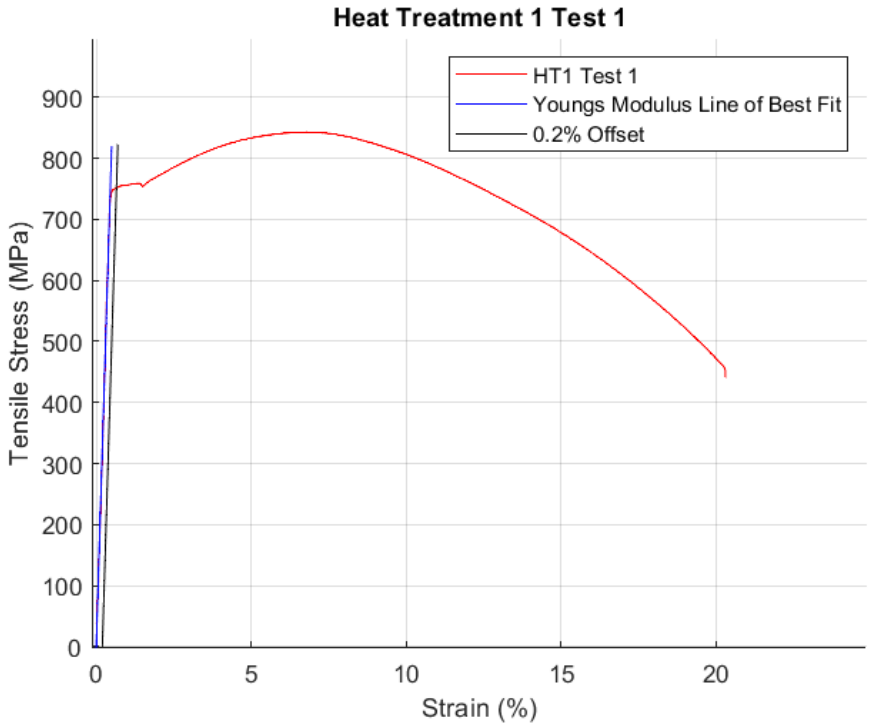
Heat Treatment 1 Test 1
HT1 Test 1
Youngs Modulus Line of Best Fit
0.2% Offset
Tensile Stress (MPa)
Strain (%)
0
100
200
300
400
500
600
700
800
900
0
5
10
15
20

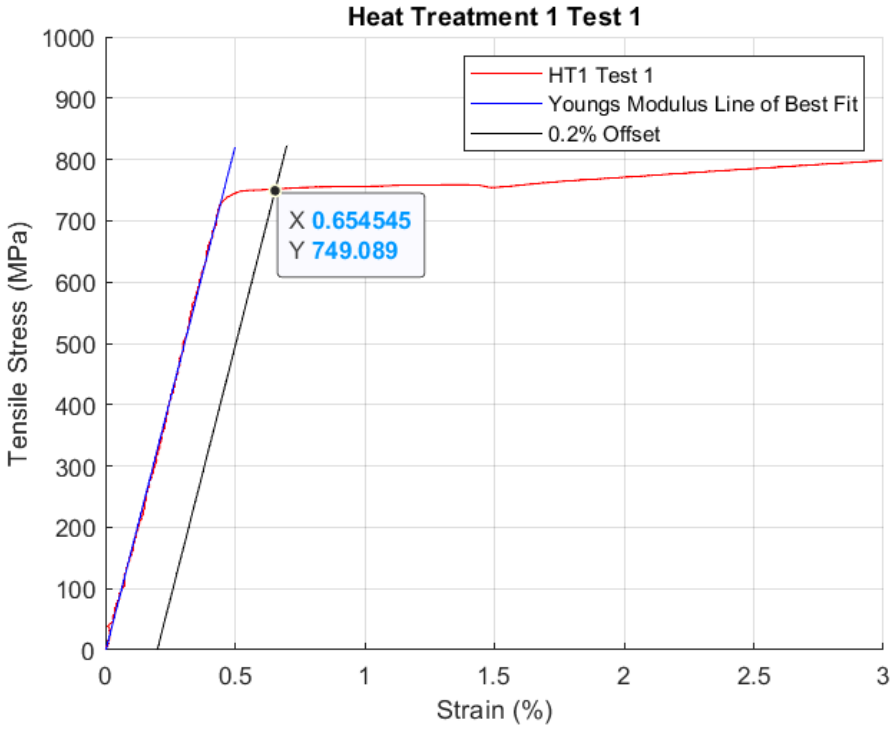
Heat Treatment 1 Test 1
HT1 Test 1
Youngs Modulus Line of Best Fit
0.2% Offset
X 0.654545
Y 749.089
Tensile Stress (MPa)
Strain (%)
0
100
200
300
400
500
600
700
800
900
1000
0
0.5
1
1.5
2
2.5
3

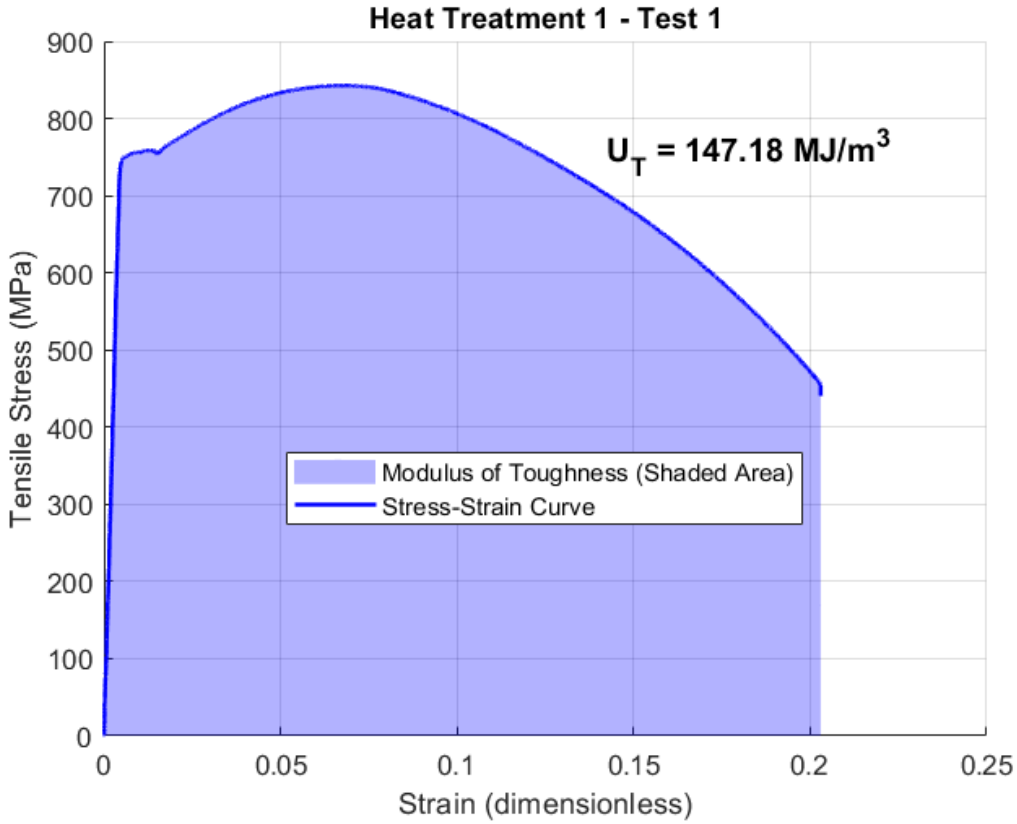

Figure 65: Graphs of the Heat Treatment 1 tensile test results

As seen in **Figure 65**, the average UTS of the material was observed to be 848 MPa, a high stress value associated with carbon steel having undergone quenching and tempering as in the case of HT1 where the internal stresses are relieved, and the grain structure is refined [4], [62]. The water quenching process resulted in the formation of martensite, affecting the mechanical properties of the material by increasing the strength and reducing ductility. The tempering process adopted in this heat treatment method then increased the ductility and reduced the hardness induced by the water quenching [71]. The U_T observed for the tensile test for the HT1T1 specimen was 147 MJ/m^3, highlighting the toughness of the tempered martensite.

Table 16 shows the results that were obtained for the HT1 regime. As observed, the elongation averaged at 21%. The material exhibits relatively ductile behaviour, as the plastic deformation region has significant strain which corresponds to the heat treatment process which improved ductility and toughness of the material.

EXPERIMENT	Elongation (%)	YIELD STRESS (MPa)	UTS (MPa)	MODULUS OF TOUGHNESS (MJ/m^3)
HT1RTPT1	20.3	749	843	147
HT1RTPT2	20.7	763	855	153
HT1RTPT3	22.8	753	846	168
AVERAGE	21.3	755	848	156

Table 16: Heat Treatment 1 tensile test results

4.2.2.3 Heat Treatment 2 Results

Figure 66 shows the stress strain relationship observed for the HT2 regime. A steep elastic region can also be seen on these graphs, highlighting the high stiffness property of the material. As observed, the 0.2% offset yield stress, σ_Y, for the HT2 condition was 385 MPa, a relatively lower yield strength in comparison with the preceding regimes. During the heat treatment process, the material was allowed to cool slowly in the furnace, resulting in various microstructural changes and mechanical properties observed in the results.

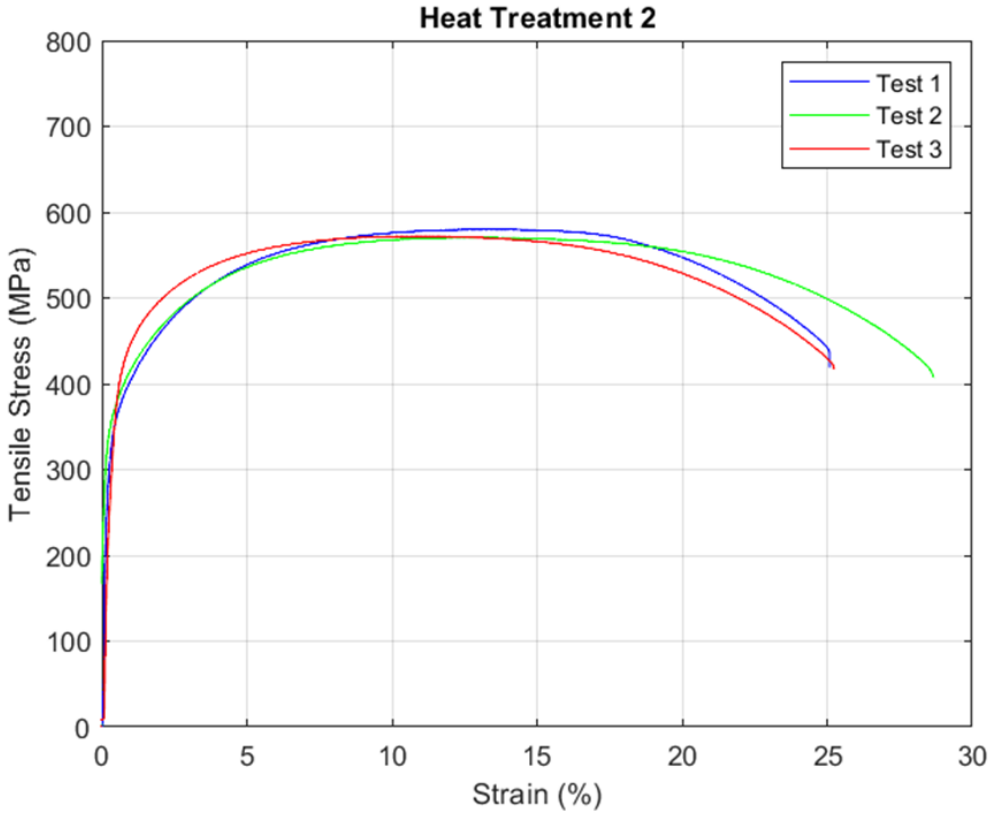

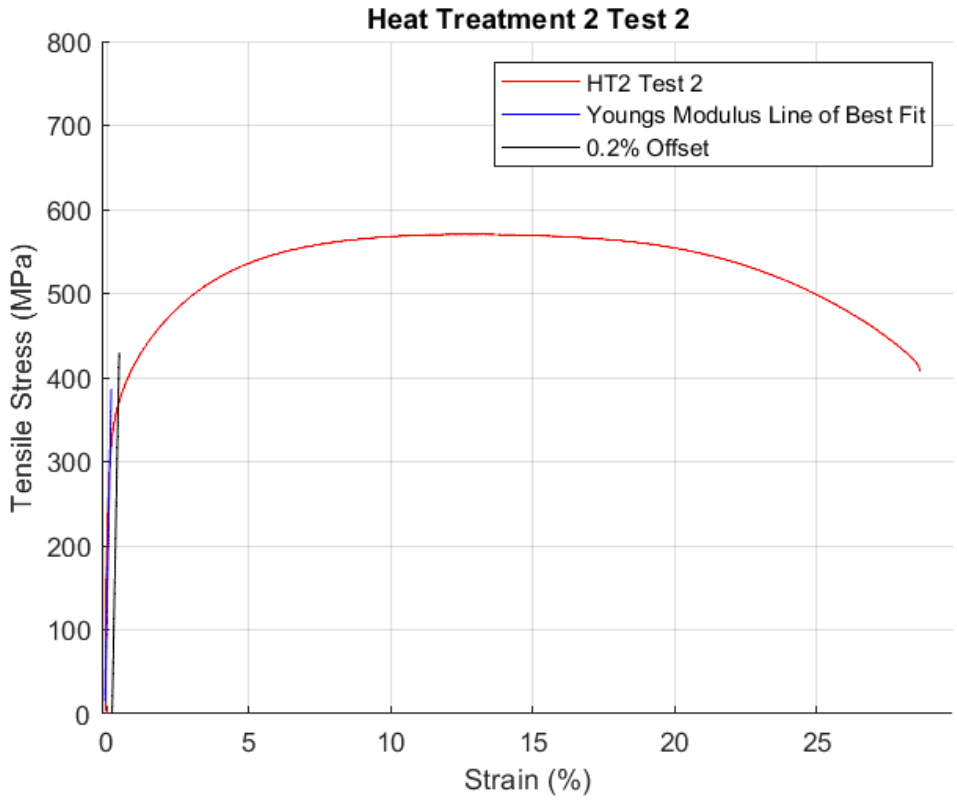
Heat Treatment 2 Test 2
HT2 Test 2
Youngs Modulus Line of Best Fit
0.2% Offset
Tensile Stress (MPa)
Strain (%)
0
100
200
300
400
500
600
700
800
0
5
10
15
20
25

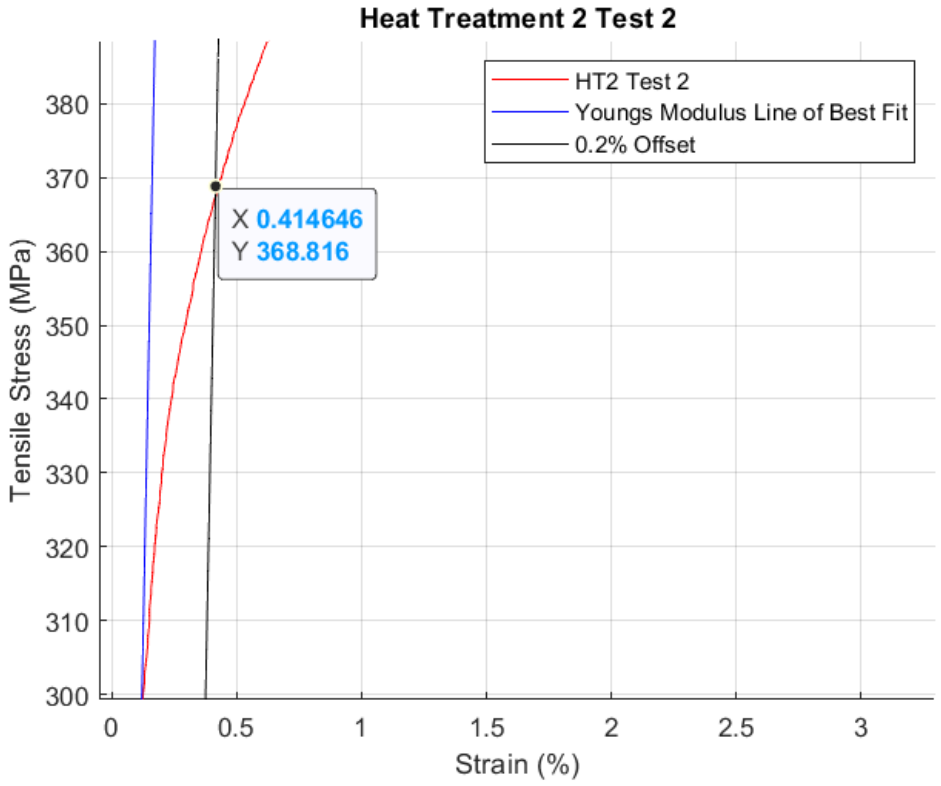
Heat Treatment 2 Test 2
HT2 Test 2
Youngs Modulus Line of Best Fit
0.2% Offset
X 0.414646
Y 368.816
Tensile Stress (MPa)
Strain (%)
300
310
320
330
340
350
360
370
380
0
0.5
1
1.5
2
2.5
3

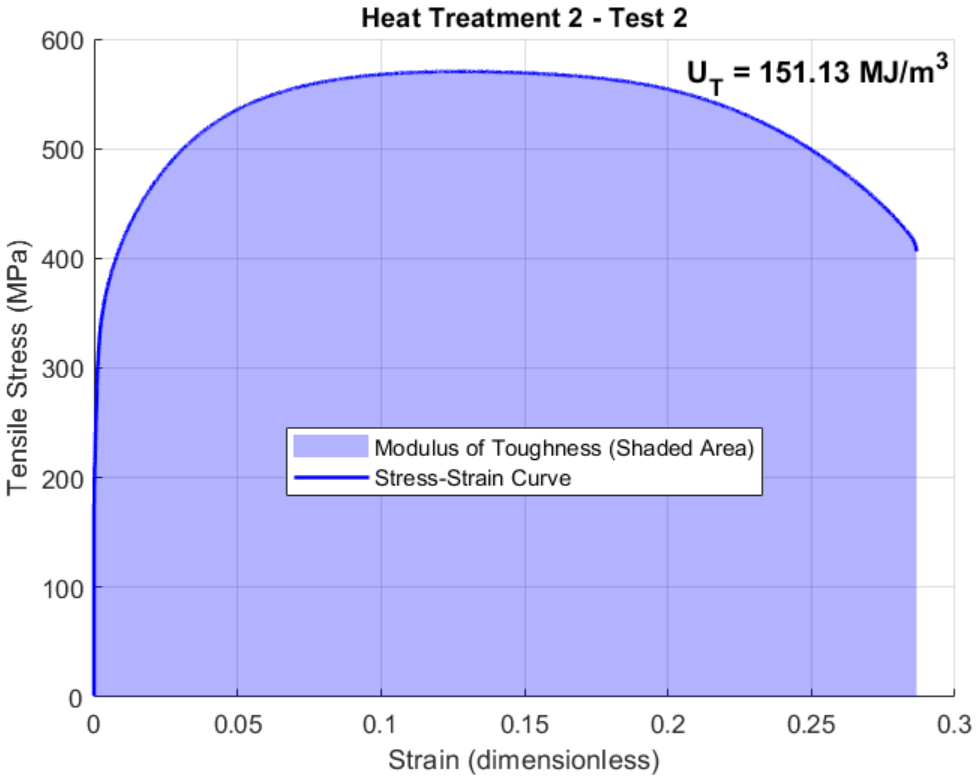

Figure 66: Graphs of the Heat Treatment 2 tensile test results

Furnace cooling resulted in the formation of a pearlite and bainite microstructure. The new strain-free grains in the microstructure, improved the ductility characteristic of the material as carbon could diffuse easily [73]. As seen in **Figure 66**, there is absence of Lüders bands meaning no localized plastic deformation occurred in the material, as the new strain free grains formed in the microstructure allowed for the movement of dislocations [4]. The material in this HT2 regime exhibits high ductility as indicated by the elongated plastic deformation phase before failure.

Table 17 shows the results that were obtained for the HT2 regime. The average U_T for the HT2 regime tests was 139 MJ/m^3 and the elongation averaged at 26%. The average UTS was observed to be 574 MPa, a relatively low tensile strength corresponding to the low hardness of the heat-treated material. The heat treatment process adopted for this regime also resulted in the formation of a refined homogeneous microstructure with reduced internal stresses corresponding to the ductility observed.

EXPERIMENT	Elongation (%)	YIELD STRESS (MPa)	UTS (MPa)	MODULUS OF TOUGHNESS (MJ/m^3)
HT2RTPT1	25.1	363	580	134
HT2RTPT2	28.7	369	570	151
HT2RTPT3	25.2	424	572	133
AVERAGE	26.3	385	574	139

Table 17: Heat Treatment 2 tensile test results

4.2.2.4 AR, HT1 and HT2 Results

The three distinct regimes could be seen through the different results obtained through the tensile tests. As seen in **Figure 67**, the three regimes exhibit the different material properties, including the yield stress, ultimate tensile stress, modulus of toughness and the elongation. This is because these mechanical properties were affected directly by the heat treatment processes adopted, as heat treatment primarily affects the mechanical properties of the materials. Features like grain size and crystalline structure can affect the intrinsic properties determined by the material's atomic and molecular structure, which determine the mechanical properties [4].

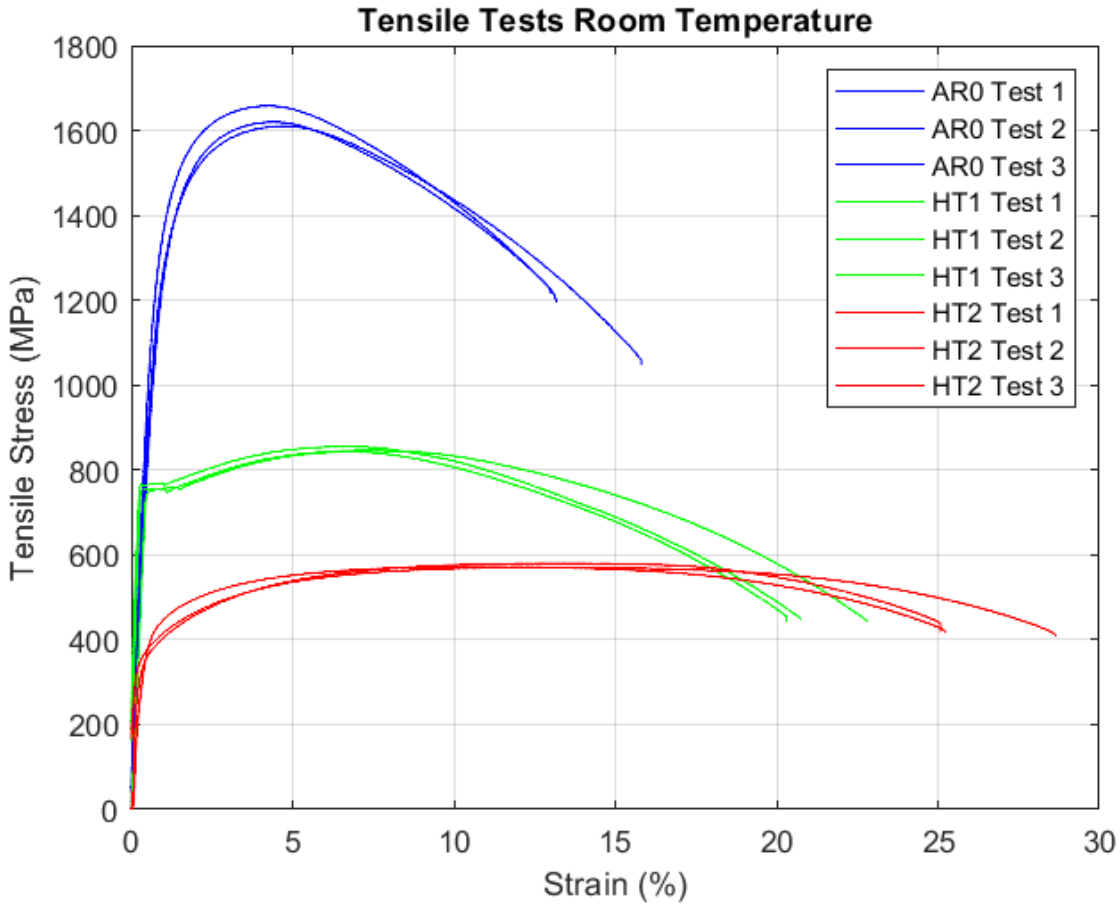

Figure 67: Graph of combined tensile test results for AR, HT1 and HT2

As seen in **Figure 67**, only the HT1 results have the appearance of Lüders bands, meaning it is the regime that was heat treated, water quenched and tempered at 600 °C for a significant period (2 hours) that had localised plastic deformation. This is because the heat treatment process adopted affected the atomic arrangement and dislocations within the crystal. HT1 microstructure was formed through the decomposition of high carbon martensite during tempering, and it is possible that the decomposition did not occur completely, resulting in higher than equilibrium carbon content in the ferrite. This promoted the appearance of Lüders bands as the carbon pinned the dislocations. In the

other regimes, the absence of Lüders bands means the microstructure in both cases allowed for a smooth elastic to plastic transition with no yield point elongation. In the case of HT2 regime, the microstructure was in full equilibrium and had normal low carbon content in the ferrite. The Lüders bands were therefore not observed, as there was very little carbon in ferrite to pin dislocations. This microstructural uniformity resulted from the slow furnace cooling where internal stresses were reduced [73].

The plastic deformation regions also exhibit the differences in mechanical properties observed. As seen in **Figure 67**, the ductility properties vary with each regime, with HT2 the most ductile and AR being the least ductile. This was expected, as the AR regime has a harder, less refined microstructure with limited plasticity, resulting in the materials high strength but lower ductility, as well as high hardness as established. HT1 material stroked a unique balance of ductility and strength as seen in **Figure 67**. HT2 exhibits the highest ductility among the three regimes, mainly because of the furnace cooling process which allowed carbon diffusion and formation of an equilibrium ferrite and pearlite microstructure. **Table 18** exhibits how the strength of the regimes is inversely proportional to the ductility observed in **Figure 67**.

EXPERIMENT	Elongation (%)	YIELD STRESS (MPa)	UTS (MPa)	MODULUS OF TOUGHNESS (MJ/m^3)
AR0	13.7	1229	1629	196
HT1	21.3	755	848	156
HT2	26.3	385	574	139

Table 18: Combined tensile test results for AR, HT1 and HT2

The AR regime had the highest yield point, but the lowest elongation as expected, followed by the tempered HT1 regime and lastly the ductile HT2 regime. These yield point properties observed also corresponded to the UTS of each regime as seen in **Table 18**. The variation in the strength properties of these regimes can be attributed to the different microstructural arrangements in each case resulting from the different heat treatment processes. AR maintained the materials high strength, toughness and hardness in comparison with the other adopted heat treatments. HT1 resulted in a tempered martensite with higher strength and toughness than the fully equilibrium pearlite and bainite structure of HT2 [71], [62]. As seen in **Figure 68**, AR had the highest toughness regardless of having the least ductility in comparison with the other test regimes, meaning the material's ability to absorb energy was reduced when strength was reduced for increase in ductility.

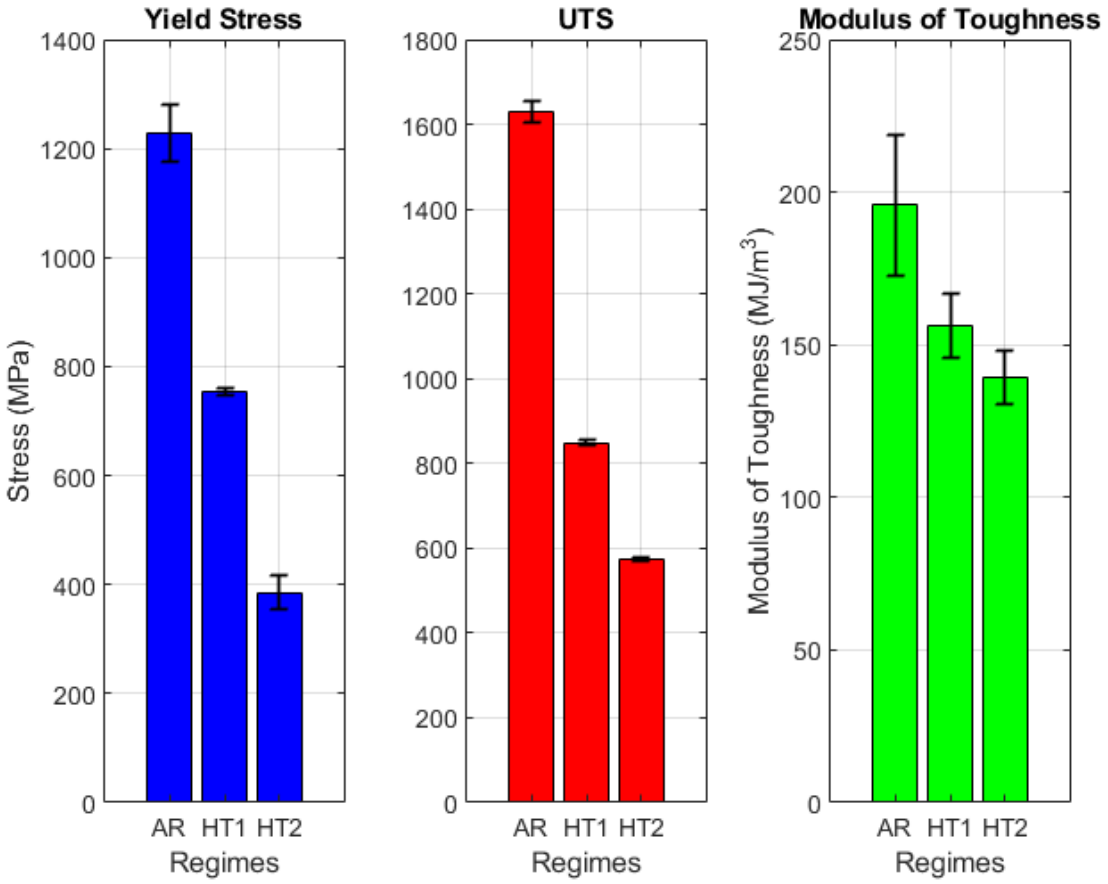

Figure 68: Bar Graph of AR, HT1 and HT2 tensile test results with error bars

HT2 on the other hand had the material heated above critical temperature, to 850 °C as well, but furnace cooled. Considering the CCT diagram, we can see how the slow cooling of the material resulted in formation of bainite and a pearlitic structure, consisting lamellae of soft phase ferrite and hard phase cementite as mentioned prior, leading to lower strength as observed. All in all, we can attribute the observed tensile properties to the heat treatments adopted, the varying carbon content and also the varying microstructural formations as a result.

4.3 CVN TESTS

The heat-treated specimens were machined into notched samples for the impact test. In accordance with the ASTM E23-18, the material to be tested was cut into blocks as mentioned in **Chapter 3**. These blocks were the specimens that were heat treated. After the material blocks were separated into the three required regimes, the specimens were then machined into the ASTM compliant dimensions for testing. For the CVN test the specimen orientation was T-L. The CVN % shear and absorbed energy results were tabulated and presented in the following sections.

4.3.1 Analysis Procedure/Method

As mentioned earlier in this dissertation, the orientation for the notch was vital to the specimen integrity. The notched specimen was ground and welded with a K-type thermocouple and then transferred to the temperature conditioning medium. The temperature conditioned specimen was then tested with the impact tester. The user interface of the impact tester recorded the impact energy absorbed against the time of impact. The computer software would then produce the value of the energy absorbed in J for each impact test carried out.

For the graphical representation of the CVN test for each regime, a cubic polynomial fit was used to estimate the FATT and the DBTT shown in the figures to follow. In accordance with the ASTM standard, the averaged value of the three specimens tested at each temperature was used in these results.

It is worth to note that the V-notch in the specimen was a point of high stress concentration. Upon impact the stress tensor reached its peak, generating a rapid stress wave propagating from the impact point and this localised stress led to deformation and fracture and failure of the material [74].

4.3.2 Results Obtained

4.3.2.1 As Received Results

Figure 69 shows the DBTT for the AR material condition was -9 ^{o}C, and the energy absorbed below and above this temperature exhibited different fracture behaviours. It can be seen that below the DBTT, the energy absorbed by the material specimen during impact is lower, as the material behaved in a brittle manner. As the test temperature increased, the energy absorbed also increased, assisting in signifying the transition from brittle fracture behaviour. On the other hand, at temperatures above DBTT, the material specimens absorbed more energy, exhibiting more ductile fracture behaviour.

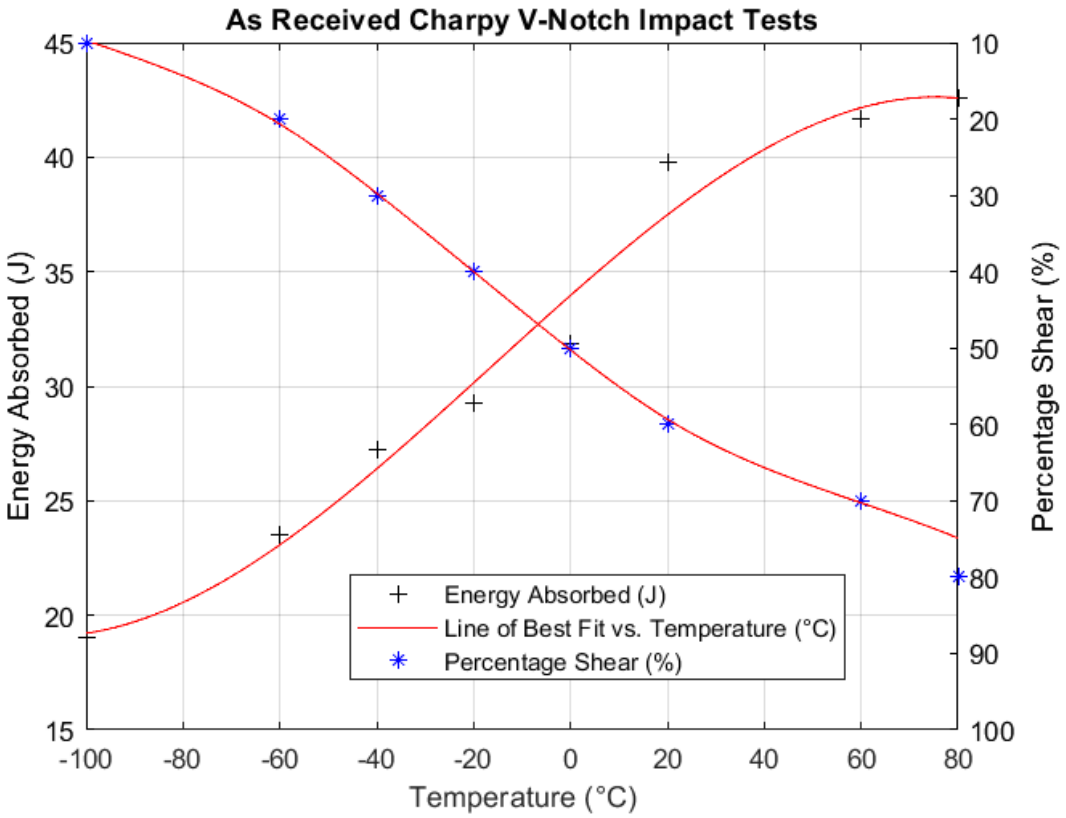

Figure 69: Graph of % Shear/Absorbed Energy vs Temperature for AR regime

These findings with regards to the DBTT correspond with the fracture appearance on the specimen, as brittle fracture had little to no deformation and a relatively flat fracture surface whereas ductile fracture showed significant deformation before failure. The appearance of characteristics like shear lips on the fracture surface were observed more as temperature increased, denoting the ductile behaviour of the material at these temperatures. The FATT was determined to be at 0 ^{o}C, and above that temperature the increase in percentage shear was observed. Temperatures lower than the FATT resulted

in the specimen exhibiting lower percentage shear, as the material deformed less because of the brittle behaviour.

4.3.2.2 Heat Treatment 1 Results

The DBTT was found to be at a significantly lower temperature of -73 ^{o}C in comparison with the as received condition. As shown in **Figure 70**, above this temperature, the energy absorbed during impact increased as expected but stagnated as the test temperature increased. This was because around these test temperatures, the material had reached its plasticity limit hence the increase in the temperature was not significantly enhancing the material's deformation or absorption capacity. The energy absorbed below the DBTT decreased as expected, as the material exhibited brittle fracture as the test temperature fell lower. As in the results for AR condition, the HT1 specimens ductile and brittle fracture above and below the DBTT respectively, corresponded with the fracture surface appearance.

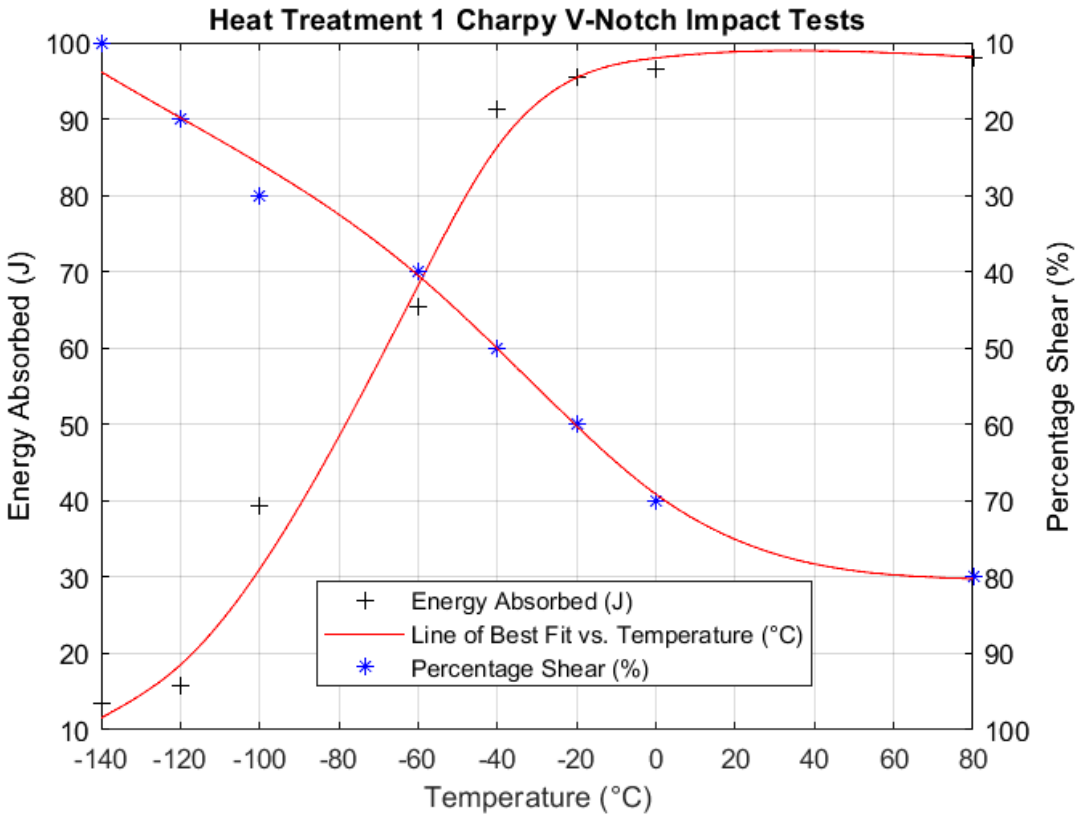

Figure 70: Graph of % Shear/Absorbed Energy vs Temperature for HT1 regime

Figure 70 shows the FATT to be -40 ^{o}C, a noticeably lower temperature as well. As the test temperature increased, the ductility in the fracture for the specimens was also observed. In this region with higher test temperatures than the FATT, the fracture surface highlighted the ductile characteristics in the material. The appearance of features like

elongated regions of the material on the fracture surface as the test temperature and percentage shear increased revealed the aforementioned ductile characteristics of the material. On the contrary, below the FATT, the percentage shear decreased, and the fracture surface appeared flatter with less features, highlighting sudden and brittle fracture.

4.3.2.3 Heat Treatment 2 Results

In the case of HT2 regime, **Figure 71** shows the DBTT which was found to be a relatively high at 57 ^{o}C. At temperatures below the DBTT, the material exhibited brittle fracture because less energy was absorbed during impact as expected. Above the DBTT, **Figure 71** shows how the absorbed energy also increased, corresponding with the ductility in fracture of the material, as well as the fracture surface appearance.

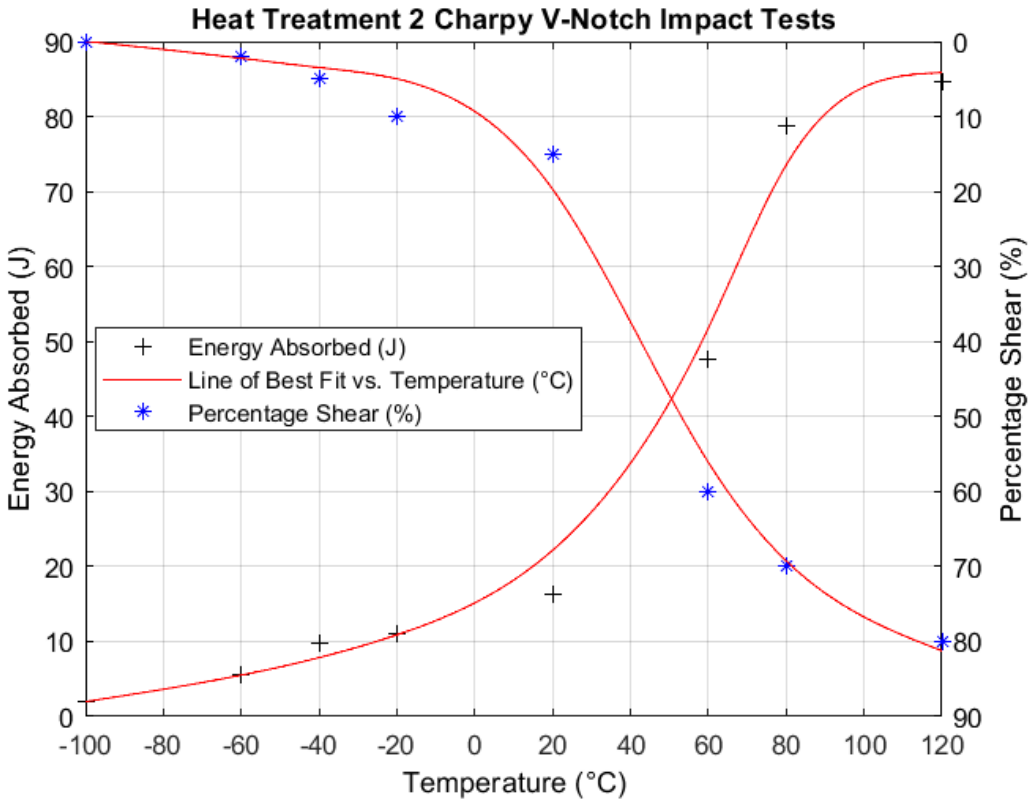

Figure 71: Graph of % Shear/Absorbed Energy vs Temperature for HT2 regime

As seen in **Figure 71**, the FATT was found to be at a relatively high temperature of 53 ^{o}C. At test temperatures lower than the FATT, the percentage shear decreased. The specimens exhibited brittle behaviour as the fracture surface had a smoother finish meaning little or no plastic deformation occurred before fracture. Above the FATT the percentage shear increased significantly, as evidence of plastic deformation could now be observed during fracture. The fracture surface had the appearance of shear lips and microvoids, corresponding to the ductile behaviour expected at these temperatures.

These values make the HT2 regime interesting to analyse, as the material properties shown by these characteristics can be explored further.

4.3.2.4 AR, HT1 and HT2 Results

Figure 72 shows the three different regimes' results on the same graph, highlighting the differences in the mechanical properties of the regimes. As seen in **Figure 72** and **Figure 73**, both the DBTT and FATT values vary with each regime, meaning the ductile and brittle behaviours of the material also vary depending on the regime heat treatment conditions adopted. HT1 has the lowest transition temperatures, followed by AR and lastly HT2 with the highest.

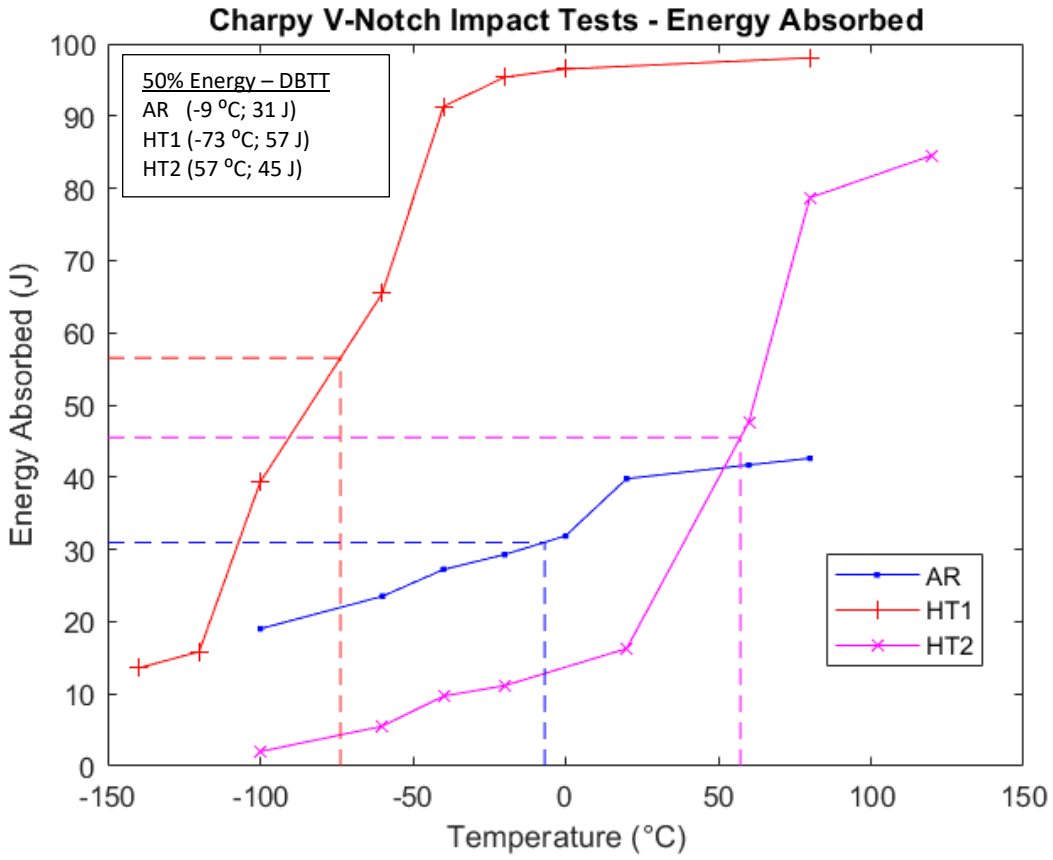

Figure 72: Graph of Energy Absorbed vs Temperature for AR0, HT1 & HT2

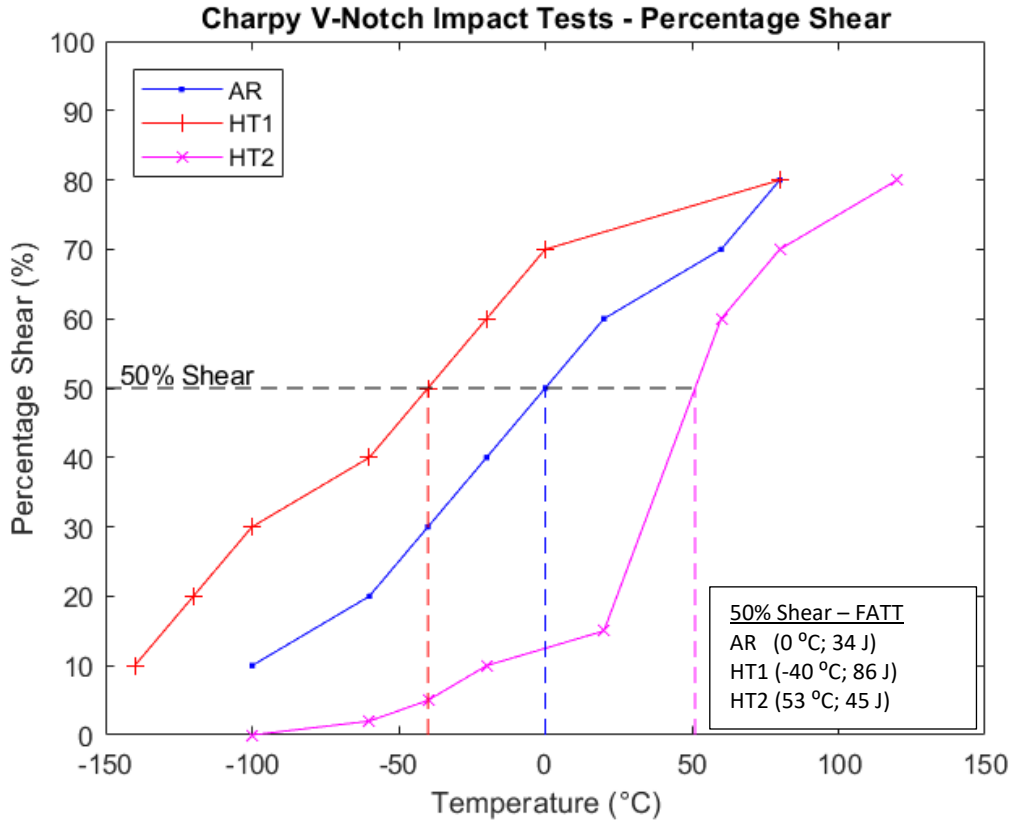

Figure 73: Graph of % Shear vs Temperature for AR0, HT1 & HT2

Table 19 shows the DBTT and FATT for the experiments that were carried out, as well as the energy absorbed at both transition temperatures. Upper Shelf Energy (USE) represents the region of energy absorbed curve where specimen fracture occurs after substantial plastic deformation as well as high energy absorbed. Lower Shelf Energy (LSE) on the other hand, represents the region of the energy absorbed curve where the specimen fracture occurs with minimal plastic deformation and relatively low energy absorbed.

REGIME	USE (J)	LSE (J)	FATT (°C)	DBTT (°C)
AR	43 @ 80 °C	19 @ -60 °C	0	-9
HT1	98 @ 80 °C	15 @ -120 °C	-40	-72
HT2	84 @ 120 °C	5 @ -60 °C	53	56

Table 19: Upper Shelf Energy (USE), Lower Shelf Energy (LSE), DBTT AND FATT for AR0, HT1 & HT2

REGIME	FATT (°C)	Energy at FATT (J)	DBTT (°C)	Energy at DBTT (J)
AR	0	34	-9	31
HT1	-40	86	-73	57
HT2	53	45	57	45

Table 20: Energy absorbed AT DBTT AND FATT for AR0, HT1 & HT2

As presented in the results in **Table 20**, AR absorbs the least impact energy at both FATT and DBTT. This is because of the fine martensitic microstructure of the material. HT2 absorbs more energy at both transition temperatures than AR, but this energy is less than that absorbed in the HT1 regime. In the case of HT2, this is because of the coarse bainitic-pearlitic structure that results from the furnace cooling, as the microstructure contains larger grains which reduce the ability of the material absorbing impact energy in comparison with HT1, thus increasing the DBTT. For HT1, the energy absorbed is a result of the tempering of the martensitic microstructure in the heat treatment process, reducing the internal stresses in the material making the material more resistant to brittle fracture at lower temperatures, hence the lowest transition temperatures.

4.4 FRACTURE TOUGHNESS TESTS

The material was wire cut into deliberately sized rectangular blocks with their orientation marked. These specimens were then heat treated accordingly and were machined into C(T) specimens with dimensions as specified in the ASTM E399 standard. The specimens were also then marked to ensure their categories were noted. For the fracture toughness test the specimen orientation was T-L. The pre-cracking results as well as the fracture toughness values calculated for each specimen are tabulated in the following sections.

4.4.1 Analysis Procedure/Method

The fracture toughness test assessed the resistance of a material to tensile and shearing forces applied during testing. The specimens were pre-cracked using the fracture toughness machine WaveMatrix 1 software until each specimen crack had propagated to the desired length. The microscope was used to accurately measure the length of the pre-crack for data recording. The fracture toughness machine Bluehill 2 software was used to carry out the fracture toughness test until specimen failure.

4.4.2. Results Obtained

4.4.2.1 As Received Results

Figure 74 shows the pre-cracked specimens under the microscope. As mentioned prior in the experimental method, after the pre cracking of the marked specimen was completed, the sample was polished and prepared for the microscope. This is how the accurate measurement of the pre-crack length was determined, by using the microscope measuring tool.

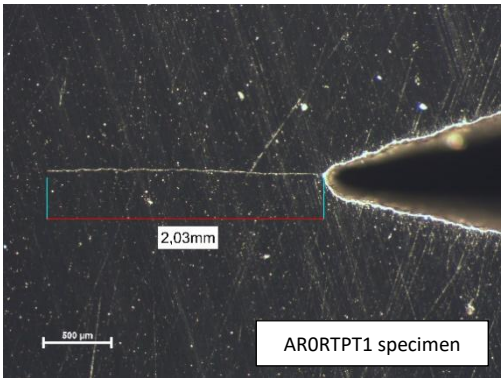

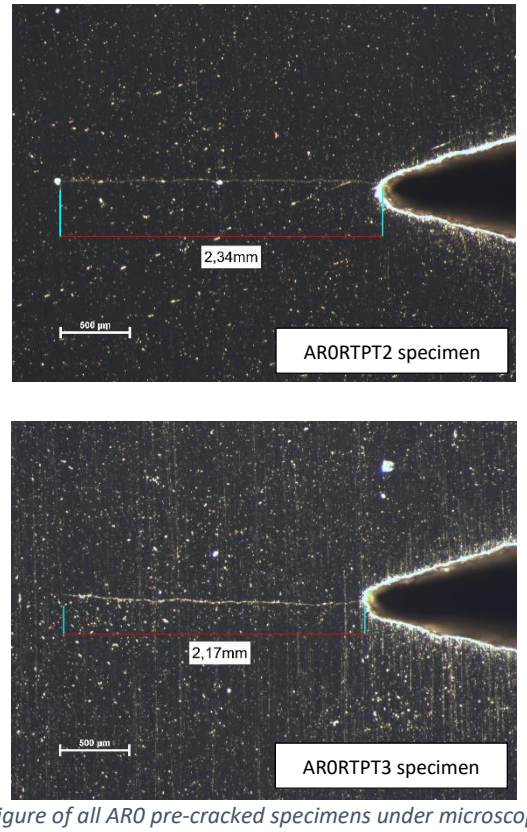

Figure 74: Figure of all AR0 pre-cracked specimens under microscope

The pre-test parameters that were adopted for the test as well as the resulting pre-crack lengths are shown in **Table 21**. The pre-crack length ranged from 2.03 mm to 2.34 mm, and these values provided the crack front length required in the fracture toughness calculations.

EXPERIMENT	Pre-crack Initiation Load (kN)	Fatigue Cycles to Grow Crack	Crack Growth Load (kN)	Pre-crack Length (mm)	Specimen Size (W/B)
AR0RTPT1	**10-12**	**10133**	**12**	**2.03**	**30/15**
AR0RTPT2	**10-12**	**12853**	**12**	**2.34**	**30/15**
AR0RTPT3	**10-12**	**12235**	**12**	**2.17**	**30/15**

Table 21: Crack growth from fatigue loading of AR0 material

The load vs the crack tip opening displacement for the as received condition is shown in **Figure 75**. A similar principal type of force-displacement (crack tip opening displacement) (CTOD) graph as suggested by the ASTM standard can be observed in the results, with the

secant line showing that the force at every point preceding P_{SQ} was lower than P_{SQ}, making P_{SQ} equal to P_{Qsi} [63].

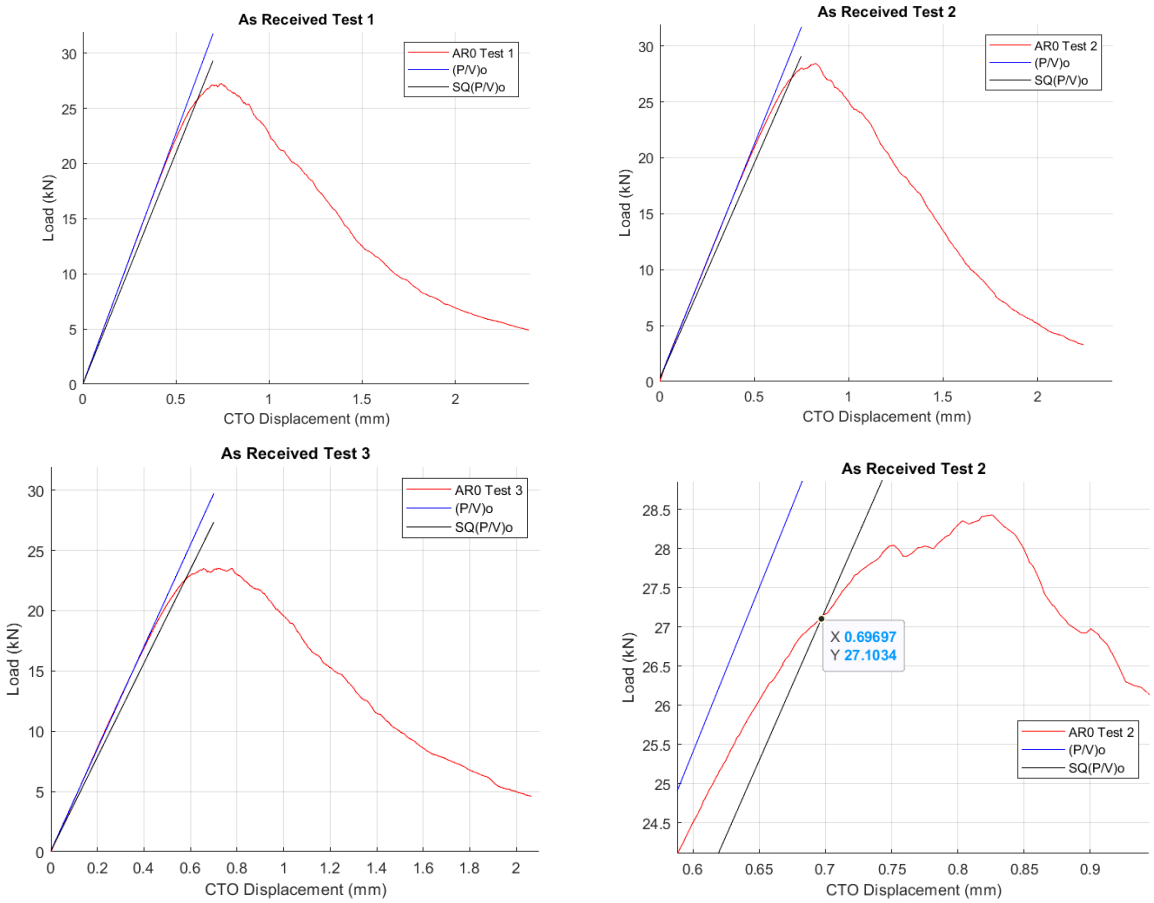

Figure 75: Graph of Load vs CTOD for AR0

Figure 76 shows the fracture toughness specimens after the test was completed to measure the parameters in accordance with the standard. The surface appearance had the distinctive pattern of a relatively smooth fracture surface signifying a brittle fracture mode for the AR condition. Mirror zones, cleavage and a reflective surface surrounding the crack initiation point were also observed, representing the creation of new fracture surfaces as the crack propagated. These observations can be attributed to the brittle nature of the AR regime and the fine martensitic microstructure of the material.

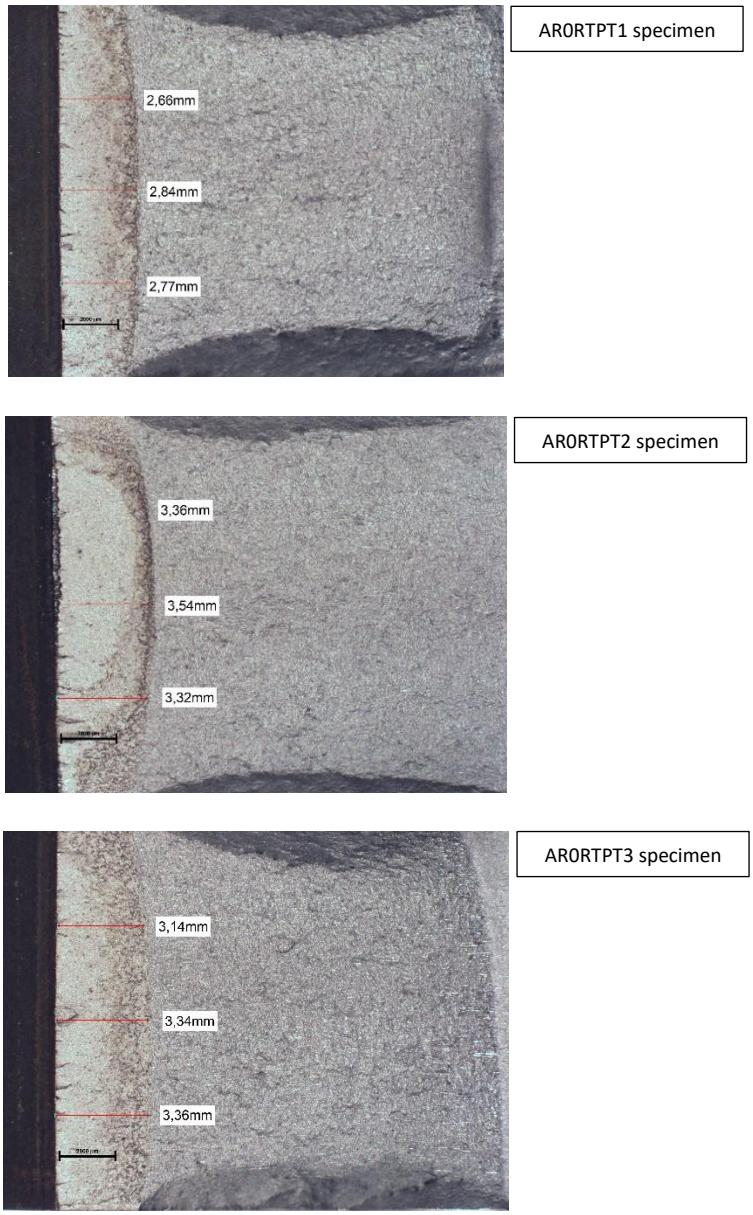

Figure 76: Figure of AR0 fracture toughness specimen after failure

The table below contains the fracture toughness crack length and force results that were obtained from **Figure 75** and **Figure 76** above. The total crack size ranged from 16.26 mm to 16.78 mm for this test regime. The secant offset percentage, S_Q, was also calculated for each test and ranged from 91.9% to 92.29%. With the secant offset percentage values adopted, the P_{SQ}, and subsequently the P_{Qsi} was determined for each test.

EXPERIMENT	Crack Front Length (mm)	Mid-Thickness Length (N)	1st Quarter-Thickness (mm)	2nd Quarter-Thickness (mm)	Average Crack Length (mm)	Total Crack Size (mm)
AR0RTPT1	2.03	2.84	2.66	2.77	2.76	16.26
AR0RTPT2	2.34	3.54	3.36	3.32	3.41	16.91
AR0RTPT3	2.17	3.34	3.14	3.36	3.28	16.78

Table 22: Raw data collected from fracture toughness specimen for AR regime

EXPERIMENT	Crack Length, a (mm)	S_Q (%)	P_{SQ} (N)	P_{MAX} (N)	P_{Qsi} (N)
AR0RTPT1	16.26	92.29	25801	27248	25801
AR0RTPT2	16.91	91.90	27103	28430	27103
AR0RTPT3	16.78	91.98	22561	23530	22561

Table 23: Values for S_Q, P_{SQ}, P_{MAX}, and calculation of P_{Qsi} for AR regime

EXPERIMENT	K_{Qsi} $(\mathbf{MPa\sqrt{m}})$	$(K_{Isi}/\sigma_{YS})^2$	Validity
AR0RTPT1	109.78	0.007331	Valid
AR0RTPT2	124.32	0.01028	Valid
AR0RTPT3	101.95	0.007479	Valid

Table 24: Validity of ASTM E399 in the fracture toughness test for AR regime

According to the E399 standard to calculate the size-insensitive linear elastic, plane strain fracture toughness, the value of K_{Qsi} was determined and it ranged from 101.95 $\mathrm{MPa}\sqrt{\mathrm{m}}$ to 124.32 $\mathrm{MPa}\sqrt{\mathrm{m}}$. In order to establish the validity requirement, $(K_{Isi}/\sigma_{YS})^2$ was calculated and was found to be valid for each test, as it satisfied $(K_{Isi}/\sigma_{YS})^2 < 0.0127$ m. Therefore, the values of K_{Qsi} were valid K_{Isi} test results.

4.4.2.2 Heat Treatment 1 Results

As mentioned prior, the specimens were marked and pre-cracked, then were polished in order to be examined. **Figure 77** shows the pre-cracked specimens under the microscope. Like in the previous section, the measurement of the pre-crack length was determined using the microscope measuring tool. The observed crack front length ranged from 1.76 mm to 2.02 mm.

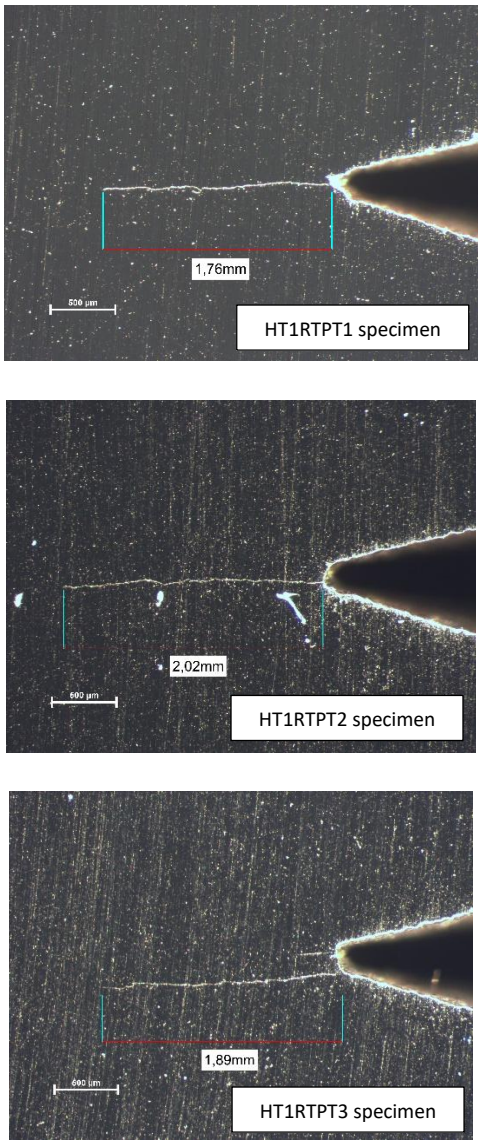

Figure 77: Figure of all HT1 pre-cracked specimens under microscope

Table 25 shows the pre-test parameters that were adopted for the test as well as the pre-crack length results. As in the previous section, these values were used in the calculation of the fracture toughness.

EXPERIMENT	Pre-crack Initiation Load (kN)	Fatigue Cycles to Grow Crack	Crack Growth Load (kN)	Pre-crack Length (mm)	Specimen Size (W/B)
HT1RTPT1	10-12	11011	12	1.76	30/15
HT1RTPT2	10-12	12395	12	2.02	30/15
HT1RTPT3	10-12	11322	12	1.89	30/15

Table 25: Crack growth from fatigue loading of HT1 material

Figure 78 shows the load vs the crack tip opening displacement for the HT1 condition. As seen in the **Figure 78**, the principal type of force-displacement (CTOD) graph was consistent in all the HT1 test results obtained. Since the force at every point preceding P_{SQ} was lower than P_{SQ}, the value of P_{SQ} was equal to P_{Qsi} for all the tests as well.

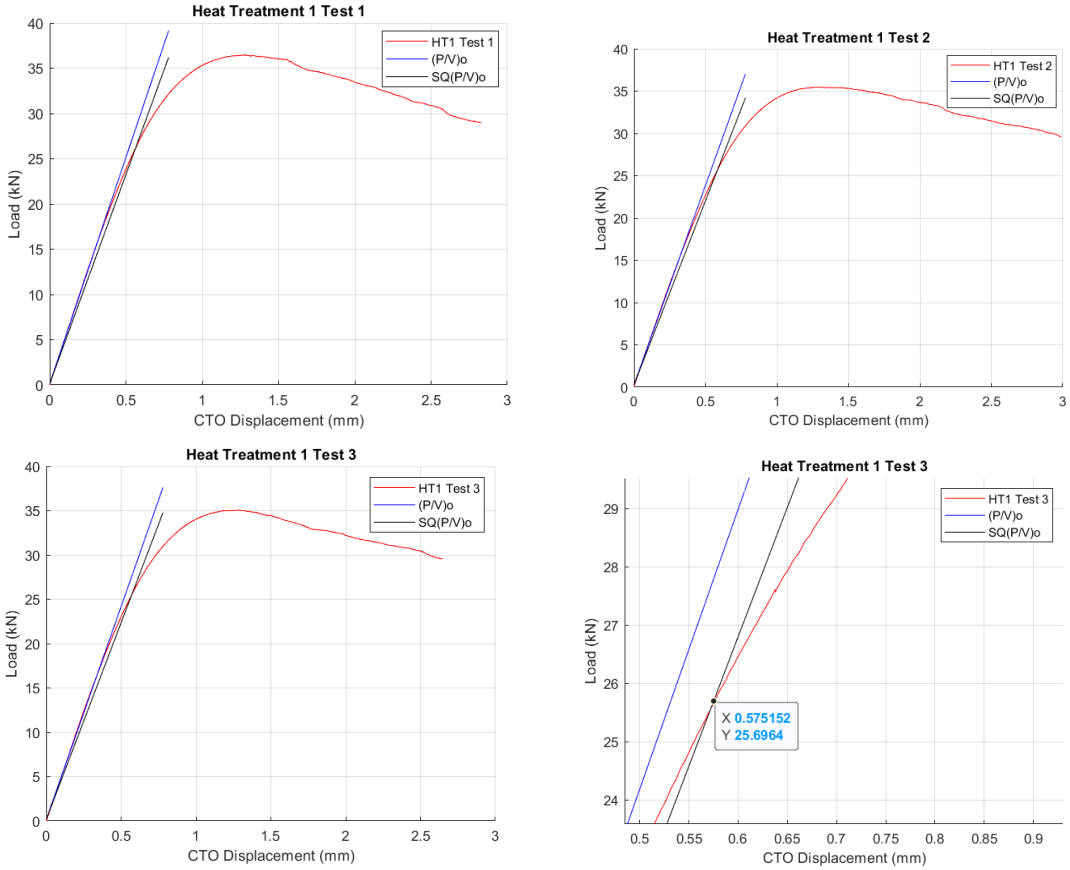

Figure 78: Graph of Load vs CTOD for HT1

Figure 79 shows the post-test fracture toughness specimen fracture surface enabling the measurement of the parameters in accordance with the standard. The fracture surface shows signs of both ductile and brittle behaviour. The cleavage features can be observed on the surface appearance exhibiting the brittle fracture mode endured by the specimens in this material regime. The features observed on the fracture surface also include dimpled regions which can be seen as a result of some plastic deformation primarily because of the tempering undergone by the material.

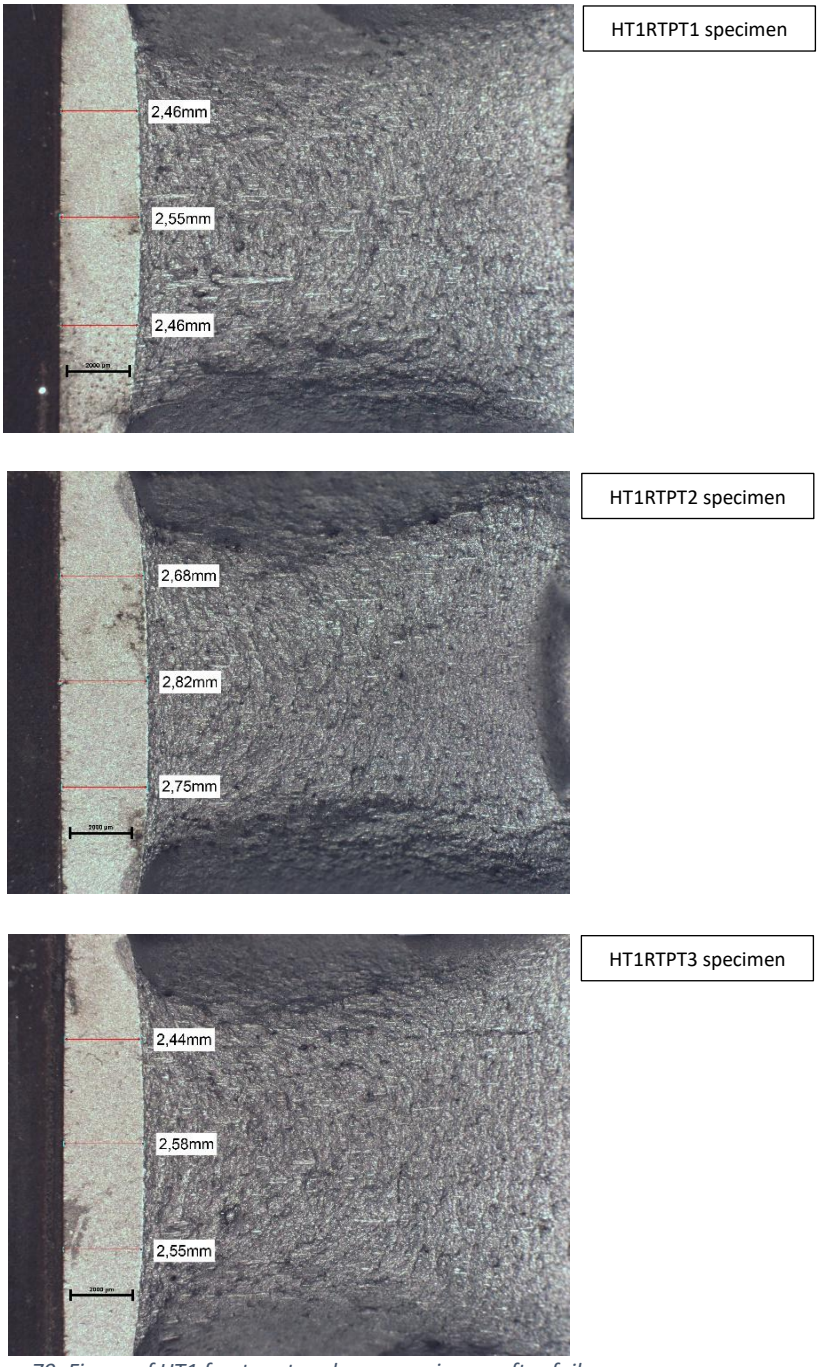

Figure 79: Figure of HT1 fracture toughness specimens after failure

Table 26 contains the fracture toughness test pre-crack measurements and forces that were obtained from the test results above. According to the standard, the crack front and the various sample thickness points where the crack length was measured, helped to establish the total crack size, ranging from 15.99 mm to 16.25 mm. For all the HT1 tests, the calculated secant offset percentage, S_Q, ranged from 92.29% to 92.43%, and the P_{SQ} and P_{Qsi} values were determined.

EXPERIMENT	Crack Front Length (mm)	Mid-Thickness Length (N)	1st Quarter-Thickness (mm)	2nd Quarter-Thickness (mm)	Average Crack Length (mm)	Total Crack Size (mm)
HT1RTPT1	1.76	2.55	2.46	2.46	2.49	15.99
HT1RTPT2	2.02	2.82	2.68	2.75	2.75	16.25
HT1RTPT3	1.89	2.58	2.44	2.55	2.52	16.02

Table 26: Raw data collected from fracture toughness specimen for HT1 regime

EXPERIMENT	Crack Length, a (mm)	S_Q (%)	P_{SQ} (N)	P_{MAX} (N)	P_{Qsi} (N)
HT1RTPT1	15.99	92.43	26013	36462	26013
HT1RTPT2	16.25	92.29	25619	35477	25619
HT1RTPT3	16.02	92.42	25696	35055	25696

Table 27: Values for S_Q, P_{SQ}, P_{MAX}, and calculation of P_{Qsi} for HT1 regime

EXPERIMENT	K_{Qsi} $(\mathbf{MPa\sqrt{m}})$	$(K_{Isi}/\sigma_{YS})^2$	Validity
HT1RTPT1	107.44	0.020572	"invalid according to Section X1.6.1 of Test Method E399"
HT1RTPT2	108.92	0.020373	"invalid according to Section X1.6.1 of Test Method E399"
HT1RTPT3	106.53	0.020007	"invalid according to Section X1.6.1 of Test Method E399"

Table 28: Validity of ASTM E399 in the fracture toughness test for HT1 regime

In accordance with the E399 standard to calculate the size-insensitive linear elastic, plane strain fracture toughness, the values of K_{Qsi} were determined for the HT1 regime. The values of K_{Qsi} ranged from 106.53 $\mathrm{MPa}\sqrt{\mathrm{m}}$ to 108.92 $\mathrm{MPa}\sqrt{\mathrm{m}}$. For the validity requirement, $(K_{Isi}/\sigma_{YS})^2$ was calculated as in the previous section. Unfortunately, the conditional K_{Qsi} were found to be invalid for the three HT1 tests. The specimens failed to satisfy $(K_{Isi}/\sigma_{YS})^2 < 0.0127$ m. This resulted in the values of K_{Qsi} being invalid according to Section X1.6.1 of Test Method E399. However, these K_{Qsi} values were adopted and used as the fracture toughness values for the HT1 material regime, with a recommendation to use a larger specimen to determine K_{Isi} in future experiments.

4.4.2.3 Heat Treatment 2 Results

As in the previous sections for the other material regimes under analysis, the HT2 specimens were marked, pre-cracked and polished for crack growth observations. **Figure 80** shows the pre-cracked specimens under the microscope to determine an accurate measurement of the pre-crack length.

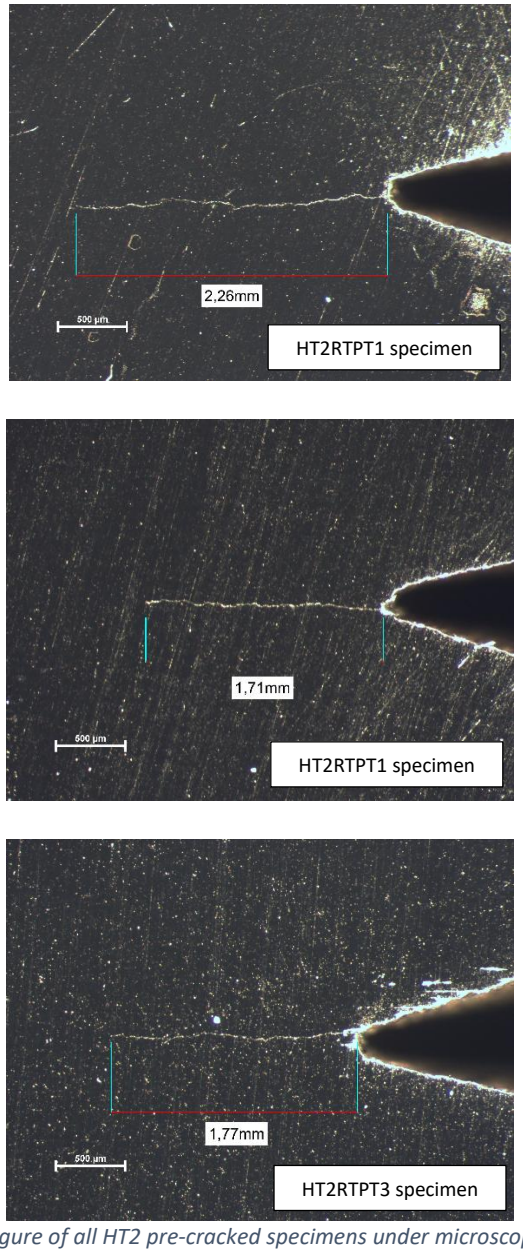

Figure 80: Figure of all HT2 pre-cracked specimens under microscope

The parameters that were adopted for the test and the observed crack front lengths are tabulated in **Table 29**. With a similar crack growth load, the pre-crack length ranged from 1.71 mm to 2.26 mm.

EXPERIMENT	Pre-crack Initiation Load (kN)	Fatigue Cycles to Grow Crack	Crack Growth Load (kN)	Pre-crack Length (mm)	Specimen Size (W/B)
HT2RTPT1	10-12	10804	12	2.26	30/15
HT2RTPT2	10-12	9242	12	1.71	30/15
HT2RTPT3	10-12	8930	12	1.77	30/15

Table 29: Crack growth from fatigue loading of HT2 material

Following the pre-cracking of the specimens, the load vs the crack tip opening displacement for the HT2 condition is shown in **Figure 81**. As observed in the **Figure 81**, a consistent principal type of force-displacement (CTOD) graph was obtained for all the tests carried out as well. The force at every point preceding P_{SQ} was also lower than P_{SQ}, therefore the value of P_{SQ} was equal to P_{Qsi} for all the tests.

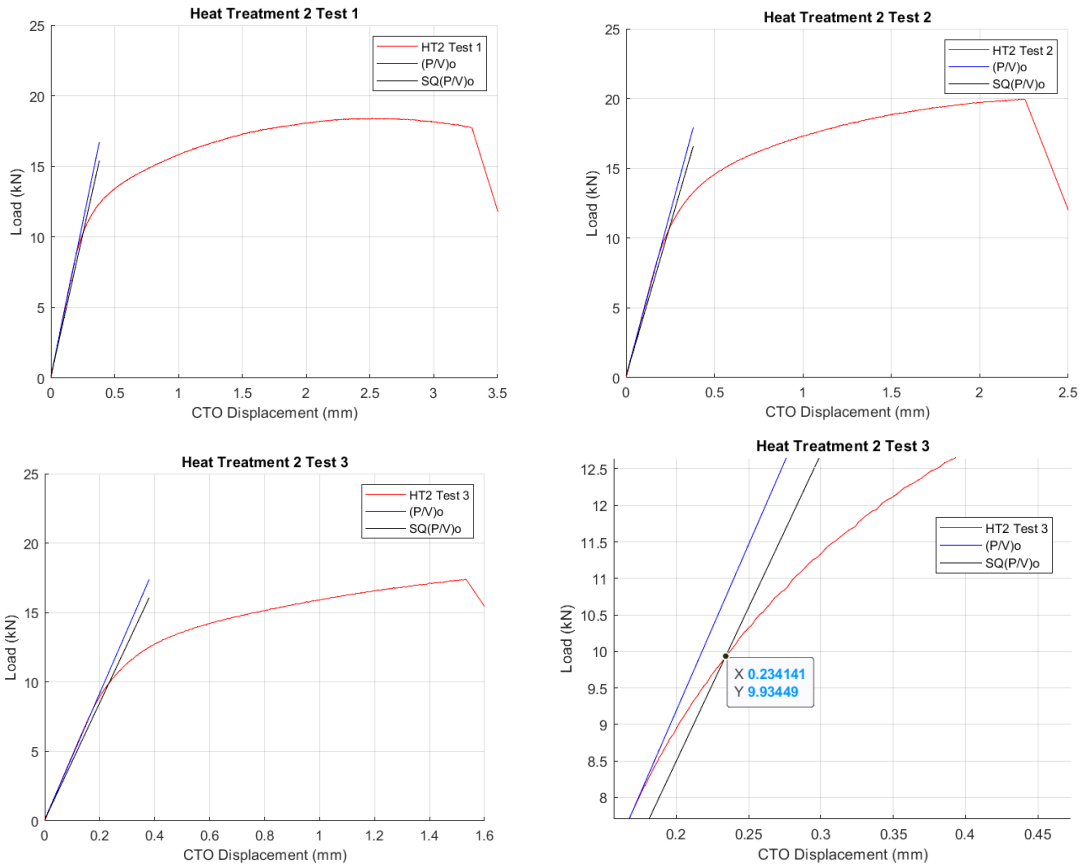

Figure 81: Graph of Load vs CTOD for HT2

Figure 82 shows the fracture toughness specimen after the test was completed to measure the parameters in accordance with the standard. The specimen surface texture has a rough granular surface with voids and step-like features that provide insight into the loading conditions resulting in failure. The observed surface texture highlights microvoid coalescence meaning the material underwent localized ductile tearing particularly near the crack initiation region.

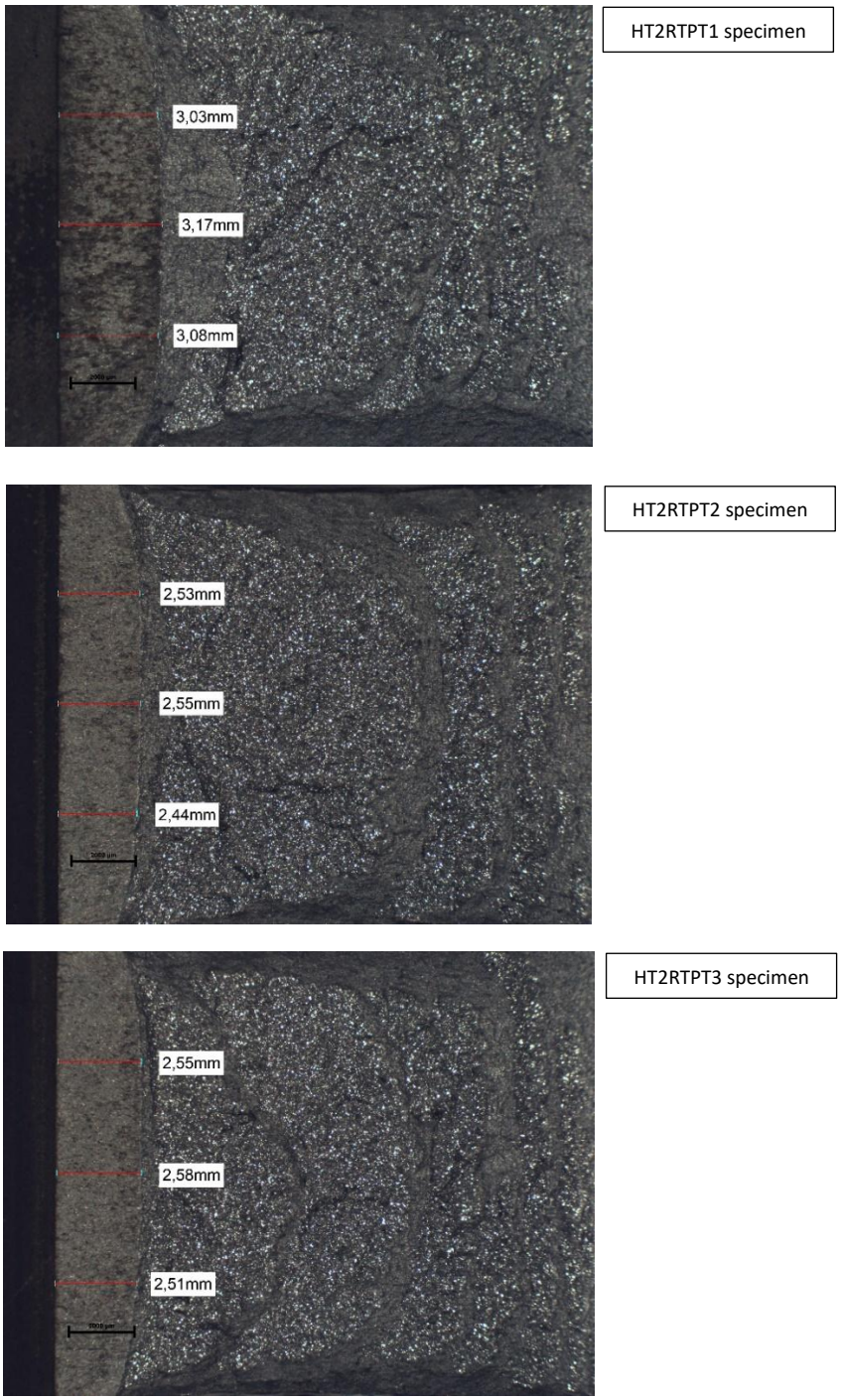

Figure 82: Figure of HT2 fracture toughness specimens after failure

The **Table 30** contains observed results that were obtained from **Figure 81** and **Figure 82** after the fracture toughness test. The total crack size was established using the various crack lengths observed and ranged from 16.01 mm to 16.59 mm. The calculated secant offset percentage, S_Q, ranged from 92.09% to 92.42%, and the P_{SQ} and P_{Qsi} values were therefore determined.

EXPERIMENT	Crack Front Length (mm)	Mid-Thickness Length (N)	1st Quarter-Thickness (mm)	2nd Quarter-Thickness (mm)	Average Crack Length (mm)	Total Crack Size (mm)
HT2RTPT1	2.26	3.17	3.03	3.08	3.09	16.59
HT2RTPT2	1.71	2.55	2.53	2.44	2.51	16.01
HT2RTPT3	1.77	2.58	2.55	2.51	2.55	16.05

Table 30: Raw data collected from fracture toughness specimen for HT2 regime

EXPERIMENT	Crack Length, a (mm)	S_Q (%)	P_{SQ} (N)	P_{MAX} (N)	P_{Qsi} (N)
HT2RTPT1	16.59	92.09	10322	18407	10322
HT2RTPT2	16.01	92.42	10622	19937	10622
HT2RTPT3	16.05	92.40	9935	17401	9935

Table 31: Values for S_Q, P_{SQ}, P_{MAX}, and calculation of P_{Qsi} for HT2 regime

EXPERIMENT	K_{Qsi} $(\mathbf{MPa\sqrt{m}})$	$(K_{Isi}/\sigma_{YS})^2$	Validity*
HT2RTPT1	45.635	0.015801	"invalid according to Section X1.6.1 of Test Method E399"
HT2RTPT2	43.953	0.014202	"invalid according to Section X1.6.1 of Test Method E399"
HT2RTPT3	41.290	0.009498	Valid

Table 32: Validity of ASTM E399 in the fracture toughness test for HT2 regime

Commensurate with the E399 standard to calculate the size-insensitive linear elastic, plane strain fracture toughness, the HT2 regime's values of K_{Qsi} were determined. These values ranged from 41.29 $\mathrm{MPa}\sqrt{\mathrm{m}}$ to 45.64 $\mathrm{MPa}\sqrt{\mathrm{m}}$**.** As in the preceding sections, $(K_{Isi}/\sigma_{YS})^2$ was calculated for the validity requirement. The conditional K_{Qsi} values were found to be invalid for the two of the three HT2 tests as the specimens failed to satisfy $(K_{Isi}/\sigma_{YS})^2 < 0.0127$ m, suggesting the use of a larger specimen for future K_{Isi} experimentations. However, HT2RTPT3 was valid according to the adopted test method, resulting in the K_{Qsi} value being a valid K_{Isi} test result.

4.4.2.4 AR, HT1 and HT2 Results

The graph in **Figure 83** shows the fracture toughness values obtained in the previous sections, the linear elastic plane-strain fracture toughness according to ASTM E399. Granted, some tests did not satisfy the validity requirements, but the results were still to be usable for comparative purposes in this dissertation. The trends that were observed in the data collected were informative in the analysis of the toughness behaviour of the material under the different heat treatment conditions. The material dimensions were a limitation, and these results were interpreted within the context of the available specimen size to provide a useful estimation of fracture behaviour.

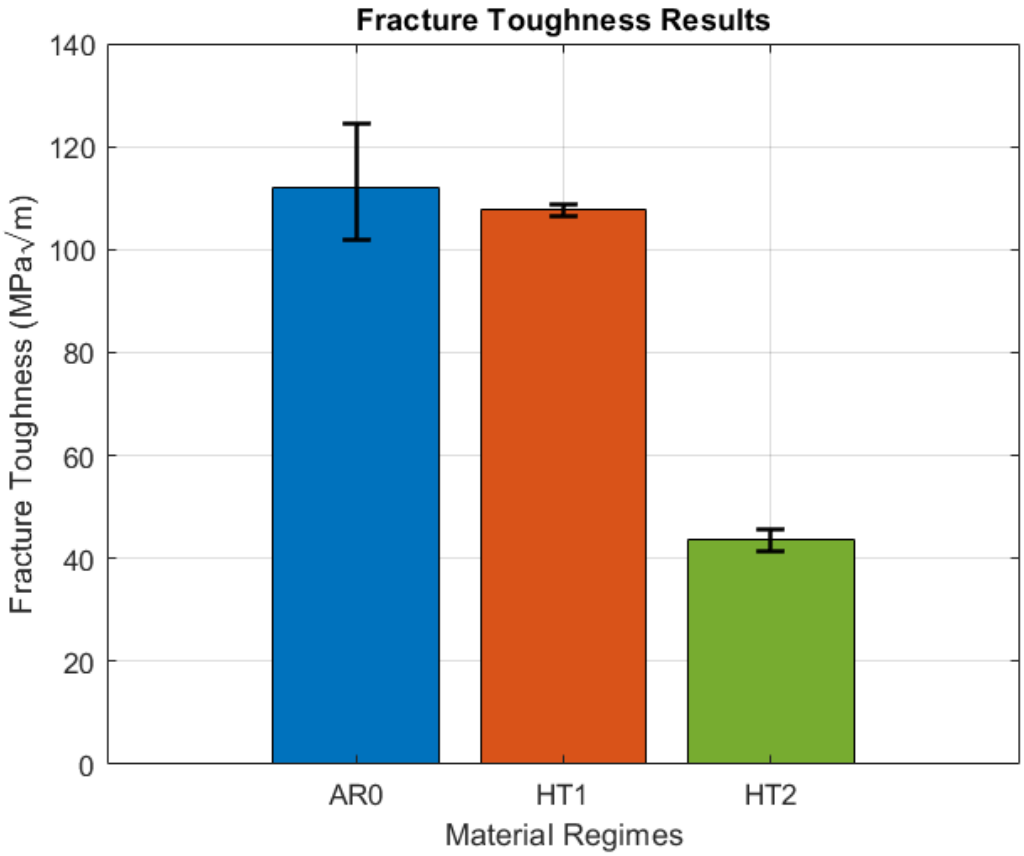

Figure 83: Bar Graph of fracture toughness values obtained for AR0, HT1 & HT2 with error bars

Table 33 shows the fracture toughness values for each regime in tabulated format. As can be seen in both **Figure 83** and **Table 33**, the fracture toughness values for AR highlight that the material in as received condition has fine martensitic microstructure helping maintain the balance between toughness and strength. This is also congruent with the high tensile properties for this regime, which also absorbs more energy before fracture resulting in high fracture toughness properties. HT1 values displayed in the graph exhibit higher fracture toughness values in comparison with HT2. This is because the HT1 material has a higher hardness, but the tempering process increased ductility and maintained good

fracture toughness. HT2 exhibited the lowest fracture toughness values, showing that the material furnace cooling process during heat treatment resulted in a coarse microstructure. According to the CCT phase diagram, the slow cooling rate promoted the formation of a bainitic-pearlitic microstructure, which has a limited ability to arrest crack propagation effectively, thus lowering the fracture toughness of the material. The fracture surface complexities observed for HT2 suggested mixed failure modes rather than just the expected cleavage.

REGIME	TEST 1 $(MPa\sqrt{m})$	TEST 2 $(MPa\sqrt{m})$	TEST 3 $(MPa\sqrt{m})$	AVERAGE $(MPa\sqrt{m})$
AR	109.78	124.32	101.95	112.02
HT1	107.44	108.92	106.53	107.63
HT2	45.64	43.95	41.29	43.63

Table 33: Fracture toughness values obtained for AR0, HT1 & HT2

We can safely conclude that the material displays the highest fracture toughness in its as received state, suggesting the good material integrity. The balanced microstructure in the AR condition allows the material to resist crack propagation to fracture, which is a crucial property for the material when subjected to fatigue or mechanical loads. The HT1 condition shows good fracture toughness as well, indicating that the tempering process restored some ductility and balance to the hardness and toughness of the material. Lastly HT2 showed the lowest fracture toughness by a considerable margin, meaning that the microstructure that resulted from the furnace cooling and the mixed failure modes had the least resistance to crack propagation.

4.5 SPTs

4.5.1 Analysis Procedure/Method

Upon completion of heat treatment of the material cylindrical rods, the specimens were wire cut and ground to the desired thickness as mentioned in the previous chapters. These samples were then polished and speckled to prepare for the concurrent punch displacement and the DIC deflection experiments. The rate of the testing was at 2 mm/min, and the SPT and DIC software and interfaces were used to carry out and record the test. The DIC cameras also captured the deflection from the top surface, until the end of the experiment which was the failure of the specimen. Various methods illustrated by the CWA, Janca et al. and Hahner et al. [7], [24], [31], [38], were adopted to characterise and quantify the mechanical properties obtained from the SPT.

4.5.2. Results Obtained

4.5.2.1 As Received Results

Figure 84 shows load against the displacement of the punch during the test for the AR specimens. The graph highlights the similarity of the mechanical properties obtained during the test, as the specimens had a similar range of results for maximum load and displacements.

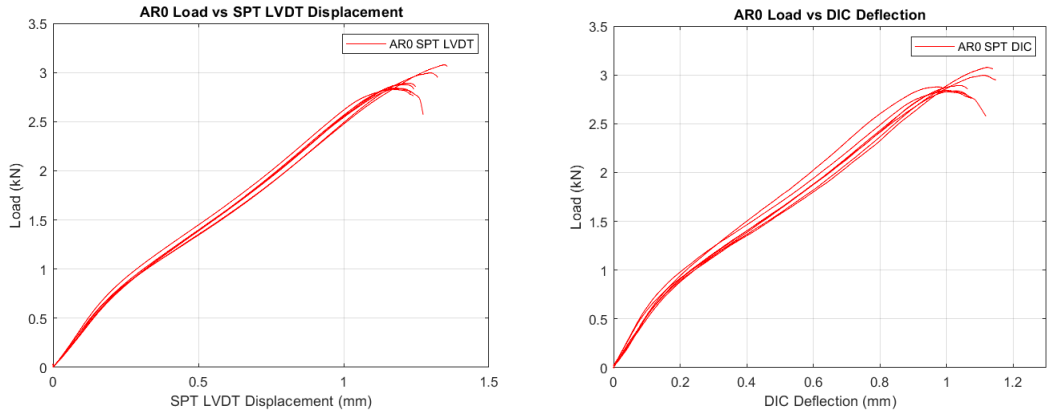

Figure 84: Graphs of Load vs SPT Punch displacement and Load vs SPT DIC deflection for AR tests

Figure 84 also shows load vs deflection for the AR specimens using the DIC camera and the curves have similarities as expected. Both the deflection and the displacement graphs can be plotted on the same axis to highlight the differences in the observations. **Figure 85** shows an image of the specimen in the SPT rig captured by DIC camera. This allowed us to obtain the deflection values as shown above, but also a step-by-step image capture until specimen fracture. As the test carried on, the Istra 4D software captured the images and highlighted the deflection profile as seen in **Figure 86** and **Figure 87**.

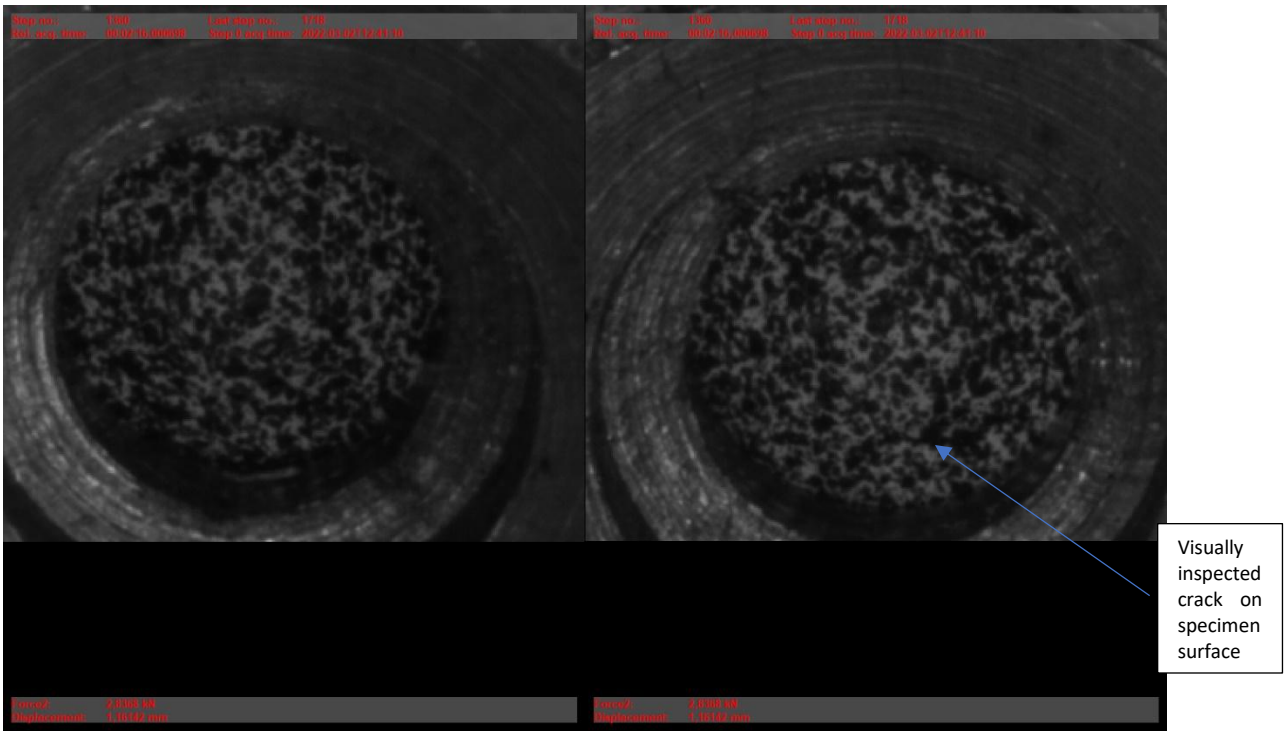

Figure 85: Figure obtained from DIC software: AR specimen in SPT rig during test with visually identified crack

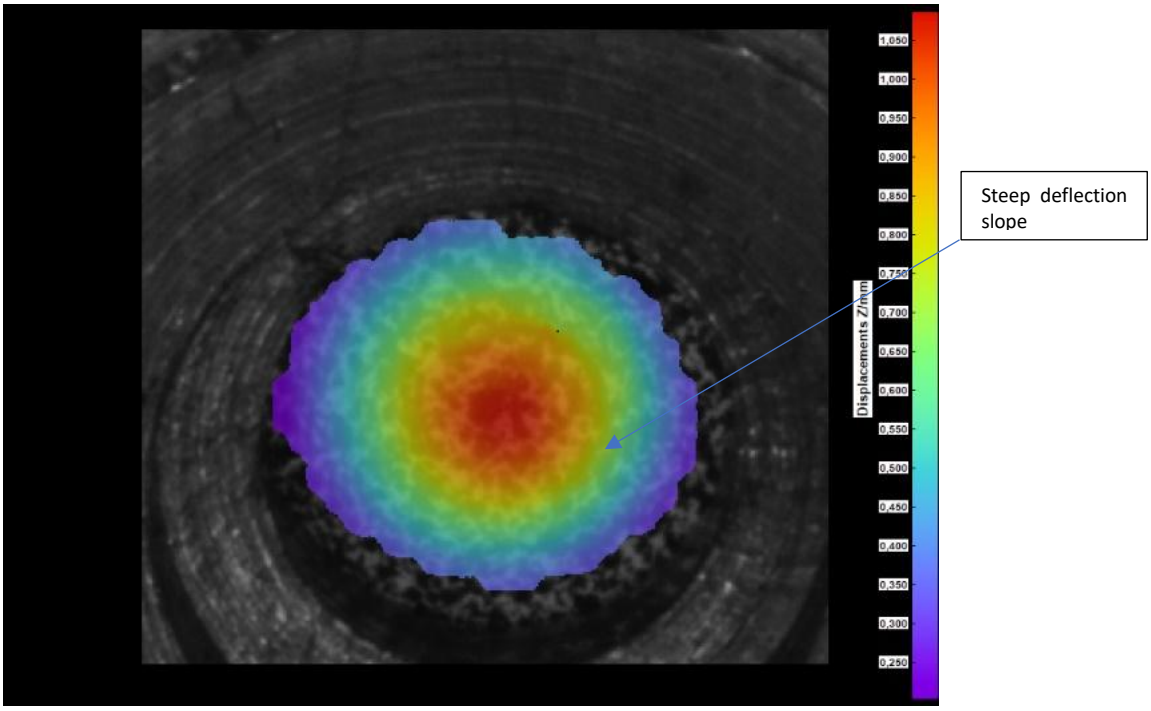

Figure 86: Figure obtained from DIC software: AR specimen deflection profile during test

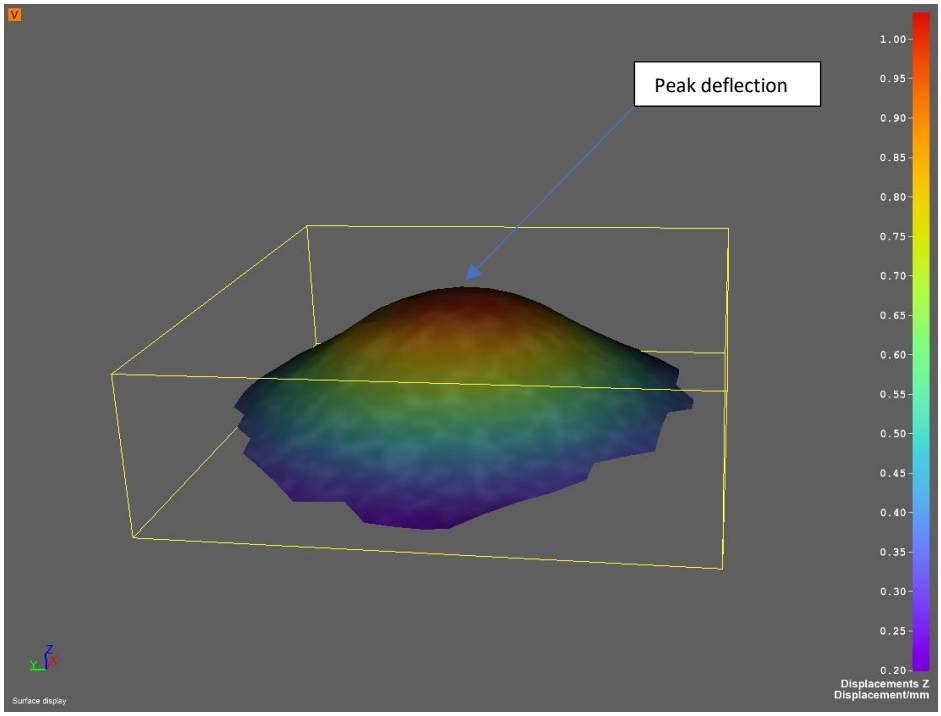

Figure 87: Figure obtained from DIC software: 3D rendering of AR specimen under test

The out-of-plane deflection profile in **Figure 87** showed peak deflection in the centre of the specimen translating to the punch contact being in a similarly central position. The steep deflection slope from the illustration in **Figure 86** showed the nonuniform deformation and highlighted the possible material fracture region, confirming the visually inspected crack shown in **Figure 85**. The DIC also tracked the maximum surface principal engineering strain, which was used to determine the SED evolution during the test and a more robust crack initiation identification.

In **Figure 88**, both load against displacement and load against deflection on selected tests were plotted on the same axis. The load values can be seen to be similar between the two graphs, but the deflection (DIC) values were lower than the displacement (LVDT) values. This was mainly because of the uneven deformation on the two sides of the specimen being tested [46].

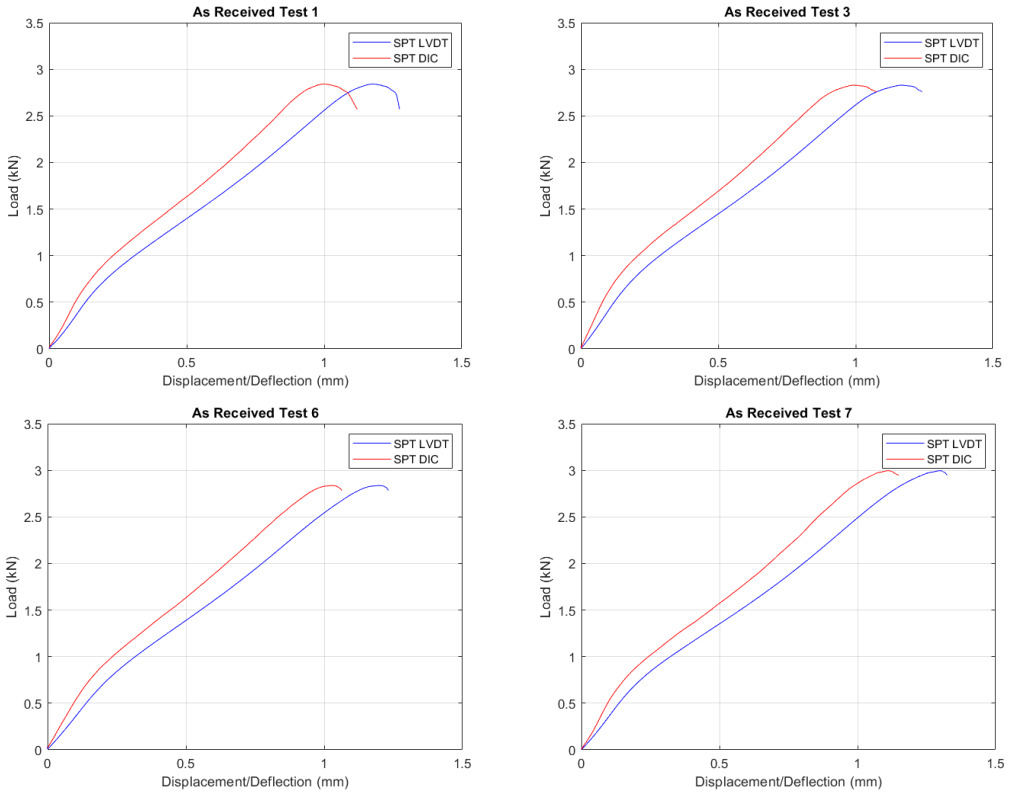

Figure 88: Graph of Load vs Displacement (LVDT) and Load vs Deflection (DIC) on same axes for AR tests

The maximum load values ranged from 2.83 kN to 3.08 kN, which can be seen as a consistent failure loading for the AR specimens because of the short range. Deflection for the SPTs was found to range from 0.999 mm to 1.15 mm and the displacement from 1.23 mm to 1.36 mm, showing a consistency in the testing as there is a minimal variation in the overall displacement and deflection values across the tests. These results also display the material property consistency, the predictability and reproducibility of the test under the same conditions.

4.5.2.1.1 Janca et al. Analysis

Characterisation of elastic to plastic transition (Yield Strength)

According to Janca et al. [31], the SP test results obtained from the LDC could be analysed further, allowing the calculation of the yield and the ultimate tensile strength of the material. The paper showed how to relate the SPT measured data to the various deformation processes observed as the specimens were being loaded. Specimen deflection obtained from the DIC camera and the LVDT displacement were both independent and uniform variables [31]. Against time increments, data obtained from the two independent displacement sensors was compared during tests. The evolution of specimen deflection against specimen displacement (DIC vs LVDT) can be seen in **Figure 89**, where deflection evolves non-uniformly and in a curved manner. The 1:1 line is the quadrant axis as established.

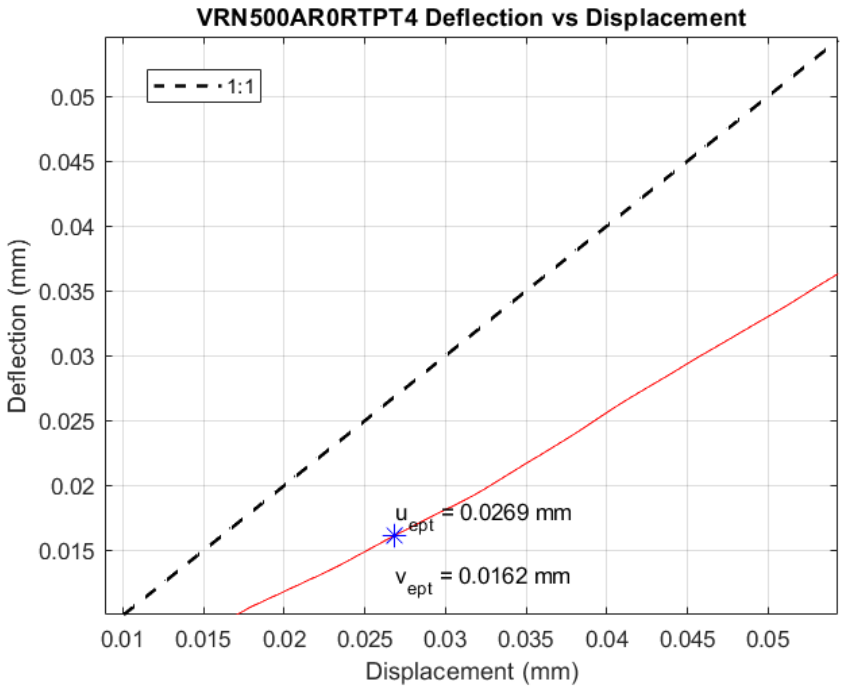

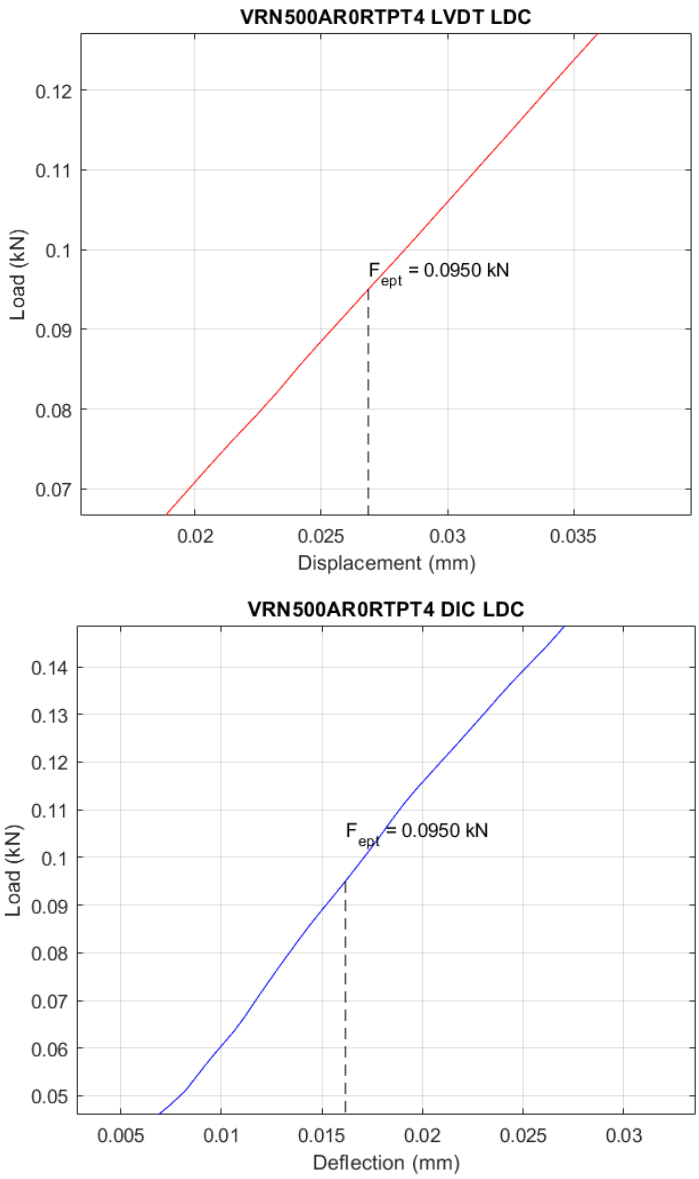

Figure 89: Graphs of specimen deflection (DIC) vs displacement (LVDT) and F_{ept} determination for AR tests

As seen in **Figure 89**, the elastic to plastic transition load characteristic, F_{ept}, was determined at the deflection point of maximal curvature (u_{ept}, v_{ept}), in accordance with the literature. This point was established as the point where the initial approximately linear phase of the DIC vs LVDT plot bends to another approximately linear phase of the plot. This point represented the change in direction of said linear phases and was then relatable to the elastic to plastic transition [31].

As established in the literature, Janca et al. [31] also introduced a more reliable method to characterise the elastic to plastic transition by comparing the area under the LDC, A, with its compliment A_c, above the curve. Since the area under the LDC is equal to the

energy (A = E_{SP}), this method was dubbed the 'energetic criterion' and was used to find the load point $F_{e1.5}$ as elaborated in section **2.5.2.1.2**. **Figure 90** shows the energetic criterion being used to find the load point.

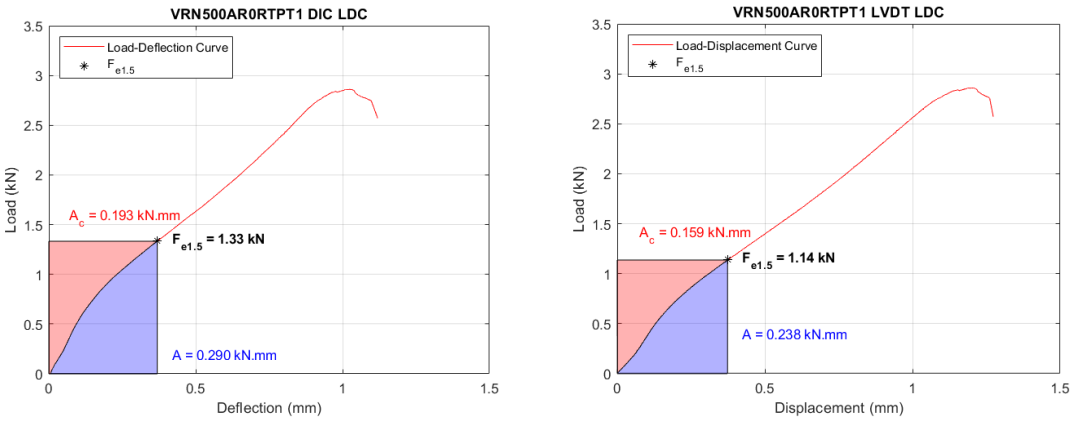

Figure 90: Graph of $F_{e1.5}$ in LDC for deflection and displacement for AR tests

Table 34 details the results obtained for the characterisation of the elastic to plastic transition of the two methods adopted from Janca et al. [31]. Assessment for the elastic to plastic transition (ept) displacement, u_{ept} and deflection, v_{ept} was found to range from 0.0243 mm to 0.0284 mm and 0.012 mm to 0.0186 mm respectively. The values for the load points F_{ept} were however the same, as the displacement and deflection values corresponded to the same load values for the two LDCs. These values ranged from 0.0872 kN to 0.095 kN and averaged 0.0915 kN. The load point $F_{e1.5}$ was also obtained for the tests and tabulated, ranging from 1.1 kN to 1.19 kN for the LVDT related experiments and 1.29 kN to 1.43 kN for the DIC related experiments.

SPT EXPERIMENT	h_0 (mm)	u_{ept}/v_{ept} (mm)		F_{ept} LVDT/DIC (kN)	$F_{e1.5}$ (kN)	
		LVDT (u)	DIC (v)		LVDT	DIC
VRN5000AR0RTPT1	0.51	0.0284	0.0178	0.0914	1.14	1.33
VRN5000AR0RTPT2	0.49	0.0266	0.0120	0.0923	1.10	1.29
VRN5000AR0RTPT3	0.50	0.0243	0.0120	0.0912	1.19	1.38
VRN5000AR0RTPT4	0.50	0.0269	0.0162	0.0950	1.12	1.32
VRN5000AR0RTPT5	0.50	0.0258	0.0146	0.0872	1.12	1.43
VRN5000AR0RTPT6	0.50	0.0267	0.0152	0.0913	1.13	1.33
VRN5000AR0RTPT7	0.50	0.028	0.0186	0.0920	1.10	1.29
AVERAGE	**0.50**	**0.0267**	**0.0152**	**0.0915**	**1.13**	**1.34**

Table 34: Results for load points F_{ept} and $F_{e1.5}$ for AR tests

Characterisation of strength

To categorize strength, Janca et al. [31] introduced further analysis of the LDC. The introduction of the concept of thinning was used to assess the data obtained from the tests. As mentioned in the literature, the values obtained from the two displacement sensors were to be theoretically equal, but due to the uneven deformation on the two sides of the specimen, the deflection (DIC) and the displacement (LVDT) differed slightly [46]. **Figure 91** shows the thinning effect against the displacement and the subsequently obtained load points on selected tests.

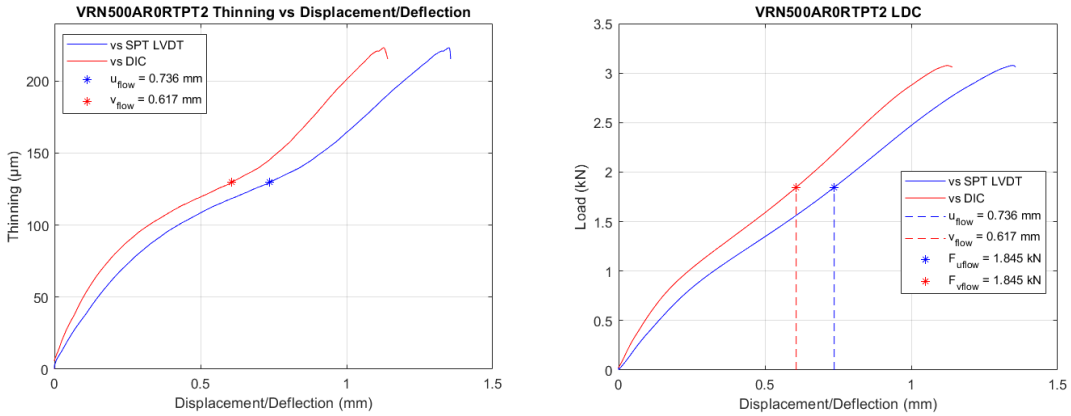

Figure 91:Graph of Thinning vs Displacement/Deflection and Load vs Thinning displacement (u_{flow} v v_{flow}) for AR tests

The point of maximal curvature in the thinning curve was obtained numerically using **Equation 15**. This allowed the attainment of the values for either u_{flow} or v_{flow}. The load point F_{flow} corresponding with the convex knee of the thinning vs displacement/deflection curve could now be obtained and recorded as seen above.

Another phenomenon introduced by Janca et al. [31] to characterise strength is the load point F_{infl} derived from the second inflection point of the load-deflection curve. These inflection points could also be analytically obtained [46], and the LDC obtained in these tests all could derive the load point F_{infl}.

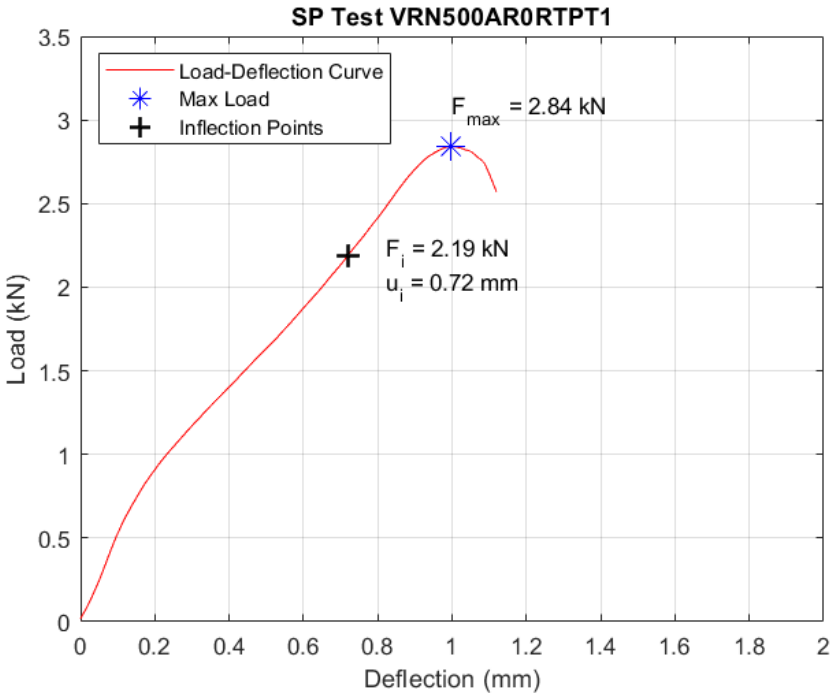

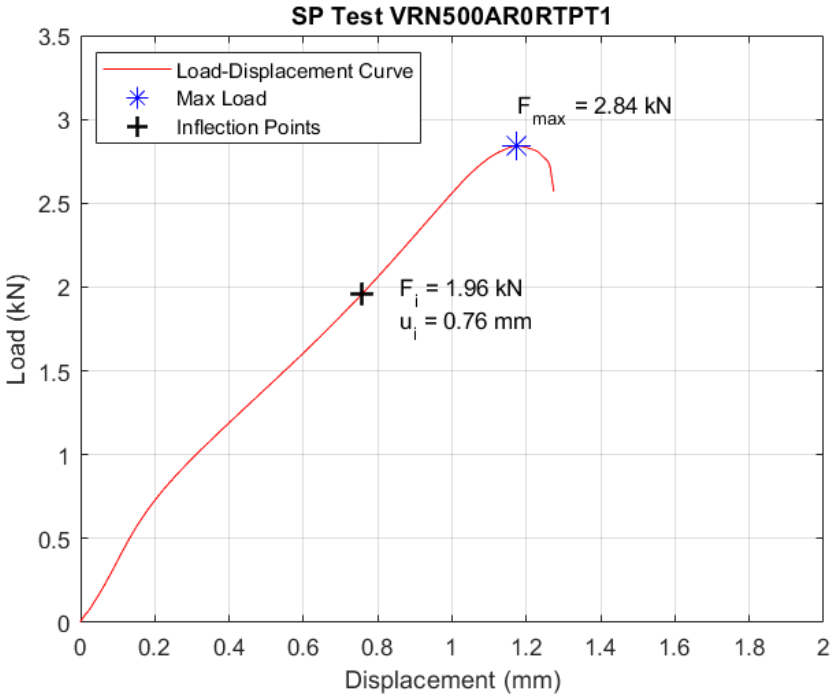

Figure 92: Graph of F_{infl} on deflection and displacement curves for AR tests

Table 35 shows results obtained from the proposed strength characterisation methods above. As can be seen, the values for F_{flow} ranged from 1.81 kN to 2.15 kN for both the LDCs. The values for the load points were similar as the thinning values for the convex knee of each DIC and corresponding LVDT curves were found to be equal.

SPT EXPERIMENT	h_0 (mm)	u_{infl}/v_{infl} (mm)		F_{infl} (kN)		u_{flow} (mm)	v_{flow} (mm)	F_{flow} (kN)	
		LVDT (u)	DIC (v)	LVDT	DIC			LVDT	DIC
VRN5000AR0RTPT1	0.51	0.76	0.72	1.96	2.19	0.722	0.601	1.88	1.88
VRN5000AR0RTPT2	0.49	0.91	0.80	2.26	2.38	0.736	0.617	1.85	1.85
VRN5000AR0RTPT3	0.50	0.83	0.72	2.20	2.26	0.666	0.546	1.81	1.81
VRN5000AR0RTPT4	0.50	0.76	0.74	1.98	2.27	0.752	0.629	1.96	1.96
VRN5000AR0RTPT5	0.50	0.78	0.63	2.00	2.10	0.820	0.627	2.11	2.11
VRN5000AR0RTPT6	0.50	0.81	0.67	2.08	2.05	0.703	0.580	1.83	1.83
VRN5000AR0RTPT7	0.50	0.88	0.66	2.18	1.95	0.863	0.734	2.15	2.15
AVERAGE	**0.50**	**0.82**	**0.71**	**2.09**	**2.17**	**0.752**	**0.619**	**1.94**	**1.94**

Table 35: Results for load points F_{infl} and F_{flow} for AR tests

From **Table 35**, the values for F_{infl} ranged in a similar region of 1.96 kN to 2.26 kN for the displacement (LVDT) experiments and for the deflection (DIC) experiments ranged from 1.95 kN to 2.38 kN. The average values obtained for both F_{infl} for deflection and displacement were 2.09 kN and 2.17 kN respectively, which were load values that were not significantly different.

The load points from **Table 35** were then used with **Equation 16** and **Equation 19** to obtain the ultimate tensile correlation function values for the specimens. The results from these calculations were tabulated in **Table 36**, highlighting the mechanical properties of the AR material in accordance with the Janca et al. [31] methodology.

LVDT EXPERIMENT	YIELD STRESS F_{ept}/h_0^2 (MPa)	YIELD STRESS $F_{e1.5}/h_0^2$ (MPa)	UTS $F_{infl}/h_0 \cdot u_{infl}$ (MPa)	UTS $F_{flow}/h_0 \cdot u_{flow}$ (MPa)
AR0RTPT1	351.40	4382.93	5056.76	5105.64
AR0RTPT2	384.42	4581.42	5068.40	5115.91
AR0RTPT3	364.80	4760.00	5301.20	5435.44
AR0RTPT4	380.00	4480.00	5210.53	5210.11
AR0RTPT5	348.80	4480.00	5128.21	5139.02
AR0RTPT6	365.20	4520.00	5135.80	5214.79
AR0RTPT7	368.00	4400.00	4954.55	4982.62
AVERAGE	**366.09**	**4514.91**	**5122.21**	**5171.93**

Table 36: Results for F_{ept}/h_0^2, $F_{e1.5}/h_0^2$, $F_{infl}/h_0 \cdot u_{infl}$ and $F_{flow}/h_0 \cdot u_{flow}$ for AR LVDT experiments

As seen in **Table 36** with LVDT displacement data, the average yield stress correlation function from the F_{ept} load point, F_{ept}/h_0^2, was found to be 366 MPa and that from the energy criterion, $F_{e1.5}/h_0^2$, was 4515 MPa. The F_{infl} induced average UTS correlation function, $F_{infl}/h_0 \cdot u_{infl}$, was found as 5122 MPa and the F_{flow} calculated average UTS correlation function, $F_{flow}/h_0 \cdot u_{flow}$, was found to be 5172 MPa.

DIC EXPERIMENT	YIELD STRESS F_{ept}/h_0^2 (MPa)	YIELD STRESS $F_{e1.5}/h_0^2$ (MPa)	UTS $F_{infl}/h_0 \cdot v_{infl}$ (MPa)	UTS $F_{flow}/h_0 \cdot v_{flow}$ (MPa)
AR0RTPT1	519.03	5113.42	5964.05	6133.57
AR0RTPT2	737.19	5372.76	6071.43	6102.60
AR0RTPT3	664.00	5520.00	6277.78	6630.04
AR0RTPT4	584.00	5280.00	6135.14	6228.93
AR0RTPT5	524.00	5720.00	6666.67	6720.89
AR0RTPT6	616.00	5320.00	6119.40	6320.69
AR0RTPT7	516.00	5160.00	5909.09	5858.31
AVERAGE	**594.32**	**5355.17**	**6163.36**	**6285.01**

Table 37: Results for F_{ept}/h_0^2, $F_{e1.5}/h_0^2$, $F_{infl}/h_0 \cdot v_{infl}$ and $F_{flow}/h_0 \cdot v_{flow}$ for AR DIC experiments

From **Table 37** with DIC deflection data, the average yield stress correlation function from the F_{ept} load point was found to be 594 MPa and that from the energy criterion was 5355 MPa. The F_{infl} induced UTS correlation function, $F_{infl}/h_0 \cdot v_{infl}$, was found at an average of 6163 MPa and the F_{flow} calculated UTS correlation function, $F_{flow}/h_0 \cdot v_{flow}$, was found to be averaged at 6285 MPa.

These values obtained through the Janca et al. [31] methodology could now be used in the correlation with the conventional mechanical tests in the upcoming chapters of this dissertation.

4.5.2.1.2 CWA Analysis

Figure 93 shows the SP test results on selected tests with respect to the CWA analytical method. With this method both the yield and ultimate tensile strength of the material could be obtained. The method also allowed the small punch fracture energy, the area under the curve up to the displacement or deflection on fracture/failure onset at maximum load, to be established as well. As explained in the literature and previous sections, for determination of the load point F_e of the DIC deflection curve, F(v), a bilinear function was fitted on the deflection curve. Likewise, a trilinear function was fitted on the LVDT displacement curve, F(u), to establish the subsequent load point F_e [24], [38].

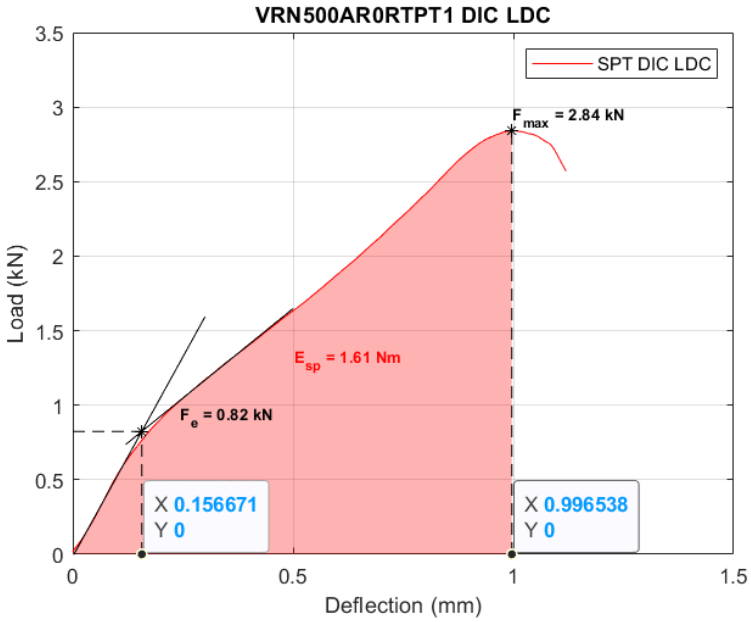

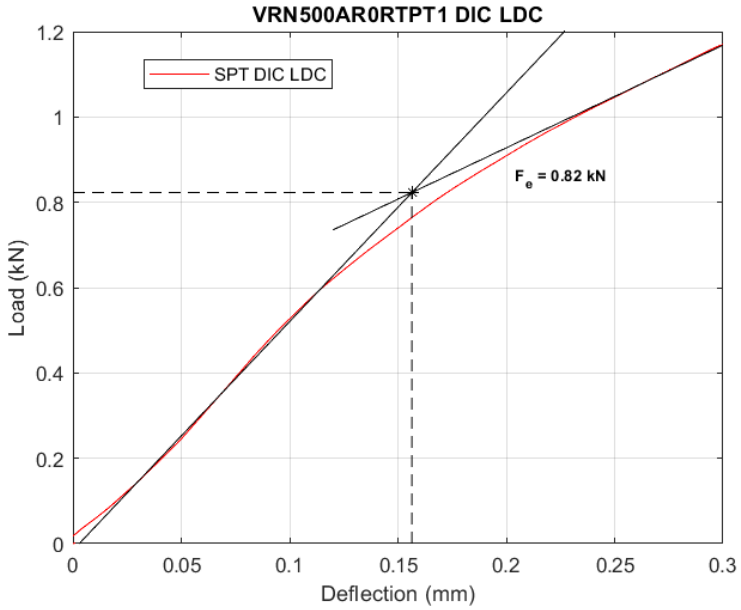

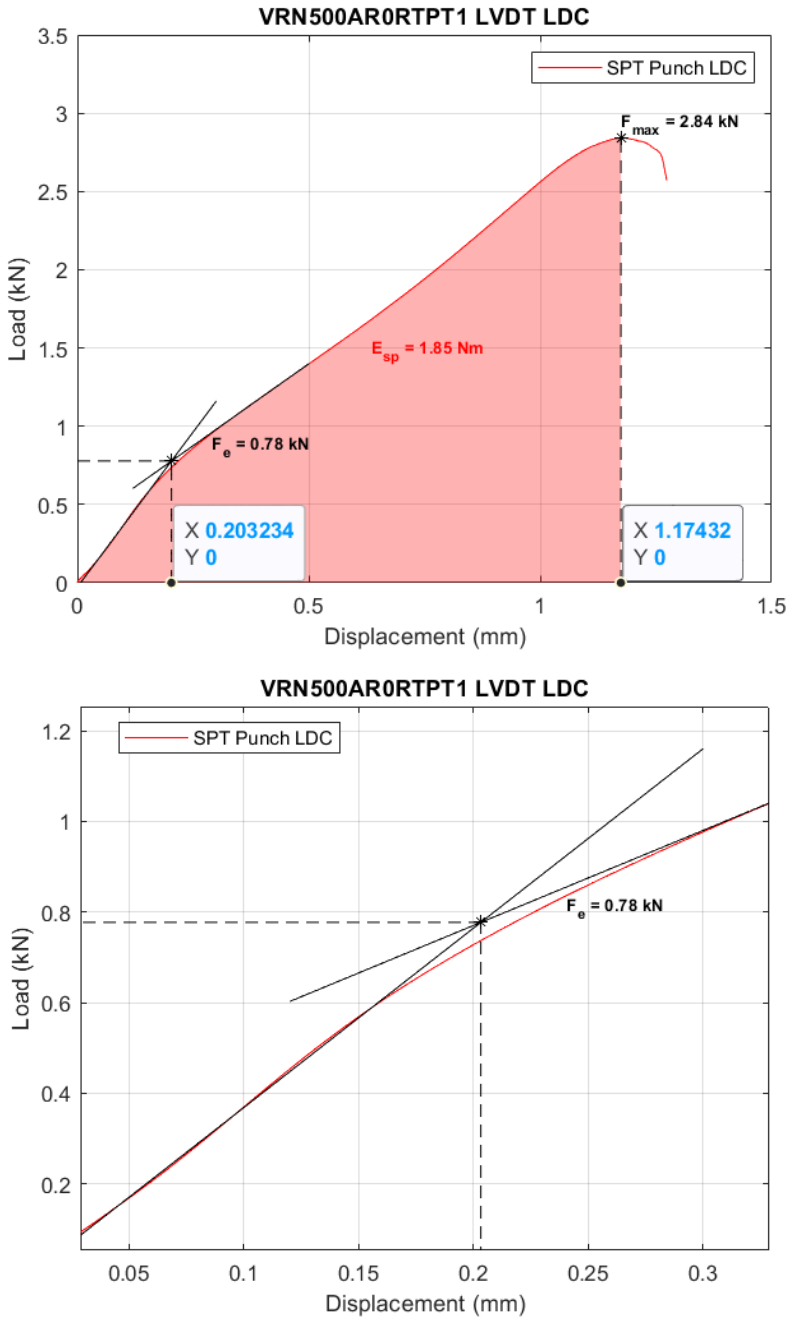

Figure 93: Graphs for determination of F_e, F_m and E_{SP} for DIC deflection (v) and LVDT displacement (u) for AR tests

Table 38 shows results obtained from the displacement graphs in accordance with the CWA Analysis for the attainment of the elastic to plastic transition load point (F_e, u_e) for LVDT displacement. It can be observed that the yield displacement averaged at 0.234 mm. The load points ranged from 0.78 kN to 0.90 kN and averaged at 0.84 kN. The table also includes results obtained from the displacement graphs above where the value of the maximum point (F_m, u_m) was identified. The maximum loads ranged from 2.83 kN to 3.08

kN and averaged at 2.91 kN, with the maximum displacement averaging at 1.23 mm. The SP fracture energy (E_{SP}) was found to range from 1.85 J to 2.35 J and averaged at 2.01 J. The small margins for these parameters obtained from the test shows the consistency in the material properties tested as well as the repeatability of the test method.

LVDT EXPERIMENT	h_0 (mm)	YIELD DISPLACEMENT u_e (mm)	YIELD LOAD F_e (kN)	MAX DISPLACEMENT u_m (mm)	MAX LOAD F_m (kN)	SMALL PUNCH ENERGY E_{SP} (J)
AR0RTPT1	0.51	0.203	0.78	1.174	2.84	1.85
AR0RTPT2	0.49	0.227	0.82	1.346	3.08	2.31
AR0RTPT3	0.50	0.232	0.90	1.164	2.83	1.88
AR0RTPT4	0.50	0.244	0.85	1.221	2.89	1.98
AR0RTPT5	0.50	0.248	0.86	1.210	2.88	1.94
AR0RTPT6	0.50	0.247	0.86	1.199	2.84	1.91
AR0RTPT7	0.50	0.239	0.84	1.299	3.00	2.17
AVERAGE	**0.50**	**0.234**	**0.84**	**1.230**	**2.91**	**2.01**

Table 38: Results of F_e, F_m and E_{SP} for AR LVDT displacement (u) tests

For the DIC deflection, the results for the attainment of the elastic to plastic transition load point (F_e, v_e), maximum load (F_m, v_m) and the small punch fracture energy (E_{SP}) were tabulated in **Table 39**. It can be observed that the yield deflection was averaging at 0.315 mm. The second test was an anomaly in the attainment of the yield deflection, as the value was higher than the rest at 1.16 mm. This could be attributed to the elastic to plastic transition occurring at a delayed point in the test. The surface condition of the specimen could have had the presence of surface defects affecting the material's response to loading, thus resulting in an anomaly yield point. However, there was similarity in all the yield loads, with yield load points ranging from 0.82 kN to 0.94 kN and averaging at 0.88 kN.

The maximum loads on the other hand ranged from 2.83 kN to 3 kN and averaged at 2.91 kN, with the maximum displacement averaging at 1.04 mm. The SP fracture energy was found to range from 1.61 J to 1.97 J and averaged at 1.74 J. The margins for these parameters obtained from the test also show the consistency in the material properties tested except for the second test where the value of the yield deflection was higher.

DIC EXPERIMENT	h_0 (mm)	YIELD DEFLECTION v_e (mm)	YIELD LOAD F_e (kN)	MAX LOAD DEFLECTION v_m (mm)	MAX LOAD F_m (kN)	SMALL PUNCH ENERGY E_{SP} (J)
AR0RTPT1	0.51	0.157	0.82	0.9970	2.84	1.61
AR0RTPT2	0.49	1.16	0.85	1.123	3.08	1.97
AR0RTPT3	0.50	0.168	0.94	0.9910	2.83	1.66
AR0RTPT4	0.50	0.187	0.88	1.039	2.89	1.73
AR0RTPT5	0.50	0.175	0.90	0.9720	2.88	1.64
AR0RTPT6	0.50	0.178	0.88	1.029	2.84	1.70
AR0RTPT7	0.50	0.181	0.88	1.112	3.00	1.90
AVERAGE	**0.50**	**0.315**	**0.88**	**1.038**	**2.91**	**1.74**

Table 39: Results of F_e, F_m and E_{SP} for AR DIC deflection (v) tests

With the results of the load points that were necessary in the calculations according to the CWA method, the yield and the ultimate tensile stresses could now be estimated. **Table 40** contains the stress values calculated from the obtained values for the displacement (LVDT).

LVDT EXPERIMENT	YIELD STRESS F_e/h_0^2 (MPa)	UTS $F_m/h_0 \cdot u_m$ (MPa)	SMALL PUNCH ENERGY E_{SP} (J)
AR0RTPT1	2998.85	4743.29	1.85
AR0RTPT2	3415.24	4669.92	2.31
AR0RTPT3	3600.00	4862.54	1.88
AR0RTPT4	3400.00	4733.82	1.98
AR0RTPT5	3440.00	4760.33	1.94
AR0RTPT6	3440.00	4737.28	1.91
AR0RTPT7	3360.00	4618.94	2.17
AVERAGE	**3379.16**	**4732.30**	**2.01**

Table 40: Results for F_e/h_0^2, $F_m/h_0 \cdot u_m$ and E_{SP} for AR LVDT experiments

As seen in **Table 40**, the yield stress correlation function, F_e/h_0^2, averaged at 3379 MPa and the UTS function, $F_m/h_0 \cdot u_m$, at 4732 MPa for the displacement assessments (LVDT). These values were in a similar range for all the tests, a good indication of the repeatability of the test process and material property consistency. **Table 41** contains the yield stress and UTS values obtained for the deflection assessments (DIC).

DIC EXPERIMENT	YIELD STRESS F_e/h_0^2 (MPa)	UTS $F_m/h_0 \cdot v_m$ (MPa)	SMALL PUNCH ENERGY E_{SP} (J)
AR0RTPT1	3152.63	5585.38	1.61
AR0RTPT2	3540.19	5597.25	1.97
AR0RTPT3	3760.00	5711.40	1.66
AR0RTPT4	3520.00	5563.04	1.73
AR0RTPT5	3600.00	5925.93	1.64
AR0RTPT6	3520.00	5519.92	1.70
AR0RTPT7	3520.00	5395.68	1.90
AVERAGE	**3516.12**	**5614.09**	**1.74**

Table 41: Results for F_e/h_0^2, $F_m/h_0 \cdot v_m$ and E_{SP} for AR DIC experiments

Table 41 shows that the deflection graph values and data gave us the yield stress estimation, F_e/h_0^2, averaging at 3516 MPa and the UTS estimation, $F_m/h_0 \cdot v_m$, averaging at 5614 MPa. As expected, these estimation values were higher than those for the LVDT experiments as the deflection values were less than the displacement values during the tests and the maximum load points were the same.

4.5.2.1.3 Hahner et al. Analysis

Figure 94 shows the SP test results on selected tests in accordance with Hahner et al.'s [7] analytical approach. As mentioned in the literature, this method allowed the yield strength to be obtained based on the curvature of the load-displacement/deflection curve instead of a single load point [7]. **Figure 94** shows the illustration of the quantification of the curvature for the displacement (LVDT) and deflection (DIC) curves at the three distinct offset points in accordance with the Hahner et al. method.

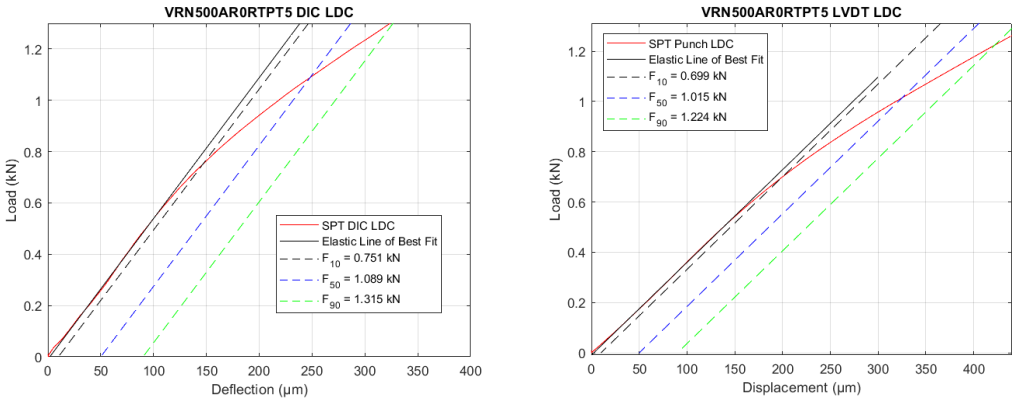

Figure 94: Figure of curvature quantification at three offsets i.e., 10 µm, 50 µm and 90 µm (DIC deflection and LVDT displacement)

The loads at the distinct offset points on the curves enabled the attainment of the yield stress estimation. **Table 42** shows results obtained from the displacement graphs as shown in **Figure 94**. The curvature K values were determined from the established load points (F_{10}, F_{50} and F_{90}) using **Equation 22** and were found to all be less than the limit of 0.33 specified in the literature. This allowed the K-dependant yield coefficient and consequently the corresponding yield stress estimation to be obtained.

LVDT EXPERIMENT	h_0 (mm)	YIELD LOAD F_{10} (kN)	YIELD LOAD F_{50} (kN)	YIELD LOAD F_{90} (kN)	CURVATURE K	YIELD STRESS σ_y (MPa)
AR0RTPT1	0.51	0.652	0.959	1.150	0.233	870.70
AR0RTPT2	0.49	0.651	0.914	1.079	0.229	879.68
AR0RTPT3	0.50	0.705	0.998	1.179	0.236	959.87
AR0RTPT4	0.50	0.734	1.041	1.254	0.181	705.32
AR0RTPT5	0.50	0.699	1.015	1.224	0.204	807.44
AR0RTPT6	0.50	0.748	1.049	1.254	0.190	758.83
AR0RTPT7	0.50	0.671	0.959	1.132	0.249	987.03
AVERAGE	**0.50**	**0.694**	**0.991**	**1.182**	**0.217**	**852.69**

Table 42: Results of offset loads F_{10}, F_{50}, F_{90}, curvature K and yield stress estimation σ_Y for AR LVDT tests

As shown in **Table 42**, the yield stress estimations ranged from 705 MPa to 987 MPa, averaging at 853 MPa for the LVDT experiments. The results showed the similarities of the material yield properties obtained highlighting the consistency in the assessment method deployed.

For the DIC experiments, the results were tabulated in **Table 43**. Likewise, the K values were determined from the load values (F_{10}, F_{50} and F_{90}) and were less than the 0.33 limit. The yield stress estimations averaged at 858 MPa for the DIC experiments. This yield value was similar to the yield value that was obtained in the LVDT analysis, showing more confidence in the material yield properties that were estimated.

DIC EXPERIMENT	h_0 (mm)	YIELD LOAD F_{10} (kN)	YIELD LOAD F_{50} (kN)	YIELD LOAD F_{90} (kN)	CURVATURE K	YIELD STRESS σ_y (MPa)
AR0RTPT1	0.51	0.714	1.024	1.206	0.260	1066.95
AR0RTPT2	0.49	0.699	0.941	1.096	0.219	856.36
AR0RTPT3	0.50	0.764	1.023	1.202	0.183	702.96
AR0RTPT4	0.50	0.794	1.072	1.268	0.173	683.66
AR0RTPT5	0.50	0.751	1.089	1.315	0.199	837.16
AR0RTPT6	0.50	0.795	1.058	1.240	0.182	723.62
AR0RTPT7	0.50	0.662	0.956	1.121	0.281	1138.55
AVERAGE	**0.50**	**0.740**	**1.023**	**1.207**	**0.214**	**858.47**

Table 43: Results of offset loads F_{10}, F_{50}, F_{90}, curvature K and yield stress estimation σ_Y for AR DIC tests

The results obtained from both **Table 42** and **Table 43** were now adopted in the later chapters of this dissertation to establish a correlation between the yield stress values from the conventional tensile test and the yield stress estimations from these SPT analyses.

4.5.2.1.4 DIC Crack Detection Analysis

As mentioned in section **2.5.3.1** in the literature, this method allowed the determination of the crack initiation point using the SED evolution. It was adopted to minimise the dependence on the subjective detection of the crack either through visual interpretation or through the discontinuity in the deflection data recorded during the test.

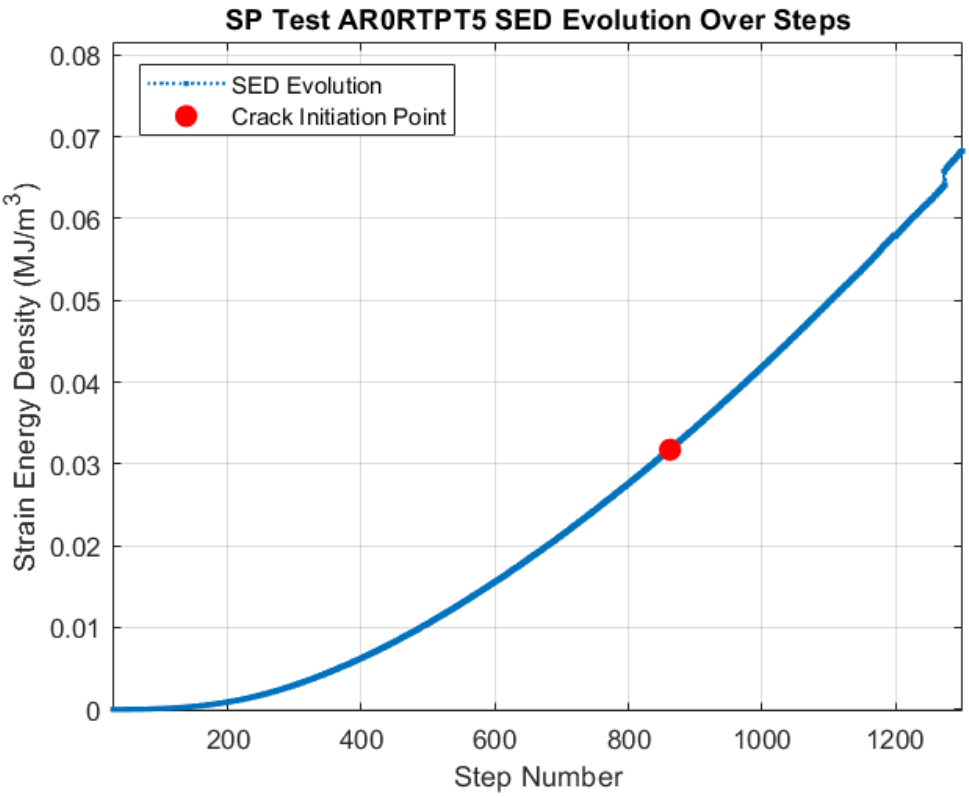

Figure 95: SED evolution for AR0RTPT5 over DIC system steps

Figure 95 shows the SED evolution for a selected test (AR0RTPT5). The crack was detected at step 862 in the test and this step translated to a deflection, v_{crack} of 0.59 mm and a displacement, u_{crack} of 0.78 mm and a load, F_{crack} of 1.99 kN. **Figure 96** and **Figure 97** show the LDC and the crack detection point.

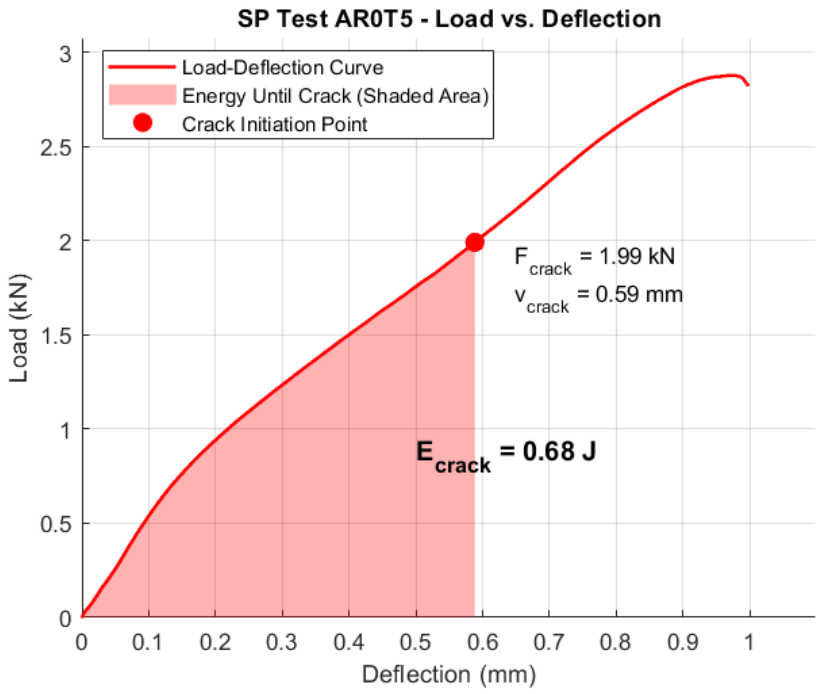

Figure 96: SPT AR0T5 DIC LDC with crack parameters v_{crack}, F_{crack} and E_{crack}

The area under the LDC up until the crack detection point was also evaluated. The small punch energy until crack detection, E_{crack}, was found to be 0.68 J and 0.85 J for the DIC deflection and the LVDT displacement graphs respectively.

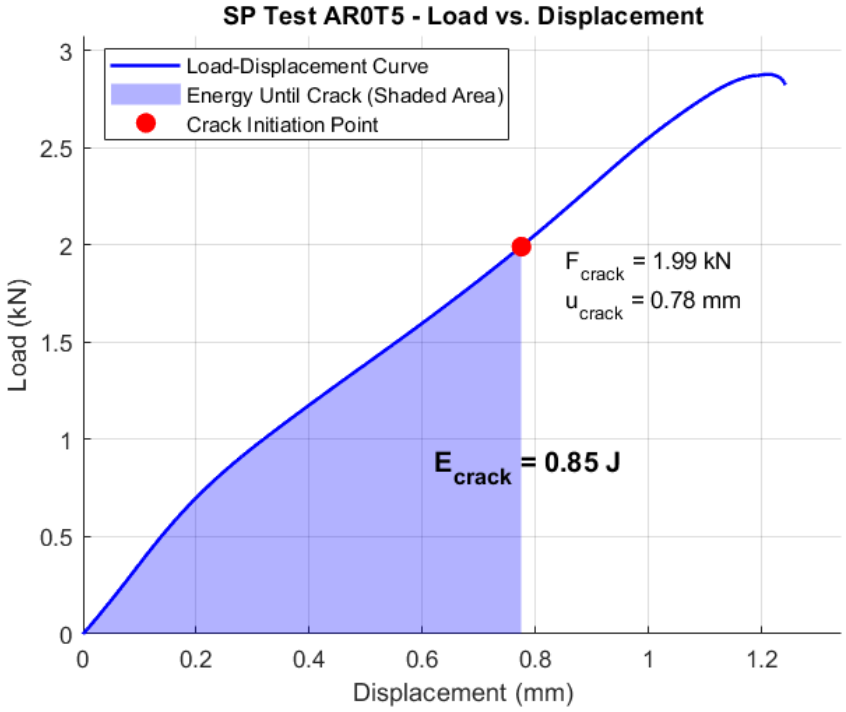

Figure 97: SPT AR0T5 LVDT LDC with crack parameters u_{crack}, F_{crack} and E_{crack}

The LVDT displacement test results were tabulated in **Table 44**. As seen in **Table 44**, the crack initiation load, F_{crack} ranged from 1.76 kN to 2.13 kN and averaged at 1.97 kN. The displacement at the crack detection point ranged from 0.65 mm to 0.84 mm at an average of 0.77 mm. The E_{crack} averaged at 0.84 J and ranged from 0.62 J to 0.97 J.

LVDT EXPERIMENT	h_0 (mm)	CRACK DISPLACEMENT u_{crack} (mm)	CRACK LOAD F_{crack} (kN)	CRACK ENERGY E_{crack} (J)
AR0RTPT1	0.51	0.78	2.01	0.87
AR0RTPT2	0.49	0.84	2.09	0.97
AR0RTPT3	0.50	0.80	2.13	0.96
AR0RTPT4	0.50	0.81	2.10	0.92
AR0RTPT5	0.50	0.78	1.99	0.85
AR0RTPT6	0.50	0.65	1.71	0.62
AR0RTPT7	0.50	0.70	1.76	0.70
AVERAGE	**0.50**	**0.77**	**1.97**	**0.84**

Table 44: Results of u_{crack}, F_{crack} and E_{crack} for AR LVDT displacement (u) tests

The DIC deflection test data was populated in **Table 45**, and exhibited the same crack initiation load, F_{crack} as the LVDT displacement tests. This is because the crack initiation step identified in the SED evolution had a single load value corresponding with the displacement and the deflection values at that instance. The deflection of the crack detection point averaged at 0.63 mm, a value lower than the displacement values as expected. The E_{crack} for the DIC deflection data was also lower than that of the LVDT displacement data, and was found to be ranging from 0.53 J to 0.86 J, averaged at 0.73 J.

DIC EXPERIMENT	h_0 (mm)	CRACK DEFLECTION v_{crack} (mm)	CRACK LOAD F_{crack} (kN)	CRACK ENERGY E_{crack} (J)
AR0RTPT1	0.51	0.65	2.01	0.76
AR0RTPT2	0.49	0.71	2.09	0.86
AR0RTPT3	0.50	0.67	2.13	0.84
AR0RTPT4	0.50	0.68	2.10	0.81
AR0RTPT5	0.50	0.59	1.99	0.68
AR0RTPT6	0.50	0.53	1.71	0.53
AR0RTPT7	0.50	0.58	1.76	0.60
AVERAGE	**0.50**	**0.63**	**1.97**	**0.73**

Table 45: Results of v_{crack}, F_{crack} and E_{crack} for AR DIC deflection (v) tests

4.5.2.1.5 Summary

The analytical methods applied in the assessment of the SPT through Janca et al. [31], the CWA [24], [38], Hahner et al. [7] and the DIC crack detection methods successfully characterised the yield, tensile strength and toughness properties of the AR condition. The data points obtained from these analytical formulations was used further in this dissertation to compare the outcomes and arrive at the relevant conclusions in validating and correlating the SPT to the mechanical tests.

4.5.2.2 Heat Treatment 1 Results

Figure 98 shows load vs displacement of the punch (LVDT) as well as the load against the DIC deflection for the HT1 tests that were carried out. There is consistency in the mechanical properties of the material regime as the curves obtained fall within similar load and displacement ranges.

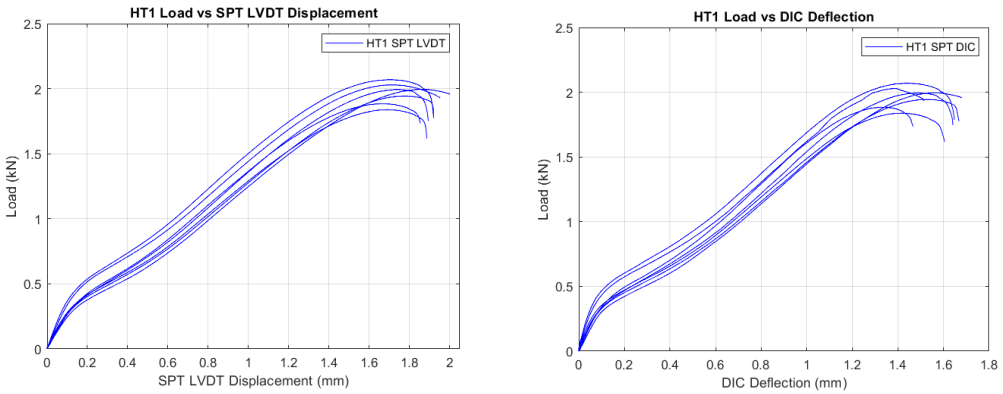

Figure 98: Graphs of Load vs SPT Punch displacement and Load vs SPT DIC deflection for HT1 tests

As established, the test specimens were mounted in the SPT rig for the test. The load against deflection graph was a result from the deflection sensing from the DIC camera as in the AR material tests. **Figure 99** shows an image captured by the DIC camera through the Istra4D software from one of the numerous step-by-step images that started from the SP test initiation leading up to specimen fracture and test completion.

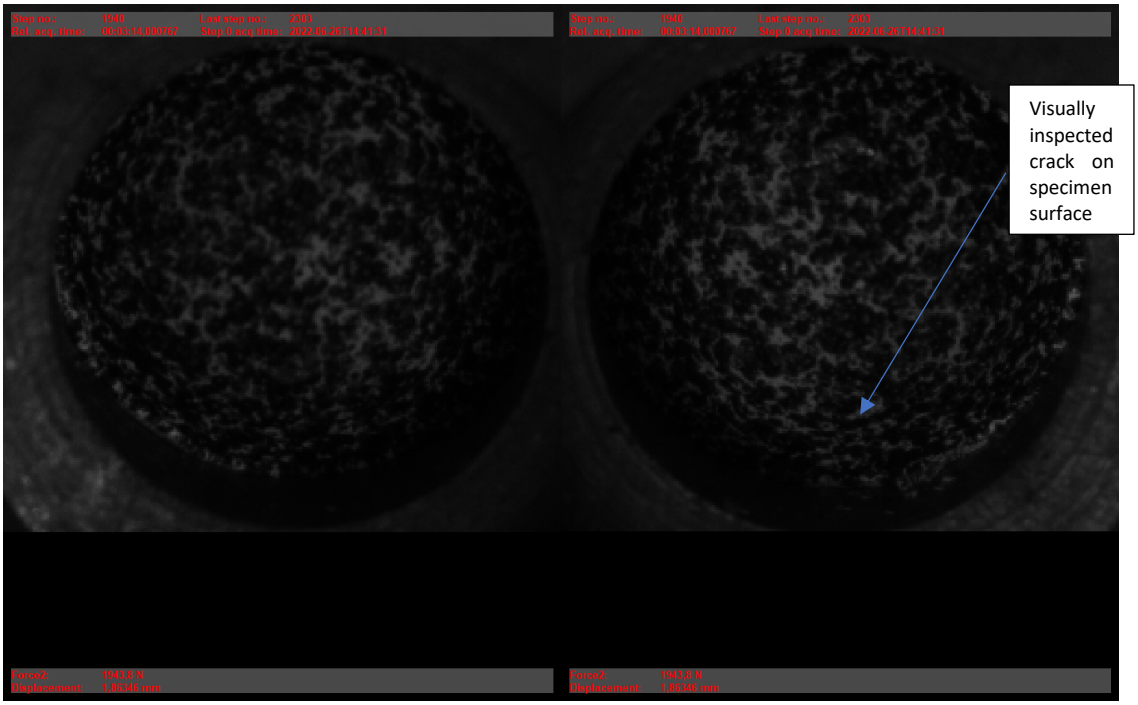

Figure 99: Figure obtained from DIC software: HT1 specimen in SPT rig during test

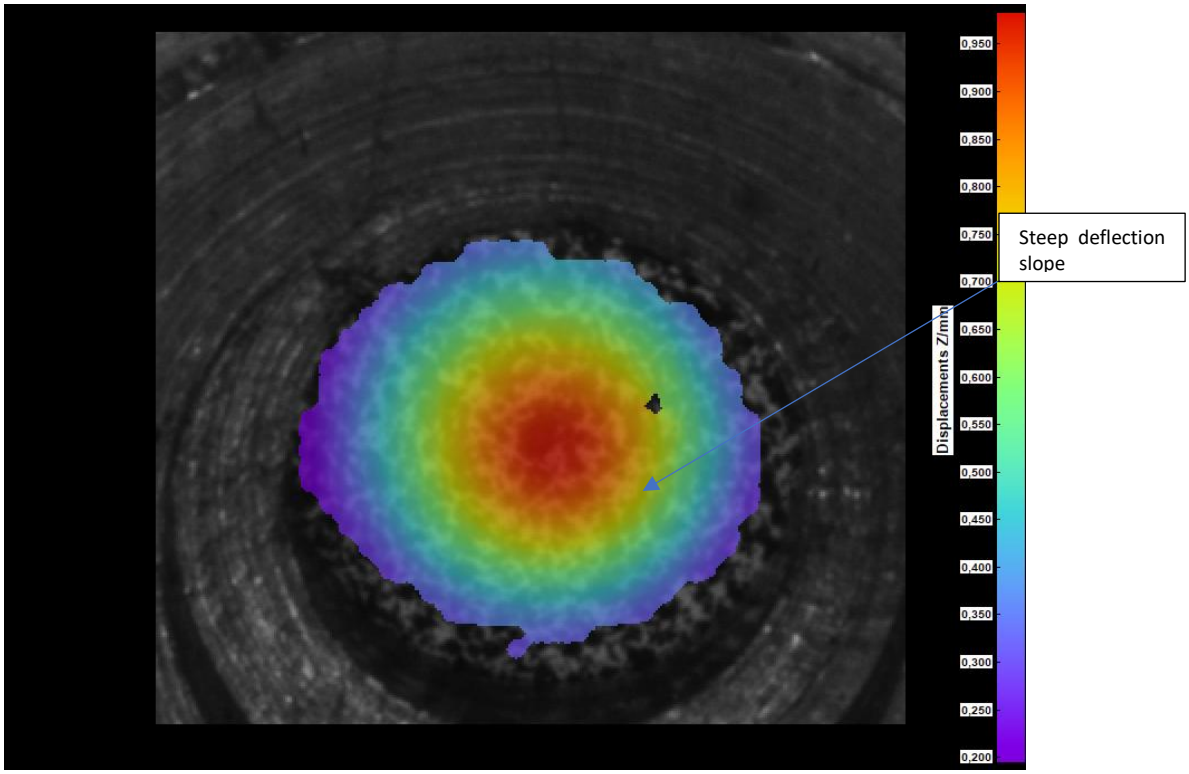

Figure 100: Figure obtained from DIC software: HT1 specimen deflection profile during test

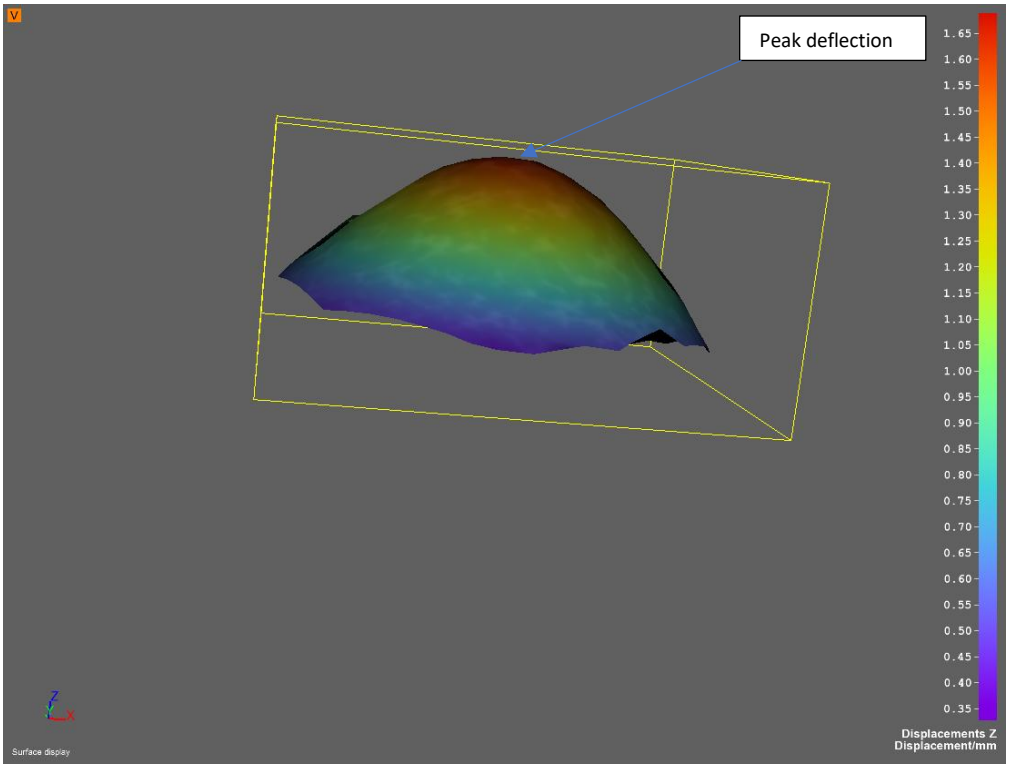

Figure 101: Figure obtained from DIC software: 3D rendering of HT1 specimen under test

Figure 101 shows the out-of-plane deflection profile that was obtained in the selected test. It can be seen that the specimen deformation exhibited the peak deflection at the centre of the specimen as expected because that region corresponded to the punch point of contact. The steeper slope of deflection also shows that deformation may not be perfectly uniform but shows a possible area of material failure as seen in **Figure 100**.

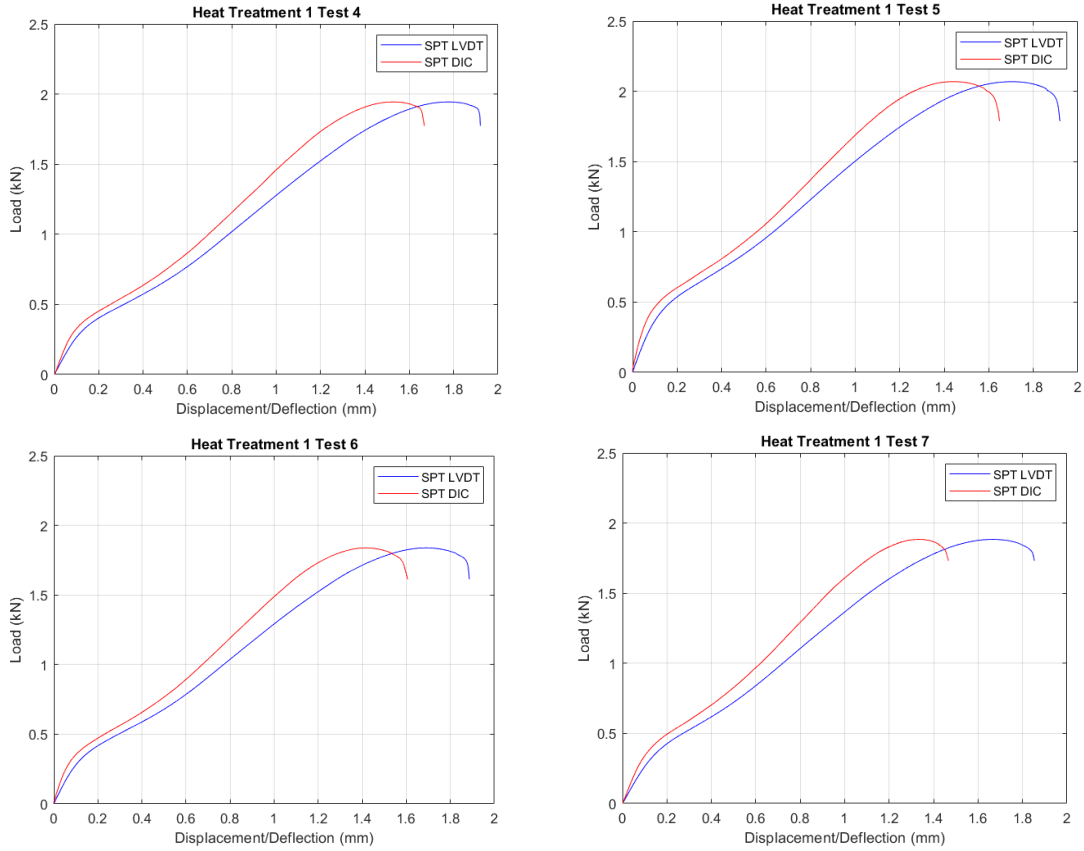

Figure 102: Graph of Load vs Displacement (LVDT) and Load vs Deflection (DIC) on same axes for HT1 tests

In **Figure 102**, the load against displacement and load against deflection curves were plotted on the same axes. As in the AR tests, the deflection values were lower than the displacement values because of the uneven deformation of the specimen upper and lower sides. The graphs show similar load values and displacement ranges showing consistency in the material behaviour and deformation response to the test conditions. The maximum load values were ranging from 1.84 kN to 2.07 kN, with the end of test deflection and displacement ranging from 1.46 mm to 1.68 mm and 1.85 mm to 2 mm respectively.

4.5.2.2.1 Janca et al. Analysis

Characterisation of elastic to plastic transition (Yield Strength)

As mentioned in the AR section, Janca et al. [31] provided an analysis methodology that allowed for the calculation of the yield and the ultimate tensile strength of the material. For the yield stress to be calculated, specimen deflection against specimen displacement (DIC vs LVDT) was displayed in **Figure 103**, where deflection evolves non-uniformly and in a curved manner against the displacement. The 1:1 quadrant axis line was also displayed in the illustration. At the point of maximal curvature displacement and deflection (u_{ept}, v_{ept}), the elastic to plastic transition load characteristic, F_{ept}, was determined and recorded.

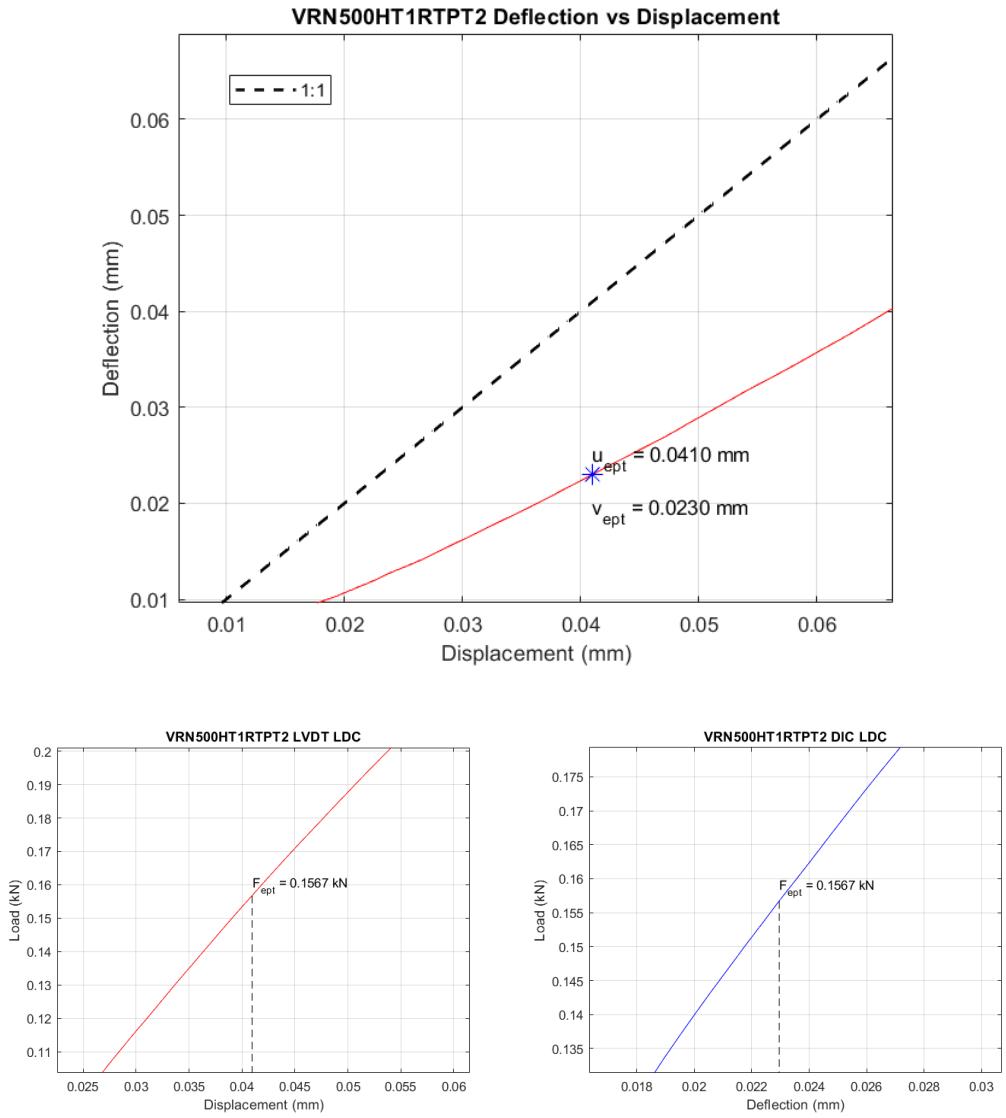

Figure 103: Graphs of specimen deflection (DIC) vs displacement (LVDT) and F_{ept} determination for HT1 tests

The 'energetic criterion' was also adopted to characterise the elastic to plastic transition, comparing the area under the curve A, with its compliment A_c above the curve. **Figure 104**

exhibits the SPT curves displaying the areas A and A_c for a selected test. The load point $F_{e1.5}$ could now be determined and recorded.

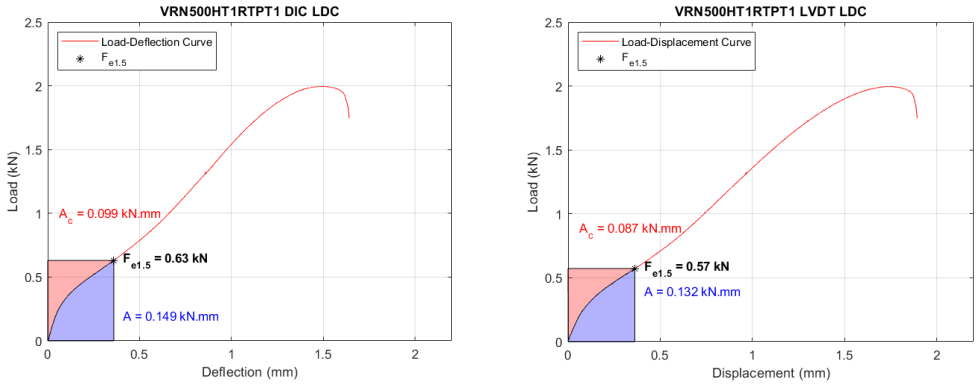

Figure 104: Graph of $F_{e1.5}$ in LDC for deflection and displacement for HT1 tests

The results for the characterisation of the elastic to plastic transition for the two methods suggested by Janca et al. [31] were recorded and tabulated in **Table 46**. The displacement against deflection plot enabled the identification of u_{ept} and v_{ept} which averaged at 0.045 mm and 0.03 mm respectively. The LVDT and DIC elastic to plastic transition load points, F_{ept}, were found to range from 0.113 kN to 0.159 kN. For the energy criterion the load points $F_{e1.5}$ were determined and tabulated. These values ranged from 0.51 kN to 0.69 kN for the LVDT related experiments and 0.56 kN to 0.76 kN for the DIC related experiments.

SPT EXPERIMENT	h_0 (mm)	u_{ept}/v_{ept} (mm)		F_{ept} LVDT/DIC (kN)	$F_{e1.5}$ (kN)	
		LVDT (u)	DIC (v)		LVDT	DIC
VRN5000HT1RTPT1	0.51	0.044	0.031	0.152	0.57	0.63
VRN5000HT1RTPT2	0.50	0.041	0.023	0.157	0.67	0.72
VRN5000HT1RTPT3	0.50	0.056	0.045	0.149	0.51	0.56
VRN5000HT1RTPT4	0.50	0.038	0.028	0.113	0.54	0.60
VRN5000HT1RTPT5	0.50	0.034	0.017	0.154	0.69	0.76
VRN5000HT1RTPT6	0.50	0.044	0.026	0.144	0.56	0.61
VRN5000HT1RTPT7	0.50	0.057	0.040	0.159	0.58	0.66
AVERAGE	**0.50**	**0.045**	**0.030**	**0.147**	**0.59**	**0.65**

Table 46: Results for load points F_{ept} and $F_{e1.5}$ for HT1 tests

Characterisation of strength

As in the AR tests, further analysis proposed by Janca et al. was adopted to categorize strength. The thinning effect on selected tests against displacement (LVDT) and deflection (DIC) was plotted in **Figure 105**, and the corresponding load points were identified and recorded.

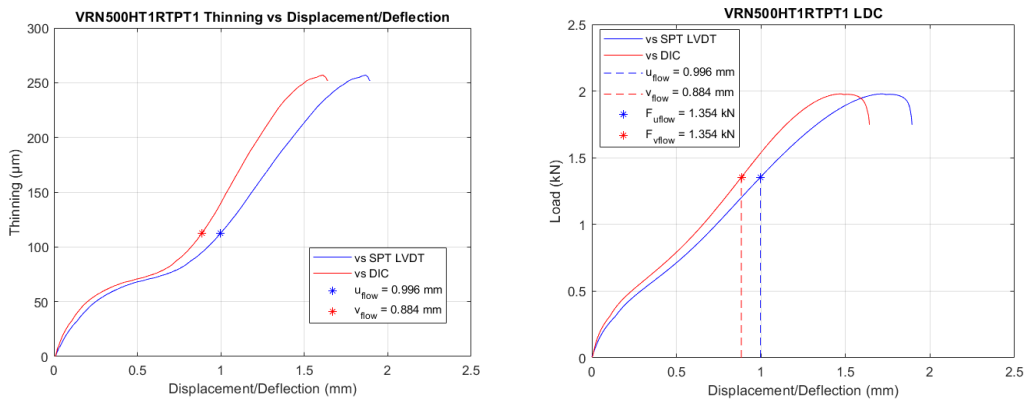

Figure 105: Graph of Thinning vs Displacement/Deflection and Load vs Thinning displacement (u_{flow} v v_{flow}) for HT1 tests

As in the prior sections, the maximal curvature points in the thinning curve, u_{flow} and v_{flow}, and subsequently F_{flow}, corresponding with the convex knee of the thinning against displacement/deflection curve was also obtained and recorded. The second phenomenon proposed by Janca et al. utilised the second inflection point of the load-deflection curve. This enabled the strength to be characterised using the load point F_{infl} as shown in **Figure 106**.

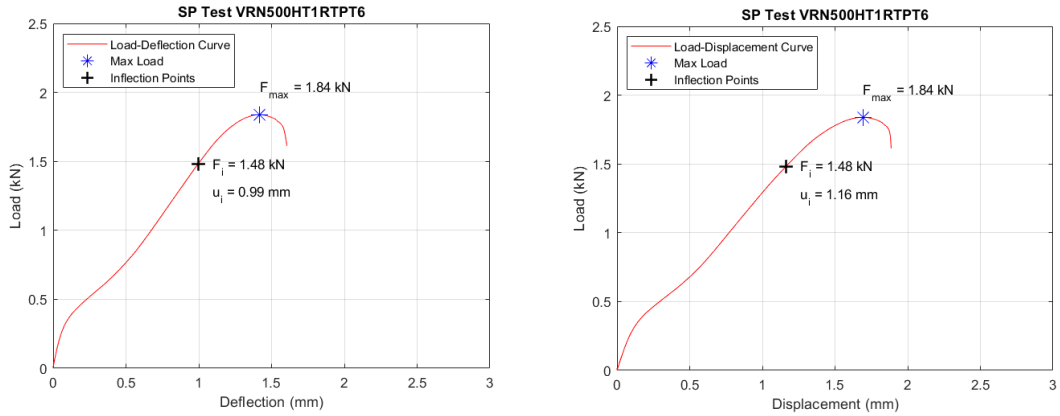

Figure 106: Graph of F_{infl} on deflection and displacement curves for HT1 tests

The strength characterisation methods provided the results obtained from the displacement/deflection graphs above and were tabulated in **Table 47**. F_{flow} values for both displacement and deflection curves ranged from 1.23 kN to 1.48 kN and averaged at 1.34 kN.

SPT EXPERIMENT	h_0 (mm)	u_{infl}/v_{infl} (mm)		F_{infl} (kN)		u_{flow} (mm)	v_{flow} (mm)	F_{flow} (kN)	
		LVDT (u)	DIC (v)	LVDT	DIC			LVDT	DIC
VRN5000HT1RTPT1	0.51	1.13	0.940	1.52	1.44	0.996	0.884	1.35	1.35
VRN5000HT1RTPT2	0.50	1.08	1.05	1.54	1.7	1.01	0.892	1.45	1.45
VRN5000HT1RTPT3	0.50	1.21	1.05	1.50	1.52	0.990	0.863	1.23	1.23
VRN5000HT1RTPT4	0.50	1.21	1.04	1.53	1.52	1.01	0.886	1.29	1.29
VRN5000HT1RTPT5	0.50	1.06	0.910	1.58	1.55	0.981	0.865	1.48	1.48
VRN5000HT1RTPT6	0.50	1.16	0.990	1.48	1.48	1.03	0.893	1.33	1.33
VRN5000HT1RTPT7	0.50	1.12	0.920	1.51	1.50	0.926	0.787	1.27	1.27
AVERAGE	**0.50**	**1.14**	**0.986**	**1.52**	**1.53**	**0.992**	**0.867**	**1.34**	**1.34**

Table 47: Results for load points F_{infl} and F_{flow} for HT1 tests

As seen in **Table 47**, F_{infl} load points for the LVDT displacement experiments fell in a narrow region of 1.48 kN to 1.58 kN and averaged at 1.52 kN. Similarly, the DIC deflection experiments F_{infl} load points averaged at 1.53 kN, exhibiting a consistency in the obtained results and load values.

These load values contained in **Table 47** enabled the yield and ultimate tensile stress values for the specimens to be calculated in accordance with the Janca et al. proposals. The material properties for HT1 specimens could now be tabulated in the following tables **Table 48** and **Table 49**.

LVDT EXPERIMENT	YIELD STRESS F_{ept}/h_0^2 (MPa)	YIELD STRESS $F_{e1.5}/h_0^2$ (MPa)	UTS $F_{infl}/h_0 \cdot u_{infl}$ (MPa)	UTS $F_{flow}/h_0 \cdot u_{flow}$ (MPa)
VRN5000HT1RTPT1	584.39	2191.46	2637.52	2665.56
VRN5000HT1RTPT2	628.00	2680.00	2851.85	2878.97
VRN5000HT1RTPT3	596.00	2040.00	2479.34	2492.93
VRN5000HT1RTPT4	452.00	2160.00	2528.93	2552.14
VRN5000HT1RTPT5	616.00	2760.00	2981.13	3009.17
VRN5000HT1RTPT6	576.00	2240.00	2551.72	2575.02
VRN5000HT1RTPT7	636.00	2320.00	2696.43	2745.14
AVERAGE	**584.06**	**2341.64**	**2675.27**	**2702.71**

Table 48: Results for F_{ept}/h_0^2, $F_{e1.5}/h_0^2$, $F_{infl}/h_0 \cdot u_{infl}$ and $F_{flow}/h_0 \cdot u_{flow}$ for HT1 LVDT experiments

DIC EXPERIMENT	YIELD STRESS F_{ept}/h_0^2 (MPa)	YIELD STRESS $F_{e1.5}/h_0^2$ (MPa)	UTS $F_{infl}/h_0 \cdot v_{infl}$ (MPa)	UTS $F_{flow}/h_0 \cdot v_{flow}$ (MPa)
VRN5000HT1RTPT1	753.56	2422.15	3003.75	3003.28
VRN5000HT1RTPT2	964.00	2880.00	3238.10	3253.36
VRN5000HT1RTPT3	744.00	2240.00	2895.24	2859.79
VRN5000HT1RTPT4	620.00	2400.00	2923.08	2900.68
VRN5000HT1RTPT5	964.00	3040.00	3406.59	3412.72
VRN5000HT1RTPT6	832.00	2440.00	2989.90	2978.72
VRN5000HT1RTPT7	860.00	2640.00	3260.87	3229.99
AVERAGE	**819.65**	**2580.31**	**3102.50**	**3091.22**

Table 49: Results for F_{ept}/h_0^2, $F_{e1.5}/h_0^2$, $F_{infl}/h_0 \cdot v_{infl}$ and $F_{flow}/h_0 \cdot v_{flow}$ for HT1 DIC experiments

In **Table 48** and **Table 49**, the F_{ept} load point for the displacement (LVDT) curves resulted in an average yield stress function, F_{ept}/h_0^2, of 584 MPa and an average yield stress function, of 820 MPa for the deflection (DIC) curves. The energy criterion for the displacement (LVDT) curves resulted in an average yield stress correlation factor, $F_{e1.5}/h_0^2$, of 2342 MPa and 2580 MPa for the deflection (DIC) curves. For the LVDT displacement curves, the F_{infl} induced average UTS correlation function, $F_{infl}/h_0 \cdot u_{infl}$, was found as 2675 MPa and the F_{flow} calculated UTS factor, $F_{flow}/h_0 \cdot u_{flow}$, was found to be an average of 2703 MPa. For the DIC displacement curves, the F_{infl} induced UTS factor, $F_{infl}/h_0 \cdot v_{infl}$, was found to average at 3103 MPa and the F_{flow} calculated UTS factor, $F_{flow}/h_0 \cdot v_{flow}$, was found to be at an average of 3091 MPa. As in the previous section with the AR regime, these results could now be used to correlate these findings with the conventional tests carried out.

4.5.2.2.2 CWA Analysis

As established in the AR section, this analytical method enabled the attainment of both the yield and ultimate tensile strength of the HT1 material. **Figure 107** also shows the SP test results on selected test curves. The graphs displayed exhibit the elastic to plastic transition load point, F_e, the maximum load point, F_m and the area under the curve, the small punch fracture energy, E_{SP}.

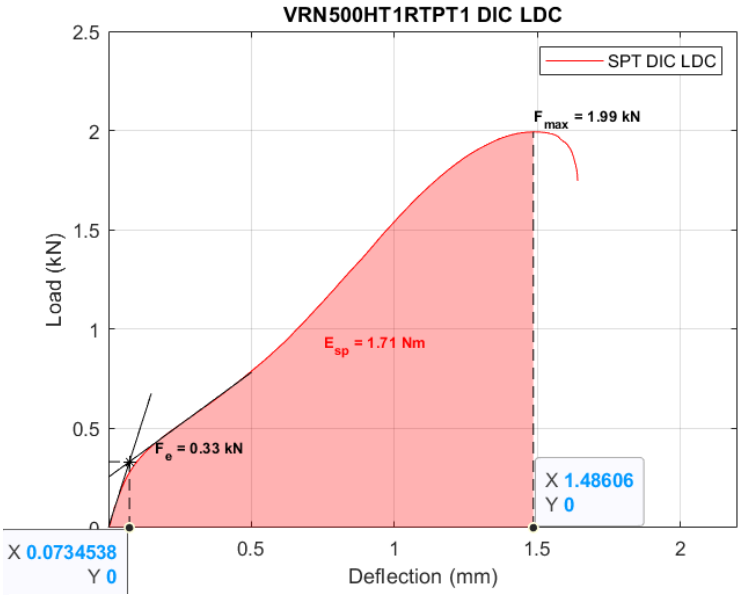

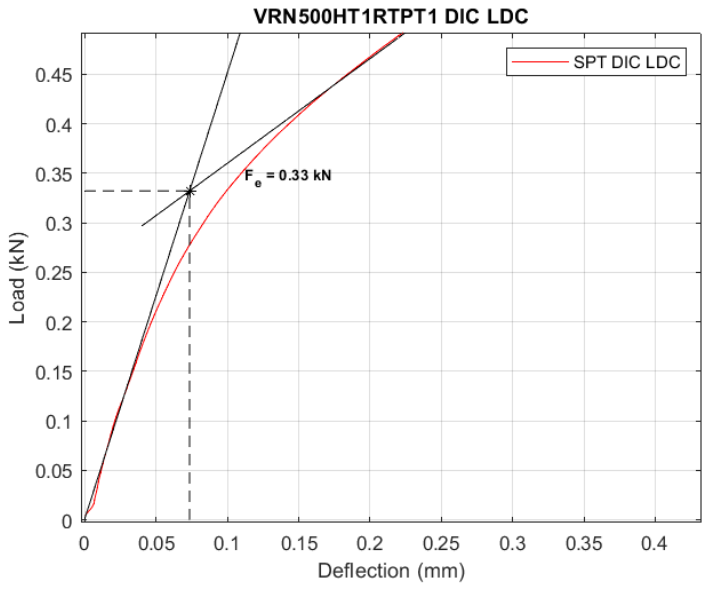

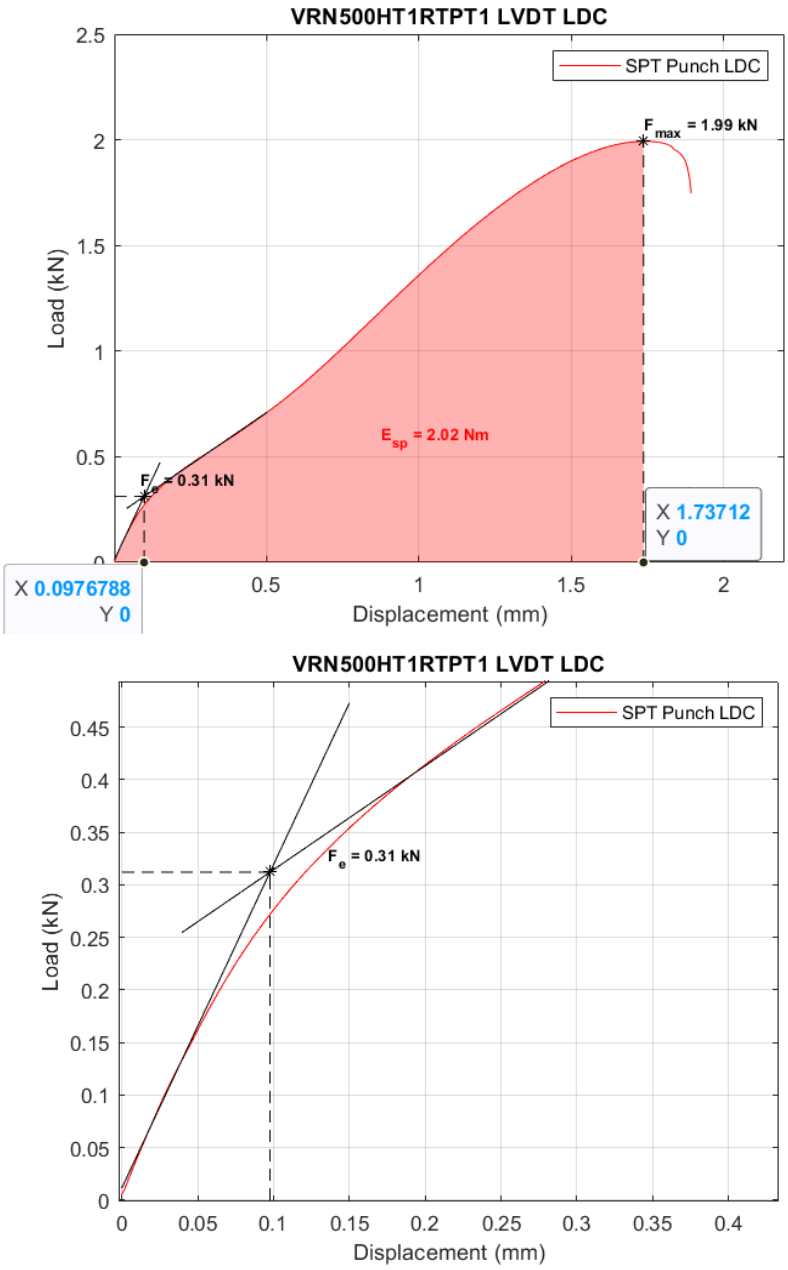

Figure 107: Graphs for determination of F_e, F_m and E_{SP} for DIC deflection (v) and LVDT displacement (u) for HT1 tests

With the establishment of the elastic to plastic transition load point, (F_e, u_e), the maximum load point (F_m, u_m) and the SP fracture energy (E_{SP}) for LVDT displacement, **Table 50** was populated with the values corresponding to each test for the HT1 material regime. From the table, it can be observed that the values of the load point F_e ranged from 0.31 kN to 0.44 kN, the maximum load points F_m fell in the range of 1.84 kN to 2.07 kN and the SP fracture energy (E_{SP}) ranged from 1.83 J to 2.13 J. F_e, F_m and E_{SP} averaged at 0.36 kN, 1.96 kN and 2.01 J respectively.

LVDT EXPERIMENT	h_0 (mm)	YIELD DISPLACEMENT u_e (mm)	YIELD LOAD F_e (kN)	MAX DISPLACEMENT u_m (mm)	MAX LOAD F_m (kN)	SMALL PUNCH ENERGY E_{SP} (J)
HT1RTPT1	0.51	0.0977	0.31	1.737	1.99	2.02
HT1RTPT2	0.50	0.115	0.44	1.710	2.03	2.10
HT1RTPT3	0.50	0.112	0.30	1.863	1.99	2.13
HT1RTPT4	0.50	0.107	0.32	1.778	1.94	2.00
HT1RTPT5	0.50	0.0969	0.44	1.699	2.07	2.16
HT1RTPT6	0.50	0.101	0.33	1.692	1.84	1.83
HT1RTPT7	0.50	0.126	0.35	1.663	1.88	1.86
AVERAGE	**0.50**	**0.108**	**0.36**	**1.735**	**1.96**	**2.01**

Table 50: Results of F_e, F_m and E_{SP} for HT1 LVDT displacement (u) tests

Table 51 shows results of the elastic to plastic transition load point (F_e, v_e), maximum load point (F_m, u_m) and the small punch fracture energy (E_{SP}) obtained from the DIC deflection experiments. The data in the table indicates that the values for F_e ranged from 0.32 kN to 0.45 kN and averaged at 0.37 kN. The maximum loads fell into the range of 1.84 kN to 2.07 kN and averaged at 1.96 kN. E_{SP} was found to average at 1.66 J and ranged from 1.46 J to 1.76 J.

DIC EXPERIMENT	h_0 (mm)	YIELD DEFLECTION v_e (mm)	YIELD LOAD F_e (kN)	MAX DEFLECTION v_m (mm)	MAX LOAD F_m (kN)	SMALL PUNCH ENERGY E_{SP} (J)
HT1RTPT1	0.51	0.0735	0.33	1.486	1.99	1.71
HT1RTPT2	0.50	0.0635	0.44	1.386	2.03	1.63
HT1RTPT3	0.50	0.0958	0.32	1.561	1.99	1.76
HT1RTPT4	0.50	0.0782	0.34	1.529	1.94	1.71
HT1RTPT5	0.50	0.0546	0.45	1.437	2.07	1.80
HT1RTPT6	0.50	0.0585	0.34	1.417	1.84	1.52
HT1RTPT7	0.50	0.0956	0.38	1.332	1.88	1.46
AVERAGE	**0.50**	**0.0742**	**0.37**	**1.450**	**1.96**	**1.66**

Table 51: Results of F_e, F_m and E_{SP} for HT1 DIC deflection (v) tests

The values obtained from the LDC then enabled the CWA methodology to be adopted in the calculation of the yield and the ultimate tensile stresses from the HT1 test samples. The LVDT displacement and DIC deflection yield and the ultimate tensile stresses for this regime were calculated and tabulated in **Table 52** and **Table 53**.

LVDT EXPERIMENT	YIELD STRESS F_e/h_0^2 (MPa)	UTS $F_m/h_0 \cdot u_m$ (MPa)	SMALL PUNCH ENERGY E_{SP} (J)
HT1RTPT1	1191.85	2246.38	2.02
HT1RTPT2	1760.00	2374.27	2.10
HT1RTPT3	1200.00	2136.34	2.13
HT1RTPT4	1280.00	2182.23	2.00
HT1RTPT5	1760.00	2436.73	2.16
HT1RTPT6	1320.00	2174.94	1.83
HT1RTPT7	1400.00	2260.97	1.86
AVERAGE	**1415.98**	**2258.84**	**2.01**

Table 52: Results for F_e/h_0^2, $F_m/h_0 \cdot u_m$ and E_{SP} for HT1 LVDT experiments

DIC EXPERIMENT	YIELD STRESS F_e/h_0^2 (MPa)	UTS $F_m/h_0 \cdot v_m$ (MPa)	SMALL PUNCH ENERGY E_{SP} (J)
HT1RTPT1	1268.74	2625.81	1.71
HT1RTPT2	1760.00	2929.29	1.63
HT1RTPT3	1280.00	2549.65	1.76
HT1RTPT4	1360.00	2537.61	1.71
HT1RTPT5	1800.00	2881.00	1.80
HT1RTPT6	1360.00	2597.04	1.52
HT1RTPT7	1520.00	2822.82	1.46
AVERAGE	**1478.39**	**2706.17**	**1.66**

Table 53: Results for F_e/h_0^2, $F_m/h_0 \cdot v_m$ and E_{SP} for HT1 DIC experiments

Table 52 shows that for the LVDT displacement experiments, the average yield stress correlation factor, F_e/h_0^2, was 1416 MPa and the subsequent ultimate tensile stress calculated, $F_m/h_0 \cdot u_m$, averaged at 2259 MPa. In the case for the DIC deflection experiments, as shown in **Table 53**, the yield stress factor, F_e/h_0^2, and the ultimate tensile stress factor, $F_m/h_0 \cdot v_m$, averaged at 1478 MPa and 2706 MPa respectively. The estimations for the DIC experiment results were higher than the LVDT experiment values, a characteristic that carried on from the AR tests.

4.5.2.2.3 Hahner Analysis

As mentioned in previous sections, Hahner's analytical approach allows the yield strength of the material to be obtained from the SPT curve (displacement/deflection). The curvature of the SPT curve was quantified to establish a different estimation of the elastic to plastic transition point by utilising the three offset points in the transition region.

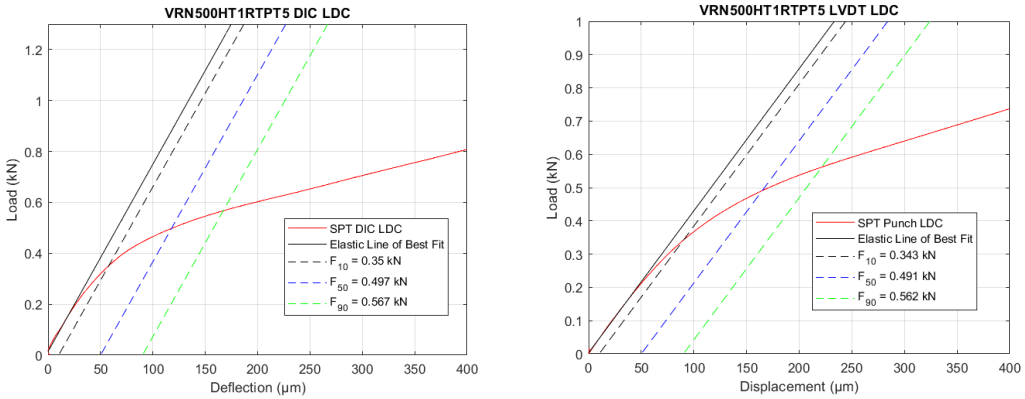

Figure 108: Figure of curvature quantification at three offsets i.e., 10 µm, 50 µm and 90 µm (DIC deflection and LVDT displacement)

As established in **Figure 108**, the curvature (K) values were determined from the SPT curve and **Equation 26** was used to obtain the K-dependent yield coefficient and then the yield stress estimation. **Table 54** and **Table 55** show the results obtained from the displacement and deflection graphs, namely the quantities for the load points F_{10}, F_{50} and F_{90}, the curvature, K, and the subsequent yield stress estimation.

LVDT EXPERIMENT	h_0 (mm)	YIELD LOAD F_{10} (kN)	YIELD LOAD F_{50} (kN)	YIELD LOAD F_{90} (kN)	CURVATURE K	YIELD STRESS σ_y (MPa)
HT1RTPT1	0.51	0.292	0.397	0.462	0.235	365.06
HT1RTPT2	0.50	0.351	0.497	0.564	0.371	715.68
HT1RTPT3	0.50	0.272	0.371	0.424	0.303	482.85
HT1RTPT4	0.50	0.266	0.382	0.438	0.349	550.08
HT1RTPT5	0.50	0.343	0.491	0.562	0.352	707.04
HT1RTPT6	0.50	0.275	0.391	0.448	0.341	563.04
HT1RTPT7	0.50	0.294	0.428	0.494	0.340	616.32
AVERAGE	**0.50**	**0.299**	**0.422**	**0.485**	**0.327**	**571.44**

Table 54: Results of offset loads F_{10}, F_{50}, F_{90}, curvature K and yield stress estimation σ_Y for HT1 LVDT tests

DIC EXPERIMENT	h_0 (mm)	YIELD LOAD F_{10} (kN)	YIELD LOAD F_{50} (kN)	YIELD LOAD F_{90} (kN)	CURVATURE K	YIELD STRESS σ_y (MPa)
HT1RTPT1	0.51	0.282	0.399	0.465	0.279	452.11
HT1RTPT2	0.50	0.331	0.479	0.548	0.364	689.76
HT1RTPT3	0.50	0.292	0.384	0.438	0.260	416.49
HT1RTPT4	0.50	0.269	0.391	0.447	0.371	563.04
HT1RTPT5	0.50	0.350	0.497	0.567	0.355	715.68
HT1RTPT6	0.50	0.269	0.388	0.446	0.345	558.72
HT1RTPT7	0.50	0.304	0.444	0.511	0.353	639.36
AVERAGE	**0.50**	**0.300**	**0.426**	**0.489**	**0.332**	**576.45**

Table 55: Results of offset loads F_{10}, F_{50}, F_{90}, curvature K and yield stress estimation σ_Y for HT1 DIC tests

For the LVDT displacement experiments, the yield stress estimation, σ_Y, averaged at 571 MPa and ranged from 365 MPa to 707 MPa. In the case of the DIC deflection experiments, the yield stress estimation, σ_Y, ranged from 416 MPa to 716 MPa and averaged at 576 MPa. Consistency was observed in the values of the average yield stress estimation in both the deflection and the displacement experiments, exhibiting the reproducibility of the material yield properties using this analytical methodology and test method. The significant disparity in the singular test estimations was mainly because of the curvature, K, values for some tests that were higher than the limitation in the piecewise **Equation 26**, resulting in different yield stress estimations.

4.5.2.2.4 DIC Crack Detection Analysis

Figure 109 shows the SED evolution of the SPT for HT1RTPT7. The evaluated step number was found to be step 761, which corresponded to a deflection, v_{crack} of 0.60 mm, a displacement, u_{crack} of 0.70 mm and a load, F_{crack} of 0.97 kN as seen in **Figure 110** and **Figure 111**.

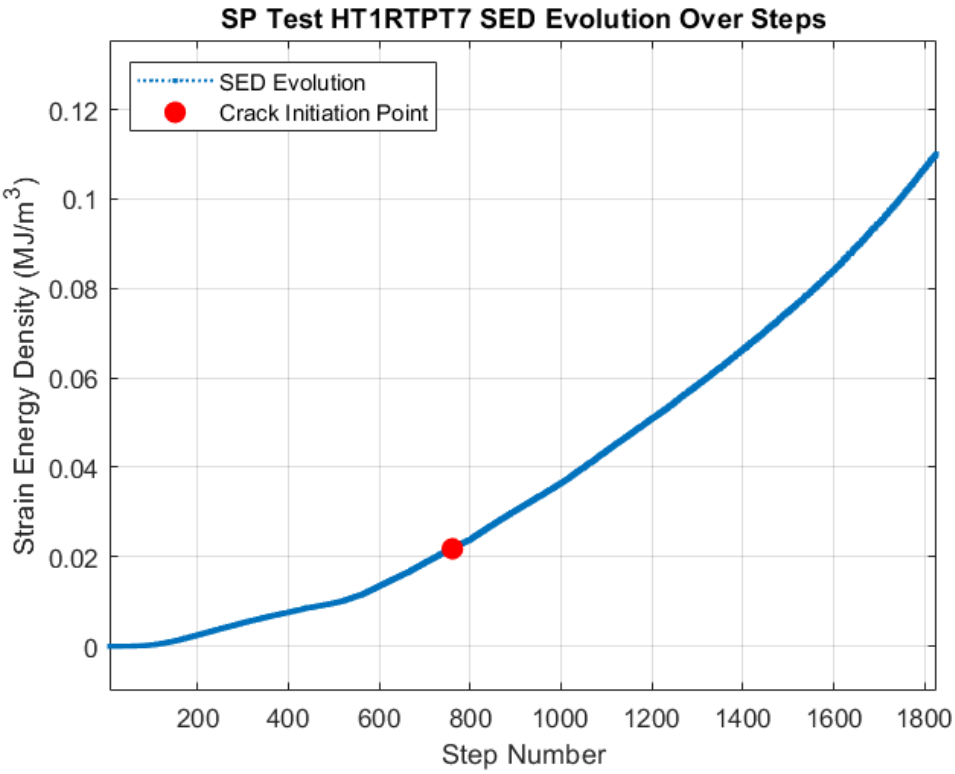

Figure 109: SED evolution for HT1RTPT7 over DIC system steps

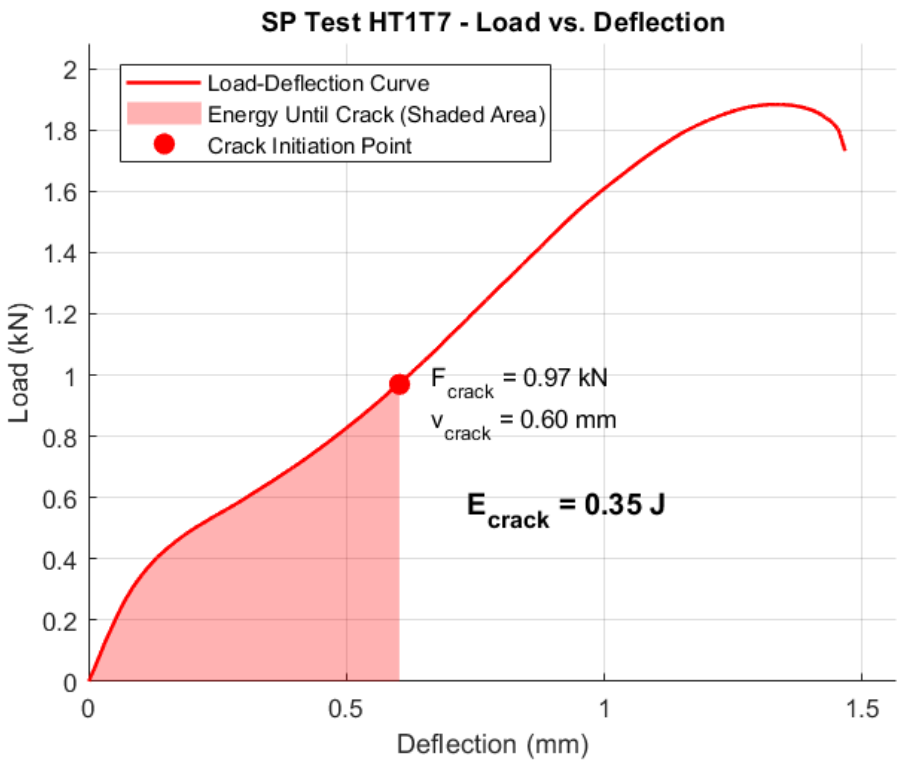

Figure 110: SPT HT1T7 DIC LDC with crack parameters v_{crack}, F_{crack} and E_{crack}

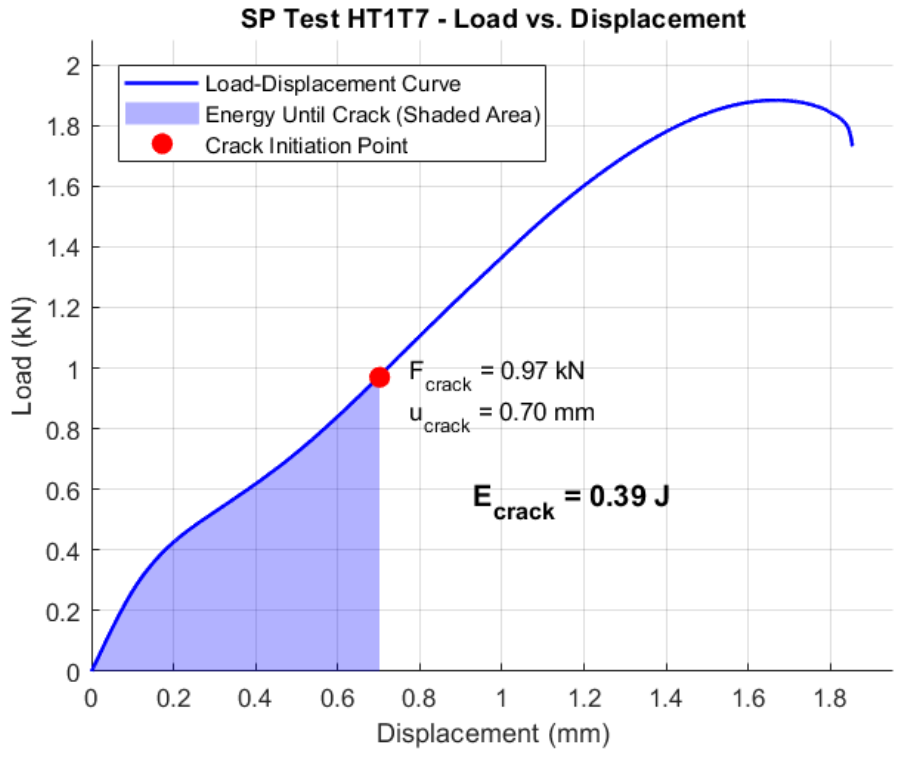

Figure 111: SPT HT1T7 LVDT LDC with crack parameters u_{crack}, F_{crack} and E_{crack}

As in the previous section for the AR condition, the crack initiation load, F_{crack}, the displacement/deflection at the crack detection point, u_{crack}/v_{crack}, and the E_{crack} for the LVDT displacement tests and the DIC deflection tests were tabulated in **Table 56** and **Table 57** respectively.

LVDT EXPERIMENT	h_0 (mm)	CRACK DISPLACEMENT u_{crack} (mm)	CRACK LOAD F_{crack} (kN)	CRACK ENERGY E_{crack} (J)
HT1RTPT1	0.51	0.93	1.26	0.63
HT1RTPT2	0.50	0.65	0.98	0.40
HT1RTPT3	0.50	0.84	1.04	0.48
HT1RTPT4	0.50	0.96	1.23	0.64
HT1RTPT5	0.50	0.81	1.24	0.59
HT1RTPT6	0.50	0.74	0.96	0.41
HT1RTPT7	0.50	0.70	0.97	0.39
AVERAGE	**0.50**	**0.80**	**1.10**	**0.51**

Table 56: Results of u_{crack}, F_{crack} and E_{crack} for HT1 LVDT displacement (u) tests

DIC EXPERIMENT	h_0 (mm)	CRACK DEFLECTION v_{crack} (mm)	CRACK LOAD F_{crack} (kN)	CRACK ENERGY E_{crack} (J)
HT1RTPT1	0.51	0.83	1.26	0.58
HT1RTPT2	0.50	0.58	0.98	0.37
HT1RTPT3	0.50	0.74	1.04	0.43
HT1RTPT4	0.50	0.85	1.23	0.57
HT1RTPT5	0.50	0.72	1.24	0.55
HT1RTPT6	0.50	0.65	0.96	0.37
HT1RTPT7	0.50	0.60	0.97	0.35
AVERAGE	**0.50**	**0.71**	**1.10**	**0.46**

Table 57: Results of v_{crack}, F_{crack} and E_{crack} for HT1 DIC deflection (v) tests

For the displacement data shown in **Table 56**, u_{crack} ranged from 0.65 mm to 0.96 mm at an average of 0.8 mm. E_{crack} averaged at 0.51 J and ranged from 0.39 J to 0.64 J. The data for the F_{crack} determined ranged from 0.96 kN to 1.26 kN and averaged at 1.1 kN. For the deflection data in **Table 57**, the v_{crack} values observed ranged from 0.58 mm to 0.85 mm and averaged at 0.71 mm. The E_{crack} averaged at 0.46 J and ranged from 0.35 J to 0.57 J.

4.5.2.2.5 Summary

Similar to the previous section on the AR condition, the analytical methods applied in the assessment of the SPT through Janca et al. [31], the CWA [24], [38], Hahner et al. [7] and the DIC crack detection methods successfully characterised the yield, tensile strength and toughness properties of the material. The data outcomes obtained were also used to assess the contributions of these analytical formulations in validating and correlating the SPT with the mechanical tests.

4.5.2.3 Heat Treatment 2 Results

The load against LVDT displacement and the load against the DIC deflection for HT2 tests were obtained and displayed in **Figure 112**. It can be observed that there are slight differences between the overall test displacement/deflection curves for each test, even though the load points are in a similar range. Notably, some test specimens reach maximum load and fracture points earlier than other tests. While this may be partially attributed to residual stresses from the preparation or the manufacturing processes, or even minor surface defects on the specimen surface which can act as stress concentrators initiating cracks earlier, such factors are not unique to the HT2 specimens and could affect all the specimens being tested. A more likely contributor is the large furnace used for the heat treatments (**Figure 42**), which may have introduced non-uniformity in the temperature across the different regions of the furnace. This potential thermal variation could have resulted in inconsistent microstructural evolution, leading to the variability observed in the mechanical responses of the HT2 specimens.

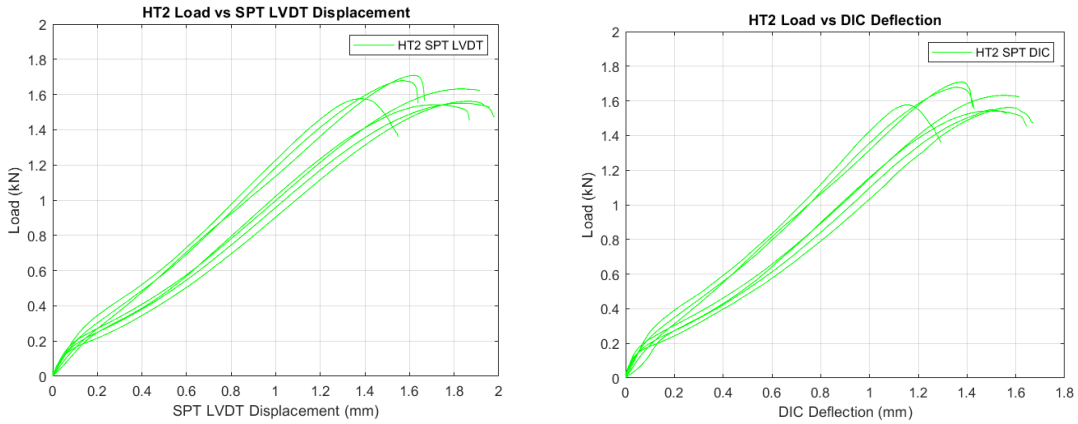

Figure 112: Graphs of Load vs SPT Punch displacement and Load vs SPT DIC deflection for HT2 tests

As in the AR and HT1 tests, **Figure 113** shows a specimen under test image from the DIC camera Istra4D software during the test. This enabled the assessment of the punch test visually, as the images captured exhibited the test process until fracture. The deflection values were recorded during the test, resulting in **Figure 114** where an out-of-plane deflection render could be obtained. This deflection render exhibited the profile of the selected test specimen during the test.

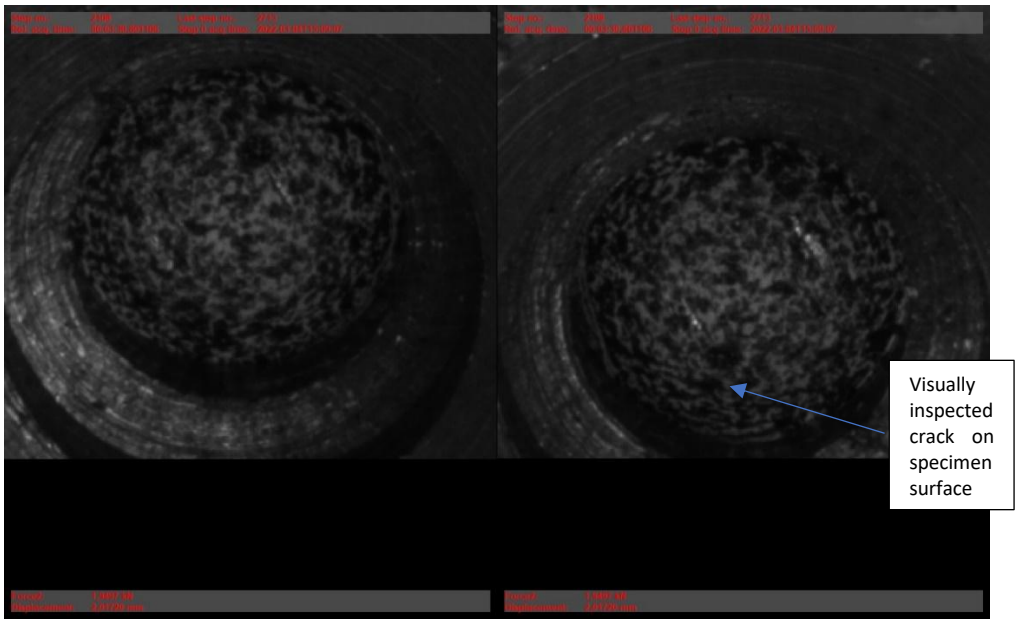

Figure 113: Figure obtained from DIC software: HT2 specimen in SPT rig during test

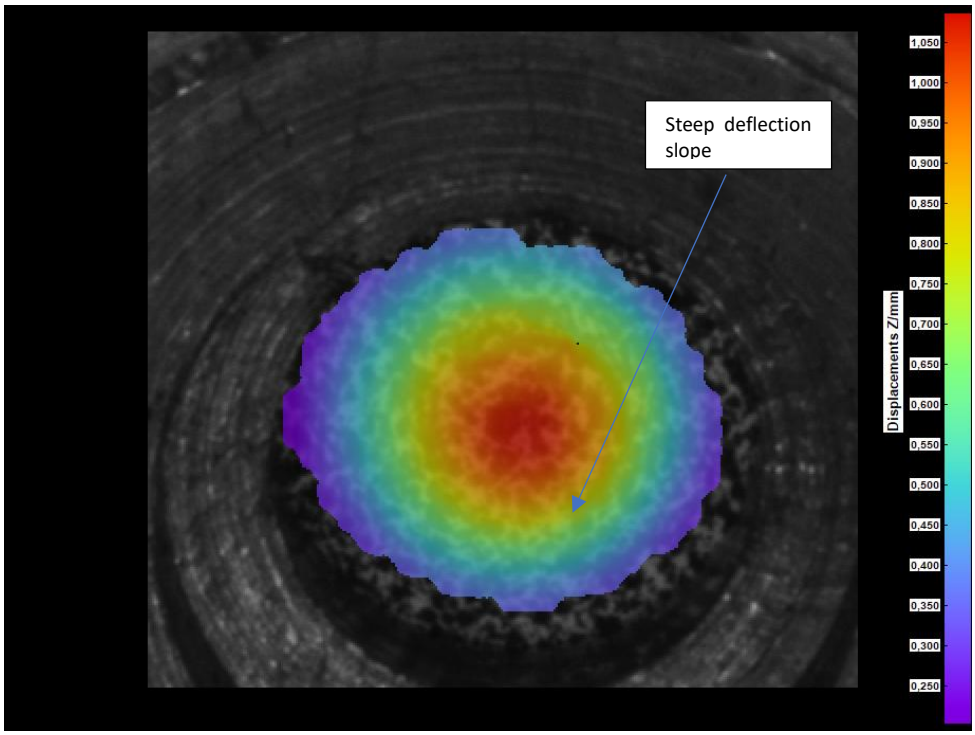

Figure 114: Figure obtained from DIC software: HT2 specimen deflection profile during test

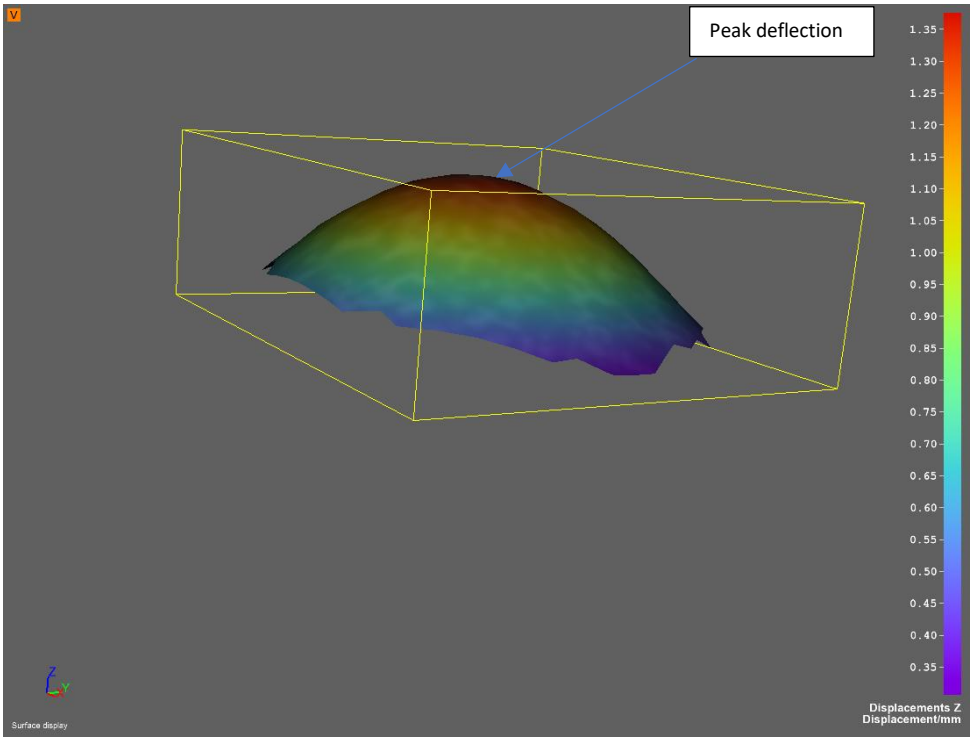

Figure 115: Figure obtained from DIC software: 3D rendering of HT2 specimen under test

As in the previous sections for AR and HT1 tests, **Figure 115** shows the peak deflection at the centre of the specimen as well, meaning the punch point of contact was in the centre as expected. The steeper slope of the deflection profile also shows that the deformation was not uniform and also highlighted the region of material failure during the test.

The load against displacement and load against deflection curves were plotted on the same axes as displayed in **Figure 116**. As observed in the previous sections the deflection values were less than the displacement values highlighting the difference in the displacement and the deflection sensors response to the deformation on the surface below and above the specimen respectively. It can be noted that the maximum load points were similar for the deflection and the displacement curves, averaging at 1.61 kN and ranging from 1.54 kN to 1.71 kN for the tests. The total displacement and deflection of the tests ranged from 1.55 mm to 1.98 mm and 1.3 mm to 1.67 mm respectively, pointing out the wide range and disparity in the overall test deflection and displacement.

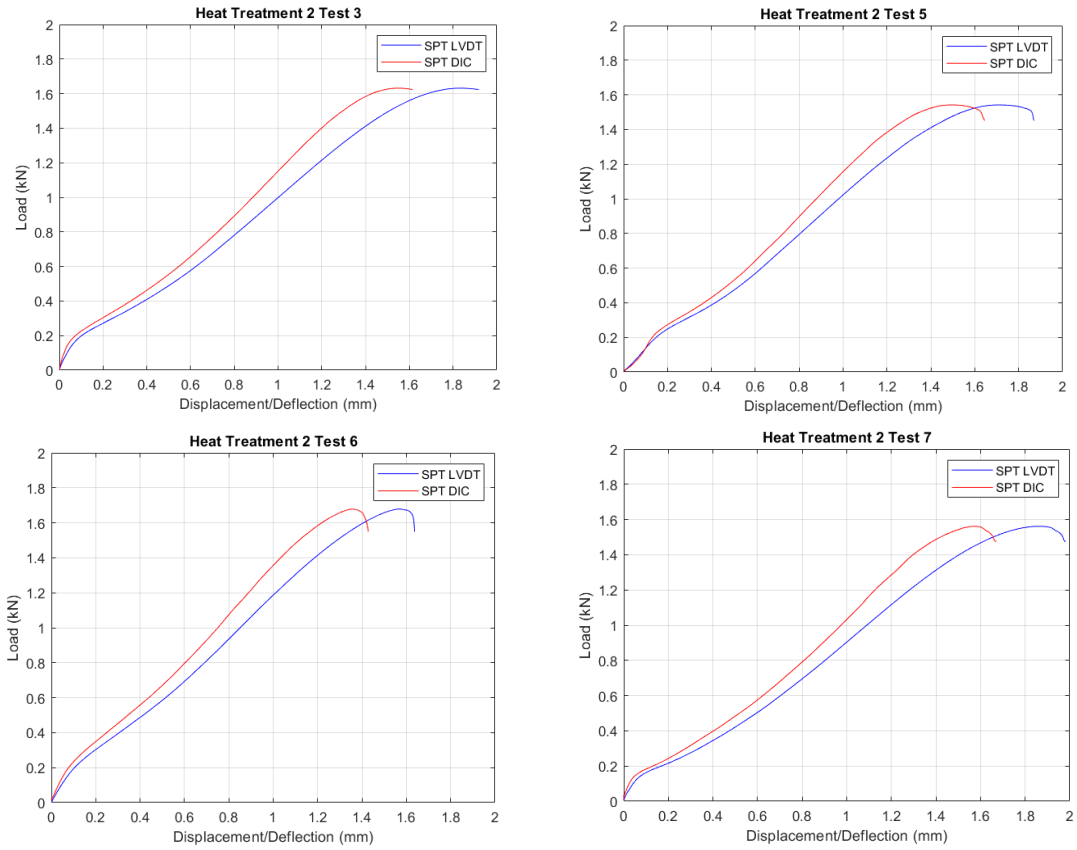

Figure 116: Graph of Load vs Displacement (LVDT) and Load vs Deflection (DIC) on same axes for HT2 tests

4.5.2.3.1 Janca et al. Analysis

Characterisation of elastic to plastic transition (Yield Strength)

According to the Janca et al. [31] analytical methodology, the calculation of the yield and the ultimate tensile strength of the material could be carried out from the data obtained in the LVDT displacement and DIC deflection curves. As established prior, **Figure 117** displays the 1:1 quadrant axis line and the specimen deflection against specimen displacement (DIC vs LVDT) plot.

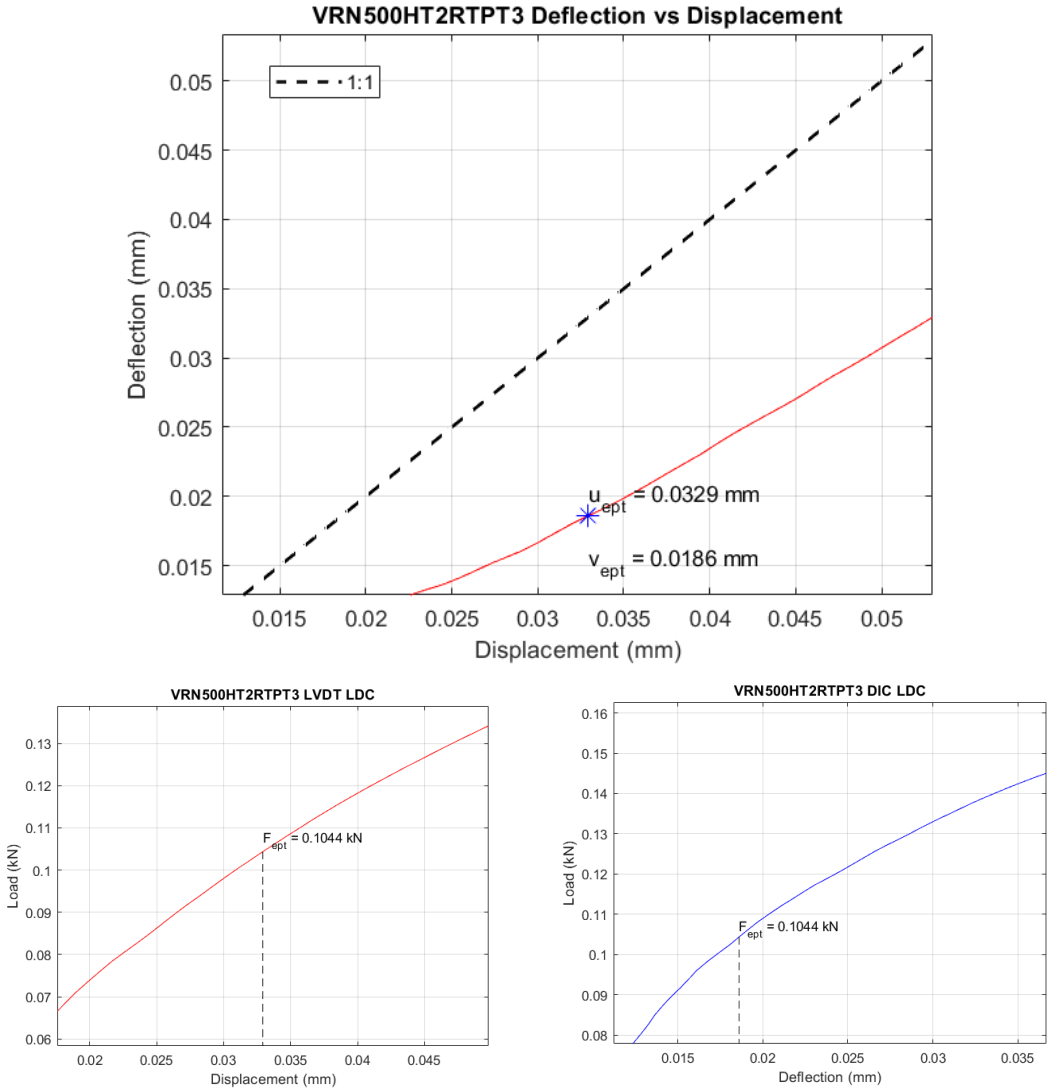

Figure 117: Graphs of specimen deflection (DIC) vs displacement (LVDT) and F_{ept} determination for HT2 tests

Figure 117 shows the determination of the elastic to plastic transition load characteristic, F_{ept}, for both the load-displacement and load-deflection curves at the point of maximal curvature displacement and deflection, (u_{ept}, v_{ept}). As in the previous sections, this load point value was obtained and recorded.

The other methodology proposed by Janca et al. [31], the 'energetic criterion', used to quantify and characterise the elastic to plastic transition through the comparison of the area under the curve A, with its compliment A_c above the curve, was adopted to obtain the load point $F_{e1.5}$. **Figure 118** displays the areas A and A_c, and subsequently the load point $F_{e1.5}$.

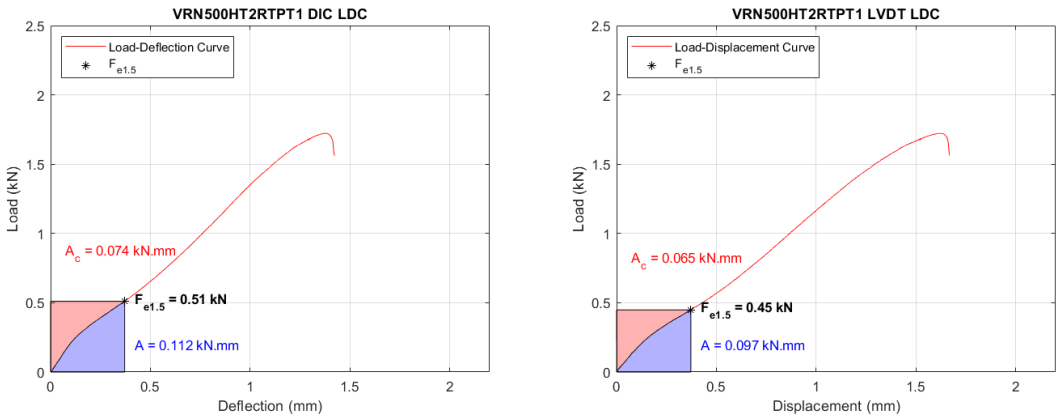

Figure 118: Graph of $F_{e1.5}$ in LDC for deflection and displacement for HT2 tests

Table 58 contains the results obtained for the characterisation of the elastic to plastic transition from Janca et al. [31]. From **Table 58**, the displacement and deflection (u_{ept} and v_{ept}), ranged from 0.033 mm to 0.091 mm averaging at 0.046 mm and 0.018 mm to 0.090 mm averaging at 0.036 mm respectively. The displacement LVDT and deflection DIC elastic to plastic transition load points, F_{ept}, ranged from 0.0762 kN to 0.123 kN and averaged at 0.0983 kN. Likewise, the energy criterion the load points, $F_{e1.5}$, were obtained and found to range between 0.32 kN and 0.49 kN for the LVDT displacement and 0.37 kN and 0.55 kN for the DIC deflection.

SPT EXPERIMENT	h_0 (mm)	u_{ept}/v_{ept} (mm)		F_{ept} LVDT/DIC (kN)	$F_{e1.5}$ (kN)	
		LVDT (u)	DIC (v)		LVDT	DIC
VRN5000HT2RTPT1	0.50	0.043	0.0373	0.0762	0.45	0.51
VRN5000HT2RTPT2	0.50	0.039	0.0337	0.0905	0.49	0.55
VRN5000HT2RTPT3	0.50	0.033	0.0186	0.104	0.38	0.43
VRN5000HT2RTPT4	0.50	0.037	0.0231	0.103	0.35	0.39
VRN5000HT2RTPT5	0.50	0.091	0.0895	0.123	0.37	0.41
VRN5000HT2RTPT6	0.50	0.042	0.0302	0.0966	0.46	0.52
VRN5000HT2RTPT7	0.50	0.035	0.0179	0.0951	0.32	0.37
AVERAGE	**0.50**	**0.046**	**0.0358**	**0.0983**	**0.40**	**0.45**

Table 58: Results for load points F_{ept} and $F_{e1.5}$ for HT2 tests

Characterisation of strength

For strength characterisation, as mentioned in the previous sections, the thinning phenomenon proposed by Janca et al. was used in further analysis of the LVDT displacement and the DIC deflection curves. **Figure 119** shows the thinning effect on selected tests to obtain the corresponding load points required for further analysis.

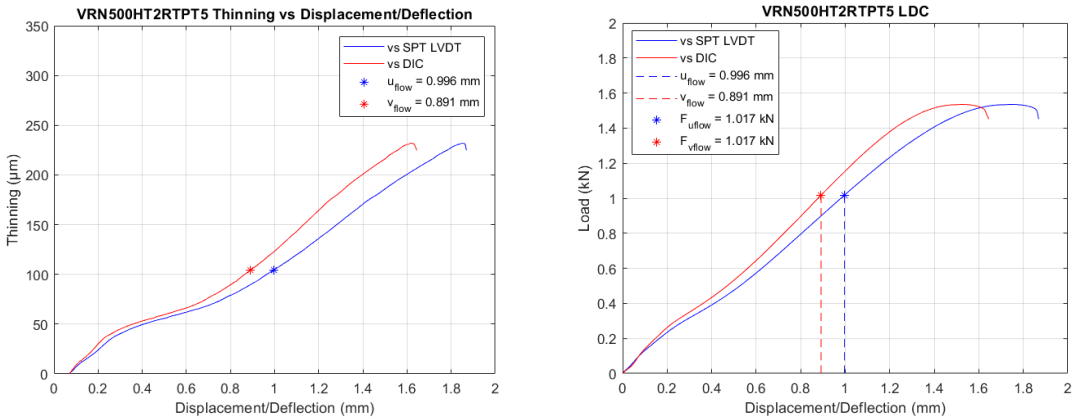

Figure 119: Graph of Thinning vs Displacement/Deflection and Load vs Thinning displacement (u_{flow} v v_{flow}) for HT2 tests

As discussed in earlier sections, the maximal curvature points in the thinning curve, u_{flow} and v_{flow} were obtained. These values were used as seen in **Figure 119**, to obtain the corresponding load point F_{flow} values which were recorded.

The strength characterisation resulted in the attainment of the required load point, F_{infl}, derived from the second inflection point of the load-deflection or load-displacement curve, as displayed in **Figure 120**.

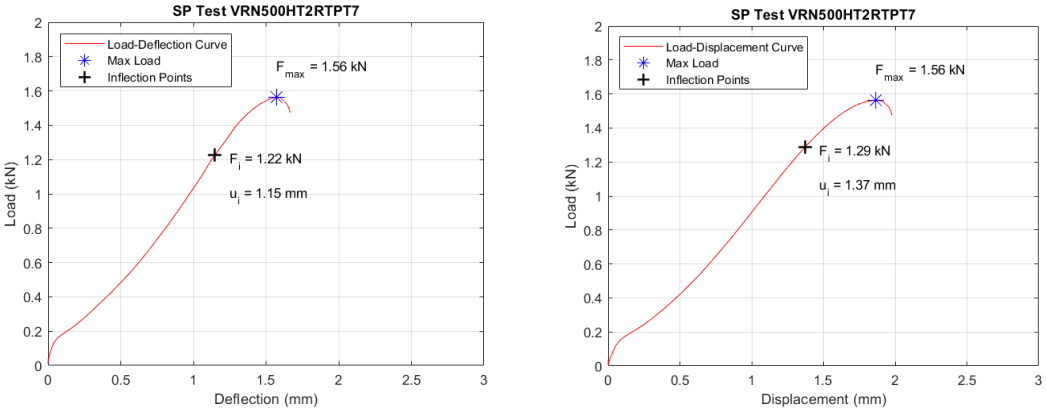

Figure 120: Graph of F_{infl} on deflection and displacement curves for HT2 tests

Table 59 contains the results obtained from the two methods of analysis proposed by Janca et al. [31] for strength estimation. It can be observed that the F_{infl} load points for the displacement experiments ranged from 1.25 kN to 1.34 kN, averaging at 1.28 kN. F_{infl}

load points for the deflection experiments on the other hand averaged at 1.23 kN and ranged from 1.19 kN to 1.27 kN. It can also be seen that the F_{flow} values for both displacement and deflection curves averaged at 1.03 kN, ranging from 0.986 kN to 1.06 kN.

SPT EXPERIMENT	h_0 (mm)	u_{infl}/v_{infl} (kN)		F_{infl} (kN)		u_{flow} (mm)	v_{flow} (mm)	F_{flow} (kN)	
		LVDT (u)	DIC (v)	LVDT	DIC			LVDT	DIC
VRN5000HT2RTPT1	0.50	1.09	0.92	1.28	1.24	0.907	0.795	1.05	1.05
VRN5000HT2RTPT2	0.50	1.09	0.88	1.34	1.24	0.893	0.782	1.09	1.09
VRN5000HT2RTPT3	0.50	1.27	1.09	1.29	1.27	1.01	0.888	1.01	1.01
VRN5000HT2RTPT4	0.50	1.27	1.12	1.25	1.25	1.04	0.926	1.00	1.00
VRN5000HT2RTPT5	0.50	1.22	1.03	1.26	1.20	0.996	0.891	1.02	1.02
VRN5000HT2RTPT6	0.50	1.08	0.88	1.28	1.19	0.900	0.792	1.06	1.06
VRN5000HT2RTPT7	0.50	1.37	1.15	1.29	1.22	1.08	0.962	0.986	0.986
AVERAGE	**0.50**	**1.20**	**1.01**	**1.28**	**1.23**	**0.974**	**0.862**	**1.03**	**1.03**

Table 59: Results for load points F_{infl} and F_{flow} for HT2 tests

The yield and ultimate tensile stresses could now be calculated from these values and populated in **Table 60** and **Table 61** as the mechanical properties of the HT2 specimens in accordance with the proposed methodology by Janca et al. [31].

LVDT EXPERIMENT	YIELD STRESS F_{ept}/h_0^2 (MPa)	YIELD STRESS $F_{e1.5}/h_0^2$ (MPa)	UTS $F_{infl}/h_0 \cdot u_{infl}$ (MPa)	UTS $F_{flow}/h_0 \cdot u_{flow}$ (MPa)
VRN5000HT2RTPT1	304.80	1800.00	2348.62	2315.33
VRN5000HT2RTPT2	362.00	1960.00	2458.72	2447.93
VRN5000HT2RTPT3	416.00	1520.00	2031.50	1998.01
VRN5000HT2RTPT4	412.00	1400.00	1968.50	1926.85
VRN5000HT2RTPT5	492.00	1480.00	2065.57	2042.17
VRN5000HT2RTPT6	386.40	1840.00	2370.37	2360.00
VRN5000HT2RTPT7	380.40	1280.00	1883.21	1831.01
AVERAGE	**393.37**	**1611.43**	**2160.93**	**2131.61**

Table 60: Results for F_{ept}/h_0^2, $F_{e1.5}/h_0^2$, $F_{infl}/h_0 \cdot u_{infl}$ and $F_{flow}/h_0 \cdot u_{flow}$ for HT2 LVDT experiments

DIC EXPERIMENT	YIELD STRESS F_{ept}/h_0^2 (MPa)	YIELD STRESS $F_{e1.5}/h_0^2$ (MPa)	UTS $F_{infl}/h_0 \cdot v_{infl}$ (MPa)	UTS $F_{flow}/h_0 \cdot v_{flow}$ (MPa)
VRN5000HT2RTPT1	350.80	2040.00	2695.65	2641.51
VRN5000HT2RTPT2	416.00	2200.00	2818.18	2795.40
VRN5000HT2RTPT3	556.00	1720.00	2330.28	2265.77
VRN5000HT2RTPT4	516.00	1560.00	2232.14	2161.99
VRN5000HT2RTPT5	504.00	1640.00	2330.10	2282.83
VRN5000HT2RTPT6	508.00	2080.00	2704.55	2681.82
VRN5000HT2RTPT7	480.00	1480.00	2121.74	2049.90
AVERAGE	**475.83**	**1817.14**	**2461.80**	**2411.31**

Table 61: Results for F_{ept}/h_0^2, $F_{e1.5}/h_0^2$, $F_{infl}/h_0 \cdot v_{infl}$ and $F_{flow}/h_0 \cdot v_{flow}$ for HT2 DIC experiments

The load points F_{ept}, were used to calculate yield stress correlation function, F_{ept}/h_0^2, which averaged at 393 MPa for the displacement (LVDT) curves and 476 MPa for the deflection (DIC) curves as shown in **Table 60** and **Table 61** respectively. The energy criterion for the displacement (LVDT) curves resulted in an average yield stress correlation function, $F_{e1.5}/h_0^2$, of 1611 MPa and 1817 MPa for the deflection (DIC) curves.

The average UTS correlation functions obtained from the F_{infl} load point, $F_{infl}/h_0 \cdot u_{infl}$ and $F_{infl}/h_0 \cdot v_{infl}$, were observed to be 2161 MPa and 2462 MPa for the LVDT displacement experiments and DIC deflection experiments respectively. In the case of F_{flow} load points, the calculated UTS correlation functions, $F_{flow}/h_0 \cdot u_{flow}$ and $F_{flow}/h_0 \cdot v_{flow}$, averaged at 2132 MPa for the LVDT displacement experiments and averaged at 2411 MPa for the DIC deflection experiments.

As in the previous sections with the AR and HT1 material regimes, correlations of these findings with the conventional tests could now be carried out.

4.5.2.3.2 CWA Analysis

For the HT2 material regime, the yield and ultimate tensile strength of the material could be obtained through the CWA analytical methodology as mentioned in the AR and HT1 sections. As seen in **Figure 121**, the elastic to plastic transition load point, F_e, the maximum load point, F_m and the small punch fracture energy, E_{SP} for the selected HT2 material specimens were displayed on the load-displacement and load-deflection curves.

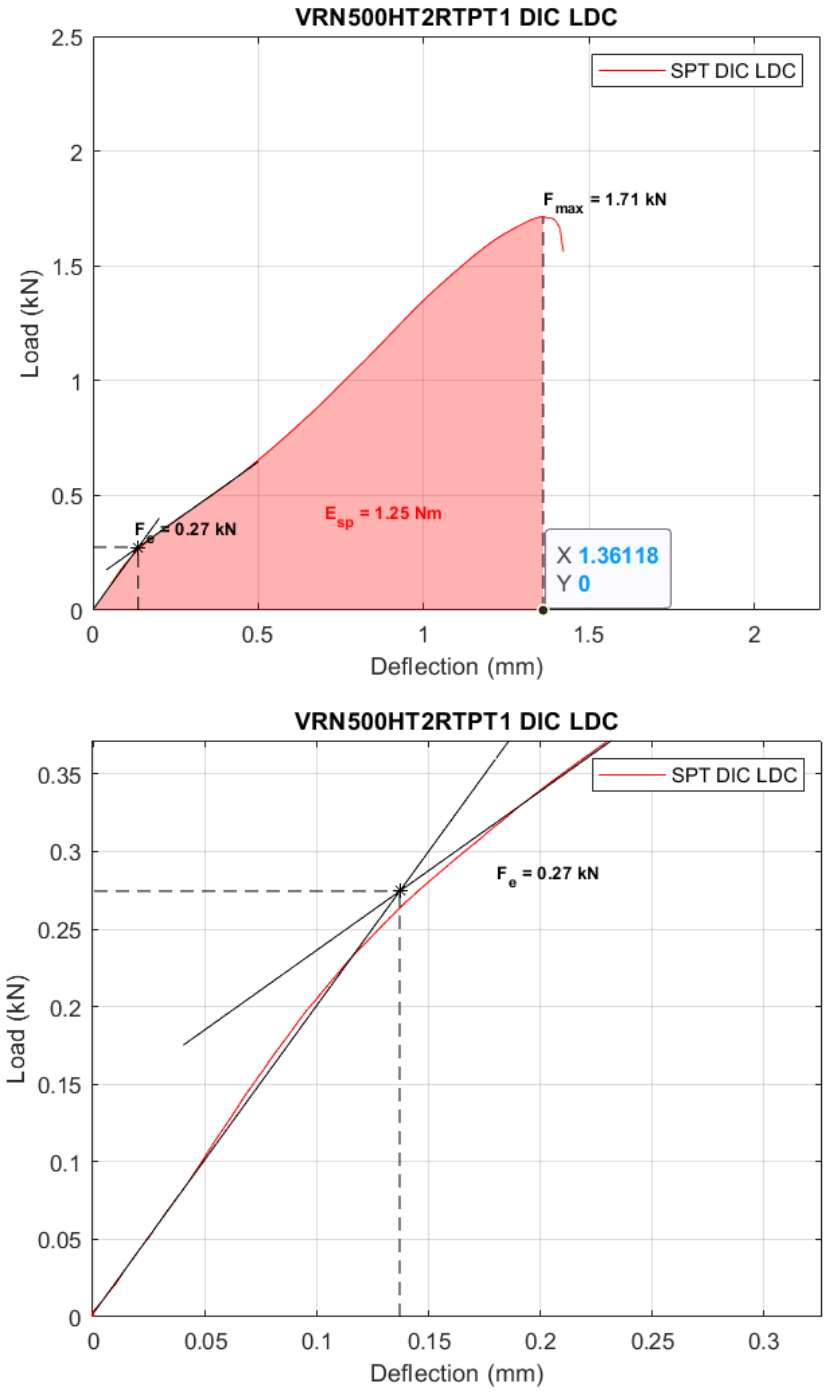

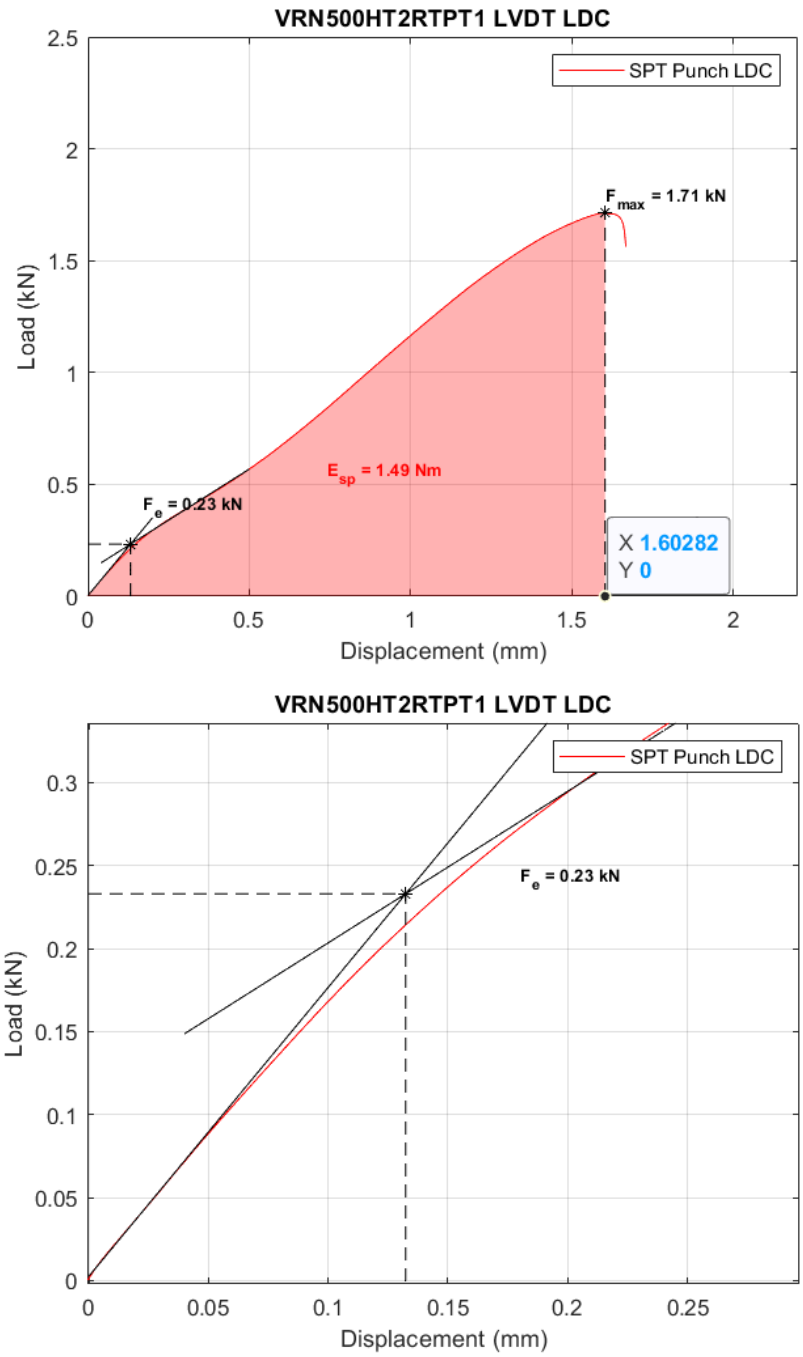

Figure 121: Graphs for determination of F_e, F_m and E_{SP} for DIC deflection (v) and LVDT displacement (u) for HT2 tests

The CWA analytical method was adopted to establish the elastic to plastic transition load point, (F_e, u_e/ F_e, v_e), the maximum load point (F_m, u_m/ F_m, v_m) and the SP fracture energy (E_{SP}) for the LVDT displacement and the DIC deflection SP curves as in the previous sections. These values were tabulated in **Table 62** for the displacement tests and **Table 63** for the deflection tests.

LVDT EXPERIMENT	h_0 (mm)	YIELD DISPLACEMENT u_e (mm)	YIELD LOAD F_e (kN)	MAX DISPLACEMENT u_m (mm)	MAX LOAD F_m (kN)	SMALL PUNCH ENERGY E_{SP} (J)
HT2RTPT1	0.50	0.132	0.23	1.603	1.71	1.49
HT2RTPT2	0.50	0.107	0.25	1.381	1.58	1.19
HT2RTPT3	0.50	0.0501	0.15	1.828	1.63	1.66
HT2RTPT4	0.50	0.0549	0.14	1.834	1.55	1.60
HT2RTPT5	0.50	0.161	0.21	1.711	1.54	1.46
HT2RTPT6	0.50	0.0942	0.20	1.570	1.68	1.45
HT2RTPT7	0.50	0.0528	0.12	1.862	1.56	1.56
AVERAGE	**0.50**	**0.0931**	**0.19**	**1.684**	**1.61**	**1.49**

Table 62: Results of F_e, F_m and E_{SP} for HT2 LVDT displacement (u) tests

From **Table 62**, the yield load points, F_e, for the LVDT displacement tests ranged from 0.12 kN to 0.25 kN, averaging at 0.19 kN. The maximum load points, F_m, averaged at 1.61 kN, ranging from 1.54 kN to 1.71 kN for the tests. E_{SP} ranged from 1.45 J to 1.66 J and averaged at 1.49 J.

For the DIC deflection curves, the data captured in **Table 63** showed that F_e values ranged from 0.12 kN to 0.29 kN. The F_m values were observed to range from 1.54 kN to 1.71 kN and the E_{SP} values ranged from 0.97 J to 1.38 J for the tests. F_e, F_m and E_{SP} averaged at 0.204 kN, 1.61 kN and 1.23 J respectively.

DIC EXPERIMENT	h_0 (mm)	YIELD DEFLECTION v_e (mm)	YIELD LOAD F_e (kN)	MAX DEFLECTION v_m (mm)	MAX LOAD F_m (kN)	SMALL PUNCH ENERGY E_{SP} (J)
HT2RTPT1	0.50	0.137	0.27	1.361	1.71	1.25
HT2RTPT2	0.50	0.103	0.29	1.155	1.58	0.97
HT2RTPT3	0.50	0.037	0.17	1.544	1.63	1.38
HT2RTPT4	0.50	0.037	0.14	1.500	1.55	1.23
HT2RTPT5	0.50	0.150	0.23	1.495	1.54	1.26
HT2RTPT6	0.50	0.0719	0.21	1.357	1.68	1.25
HT2RTPT7	0.50	0.0252	0.12	1.570	1.56	1.29
AVERAGE	**0.50**	**0.0802**	**0.204**	**1.426**	**1.61**	**1.23**

Table 63: Results of F_e, F_m and E_{SP} for HT2 DIC deflection (v) tests

With the F_e, F_m and E_{SP} values obtained for both the LVDT displacement and the DIC deflection curves, the estimations of the yield and the ultimate tensile stresses of the HT2 test samples could now be calculated. **Table 64** and **Table 65** were then populated with the calculated yield and ultimate tensile stress estimations in accordance with the CWA analytical method.

LVDT EXPERIMENT	YIELD STRESS F_e/h_0^2 (MPa)	UTS $F_m/h_0 \cdot u_m$ (MPa)	SMALL PUNCH ENERGY E_{SP} (J)
HT2RTPT1	920.00	2133.50	1.49
HT2RTPT2	1000.00	2288.20	1.19
HT2RTPT3	600.00	1783.37	1.66
HT2RTPT4	560.00	1690.29	1.60
HT2RTPT5	840.00	1800.12	1.46
HT2RTPT6	800.00	2140.13	1.45
HT2RTPT7	480.00	1675.62	1.56
AVERAGE	**742.86**	**1930.17**	**1.49**

Table 64: Results for F_e/h_0^2, $F_m/h_0 \cdot u_m$ and E_{SP} for HT2 LVDT experiments

DIC EXPERIMENT	YIELD STRESS F_e/h_0^2 (MPa)	UTS $F_m/h_0 \cdot v_m$ (MPa)	SMALL PUNCH ENERGY E_{SP} (J)
HT2RTPT1	1080.00	2512.86	1.25
HT2RTPT2	1160.00	2735.93	0.97
HT2RTPT3	680.00	2111.40	1.38
HT2RTPT4	560.00	2066.67	1.23
HT2RTPT5	920.00	2060.20	1.26
HT2RTPT6	840.00	2476.05	1.25
HT2RTPT7	480.00	1987.26	1.29
AVERAGE	**817.14**	**2278.62**	**1.23**

Table 65: Results for F_e/h_0^2, $F_m/h_0 \cdot v_m$ and E_{SP} for HT2 DIC experiments

There is a significant range in the calculated yield, 480 MPa to 1000 MPa and 480 MPa to 1160 MPa for the LVDT and DIC experiments respectively. This variability can be attributed to the small nature of the test sample, as the yield values obtained are influenced by localised differences in the material, which may vary from one region to another. In the case of the LVDT displacement experiments, the average yield stress correlation function, F_e/h_0^2 and the subsequent average ultimate tensile stress correlation function, $F_m/h_0 \cdot u_m$, calculated as shown in **Table 64** was 743 MPa and 1930 MPa respectively. In the case for the DIC deflection experiments, **Table 65** showed the yield stress function, F_e/h_0^2, and the ultimate tensile stress function, $F_m/h_0 \cdot v_m$, averaged at 817 MPa and 2279 MPa respectively. As in the previous sections and material regimes, the estimations for the DIC experiment results were higher than the LVDT experiment values.

4.5.2.3.3 Hahner Analysis

As established in the previous sections, the yield stress for the HT2 material can be obtained from the SP deflection and displacement curves using the analytical approach proposed by Hahner et al. [7]. The three offset points can be seen in **Figure 122**, and these points were used to quantify the elastic to plastic transition region.

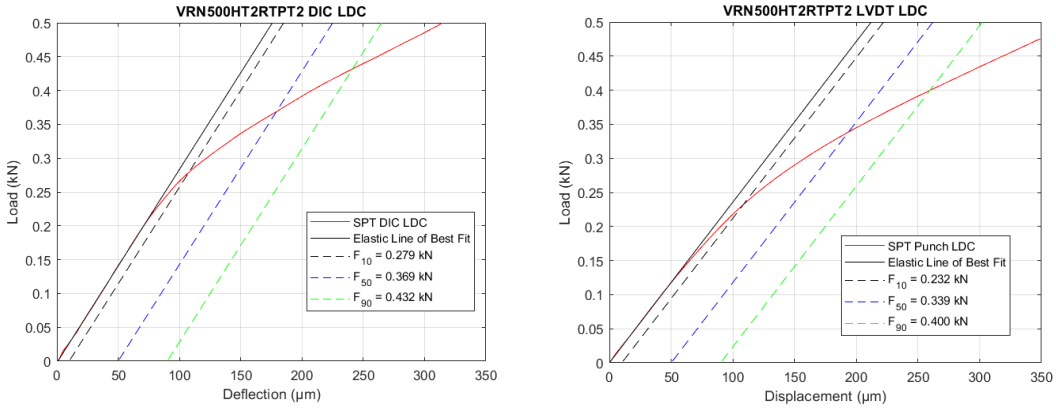

Figure 122: Figure of curvature quantification at three offsets i.e., 10 µm, 50 µm and 90 µm (DIC deflection and LVDT displacement)

As seen in **Figure 122**, the load points corresponding to the three offset points were identified and recorded. Using **Equation 26**, the curvature (K) values were derived from the load values that were obtained from the SPT deflection and displacement curves. The load points F_{10}, F_{50} and F_{90}, the curvature, K, and the subsequent yield stress estimation were recorded and tabulated in **Table 66** and **Table 67**.

LVDT EXPERIMENT	h_0 (mm)	YIELD LOAD F_{10} (kN)	YIELD LOAD F_{50} (kN)	YIELD LOAD F_{90} (kN)	CURVATURE K	YIELD STRESS σ_y (MPa)
HT2RTPT1	0.50	0.219	0.338	0.409	0.253	353.37
HT2RTPT2	0.50	0.232	0.339	0.400	0.274	391.17
HT2RTPT3	0.50	0.122	0.208	0.247	0.376	299.52
HT2RTPT4	0.50	0.062	0.157	0.201	0.367	226.08
HT2RTPT5	0.50	0.217	0.287	0.336	0.176	188.14
HT2RTPT6	0.50	0.151	0.263	0.326	0.280	311.81
HT2RTPT7	0.50	0.142	0.181	0.207	0.200	140.46
AVERAGE	**0.50**	**0.164**	**0.253**	**0.304**	**0.275**	**272.94**

Table 66: Results of offset loads F_{10}, F_{50}, F_{90}, curvature K and yield stress estimation σ_Y for HT2 LVDT tests

DIC EXPERIMENT	h_0 (mm)	YIELD LOAD F_{10} (kN)	YIELD LOAD F_{10} (kN)	YIELD LOAD F_{10} (kN)	CURVATURE K	YIELD STRESS σ_y (MPa)
HT2RTPT1	0.50	0.267	0.371	0.448	0.149	191.35
HT2RTPT2	0.50	0.279	0.369	0.432	0.176	241.89
HT2RTPT3	0.50	0.168	0.229	0.270	0.196	173.11
HT2RTPT4	0.50	0.110	0.188	0.228	0.322	263.35
HT2RTPT5	0.50	0.209	0.276	0.330	0.107	83.37
HT2RTPT6	0.50	0.186	0.287	0.352	0.217	247.50
HT2RTPT7	0.50	0.103	0.167	0.194	0.407	240.48
AVERAGE	**0.50**	**0.189**	**0.270**	**0.322**	**0.225**	**205.86**

Table 67: Results of offset loads F_{10}, F_{50}, F_{90}, curvature K and yield stress estimation σ_Y for HT2 DIC tests

From the LVDT displacement related results, the yield stress estimation, σ_Y, ranged from 140 MPa to 391 MPa and averaged at 273 MPa as shown in **Table 66**. **Table 67**, containing the DIC deflection related results, had the yield stress estimation, σ_Y, averaging at 206 MPa, as the yield values ranged from 83 MPa to 263 MPa. As in the HT1 material estimations, significant differences in the singular test yield stress were observed, as some test curvature values did not satisfy the piece-wise **Equation 26**, resulting in the disparity in the yield stress estimations. Even though most yield stress values obtained were in a similar stress range, the results showed limited consistency in the analysis and tests for the HT2 material regime.

4.5.2.3.4 DIC Crack Detection Analysis

The SED evolution of the SPT for HT2RTPT4 is displayed in **Figure 123**. The evaluated step 1013 corresponded to a deflection, v_{crack} of 0.86 mm, a displacement, u_{crack} of 0.97 mm and a load, F_{crack} of 0.92 kN as shown in **Figure 124** and **Figure 125**.

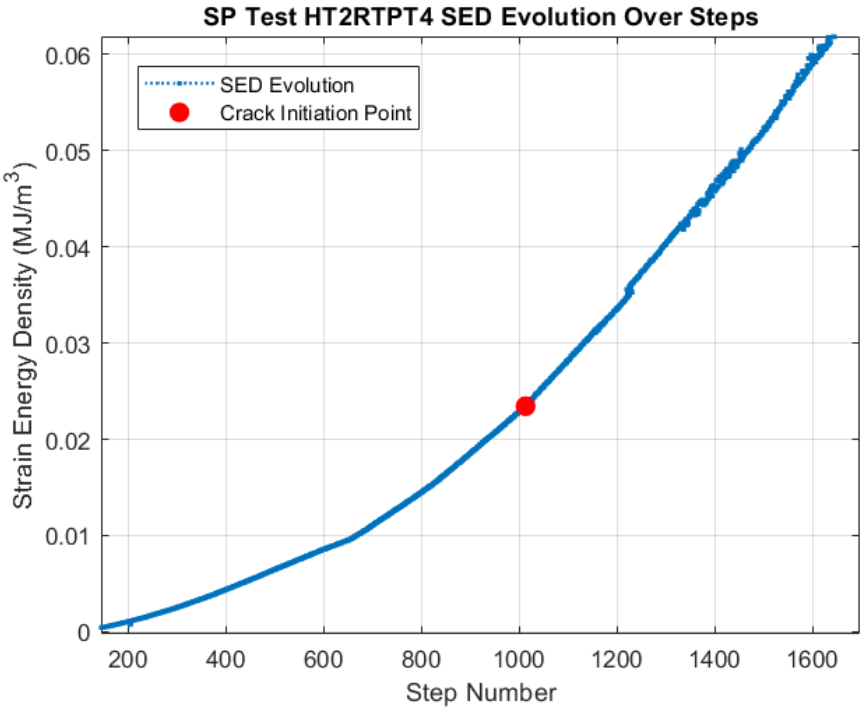

Figure 123: SED evolution for HT2RTPT4 over DIC system steps

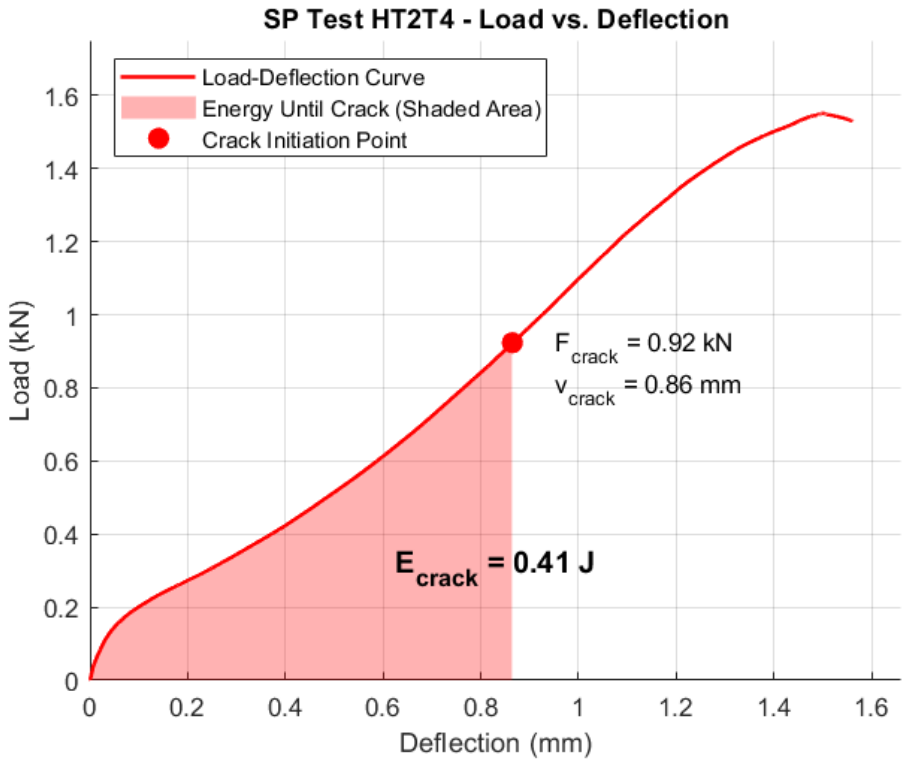

Figure 124: SPT HT2T4 DIC LDC with crack parameters v_{crack}, F_{crack} and E_{crack}

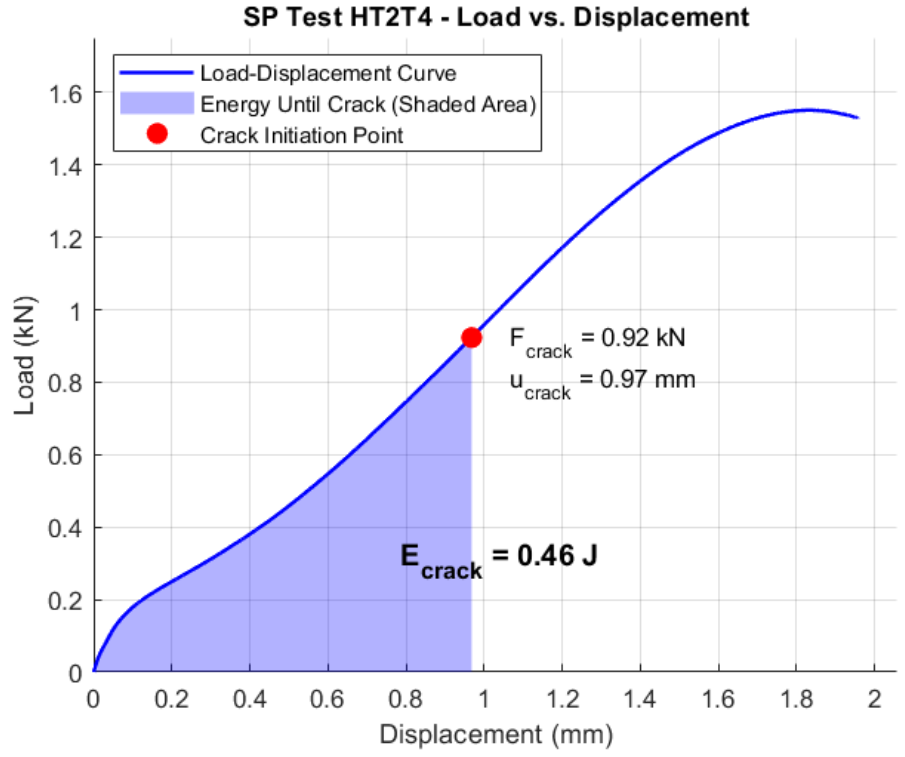

Figure 125: SPT HT2T4 LVDT LDC with crack parameters u_{crack}, F_{crack} and E_{crack}

Table 68 and **Table 69** contain the crack initiation load, F_{crack}, the displacement/deflection at the crack detection point, u_{crack}/v_{crack}, and the E_{crack} for the LVDT displacement tests and the DIC deflection tests respectively.

LVDT EXPERIMENT	h_0 (mm)	CRACK DISPLACEMENT u_{crack} (mm)	CRACK LOAD F_{crack} (kN)	CRACK ENERGY E_{crack} (J)
HT2RTPT1	0.50	0.95	1.11	0.54
HT2RTPT2	0.50	0.72	0.87	0.35
HT2RTPT3	0.50	0.82	0.80	0.35
HT2RTPT4	0.50	0.97	0.92	0.46
HT2RTPT5	0.50	0.66	0.63	0.22
HT2RTPT6	0.50	0.30	0.40	0.07
HT2RTPT7	0.50	0.70	0.60	0.23
AVERAGE	**0.50**	**0.73**	**0.76**	**0.32**

Table 68: Results of u_{crack}, F_{crack} and E_{crack} for HT2 LVDT displacement (u) tests

DIC EXPERIMENT	h_0 (mm)	CRACK DEFLECTION v_{crack} (mm)	CRACK LOAD F_{crack} (kN)	CRACK ENERGY E_{crack} (J)
HT2RTPT1	0.50	0.83	1.11	0.48
HT2RTPT2	0.50	0.63	0.87	0.31
HT2RTPT3	0.50	0.72	0.80	0.32
HT2RTPT4	0.50	0.86	0.92	0.41
HT2RTPT5	0.50	0.57	0.63	0.19
HT2RTPT6	0.50	0.24	0.40	0.06
HT2RTPT7	0.50	0.62	0.60	0.21
AVERAGE	**0.50**	**0.64**	**0.76**	**0.28**

Table 69: Results of u_{crack}, F_{crack} and E_{crack} for HT2 DIC deflection (v) tests

In **Table 68**, the displacement test data highlighted that u_{crack} ranged from 0.3 mm to 0.97 mm and had an average of 0.73 mm. E_{crack} averaged at 0.32 J and ranged from 0.07 J to 0.54 J. For the deflection data in **Table 69**, the v_{crack} values observed ranged from 0.24 mm to 0.86 mm and averaged at 0.64 mm. The E_{crack} averaged at 0.28 J and ranged from 0.06 J to 0.48 J. The F_{crack} was observed to range from 0.4 kN to 1.11 kN and averaged at 0.76 kN. It can be observed that test 6 presented outlying data, as the results deviated significantly from the rest of the tests.

4.5.2.3.5 Summary

The yield, tensile strength and toughness properties of the HT2 condition were successfully evaluated and data was obtained and tabulated for the comparison between the various analytical methods employed. The LDC parameters required for the correlation formulations and the validation of the SPT were obtained.

4.5.2.4 AR, HT1 and HT2 Results

Figure 126 shows the graph of the load against displacement experiments for the three material regimes AR, HT1 and HT2 on one set of axes. This illustration allowed the assessment of the SP LVDT displacement tests, and the curves obtained. As expected, AR material regime exhibited the highest load points during the tests, with the least total test displacement of all three material regimes. HT1 had lower load points than AR but can be seen to be higher than HT2 material load points. These load point differences were congruent with the material expected behaviour, as the AR material had the highest strength properties, followed by the HT1 and the HT2 material in that order.

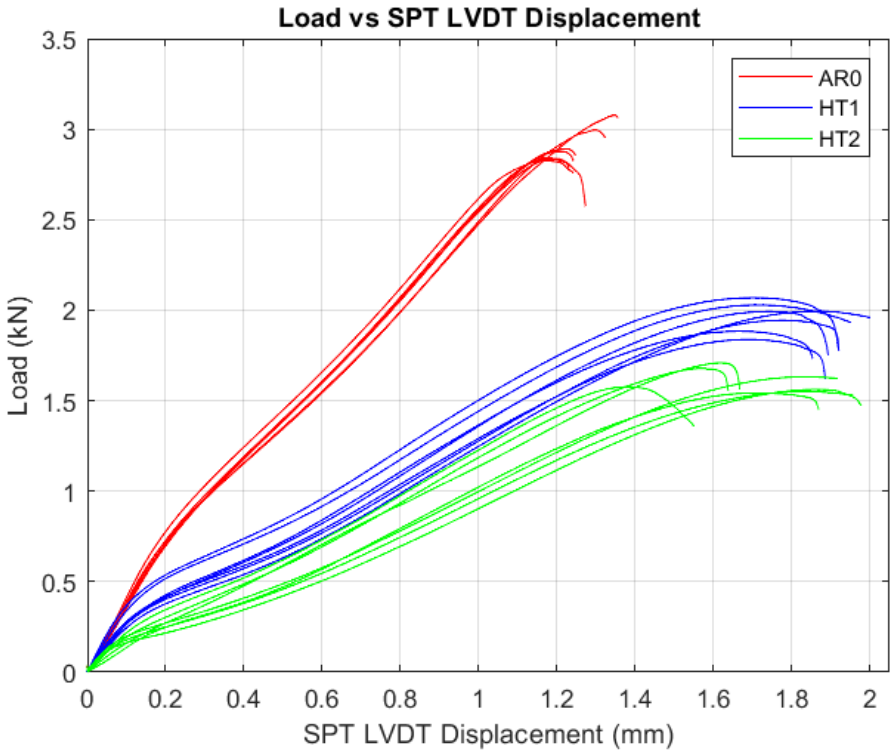

Figure 126: Graph of AR, HT1 and HT2 Load vs LVDT displacement tests

Similarly, as can be seen in **Figure 127**, the load against deflection experiments were also plotted on the same set of axes for observation. The curve behaviours observed in the illustration were similar to those in **Figure 126** as expected, as it was the same test but with a different displacement sensor as established in the previous chapters. In both cases for displacement and deflection tests, the AR material showed its lower ductility behaviour in comparison with the other material regimes since it had the highest load points but the least total displacement/deflection for the tests.

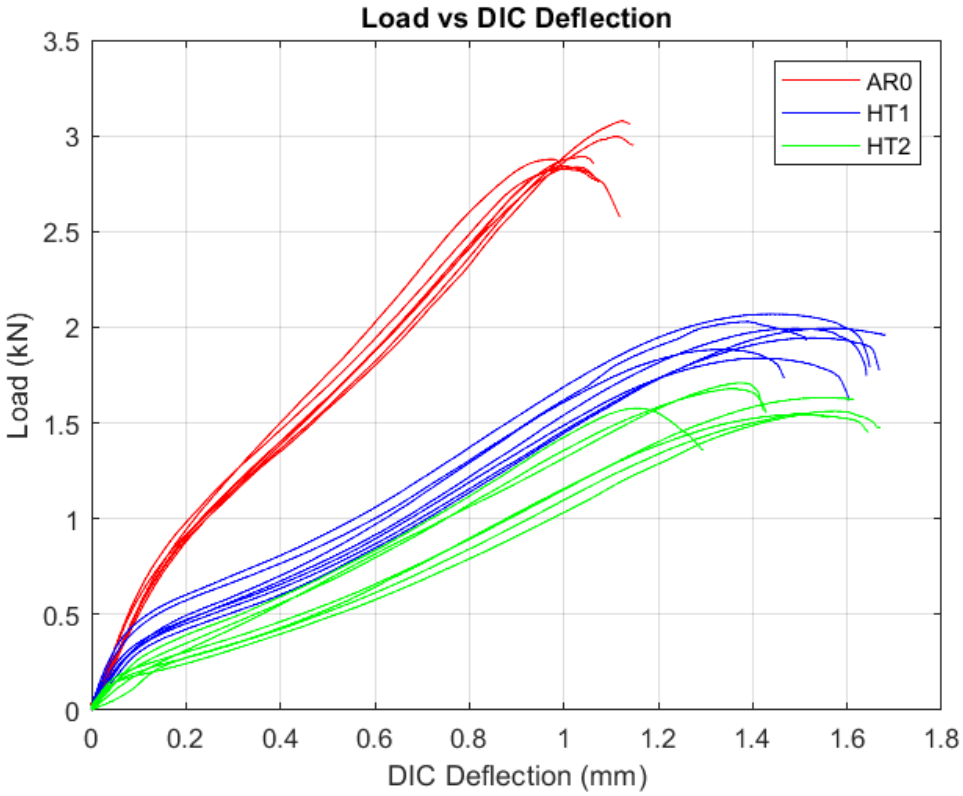

Figure 127: Graph of AR, HT1 and HT2 Load vs DIC deflection tests

However, the total displacement/deflection of the HT1 and HT2 material tests were in the same ranges, meaning that the ductility of the materials was similar. Ideally, a variation in these total test displacements/deflections could have been used to highlight the different ductile or brittle behaviour extent of the materials, allowing demarcation using the SPT curves. But this was not the case for HT1 and HT2 materials. It can be seen that some of the HT2 tests reached the maximum load points and failure earlier than the rest of the tests, which was attributed to the minor surface defects on the specimen (either from manufacturing or preparation processes) causing stress concentration and earlier crack initiation and failure.

4.6 Correlation of Mechanical Tests and SPT

The various mechanical tests that were adopted in this project enabled the attainment of the mechanical properties of the material being tested. The results from the previous section were used to validate and establish correlations between the SPT and the conventional mechanical tests.

4.6.1 SPT and Tensile Test Correlation

4.6.1.1 Yield Stress Correlation

Figure 128 to **Figure 135** display the correlation graphs between the various SPT analytic techniques employed in this project and the tensile yield properties for the AR, HT1 and HT2 material regimes.

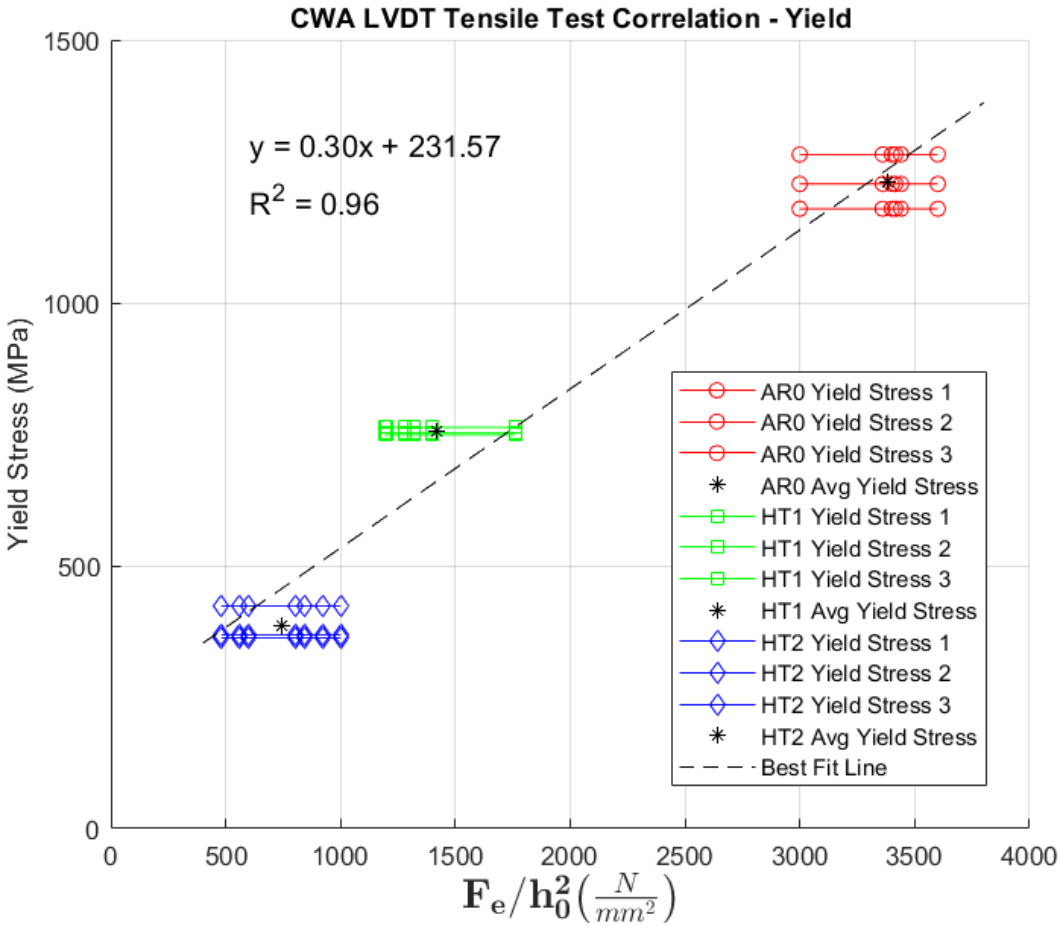

Figure 128: Correlation of Yield Stress, σ_Y and F_e/h_0^2 from CWA displacement

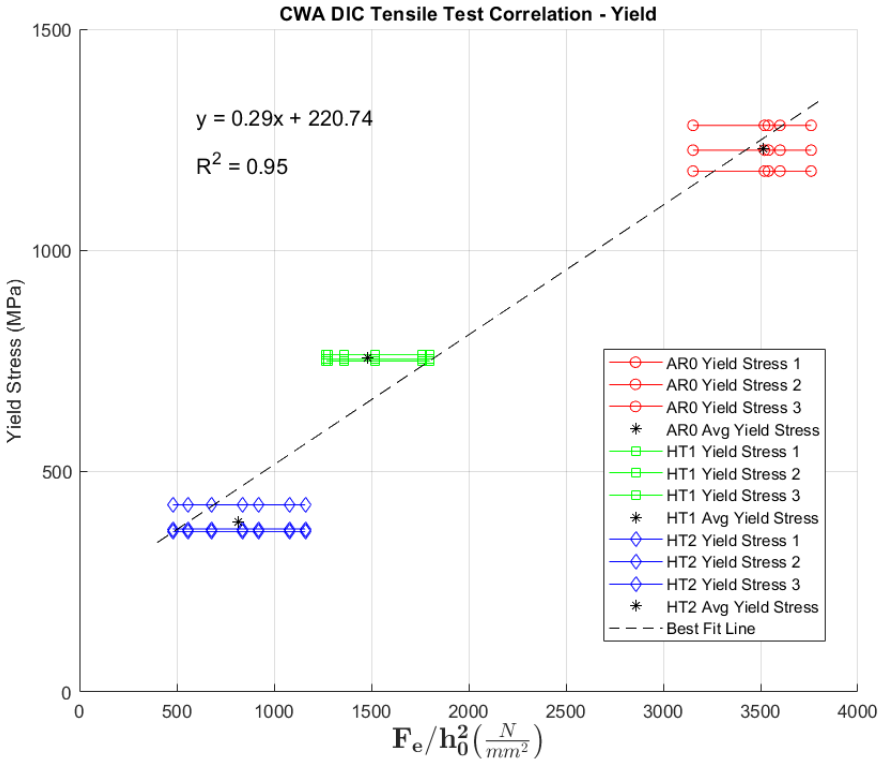

Figure 129: Correlation of Yield Stress, σ_Y and F_e/h_0^2 from CWA deflection

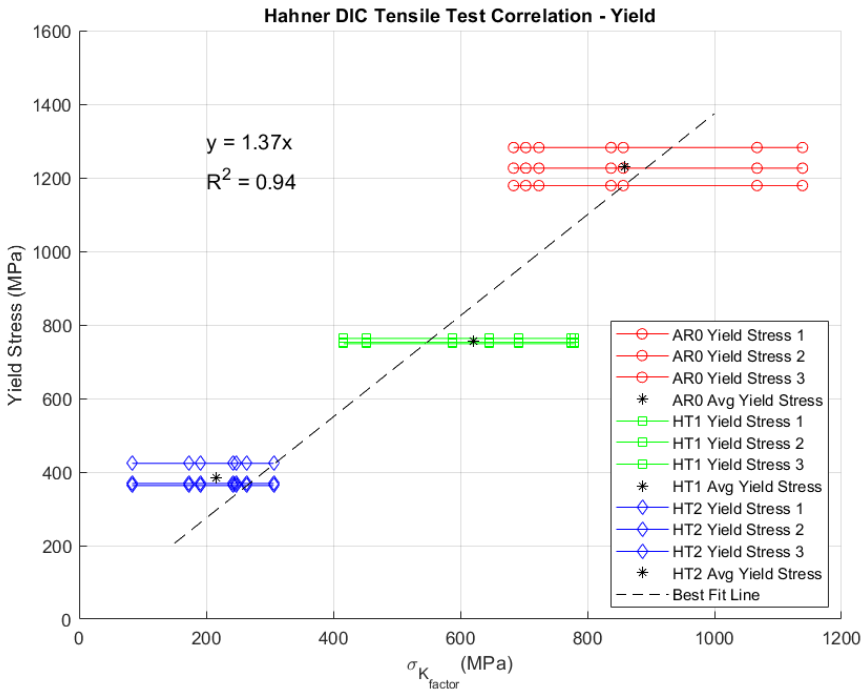

Figure 130: Correlation of Yield Stress, σ_Y and $\sigma_{Kfactor}$ from Hahner et al. deflection

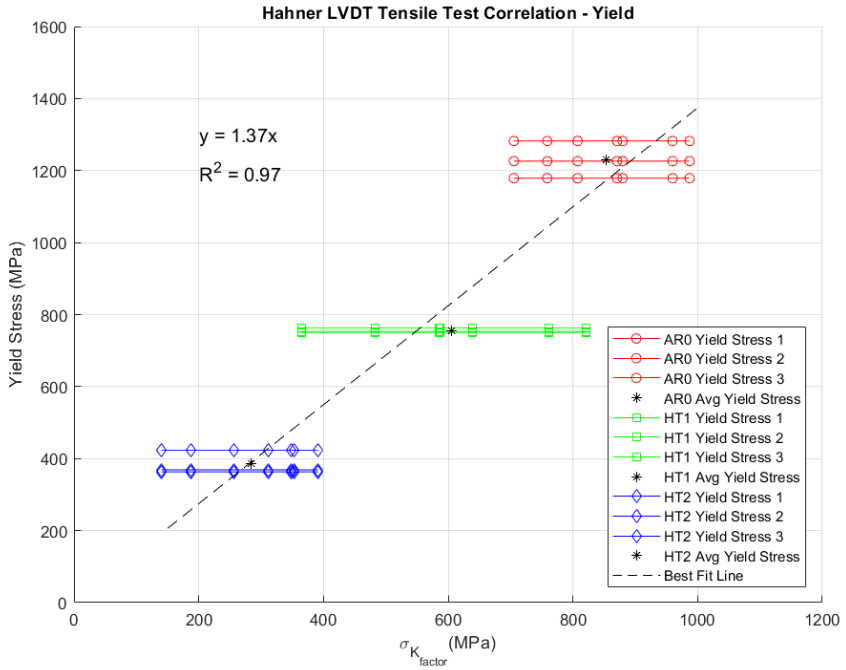

Figure 131: Correlation of Yield Stress, σ_Y and $\sigma_{Kfactor}$ from Hahner et al. displacement

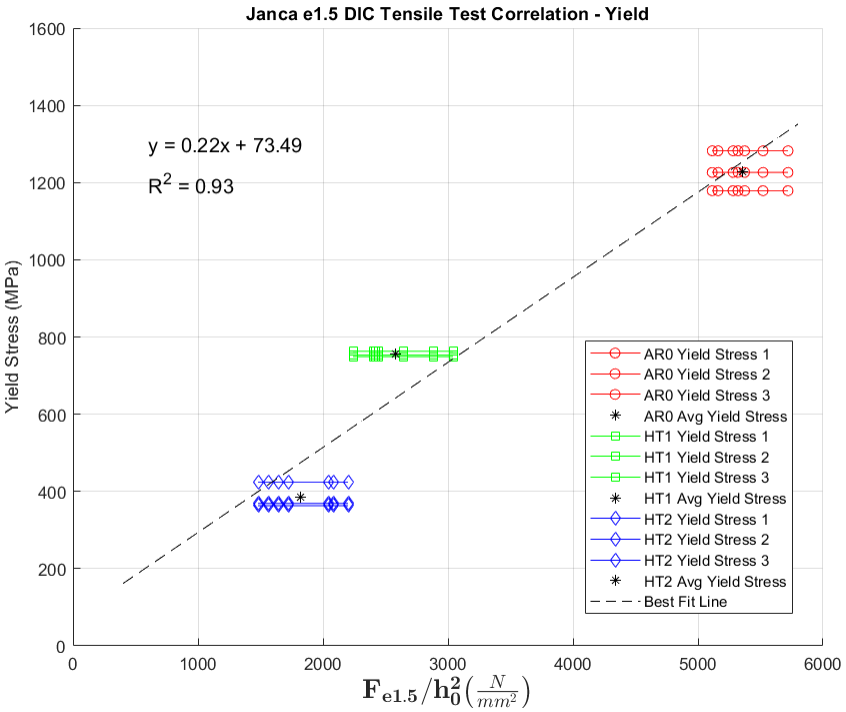

Figure 132: Correlation of Yield Stress, σ_Y and $F_{e1.5}/h_0^2$ from Janca et al. deflection

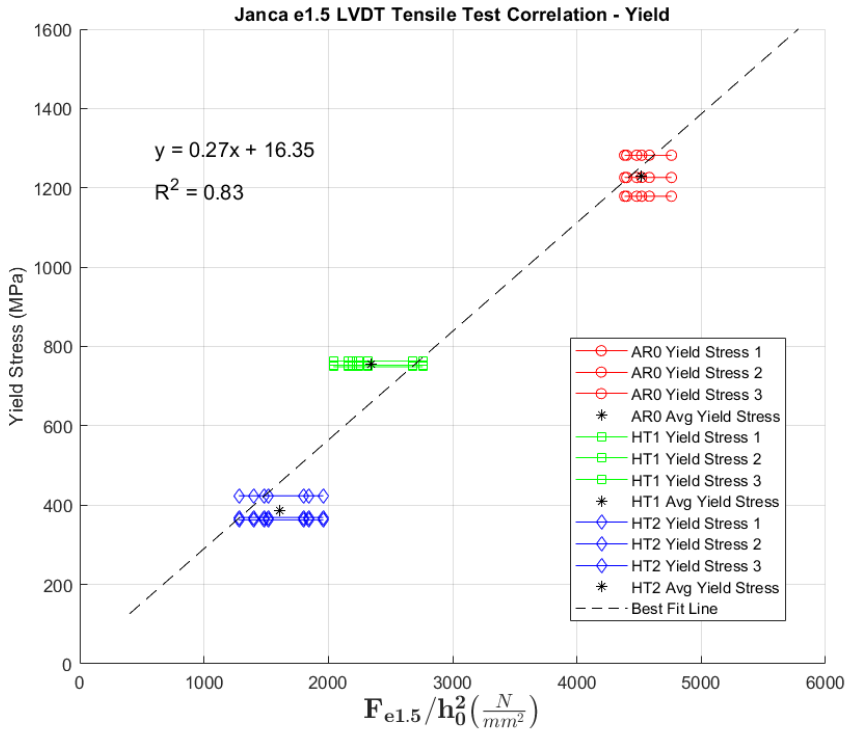

Figure 133: Correlation of Yield Stress, σ_Y and $F_{e1.5}/h_0^2$ from Janca et al. displacement

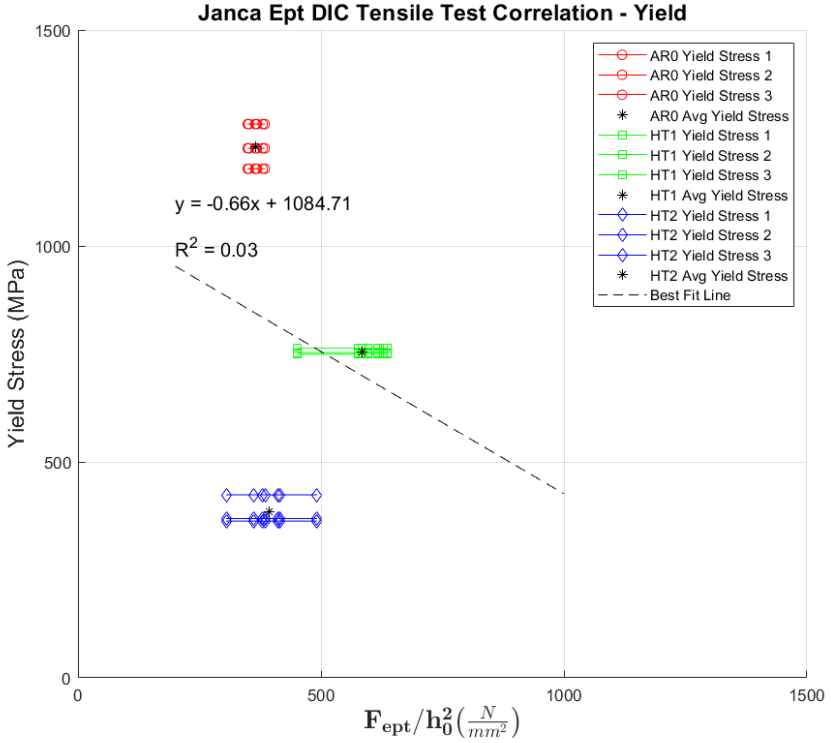

Figure 134: Correlation of Yield Stress, σ_Y and F_{ept}/h_0^2 from Janca et al. deflection

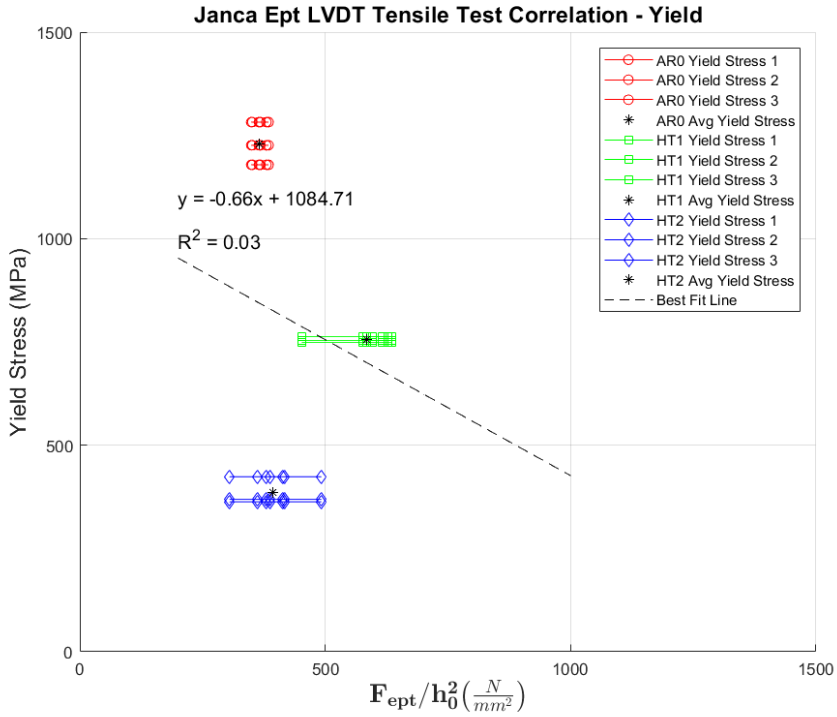

Figure 135: Correlation of Yield Stress, σ_Y and F_{ept}/h_0^2 Janca et al. displacement

LDC PARAMETER Displacement	CORRELATION FUNCTION	GOODNESS OF FIT (R^2)
F_e	$\sigma_{YS} = 0.30 \cdot \left(\frac{F_e}{h_0^2}\right) + 231.57$	0.96
F_{ept}	$\sigma_y = -0.66\left(\frac{F_{ept}}{h_0^2}\right) + 1084.71$	0.03
$F_{e1.5}$	$\sigma_y = 0.27\left(\frac{F_{e1.5}}{h_0^2}\right) + 16.35$	0.83
K_{factor}	$\sigma_y = 1.37 \cdot \sigma_{Kfactor}$	0.97

Table 70: Yield Stress correlation functions and their corresponding R^2 fit evaluations established from LVDT displacement SPT and tensile test results

LDC PARAMETER Deflection	CORRELATION FUNCTION	GOODNESS OF FIT (R^2)
F_e	$\sigma_{YS} = 0.29 \cdot \left(\frac{F_e}{h_0^2}\right) + 220.74$	0.95
F_{ept}	$\sigma_y = -0.66\left(\frac{F_{ept}}{h_0^2}\right) + 1084.71$	0.03
$F_{e1.5}$	$\sigma_y = 0.22\left(\frac{F_{e1.5}}{h_0^2}\right) + 73.49$	0.93
K_{factor}	$\sigma_y = 1.37 \cdot \sigma_{Kfactor}$	0.94

Table 71: Yield Stress correlation functions and their corresponding R^2 fit evaluations established from DIC deflection SPT and tensile test results

4.6.1.2 Ultimate Tensile Stress Correlation

Figure 136 to **Figure 143** display the correlation graphs between the various SPT analytic techniques employed in this project and the ultimate tensile stress properties for the AR, HT1 and HT2 material regimes.

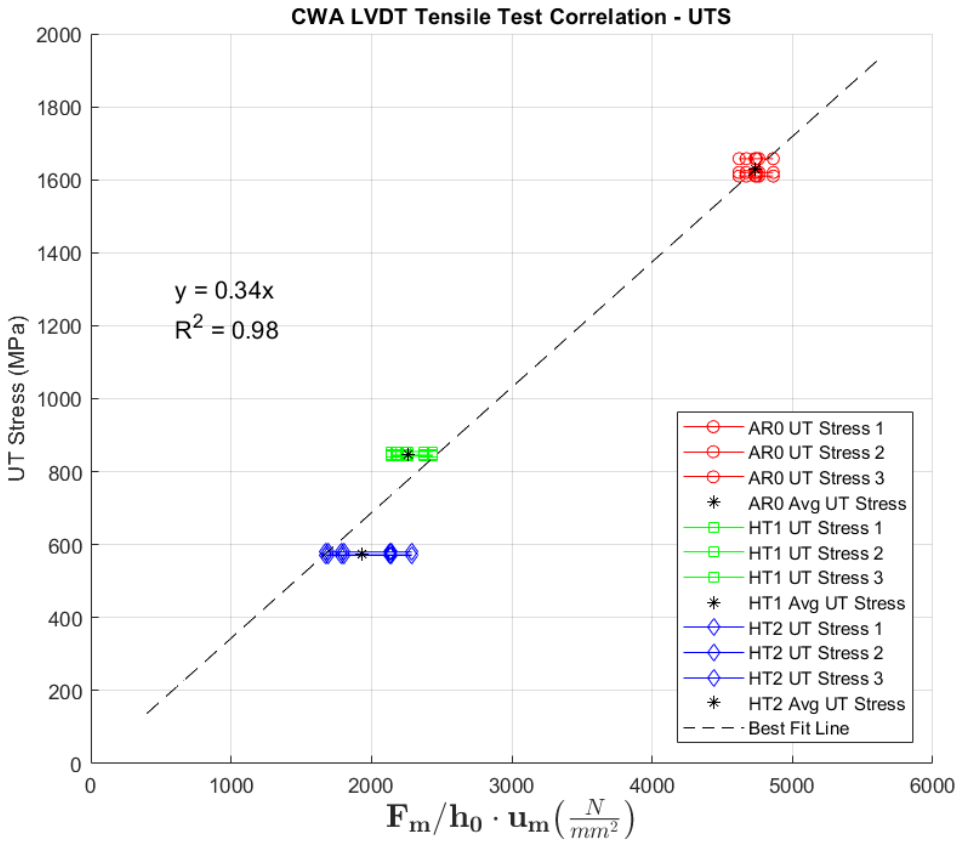

Figure 136: Correlation of Ultimate Tensile Stress, σ_{UTS} and $F_m/h_0 \cdot u_m$ from CWA displacement

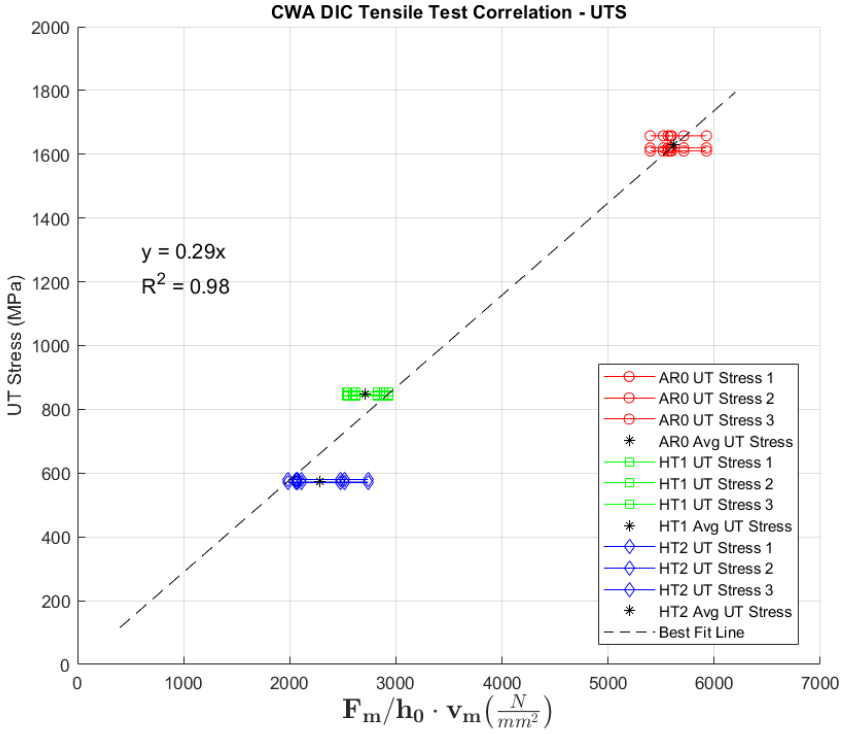

Figure 137: Correlation of Ultimate Tensile Stress, σ_{UTS} and $F_m/h_0 \cdot v_m$ from CWA deflection

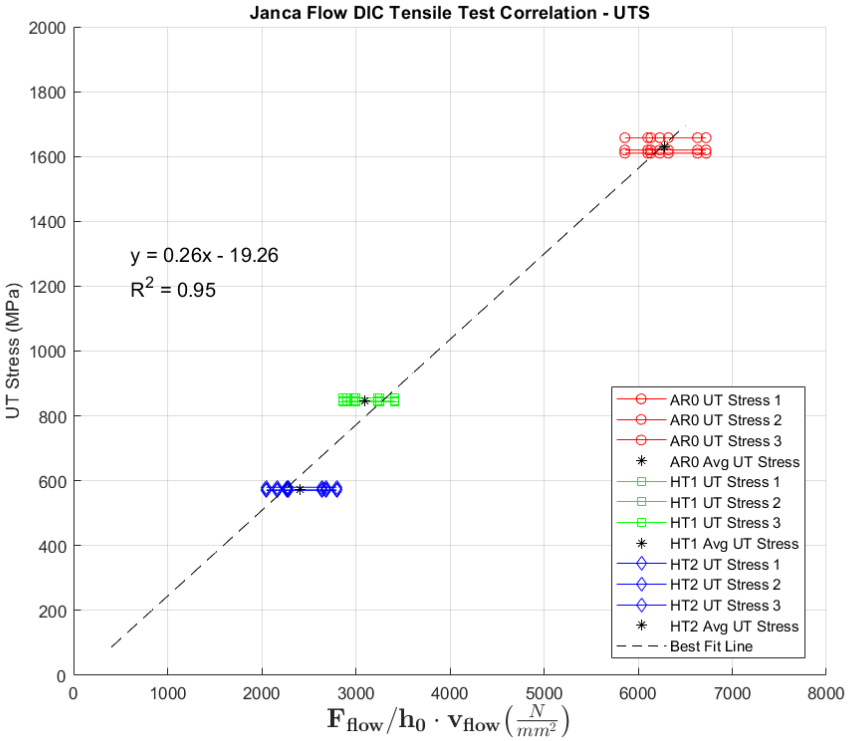

Figure 138: Correlation of Ultimate Tensile Stress, σ_{UTS} and $F_{flow}/h_0 \cdot v_{flow}$ from Janca et al. deflection

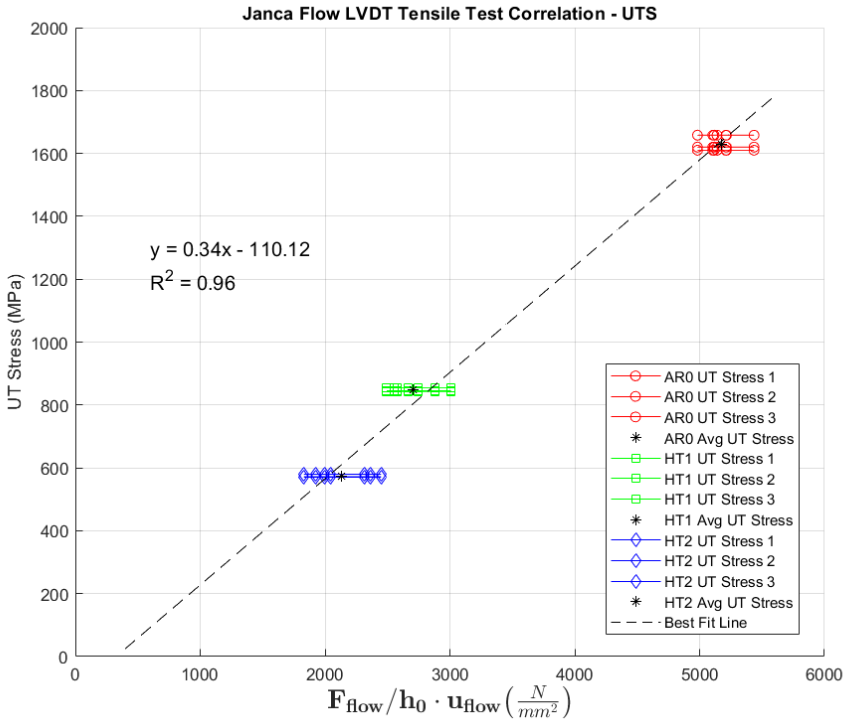

Figure 139: Correlation of Ultimate Tensile Stress, σ_{UTS} and $F_{flow}/h_0 \cdot u_{flow}$ from Janca et al. displacement

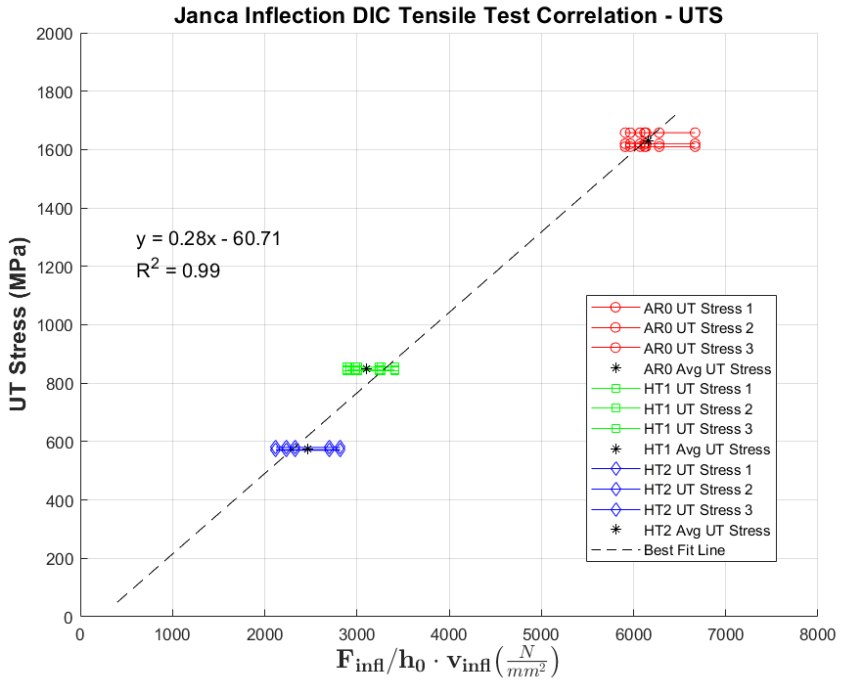

Figure 140: Correlation of Ultimate Tensile Stress, σ_{UTS} and $F_{infl}/h_0 \cdot v_{infl}$ from Janca et al. deflection

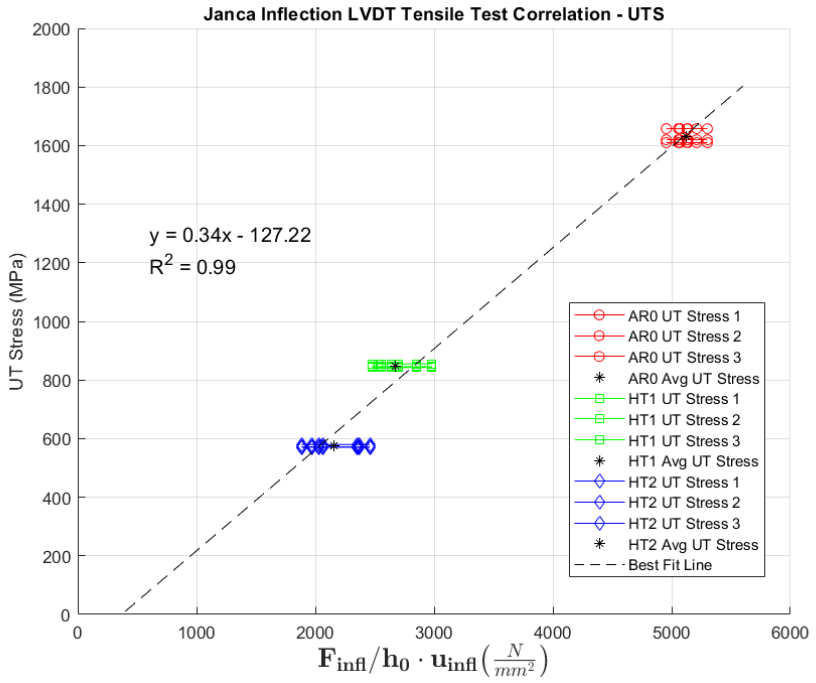

Figure 141: Correlation of Ultimate Tensile Stress, σ_{UTS} and $F_{infl}/h_0 \cdot u_{infl}$ from Janca et al. displacement

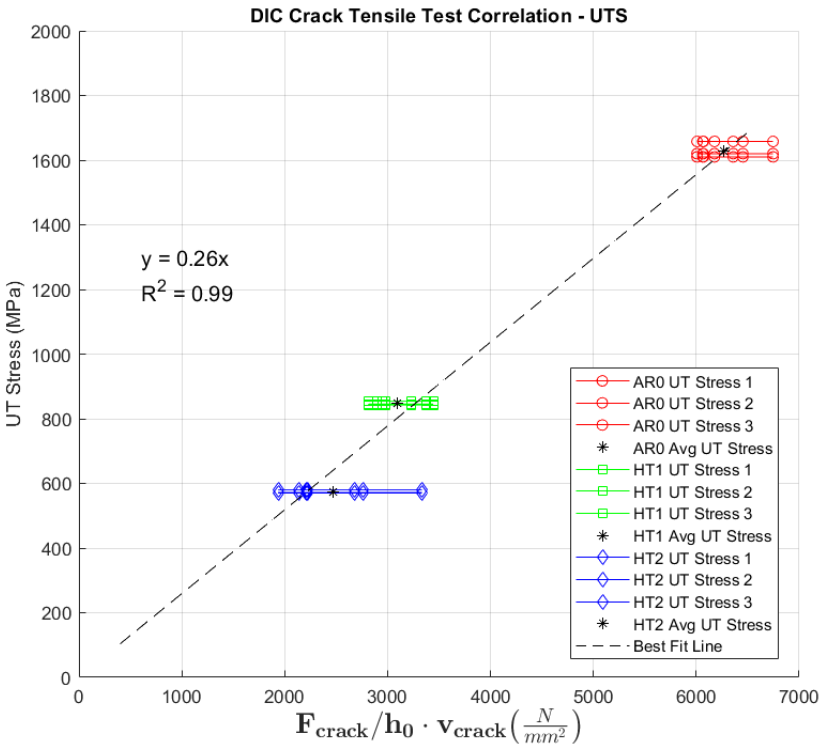

Figure 142: Correlation of Ultimate Tensile Stress, σ_{UTS} and $F_{crack}/h_0 \cdot v_{crack}$ from DIC crack detection (deflection)

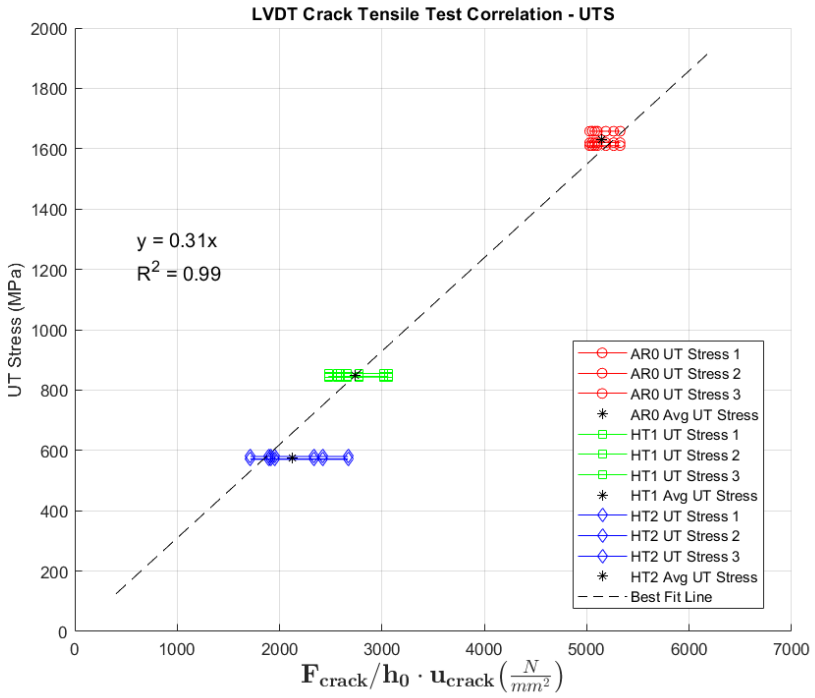

Figure 143: Correlation of Ultimate Tensile Stress, σ_{UTS} and $F_{crack}/h_0 \cdot u_{crack}$ from DIC crack detection (displacement)

LDC PARAMETER Displacement	CORRELATION FUNCTION	GOODNESS OF FIT (R^2)
F_m	$\sigma_{UTS} = 0.34 \cdot \left(\frac{F_m}{h_0 \cdot u_m}\right)$	0.98
F_{infl}	$\sigma_{UTS} = 0.34\left(\frac{F_{infl}}{h_0 \cdot u_{infl}}\right) - 127.22$	0.99
F_{flow}	$\sigma_{UTS} = 0.34\left(\frac{F_{flow}}{h_0 \cdot u_{flow}}\right) - 110.12$	0.96
F_{crack}	$\sigma_{UTS} = 0.31 \cdot \left(\frac{F_{crack}}{h_0 \cdot u_{crack}}\right)$	0.99

Table 72: Tensile Stress correlation functions and their corresponding R^2 fit evaluations established from LVDT displacement SPT and tensile test results

LDC PARAMETER Deflection	CORRELATION FUNCTION	GOODNESS OF FIT (R^2)
F_m	$\sigma_{UTS} = 0.29 \cdot \left(\frac{F_m}{h_0 \cdot v_m}\right)$	0.98
F_{infl}	$\sigma_{UTS} = 0.28\left(\frac{F_{infl}}{h_0 \cdot v_{infl}}\right) - 60.71$	0.99
F_{flow}	$\sigma_{UTS} = 0.26\left(\frac{F_{flow}}{h_0 \cdot v_{flow}}\right) - 19.26$	0.95
F_{crack}	$\sigma_{UTS} = 0.29 \cdot \left(\frac{F_{crack}}{h_0 \cdot v_{crack}}\right)$	0.99

Table 73: Tensile Stress correlation functions and their corresponding R^2 fit evaluations established from DIC deflection SPT and tensile test results

4.6.1.3 Modulus of Toughness Correlation

The energy absorbed during the SPT, the area under the LDC from the start of the test until the maximum load, E_{SP}, could be correlated with the U_T. With the identification of the crack initiation using the SED and DIC analysis, the energy absorbed during the SPT until the crack detection point, E_{crack}, could also be correlated with the U_T. The proposed power law relationship needed to be confirmed through the ln-ln plots in **Figure 144** to **Figure 147**.

Figure 144: Ln-Ln Plot – Modulus of Toughness U_T vs Small Punch Energy E_{SP} (DIC deflection)

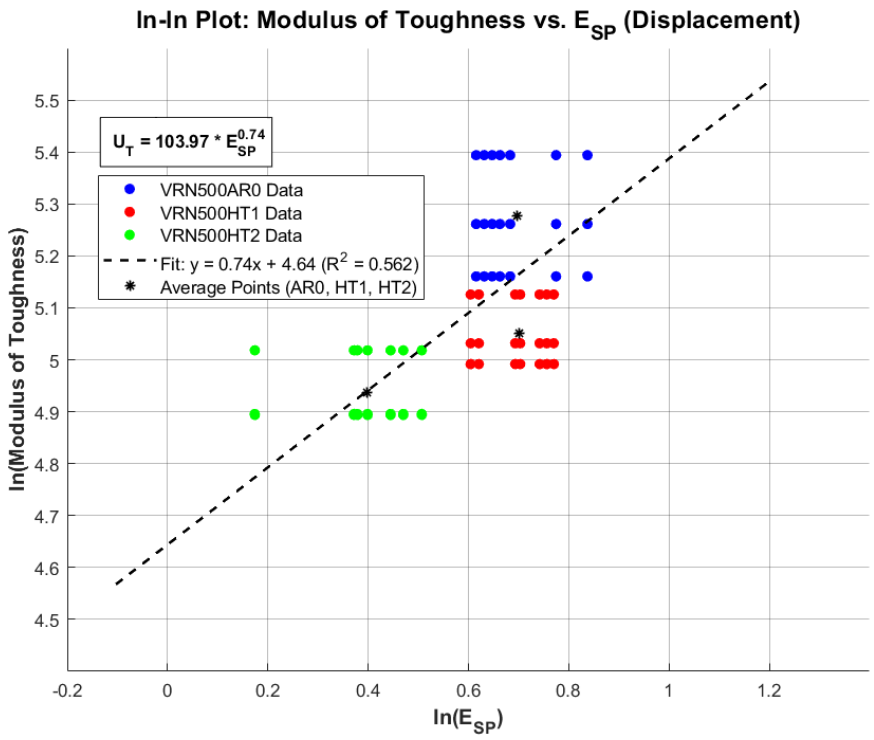

Figure 145: Ln-Ln Plot – Modulus of Toughness U_T vs Small Punch Energy E_{SP} (LVDT displacement)

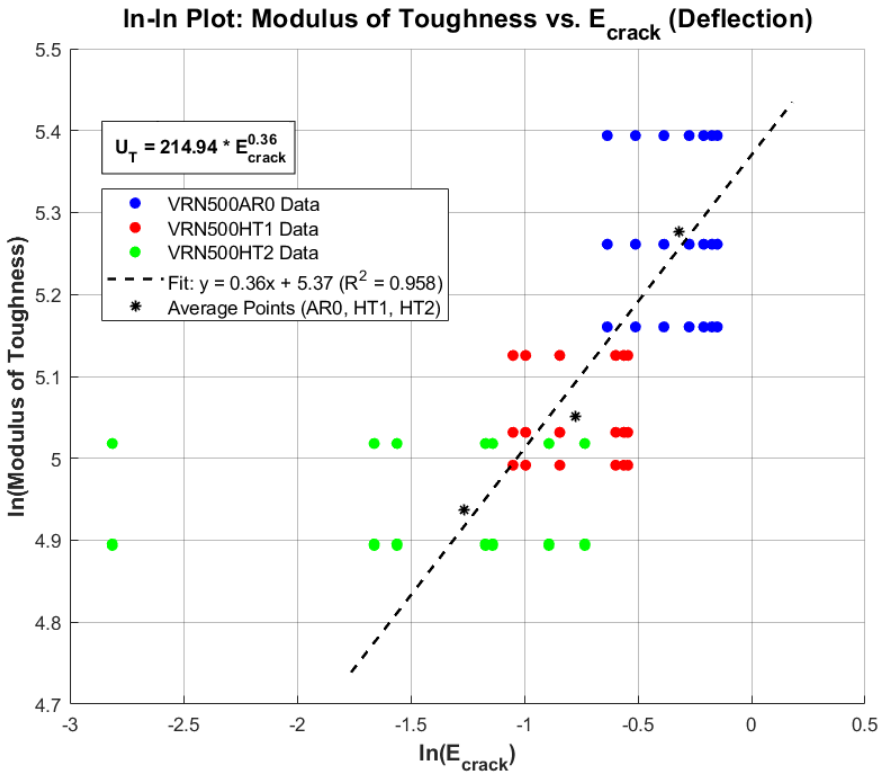

Figure 146: Ln-Ln Plot – Modulus of Toughness U_T vs Crack Detection Small Punch Energy E_{crack} (DIC deflection)

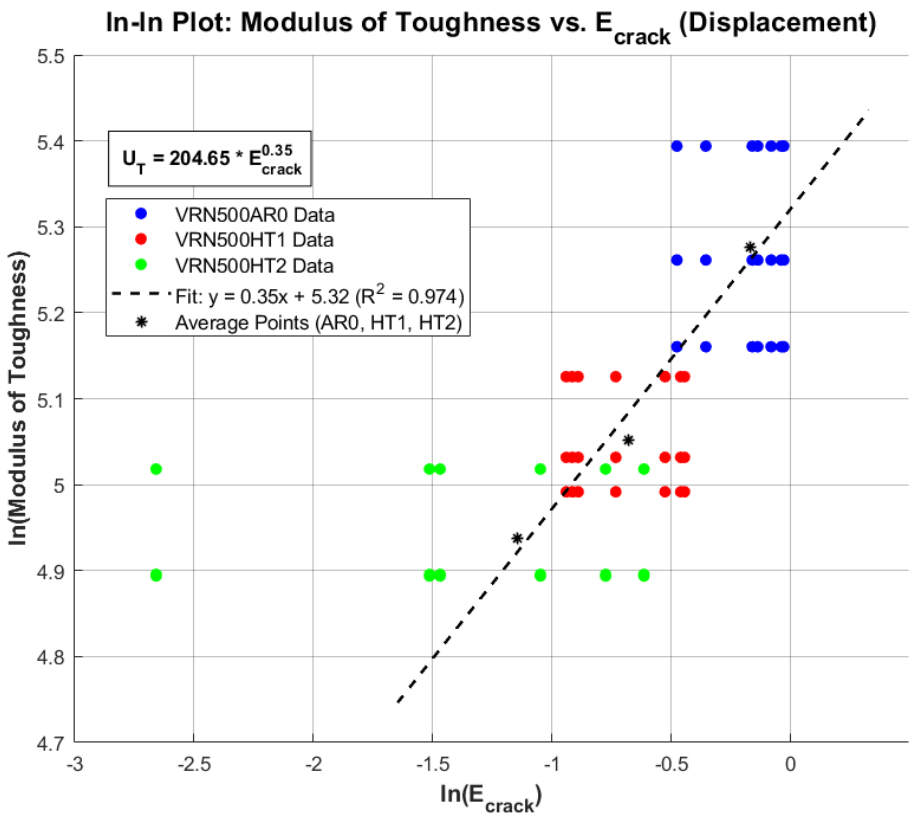

Figure 147: Ln-Ln Plot – Modulus of Toughness U_T vs Crack Detection Small Punch Energy E_{crack} (LVDT displacement)

LDC PARAMETER Displacement	CORRELATION FUNCTION	GOODNESS OF FIT (R^2)
E_{SP}	$U_T = 103.974 \cdot E_{SP}^{0.74}$	0.582
E_{crack}	$U_T = 204.65 \cdot E_{crack}^{0.35}$	0.974

Table 74: Modulus of Toughness correlation functions and their corresponding R^2 fit evaluations established from LVDT displacement SPT and tensile test results

LDC PARAMETER Deflection	CORRELATION FUNCTION	GOODNESS OF FIT (R^2)
E_{SP}	$U_T = 116.77 \cdot E_{SP}^{0.78}$	0.707
E_{crack}	$U_T = 214.94 \cdot E_{crack}^{0.36}$	0.958

Table 75: Modulus of Toughness correlation functions and their corresponding R^2 fit evaluations established from DIC deflection SPT and tensile test results

4.6.1.4 DIC Deflection and LVDT Displacement Correlation

The displacement and deflection values showed a deviation between the two sensors (DIC camera and LVDT). A correlation between the LVDT displacement and the DIC deflection was established, to provide the evidence for the deviation as well as offering a framework for understanding the relationship between the contact surface and the opposite side of the specimen. This correlation helps define the relationship between the displacement and deflection measurements obtained by the two sensors.

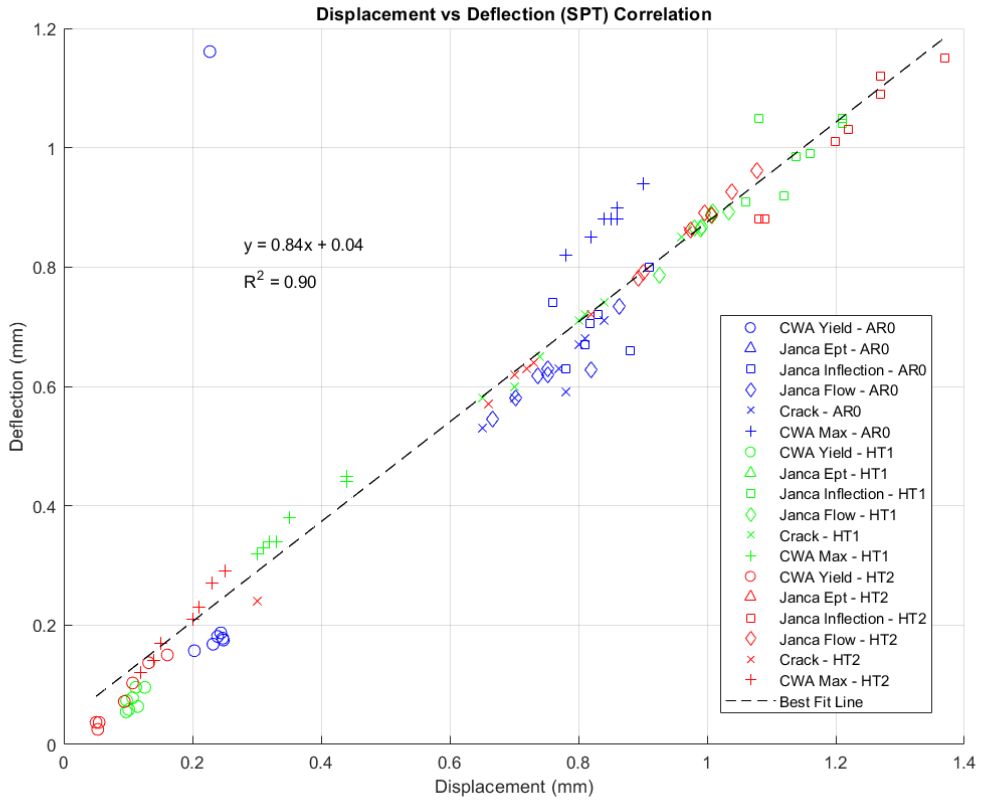

Figure 148: Correlation of DIC deflection and LVDT displacement for selected load points

The load points that were established in this project through the various analytical methods were each associated with corresponding deflection and displacement values. Plotting all the data points from every test would have resulted in excessive visual density, which in turn could obscure underlying trends and hinder meaningful interpretation of the correlation between LVDT displacement and DIC deflection. To enhance the clarity of the observed trend and to avoid using a large number of data points from all the LDCs to illustrate the discrepancies between the deflection and displacement values, only a subset of load points representative of key stages of mechanical response were selected: peak load, yield, inflection and crack initiation. The deflection vs displacement values at these selected load points were plotted in **Figure 148** to facilitate a clearer visual interpretation.

4.6.1.5 Discussion

The correlations that were established with the data gave a good insight on the material property relationship between the SPT and the tensile test. As shown in **Table 12**, several parameters could be obtained on the LDC and be used in the correlation with the tensile test properties, particularly yield strength, ultimate tensile strength and modulus of toughness.

4.6.1.5.1 Yield Stress correlation

The observations from the correlation for the yield stress highlighted a strong relationship between the SPT yield load and the tensile test yield stress. The onset of yield, characterised by the deviation from linear elastic deformation to plastic deformation, is analogous to the yield point in the SPT LDC. This deviation from linearity of the observed stress-strain or load-displacement curve, indicates the initiation of plastic deformation and provides a consistent basis for the correlation of the two test methods.

As seen in **Table 70** and **Table 71**, the different analytical methods adopted exhibited a wide range of regression goodness of fit (R^2) values, from as low as 0.03 to as high as 0.99 for the LVDT deflection curves and for the DIC deflection curves. This resulted in different correlation factors and consequently varying strengths of relationships between the different load points on the LDC and the tensile properties. A very low goodness of fit result of 0.03 for displacement and deflection curves, as observed in Janca et al.'s [31] F_{ept} method indicates that there is no linear relationship between the elastic to plastic transition load F_{ept} and the yield stress. In contrast, Hahner et al.'s [7] K-factor method for determining the yield load using the triplet of forces and the CWA method (F_e yield load) [24], [38], both demonstrated high R^2 values. The triplet of forces method exhibited R^2 values of 0.97 and 0.94 for the LVDT displacement curves and the DIC deflection curves respectively, while the CWA method achieved R^2 values of 0.96 and 0.95 for the LVDT displacement curves and the DIC deflection curves, respectively. The use of three load points to characterise the LDC curve in the critical elastic to plastic transition stage, as compared to the singular transition load point used in the CWA method, made the K-factor method the most reliable yield correlation method selected for this dissertation. Therefore, to correlate the SPT with the tensile test to determine yield stress[7]:

$$\sigma_y = 1.37 \cdot \sigma_{Kfactor}$$

Equation 35

Where $\sigma_{Kfactor}$ is found using **Equation 26**:

[7] Correlation factor is equal for both LVDT LDC and DIC LDC

$$\sigma_{Kfactor} = \begin{cases} [1.28K - 0.062]\dfrac{F_{50}}{h^2} & \text{for K} < 0.330 \\ 0.360\dfrac{F_{50}}{h^2} & \text{otherwise} \end{cases}$$

4.6.1.5.2 Ultimate Tensile Stress correlation

Another strong correlation between the SPT and the tensile test was also established through the maximum tensile stress and the SPT maximum load, both reflecting the load bearing capacity of a material. These parameters indicate the material's resistance to deformation before fracture. As established in this study, the onset of cracking presents a more accurate parameter for indicating the failure of the material during the SPT, as it occurs before the maximum load is reached on the LDC, providing an earlier and more precise assessment of the material's mechanical limits.

As seen in **Table 72** and **Table 73**, very high R^2 values were obtained for the correlation of the maximum load, F_m, as proposed by the CWA document [38], the second inflection point of load, F_{infl}, proposed by Janca et al. [31] and the load at crack detection, F_{crack}, with strong correlation fits of 0.98, 0.99 and 0.99 respectively, for both displacement and deflection curves. This showed the suitability of all the three approaches in establishing robust correlations in the data. However, as seen in the SPT results, F_{infl} loads, displacements (u_{infl}) and deflections (v_{infl}) were consistently higher than F_{crack} loads, displacements (u_{crack}) and deflections (v_{crack}), indicating that the crack detection point occurred earlier than the second inflection point. This led to the crack initiation point being selected in this study to best reflect the material failure. To correlate the SPT with the tensile test to determine the ultimate tensile stress:

$$\sigma_{UTS} = \alpha \cdot \left(\frac{F_{crack}}{h_0 \cdot v_{crack}}\right)$$

Where the correlation factor α is:
0.31 for LVDT LDC
0.29 for DIC LDC
Equation 36

4.6.1.5.3 Modulus of Toughness correlation

To verify the toughness measurement capability of the SPT, the energy absorbed by the small punch specimen during the SPT was related to the energy absorbed by the tensile specimen during the tensile test. In both cases, the energy assessments reflect the energy absorption ability of the material before fracture, giving a direct indication of toughness.

The processed data provided in **Table 74** and **Table 75**, evaluates the suitability of the power law correlations in establishing a relationship between the energy absorbed during the SPT and the U_T. The R^2 values were the primary criterion for assessing the accuracy of

the correlations and the degree of linearity provided confirmation of the best suited parameters for the correlation. The use of the E_{SP} as a variable in the power law correlation with U_T, resulted in goodness of fit values of 0.582 for the displacement LDCs and 0.707 for the deflection LDCs. On the other hand, the use of the E_{crack}, yielded significantly stronger R^2 values of 0.974 and 0.958 for the displacement curves and the deflection curves respectively. The crack detection point was selected in this study as the most reliable parameter to describe the power law relationship between the SPT and the U_T. To determine toughness using the SPT:

$$U_T = A \cdot E_{crack}^{B}$$

Where coefficient A is:
204.65 for LVDT LDC
214.94 for DIC LDC

And the exponent B is:
0.35 for LVDT LDC
0.36 for DIC LDC
Equation 37

4.6.1.5.4 Deflection vs Displacement correlation

To provide evidence for the discrepancy between deflection and displacement in this project, the correlation shown in **Figure 148** was established. As expected, the correlation achieved a strong linear fit (R^2 = 0.90), illustrating the relationship between the LVDT displacement and the DIC deflection during the SPTs. This correlation confirmed the presence of the deviation between the two measurement methods and the extent to which the variation influenced the interpretation of the LDC data. Notably, the LDC data and the deflection-displacement correlation both indicated that the LVDT consistently recorded higher displacement values than the DIC system. The thinning of the specimen during the test could have contributed to this variance, as it affected the punch-facing side of the specimen, monitored by the LVDT, more significantly (resulting in higher LVDT displacement values). In contrast, the DIC assessed the opposite surface of the specimen - not in contact with the punch - which may have experienced less apparent deformation, thereby providing lower deflection values. To determine the relationship between the LVDT displacement and the DIC deflection:

$$v = 0.84 \cdot u + 0.04$$

Where v is deflection
u is displacement
Equation 38

4.6.2 SPT, Fracture Toughness and CVN Tests Correlation

As established in literature, the correlation between the SPT and the CVN and the fracture toughness test is fundamentally related to the energy absorbed during each test. In order for a comprehensive correlation, the SPT needed to be conducted at various temperatures to attain the small punch transition temperature, T_{SP}. This critical parameter would enable the correlation of SPT results with fracture toughness and CVN tests.

While the value for the energy absorbed during the SPT, the E_{SP} was successfully determined in this study, the tests were limited to room temperature. Cryogenic and elevated temperature testing are therefore recommended as crucial test conditions in future studies to allow this correlation to be established.

However, the results obtained from the CVN and the fracture toughness test served as validation of the effect of heat treatment on the impact and fracture toughness of the VRN500 steel. The heat treatment on the AR condition resulted in notable changes in the impact toughness of the material. Through the CVN test, the AR absorbed the least impact energy at both FATT and DBTT, recording 34 J at FATT and 31 J at DBTT. In contrast, the HT1 samples exhibited significantly higher energy absorption, with 86 J at DBTT and 57 J at DBTT, while HT2 samples absorbed 45 J at FATT and DBTT. This signified the variations in the impact toughness of the heat-treated materials, thus validating the heat treatment processes adopted.

Similarly, the fracture toughness tests, albeit the invalidity of some of the test results in accordance with the ASTM E399 standard to attain the size-insensitive linear elastic, plane strain fracture toughness, K_{Qsi}, demonstrated a clear distinction in the fracture toughness properties of the heat-treated samples. HT1 exhibited a higher fracture toughness of 108 $\mathrm{MPa}\sqrt{\mathrm{m}}$ compared to HT2, which was significantly lower fracture toughness of 45 $\mathrm{MPa}\sqrt{\mathrm{m}}$. The AR condition exhibited the highest fracture toughness of 112 $\mathrm{MPa}\sqrt{\mathrm{m}}$. These findings confirmed that the heat treatments were effective in achieving the desired range in fracture toughness, thereby supporting the validity of the experimental methods in this study.

CHAPTER 5: CONCLUSIONS

The SPT was successfully carried out and data was obtained for each specimen tested. The test procedure managed to produce similar LDCs for the tests done on the same material, as key load points such as F_{infl}, F_m, F_e and F_{crack} for each material designation fell within 10% for most tests conducted. The test highlighted the variations in mechanical properties induced by the heat-treatments, evidenced by the different responses to the applied load much like in the conventional mechanical tests. AR material exhibited the highest maximum load points reached before failure (reaching loads as high as 3.08 kN). HT1 and HT2 reached 2.07 kN and 1.71 kN respectively, demonstrating the impact of heat treatment on the strength of the material. The "off the shelf" VRN500 steel was therefore successfully heat treated since the AR, HT1 and HT2 variations demonstrated a significant range in the mechanical properties as was intended.

The application of DIC allowed the visual assessment of the specimen deformation during the test and provided an alternate perspective in the fracture mechanics as the test proceeded, as the strain on the specimen surface could be tracked by the cameras. The DIC influenced LDCs had profiles very similar to the LDCs produced through the LVDT displacement. However, there was a slight difference in the displacement values obtained from the DIC (deflection) and those from the LVDT (displacement). This was possibly because the two measuring instruments were measuring the specimen deformation from opposites sides of the specimen. Given that DIC is non-contact coupled with its assessment of the deformation on the opposite surface to the punch, the slight difference was to be expected as factors like friction, thinning and specimen thickness affect these measurements. The crack onset on the DIC cameras was difficult to visually identify, as the camera resolution only allowed visual identification after significant crack propagation had already occurred. The use of DIC in measuring the surface strain on the specimen was then proposed, and this allowed the introduction of SED analysis to detect the crack onset.

The tensile test results for the as received condition, the yield, ultimate tensile stress, elongation and the U_T, were found to be 1229 MPa, 1629 MPa, 14% and 196 MJ/m^3 respectively. The UTS and the elongation established in the test was within a 2% range with the material datasheet from the supplier, showing the accuracy to which the test was conducted. The AR regime did not exhibit significant elongation in comparison with HT1 and HT2 during the tensile test, as HT2 had the most plastic deformation and an elongation of 26%. This regime also had the lowest UTS and yield stress of the three material variations, with a yield and ultimate tensile stress of 385 MPa and 574 MPa respectively, showing lower strength and higher ductility. This, however, did not translate to the tensile toughness, as the U_T for HT2 was also the lowest of the three material regimes, at 139 MJ/m^3. HT1 demonstrated intermediate properties, with the yield (744 MPa), ultimate tensile stress (847 MPa), elongation (21%) and the modulus of toughness, U_T (156 MJ/m^3).

The fracture toughness results also showed variation of properties between the material regimes. Although most of the fracture toughness results obtained failed to satisfy the validity requirements of the test method, the quantitave outcomes of the test could be used for comparison. The only samples that produced valid results were the AR, with the highest fracture toughness values averaging 112 $\mathrm{MPa}\sqrt{\mathrm{m}}$ in comparison with the HT1 and HT2 which averaged 108 $\mathrm{MPa}\sqrt{\mathrm{m}}$ and 44 $\mathrm{MPa}\sqrt{\mathrm{m}}$ respectively. The invalidity of the experiments could be rectified by using specimens of bigger size, but the material constraints made this difficult.

The CVN tests were successfully carried out at various temperatures and the FATT and DBTT values were obtained for all the test specimens. The FATT was 0 ^{o}C, -40 ^{o}C and 53 ^{o}C for the AR, HT1 and HT2 specimens respectively. The DBTT values were -9 ^{o}C for AR, -73 ^{o}C for HT1 and 57 ^{o}C for HT2. In terms of impact toughness, AR absorbed the least impact energy at both FATT and DBTT, recording 34 J at FATT and 31 J at DBTT. The HT1 samples exhibited significantly higher energy absorption, with 86 J at DBTT and 57 J at DBTT. The HT2 samples absorbed 45 J at both FATT and DBTT. This trend in the impact toughness was congruent with both the tensile toughness and the fracture toughness of the material regimes tested. However, there were several discrepancies associated with the test process, as the specimens had to be rushed to the drop test quickly in order to impact the specimen at the desired test temperature. Improvements on the temperature regulation for the impact testing is recommended for future studies, as this will improve the accuracy of the impact loading at different temperatures.

Since both the SP tests and the tensile tests were carried out at room temperature, the correlation between the LDC parameters and the tensile properties of the tested materials could be established. As shown from **Table 70** to **Table 75**, the goodness of fit values from some of the correlations ranged as high as 0.99, highlighting that the linear models were appropriate for the data. In the cases where R^2 was low, as shown in **Figure 134** and **Figure 135**, the indication was that there was a lack of linear relationship between the models and the tensile data. This F_{ept} model, which was applied in both figures, employed deflection against displacement data to identify the point of maximum curvature, assumed to correspond with the yield point of the material. However, its poor performance can be attributed to the very low magnitude of displacement and deflection values in the early stages of an SPT, making the model highly sensitive to initial data noise and measurement uncertainty. Furthermore, this method's focus on the initial stages of the SPT LDC may have caused it to overlook more prominent elastic to plastic deformation features that appear later in the test, leading to inconsistent yield predictions across samples. To validate the SPT with the yield stress of a tensile test, a strong correlation (R^2 = 0.97 for displacement LDCs and R^2 = 0.94 for deflection LDCs) in **Equation 35** was established, with a correlation factor of 1.37 for both the displacement and deflection LDCs. The yield point load on the LDC was reliably determined by the triplet of forces method proposed by Hahner et al. [7]. Additionally, the CWA method [24], [38] also demonstrated a strong correlation (R^2 = 0.96 for displacement LDCs and R^2 = 0.95 for deflection LDCs). As an established standard, it can serve as a viable alternative method for validating the SPT with the tensile yield stress.

To validate the SPT with the tensile test, the identified crack initiation point on the LDC was utilized to establish a strong correlation (R^2 = 0.99) with the UTS, in **Equation 36**. A correlation factor of 0.31 and 0.29 was determined for the displacement and deflection LDCs respectively. To utilize the SPT in the measurement of toughness, the identified crack initiation point on the LDC was yet again used to formulate the power law correlation (R^2 = 0.974 and R^2 = 0.958 for displacement and deflection LDCs respectively) in **Equation 37**. The coefficient of the expression, A, was 204.65 for the displacement LDCs and 214.94 for the deflection LDCs. The exponent, B, was determined to be 0.35 for the displacement LDCs and 0.36 for the deflection LDCs. **Equation 38** quantified the relationship between the LVDT displacement and the DIC deflection as observed during the SPTs, thereby highlighting the discrepancy between the two measurement techniques adopted in this study.

In conclusion, the results indicate that the even though they were restricted to room temperature, the SPTs were successfully conducted and effectively characterised the mechanical properties of VRN500 steel. DIC was used to obtain more information on the specimen deformation and was used in conjunction with SED for crack detection. The correlation between the SPT and the tensile test validated the SPT as a reliable mechanical testing method, as correlations were successfully established for the yield stress, ultimate tensile stress and the modulus of toughness. In the future, more SP tests could be carried out at different temperatures to correlate the energy absorbed at the different temperatures with that of the impact and fracture toughness tests to gain more information on the SPT for impact and fracture toughness correlations. The fracture toughness tests could also achieve validity according to standard requirements, provided the appropriate specimen size and machinery can be used to meet the necessary testing parameters. Future research can use the findings of this study as a foundation to carry out SPT investigations on ex-service and in-service power plant steels.

CHAPTER 6: RECOMMENDATIONS

During the experimental process, various limitations were encountered, and these influenced the extent at which the materials tested could be assessed. The following recommendations are proposed to improve and address the objectives of this project:

- **Test instruments/test machines**: this will improve some test methods particularly the CVN test, where machinery with temperature altering capabilities will improve the accuracy of the test as specimens will be tested at uniform temperature in a conditioned medium. Enhanced thermal control (e.g., using smaller furnaces or multiple thermocouples) to reduce variability attributable to heat treatment conditions can also benefit future studies
- **Sample removal and preparation**: consistent sample removal and better methods of sample preparation, use of airbrush for DIC speckle pattern evenness, use of water jet cutting instead or wire cutters, avoiding use of material cutters that could result in hot working of material
- **Metallography**: confirmation of microstructure to provide more detailed descriptions of the heat-treated material
- **Elevated and Cryogenic testing**: this will increase the quality and quantity of data obtained in the SPT, allowing for the experimental establishment of the elusive SPT transition temperatures
- **DIC**: standardized test procedure from calibration to post-test assessment which will improve test repeatability and consistency. Also, the use of higher resolution cameras to enable earlier crack onset detection during the post-test processing
- **Fracture toughness test**: use of larger specimens to ensure validity of the test process and the results obtained

It is recognised that the tensile and SPT specimens experience different stress states — uniaxial vs biaxial membrane deformation. The focus of this study was on the applied load with respect to the material block. In a tensile test, this loading direction defines the principal axis of deformation (T direction). In an SPT the punch applies force through the T direction (normal to the S-L plane), but this results in biaxial "stretching" within the sample membrane. This study emphasized maintaining consistent loading orientation and not necessarily the equivalent stress states. A detailed assessment of this distinction and its potential impact on the material mechanical response is also recommended for future studies.

BIBLIOGRAPHY

[1] S. Yang, Y. Cao, X. Ling, and Y. Qian, "Assessment of mechanical properties of Incoloy800H by means of small punch test and inverse analysis," *J Alloys Compd*, vol. 695, pp. 2499–2505, 2017, doi: 10.1016/j.jallcom.2016.11.151.

[2] G. K. Manjunath, K. U. Bhat, and G. V. Preetham Kumar, "Tensile toughness characteristics of cast Al-Zn-Mg alloys processed by equal channel angular pressing," in *Materials Science Forum*, Trans Tech Publications Ltd, 2020, pp. 161–166. doi: 10.4028/www.scientific.net/MSF.978.161.

[3] B. Bandanadjaja, W. Purwadi, N. Lilansa, D. Idamayanti, and T. R. S. Putra, "The effect of a single quenching double tempering process on the mechanical properties of NiCrMo alloyed steel casting," in *IOP Conference Series: Materials Science and Engineering*, Institute of Physics Publishing, May 2020. doi: 10.1088/1757-899X/850/1/012040.

[4] D. G. R. William D. Callister, Jr., *Materials Science and Engineering An Introduction*, 8th ed., vol. 1. Hoboken: John Wiley & Sons. Inc., 2010.

[5] J. Parker, "Embrittlement of Power Plant Steels," EPRI, Palo Alto, CA, 2013. doi: 3002001474.

[6] A. Shekhter, S. Kim, D. G. Carr, A. B. L. Croker, and S. P. Ringer, "Assessment of temper embrittlement in an ex-service 1Cr-1Mo-0.25V power generating rotor by Charpy V-Notch testing, KIc fracture toughness and small punch test," *International Journal of Pressure Vessels and Piping*, vol. 79, no. 8–10, pp. 611–615, 2002, doi: 10.1016/S0308-0161(02)00087-X.

[7] P. Hähner, C. Soyarslan, B. Gülçimen Çakan, and S. Bargmann, "Determining tensile yield stresses from Small Punch tests: A numerical-based scheme," *Mater Des*, vol. 182, p. 107974, 2019, doi: 10.1016/j.matdes.2019.107974.

[8] I. Stracey, "Development of a Small Punch Test Rig Incorporating Digital Image Correlation for Detecting Crack Initiation," University of Cape Town, Feb. 2023.

[9] F. Masuyama, "History of power plants and progress in heat resistant steels," *ISIJ International*, vol. 41, no. 6, pp. 612–625, 2001, doi: 10.2355/isijinternational.41.612.

[10] "Kriel Power Station." Accessed: Apr. 14, 2021. [Online]. Available: https://www.eskom.co.za/sites/heritage/Pages/KRIELPOWERSTATION.aspx

[11] A. Singh, V. Sharma, S. Mittal, G. Pandey, D. Mudgal, and P. Gupta, "An overview of problems and solutions for components subjected to fireside of boilers," *International Journal of Industrial Chemistry*, vol. 9, no. 1, pp. 1–15, 2018, doi: 10.1007/s40090-017-0133-0.

[12] N. Fuel, F. Air, and S. Operational, "Boiler plant and auxiliaries," *The Efficient Use of Energy*, pp. 200–248, 1982, doi: 10.1016/b978-0-408-01250-8.50019-2.

[13] "Supercritical mass: inside the new generation of coal-fired power plants." Accessed: Apr. 26, 2021. [Online]. Available: https://www.power-technology.com/features/featuresupercritical-mass-inside-the-new-generation-of-coal-fired-power-plants-4872235/

[14] S. Kubba, "Impact of Energy and Atmosphere," *Handbook of Green Building Design and Construction*, pp. 385–492, 2012, doi: 10.1016/b978-0-12-385128-4.00009-3.

[15] O. Jonas, “Steam turbines and generators,” *The Engineering Handbook, Second Edition*, pp. 74-1-74–18, 2004, doi: 10.1016/b978-0-12-804006-5.00010-1.
[16] “Majuba Power Station -’Dove’ of the Highveld.” Accessed: Apr. 14, 2021. [Online]. Available: https://www.eskom.co.za/sites/heritage/Pages/Majuba-Power-Station.aspx
[17] L. O. Tshamano, “Development of the small punch test platform to evaluate the embrittlement of power plant materials,” University of Cape Town, 2017.
[18] X. F. Guo *et al.*, “Formation of G-phase in 20Cr32Ni1Nb stainless steel and its effect on mechanical properties,” *Acta Metallurgica Sinica (English Letters)*, vol. 30, no. 9, pp. 829–839, 2017, doi: 10.1007/s40195-017-0589-0.
[19] L. Mraz, F. Matsuda, Y. Kikuchi, N. Sakamoto, and S. Kawaguchi, “Temper Embrittlement of Cast Duplex Stainless Steels After Long-Term Aging,” *Transactions of JWRI*, vol. 23, no. 2, pp. 213–222, 1994.
[20] S. Hémery, T. Auger, J. L. Courouau, and F. Balbaud-Célérier, “Effect of oxygen on liquid sodium embrittlement of T91 martensitic steel,” *Corros Sci*, vol. 76, pp. 441–452, 2013, doi: 10.1016/j.corsci.2013.07.018.
[21] R. K. Dayal and N. Parvathavarthini, “Hydrogen embrittlement in power plant steels,” *Sadhana - Academy Proceedings in Engineering Sciences*, vol. 28, no. 3–4, pp. 431–451, 2003, doi: 10.1007/BF02706442.
[22] T. L. Anderson, *Fracture Mechanics: Fundamentals and Applications*, 3rd ed., vol. 1, no. 1. Boca Raton: Taylor & Francis Group, 2005. doi: 10.1007/s42947-020-0181-2.
[23] J. D. Glassman, A. Gomez, M. E. M. Garlock, and J. Ricles, “Mechanical properties of weathering steels at elevated temperatures,” *J Constr Steel Res*, vol. 168, p. 105996, 2020, doi: 10.1016/j.jcsr.2020.105996.
[24] CEN (Comité Européen de Normalisation), “Workshop Agreement Small Punch Test Method for Metallic Materials,” *Small Punch Test Method for Metallic Materials*, pp. 1-38 Part A and 1-32 Part B, 2006.
[25] X. Mao and H. Takahashi, “Development of a further-miniaturized specimen of 3 mm diameter for tem disk (ø 3 mm) small punch tests,” *Journal of Nuclear Materials*, vol. 150, no. 1, pp. 42–52, 1987, doi: 10.1016/0022-3115(87)90092-4.
[26] D. Petersen, J. Foulds, P. Woytowitz, T. Parnell, and C. Jewett, “Fracture Toughness by Small Punch Testing,” *J Test Eval*, vol. 23, no. 1, p. 3, 1995, doi: 10.1520/jte10392j.
[27] T. E. García, C. Rodríguez, F. J. Belzunce, and C. Suárez, “Estimation of the mechanical properties of metallic materials by means of the small punch test,” *J Alloys Compd*, vol. 582, pp. 708–717, 2014, doi: 10.1016/j.jallcom.2013.08.009.
[28] M. A. Sokolov, J. D. Landes, and G. E. Lucas, *Small Specimen Test Techniques: Fourth Volume*, vol. 4. 2002.
[29] E. Fleury and J. S. Ha, “Small punch tests to estimate the mechanical properties of steels for steam power plant : I . Mechanical strength,” vol. 75, pp. 2–9, 1998.
[30] J. S. Ha and E. Fleury, “Small punch tests on steels for steam power plant (I) - Ductile-brittle transition temperature,” *KSME International Journal*, vol. 12, no. 5, pp. 818–826, 1998, doi: 10.1007/bf02945549.

[31] A. Janča, J. Siegl, and P. Haušild, “Small punch test evaluation methods for material characterisation,” *Journal of Nuclear Materials*, vol. 481, pp. 201–213, 2016, doi: 10.1016/j.jnucmat.2016.09.015.
[32] T. Milot, “Establishing correlations for predicting tensile properties based on the shear punch test and Vickers microhardness data,” no. November 2012, p. 196, 2013.
[33] E. Altstadt *et al.*, “Critical evaluation of the small punch test as a screening procedure for mechanical properties,” *Journal of Nuclear Materials*, vol. 472, pp. 186–195, 2016, doi: 10.1016/j.jnucmat.2015.07.029.
[34] E. Altstadt, M. Houska, I. Simonovski, M. Bruchhausen, S. Holmström, and R. Lacalle, “On the estimation of ultimate tensile stress from small punch testing,” *Int J Mech Sci*, vol. 136, no. December 2017, pp. 85–93, 2018, doi: 10.1016/j.ijmecsci.2017.12.016.
[35] C. Rodríguez, M. Fernández, J. G. Cabezas, T. E. García, and F. J. Belzunce, “The use of the small punch test to solve practical engineering problems,” *Theoretical and Applied Fracture Mechanics*, vol. 86, pp. 109–116, 2016, doi: 10.1016/j.tafmec.2016.08.021.
[36] B. Arroyo, J. A. Álvarez, R. Lacalle, C. Uribe, T. E. García, and C. Rodríguez, “Analysis of key factors of hydrogen environmental assisted cracking evaluation by small punch test on medium and high strength steels,” *Materials Science and Engineering A*, vol. 691, no. March, pp. 180–194, 2017, doi: 10.1016/j.msea.2017.03.006.
[37] E. Altstadt, M. Serrano, M. Houska, and A. García-Junceda, “Effect of anisotropic microstructure of a 12Cr-ODS steel on the fracture behaviour in the small punch test,” *Materials Science and Engineering A*, vol. 654, pp. 309–316, 2016, doi: 10.1016/j.msea.2015.12.055.
[38] “SLOVENSKI STANDARD (SIST),” *European Standard EN 10371: Metallic materials - Small punch test method*, Apr. 2021.
[39] M. Palanca, G. Tozzi, and L. Cristofolini, “The use of digital image correlation in the biomechanical area: A review,” *Int Biomech*, vol. 3, no. 1, pp. 1–21, 2016, doi: 10.1080/23335432.2015.1117395.
[40] S. Miao, P. Z. Pan, S. Zhao, J. Han, and P. Konicek, “A New DIC-Based Method to Identify the Crack Mechanism and Applications in Fracture Analysis of Red Sandstone Containing a Single Flaw,” *Rock Mech Rock Eng*, vol. 54, no. 8, pp. 3847–3871, 2021, doi: 10.1007/s00603-021-02472-5.
[41] Y. L. Dong and B. Pan, “A Review of Speckle Pattern Fabrication and Assessment for Digital Image Correlation,” *Exp Mech*, vol. 57, no. 8, pp. 1161–1181, Oct. 2017, doi: 10.1007/s11340-017-0283-1.
[42] F. Trebuňa, R. Huňady, Z. Bobovský, and M. Hagara, “Results and Experiences from the Application of Digital Image Correlation in Operational Modal Analysis,” Technical University of Košice, 2013.
[43] R. Bigger *et al.*, “A Good Practices Guide for Digital Image Correlation,” Oct. 2018. doi: 10.32720/idics/gpg.ed1.
[44] J. Górszczyk, K. Malicki, and T. Zych, “Application of digital image correlation (DIC) method for road material testing,” *Materials*, vol. 12, no. 15, Aug. 2019, doi: 10.3390/ma12152349.
[45] J. T. Connor, T. G. Digges, S. J. Rosenberg, and G. W. Geil, “Heat treatment and properties of iron and steel,” *National Bureau of Standards Monograph*, pp. 1–48, 1966.

[46] A. Janča, J. Siegl, and P. Haušild, “Small punch test evaluation methods for material characterisation,” *Journal of Nuclear Materials*, vol. 481, pp. 201–213, 2016, doi: 10.1016/j.jnucmat.2016.09.015.
[47] J. Torres and A. P. Gordon, “Mechanics of the small punch test: a review and qualification of additive manufacturing materials,” 2021. doi: 10.1007/s10853-021-05929-8.
[48] W. Mat and S. En, “Slovenski Standard Sist EN 10371 : 2021,” 2021.
[49] ASTM Standard E399-20, “Standard Test Method for Plane-Strain Fracture Toughness of Metallic Materials 1,” *ASTM Book of Standards*, vol. 90, no. Reapproved, pp. 1–31, 1997, doi: 10.1520/E0399-09E02.2.
[50] ASTM Standard E1820-20a, “Standard Test Method for Measurement of Fracture Toughness,” *ASTM Book of Standards*, no. January, pp. 1–54, 2013, doi: 10.1520/E1820-13.Copyright.
[51] ASTM Standard E23-18, “Standard Test Methods for Notched Bar Impact Testing of Metallic Materials,” *ASTM Book of Standards*, vol. i, pp. 1–25, 2013, doi: 10.1520/E0023-18.
[52] A. Shekhter, A. B. L. Croker, A. K. Hellier, C. J. Moss, and S. P. Ringer, “Towards the correlation of fracture toughness in an ex-service power generating rotor,” *International Journal of Pressure Vessels and Piping*, vol. 77, no. 2–3, pp. 113–116, 2000, doi: 10.1016/S0308-0161(99)00091-5.
[53] V. Karthik, K. V. Kasiviswanathan, and B. Raj, *Miniaturized testing of engineering materials*. Boca Raton: CRC Press, 2016. doi: 10.1201/9781315372051.
[54] J. Foulds and R. Viswanathan, “Determination of the toughness of in-service steam turbine disks using small punch testing,” *J Mater Eng Perform*, vol. 10, no. 5, pp. 614–619, 2001, doi: 10.1361/105994901770344782.
[55] G. Oh, “A simplified toughness estimation method based on standard tensile data,” *International Journal of Pressure Vessels and Piping*, vol. 199, Oct. 2022, doi: 10.1016/j.ijpvp.2022.104733.
[56] “Concepts: Power Law — New England Complex Systems Institute.” Accessed: Feb. 15, 2025. [Online]. Available: https://necsi.edu/power-law
[57] B. N. Lucas and W. C. Oliver, “Indentation Power-Law Creep of High-Purity Indium,” pp. 601–610, Mar. 1999.
[58] G. C. . Sih and L. de Oliveira. Faria, *Mechanics of Fracture Initiation and Propagation: Surface and volume energy density applied as failure criterion*. Springer-Science+Business Media, B.V., 1991. doi: 10.1007/978-94-011-3734-8.
[59] R. Branco, R. F. Martins, J. A. F. O. Correia, Z. Marciniak, W. Macek, and J. Jesus, “On the use of the cumulative strain energy density for fatigue life assessment in advanced high-strength steels,” *Int J Fatigue*, vol. 164, Nov. 2022, doi: 10.1016/j.ijfatigue.2022.107121.
[60] D. Wang *et al.*, “Fatigue failure and energy evolution of double-stepped fissures contained marble subjected to multilevel cyclic loads: a lab-scale testing,” *Front Mater*, vol. 10, 2023, doi: 10.3389/fmats.2023.1204264.
[61] “MACSTEEL HARD WEARING AND ABRASION RESISTANT STEELS | VRN400-450-500 Data Sheet,” 2021.

[62] N. E. Mealy and M. Bayés, *ASM Handbook Volume 8: Mechanical Testing and Evaluation*, vol. 8, no. 1. ASM International, 2000.
[63] "ASTM E399 Metallic Material Fracture Toughness Testing - ADMET." Accessed: Apr. 29, 2021. [Online]. Available: https://www.admet.com/testing-applications/testing-standards/astm-e399-metallic-material-fracture-toughness-testing/
[64] P. T. Zagierski, "Etching for microscopy," in *Surface Characterization: A User's Sourcebook*, D. Brune, R. Hellborg, H. J. Whitlow, and O. Hunderi, Eds., 2007, pp. 101–108. doi: 10.1002/9783527612451.ch5.
[65] R. D. Knutsen, "A Microstructural Examination of Duplex Ferrite-Martensite Corrosion Resisting Steels," University of Cape Town, Cape Town, 1989.
[66] ASTM E8/E8M-16a, "ASTM E8/E8M standard test methods for tension testing of metallic materials 1," *ASTM Book of Standards*, no. C, pp. 1–27, 2010, doi: 10.1520/E0008.
[67] ASTM Standard E92-17, "Standard Test Methods for Vickers Hardness and Knoop Hardness of Metallic Materials BT - Standard Test Methods for Vickers Hardness and Knoop Hardness of Metallic Materials," *ASTM Book of Standards*, vol. i, pp. 1–27, 2017, doi: 10.1520/E0092-17.2.
[68] B. Edenhofer, D. Joritz, M. Rink, and K. Voges, "Carburizing of steels," in *Thermochemical Surface Engineering of Steels: Improving Materials Performance*, Elsevier Inc., 2015, pp. 485–553. doi: 10.1533/9780857096524.3.485.
[69] "SLOVENSKI STANDARD (SIST)," *European Standard EN 60584-1: Thermocouples - Part 1: EMF specifications and tolerances (IEC 60584-1:2013)*, Oct. 2013.
[70] J. C. Chica, P. M. B. Díez, and M. P. Calzada, "A new prediction method for the ultimate tensile strength of steel alloys with Small Punch Test," *Materials*, vol. 11, no. 9, 2018, doi: 10.3390/ma11091491.
[71] B. Qin, Z. Y. Wang, and Q. S. Sun, "Effect of tempering temperature on properties of 00Cr16Ni5Mo stainless steel," *Mater Charact*, vol. 59, no. 8, pp. 1096–1100, Aug. 2008, doi: 10.1016/j.matchar.2007.08.025.
[72] Z. C. Li, H. Ding, R. D. K. Misra, and Z. H. Cai, "Deformation behavior in cold-rolled medium-manganese TRIP steel and effect of pre-strain on the Lüders bands," *Materials Science and Engineering: A*, vol. 679, pp. 230–239, Jan. 2017, doi: 10.1016/j.msea.2016.10.042.
[73] K. K. Alaneme and E. A. Okotete, "Recrystallization mechanisms and microstructure development in emerging metallic materials: A review," Mar. 01, 2019, *Elsevier B.V.* doi: 10.1016/j.jsamd.2018.12.007.
[74] B. Tanguy, J. Besson, R. Piques, and A. Pineau, "Ductile to brittle transition of an A508 steel characterized by Charpy impact test Part I: Experimental results," *Engineering Fracture Mechanics* ., vol. 72, no. 1, pp. 49–72, Jan. 2005, doi: 10.1016/j.engfracmech.2004.03.010.